UNIVERSITY OF SOUTHAMPTON

Mathematical Modelling of Lymphangiogenesis

by

Kenneth Y. Wertheim

A thesis submitted in partial fulfillment for the degree of Doctor of Philosophy

in the

Faculty of Engineering and the Environment

Engineering Sciences, Bioengineering Sciences Research Group

March 2017

UNIVERSITY OF SOUTHAMPTON

ABSTRACT

FACULTY OF ENGINEERING AND THE ENVIRONMENT
ENGINEERING SCIENCES

Doctor of Philosophy

by Kenneth Y. Wertheim

This thesis is concerned with lymphangiogenesis, the formation of new lymphatic vessels. The lymphatic system of a vertebrate is important for its homeostasis and immune responses to pathogens. Additionally, lymphangiogenesis is a means of cancer metastasis. This thesis is concerned with how the vascular endothelial growth factor C (VEGFC) may regulate lymphangiogenesis in the zebrafish embryo.

We built a reaction-diffusion-convection model to describe the distribution of VEGFC in an idealised zebrafish trunk. We solved the model with the finite element method under a wide range of conditions. The results suggest that VEGFC can act as a morphogen for the progenitor cells of the lymphatic system: it induces their differentiation during lymphangiogenesis. However, it is unlikely to be a chemotactic factor which guides their migration. The abundance of collagen I in the trunk is the key regulator: it determines the dominant transport phenomenon and the extent of VEGFC-collagen I binding, thus affecting the distribution of VEGFC. The abundance of collagen I is in turn regulated by the matrix metalloproteinase 2 (MMP2). Then, we simplified the model and studied it by Turing pattern analysis. The results suggest that VEGFC can form Turing patterns in the zebrafish embryo. However, further studies are needed before we can use this patterning mechanism to explain lymphangiogenesis.

Our conclusions about VEGFC can be tested experimentally. The demonstrated patterning mechanisms are not specific to VEGFC, MMP2, and collagen I; they can pattern other potential regulators of lymphangiogenesis, such as Cxcl12a; they can even be used to explain events other than lymphangiogenesis. Due to evolutionary conservation, they can be generalised to vertebrates other than the zebrafish too. The two mathematical models are new tools which will help in further studies about lymphangiogenesis and other biological phenomena too.

Contents

List of Figures

List of Tables

Nomenclature

Abbreviations	Meanings
2D	Two Dimensions
ADAMTS3	A Disintegrin and Metalloprotease with Thrombospondin Motifs-3
aISV	Intersegmental Artery
AKT	Protein Kinase B
BDF	Backward Differentiation Formula
BEC	Blood Endothelial Cell
BRG1	Brahma-Related Gene 1
CCBE1	Collagen-and-Calcium-Binding-Epidermal-Growth-Factor-Domain-Containing Protein 1
CLEC2	C-Type Lectin Domain Family 2
Collagen I or C1	Collagen Type I
COUP-TFII	Chicken Ovalbumin Upstream Promoter Transcription Factor II
Cxcl12a	Chemokine (C-X-C Motif) Ligand 12a
Cxcl12b	Chemokine (C-X-C Motif) Ligand 12b
Cxcr4	Chemokine (C-X-C Motif) Receptor 4
DA	Dorsal Aorta
DLAV	Dorsal Longitudinal Anastomotic Vessel
DLLV	Dorsal Longitudinal Lymphatic Vessel
DPF	Days Post-Fertilisation
ECM	Extracellular Matrix
eNOS	Endothelial Nitric Oxide Synthase
ERK	Extracellular-Signal-Regulated Kinase
FDM	Finite Difference Method
FEM	Finite Element Method
FOXC2	Forkhead Box Protein C2
FVM	Finite Volume Method
HPF	Hours Post-Fertilisation
ISLV	Intersegmental Lymphatic Vessel
ITGA9	Integrin Alpha-9
LEC	Lymphatic Endothelial Cell
LYVE1	Lymphatic Vessel Endothelial Hyaluronan Receptor 1
MAPK	Mitogen-Activated Protein Kinase
MMP	Matrix Metalloproteinase
MMP2 or M2	Matrix Metalloproteinase 2
MMP9	Matrix Metalloproteinase 9
MT1-MMP or MT1	Membrane Type I Matrix Metalloproteinase
NO	Nitric Oxide
NRP2	Neuropilin-2
ODE	Ordinary Differential Equation
PCV	Posterior Cardinal Vein
PDE	Partial Differential Equation
PDPN	Podoplanin
PI3K	Phosphoinositide 3 Kinase
PL	Parachordal Lymphangioblast
PLCγ2	Phospholipase Cγ2
proMMP2 or M2P	Precursor of MMP2
proVEGFC	Vascular Endothelial Growth Factor C Preproprotein

PROX1	Prospero Homeobox Protein 1
SLP-76	Sarcoma-Homology-2-Domain-Containing Leukocyte Protein of 76 kDa
SMC	Smooth Muscle Cell
SOX18	Sex-Determining Region Y Box 18
SYK	Spleen Tyrosine Kinase
TD	Thoracic Duct
TIMP	Tissue Inhibitor of Metalloproteinases
TIMP2 or T2	Tissue Inhibitor of Metalloproteinases 2
VEC	Venous Endothelial Cell
VEGF	Vascular Endothelial Growth Factor
VEGFC or VC	Vascular Endothelial Growth Factor C
VEGFD	Vascular Endothelial Growth Factor D
VEGFR2	Vascular Endothelial Growth Factor Receptor 2
VEGFR3	Vascular Endothelial Growth Factor Receptor 3
vISV	Intersegmental Vein

Symbols	Meanings	Units
$\sim$	Indicator of a Nondimensionalised Variable	None
a	Dimensionless Transport Parameters in the Nondimensionalised Model of the Secondary System	None
a^{ref}	Reference Values of a	None
A	Jacobian Matrix in the Linear Stability Analysis for Homogeneous Perturbations	None
α	Parameter in the Relation Between Hydraulic Conductivity and Collagen I Content	None
b	Dimensionless Kinetic Parameters in the Nondimensionalised Model of the Secondary System	None
b^{ref}	Reference Values of b	None
B	Modified Jacobian Matrix in the Linear Stability Analysis for Heterogeneous Perturbations	None
β	Parameter in the Relation Between Hydraulic Conductivity and Collagen I Content	m^2
c or $\boldsymbol{c}$	Constants or Constant Vectors in $\Delta\tilde{C}_i$'s or the $\Delta\tilde{C}_i$'s Vector	None
$C_{C1,0}$	Initial Concentration of Collagen I in the Interstitial Space Domain (Primary System)	mol m^{-3}
C_i	Concentration of Species i	mol m^{-3}
$C_{i,s}$	Concentration Scale of Species i	mol m^{-3}
$C_{i,ss}$	Steady State Concentration of Species i	mol m^{-3}
$C_{MT1,0}$	Initial Concentration of MT1-MMP in the LEC domain (Primary System)	mol m^{-3}
$[Cl]_m$	Total Mass Concentration of Collagen I, Free and VEGFC-Bound	kg m^{-3}
$[Collagen\ I]$	Mass Fraction of Collagen I (Free and VEGFC-Bound) in the Interstitial Space Domain (Primary System)	None
d	Dimensionless Parameters in B	None
D_i^{eff}	Effective Diffusivity of Species i	m^2 s^{-1}
D_i^{∞}	Diffusivity of Species i in Interstitial Fluid	m^2 s^{-1}
ΔC_i	Perturbation to $C_{i,ss}$	mol m^{-3}
η	Dimensionless Parameters in the Nondimensionalised Interstitial Flow Equations (Primary System)	None
F	Frequency in Nondimensionalised Space	None
I	Identity Matrix	None
j	Imaginary Unit	None
k	Wavenumber	None
k_B	Boltzmann Constant	kg m^2 s^{-2} K^{-1}
$k_{M2,C1}^{cat}$	Turnover Number in M2-Catalysed C1 Degradation	s^{-1}
k_i^{deg}	Degradation Rate Constant of Species i	s^{-1}
k_{act}^{eff}	Effective Activation Rate Constant of M2	mol^{-1} m^3 s^{-1}
$k_{i,j}^{on}$	Binding Rate Constant of Species i and j	mol^{-1} m^3 s^{-1}
$k_{i,j}^{off}$	Unbinding Rate Constant of Species i and j	s^{-1}
$K_M^{M2,C1}$	Michaelis-Menten Constant in M2-Catalysed C1 Degradation	mol m^{-3}
κ	Specific Hydraulic Conductivity of the Interstitial Space Domain (Primary System)	m^2
κ'	Hydraulic Conductivity of the Interstitial Space Domain (Primary System)	kg^{-1} m^3 s
L	Length Scale	m

L_{DA}	DA Vascular Permeability	kg^{-1} m^2 s
L_{DLAV}	DLAV Vascular Permeability	kg^{-1} m^2 s
L_{PCV}	PCV Vascular Permeability	kg^{-1} m^2 s
λ	Dimensionless Parameters in the Nondimensionalised Equations Governing the Modelled Concentration Dynamics (Primary System)	None
m	Magnitude of the Discrete Fourier Transform's Output	None
M_{C1}	Molar Mass of Collagen I	kg mol^{-1}
μ	Interstitial Fluid Dynamic Viscosity	kg m^{-1} s^{-1}
$\boldsymbol{n}$	Normal Vector Pointing out of the Domain it Resides in	None
ν	Volume Fraction of Dry Collagen I	None
P	Pressure	kg m^{-1} s^{-2}
P_{C1}	C1 Production Rate in the Interstitial Space Domain (Secondary System)	mol m^{-3} s^{-1}
P^{DA}	Pressure in the DA	kg m^{-1} s^{-2}
P^{DLAV}	Pressure in the DLAV	kg m^{-1} s^{-2}
P_{M2}	M2 Production Rate in the Interstitial Space Domain (Secondary System)	mol m^{-3} s^{-1}
P_{M2P}	M2P Production Rate in the LEC Domain (Primary System)	mol m^{-3} s^{-1}
P^{PCV}	Pressure in the PCV	kg m^{-1} s^{-2}
$\tilde{P}^s$	Nondimensionalised Simulated Pressure	None
P_{T2}	T2 Production Rate in the LEC Domain (Primary System)	mol m^{-3} s^{-1}
P_{VC}	VC Production Rate in the Interstitial Space Domain (Secondary System)	mol m^{-3} s^{-1}
Pe	Péclet number	None
q	Net Production Rate of Interstitial Fluid in the Interstitial Space Domain (Primary System)	kg m^{-3} s^{-1}
r_f	Radius of a Collagen I Fibril	m
$r_{s,i}$	Stokes-Einstein Radius of Species i	m
R_{VC}^{DA}	VEGFC Production Rate on the DA Surface (Primary System)	mol m^{-2} s^{-1}
R_i^{IS}	Net Production Rate of Species i in the Interstitial Space Domain (Primary System)	mol m^{-3} s^{-1}
R_i^{LEC}	Net Production Rate of Species i in the LEC Domain (Primary System)	mol m^{-3} s^{-1}
ρ	Interstitial Fluid Density	kg m^{-3}
S	Distance Between a Turing Point and the Reference Point in the Parametric Space	None
σ	Eigenvalue in Turing Pattern Analysis	None
σ_{max}	Maximum σ at One Point in the Parametric Space and at One Value of k^2	None
t	Time	s
T	Temperature	K
τ	Time Scale	s
$\boldsymbol{u}$	Interstitial Fluid Velocity	m s^{-1}
U	Velocity Scale	m s^{-1}
v_{C1}	Partial Specific Volume of Dry Collagen I	m^3 kg^{-1}
v_{C1h}	Partial Specific Volume of Hydrated Collagen I	m^3 kg^{-1}
$\boldsymbol{x}$	Position Vector	m
$\boldsymbol{w}_n$	Fourier Mode of the $\Delta\tilde{C}_i$'s Vector with the Wavenumber k; $k = n\pi$	None
ω	Volume Fraction Where Diffusion Occurs	None
$\partial\Omega_{DA}$	DA Surface (Primary System)	None

$\partial\Omega_{DLAV}$	DLAV Surface (Primary System)	None
$\partial\Omega_{LEC/IS+}$	Interface Between the Interstitial Space and LEC Domains, Seen from the Interstitial Space Domain (Primary System)	None
$\partial\Omega_{LEC/IS-}$	Interface Between the Interstitial Space and LEC Domains, Seen from the LEC Domain (Primary System)	None
$\partial\Omega_{PCV}$	PCV Surface (Primary System)	None
$\partial\Omega_{x,y}$	Outer Boundaries of the Model Zebrafish Trunk (Primary System)	None

Declaration Of Authorship

I, Kenneth Yann Wertheim, declare that the thesis entitled *Mathematical Modelling of Lymphangiogenesis* and the results presented in it are my own work, and have been generated by me as the result of my own original research. I confirm that:

- This work was done wholly or mainly while in candidature for a research degree at this University;
- Where any parts of this thesis have previously been submitted for any qualifications at this University or any other institutions, this has been clearly stated;
- Where I have consulted the published works of others, this is always clearly attributed;
- Where I have quoted from the works of others, their sources are always given. With the exception of such quotations, this thesis is entirely my own work;
- I have acknowledged all main sources of help;
- Where the thesis is based on work done by myself jointly with others, I have made clear exactly what was done by others and what was done by myself;
- This work and the results presented in it had not been published before submission in December 2016;
- Parts of this work were presented at the British Applied Mathematics Colloquium 2015 and the European Conference on Mathematical and Theoretical Biology 2016, as stated in chapter 7.

Signed: .....
Date: .....

Acknowledgements

An epic in three words: Doctor of Philosophy.

In Fall 2013, I was finishing my MS degree at Columbia University. I must choose between staying there for my doctoral studies and transferring elsewhere. I decided against the convenient choice due to my love for developmental biology. Three years later, I am certain that I made the right choice. Now that the action is over, I can look back and muse about the development of this thesis.

First and foremost, I must thank my supervisor, Professor Tiina Roose. I could not have completed this thesis without her guidance. When I arrived in Southampton, I was a chemical engineer with some extra training in biophysics. Tiina has taught me a lot about applied mathematics, in particular mathematical biology. Throughout my PhD journey, she set a high standard for me, but she was reasonable in her demands and tolerant of my mistakes and quirks. Most importantly, she granted me a high degree of independence. I hope we will have the chance to work together again.

Tiina introduced me to Alan Turing, my *de facto* second supervisor. What a legend. We were both rejected by Trinity College of Cambridge. That fact alone makes him an inspiration to me.

I am appreciative of Doctors Bram Sengers' and Giles Richardson's feedback on my progress reports.

The porous media and bioengineering sciences research groups were two supportive communities; they were always happy to help with and advise on my affairs, be they academic or personal. Like Tiina, they were tolerant of my eccentricities. Special mentions go to the ever-friendly Laura Cooper; Umesh Sai Jonnalagadda and Simone Perazzolo, who went past the milestones at the same time as myself; and Ali Mosayyebi, a multitalented and helpful colleague.

I thank the COMSOL support team for their advice.

I am grateful for the EPSRC studentship (reference number: EP/M50662X/1) that funded my PhD degree.

I have enjoyed demonstrating in two undergraduate courses (Thermofluids; Design and Computing) since Fall 2014. I thank my students for their enthusiasm and curiosity; they remind me of my undergraduate days and make me feel nostalgic. When my final demonstration duty is over next year, I will feel sad and miss it.

Chess suits my personality well. I regret that I only started during my PhD years. I do not buy the myth that one must start young to become a FIDE master. If I do become one, I will be prouder of it than my PhD. Ironically for a game with its reputation, I found friendship in chess. I thank my chess team for making my PhD journey less lonely. Special mentions go to my two captains, Peter Wei and Ryan Cheung; Momchill Kiranov, Phloe Gabriel, Stephen Gow, Thomas Evans, Johnny Luk, Matt Chapman, Mohit Gupta, and Hardeep Chahal.

I also regret not playing squash before my PhD years. It is tactical and does not require as much physical strength as other sports; it suits me. Diana Gillen-Buchert and Francesca Whyte taught the introductory course well. When I signed up for the course, I did not expect to found a squash group with Michele Zadra, Stefania Fabbri, Bo Yang, and Hosam Hasan Fraig. The group has expanded to include Andrea Ricci, Faiz Mohammad Khan, Rachel McKerracher, Nicolas Hernandez, Horacio Figueredo, and Christian Harito. I thank all of them for the fun.

It is too early for me to write my acknowledgements in German, but one day, I will mirror Wittgenstein by publishing a philosophical treatise in German. I thank Elisabeth Ruggles, Corinna Schelp, and Theresa Paumen for their contributions to my German learning. Elisabeth's regular classes were a pleasant distraction from lymphangiogenesis, while I learnt a lot under the tutelage of first Corinna and then Theresa. I improved dramatically under Theresa, with whom I conversed about multiple academic disciplines in German.

In 2008, yoga came into my life with higher education. I use it to gauge my sensitivity to external stimuli and internal thoughts. I have certainly become more restless since I saluted the sun for the first time, definitely more irritable since I moved to Southampton. Nonetheless, Wai Chung's and Hannah Brown's classes still calmed me on many occasions and I am grateful. I also met Mike Okeowo, TingKe Hu, Kate Woodley, Chiharu Iida, and Bryony Mann: friendly people who livened up the classes, workshops, and retreats. *Namaste* and thank you.

I am dead clumsy, but Bob Crittell gave me the belief that I can drive. In the end, we simply ran out of time and money. I will finish what we started and thank him when I get my license.

I have moved house at least eighteen times, including three addresses in the last three years. At 276A Winchester Road, I lived above a kebab shop with Sachin Kumar, his wife Sandhya Sah, and Majed. I have missed the skylight in my room since I moved out.

My two years at 230 Burgess Road were a relatively stable period; it was the only place where I stayed for more than a year after 2008; it was also the place where I lived for the bulk of this degree. I enjoyed living under the same roof with Emma Gaynor, Utsav Oza, Faiz Mohammad Khan, Kyan Koranteng, David Bull, and others. Then, I moved to 122 Earls Road, where I met four great housemates, Devin Jay Valentine, Kalina Axentieva, Kamila Martyna, and Gerald. These undergraduates and the cat have helped me stay mentally young since then; I will miss them after I move out. I also had the pleasure of meeting Devin's girlfriend, Daisy Watkins, and his friends, Maya Owen and Caspian Priest. I am thankful to all my housemates and guests for our time together.

After my ordeal of toxoplasmosis, I stopped cooking, so I must thank the university catering department. I also thank the Stile, the pub which has effectively been my living room for the last few years; Cheryl, Jo, Clare, Christine, Chelsey, and Iona always make me feel welcome there. Thanks to Philip Lau, Alexander Tam, Isaac Wong, and Chef Hong Kong, I have been able to speak a little Cantonese since my move to Southampton.

Towards the end of my PhD journey, I met Emilia Korczynska, a linguist, entrepreneur, and rare find on Tinder. We are kind of business partners now. Clearly, I did not use the mobile app correctly. Thanks for killing time with me.

I thank my parents for providing me with an education.

This is where I am supposed to thank whoever is emotionally close to me, but I cannot think of anyone. Where is my VEGFC? Let us study my own development.

1. In late June 2014, I was told that I had lymphoma. A few weeks before that, I decided to stop talking to my family without a reasonable immediate cause. I was insouciant about cancer; I only freaked out when Mister Tahwinder Upile said he must perform a biopsy on me and it would give me a scar. He said my reaction was far from normal. I thank him for making me rethink my life.

2. After I left Mister Upile's room, my first thought was an absurd idea that I should invent a cure for myself. Then, I wanted to tell Doctor Jawahar Krishnan. He responded with comforting words, good advice, and a list of sixteen books to distract me from pointless speculations. Needless to say, I was very touched, but I must also admit I have not read those books yet. Doctor Krishnan is a source of wisdom about everything in academia and life. He introduced me to the quantitative aspects of biology and taught me to think like an academic; I appreciate his influence on me. A father figure, he was a big part of my Imperial experience.

3. I have a love-hate relationship with 'Where are you from?' Does the questioner mean where I was born, or what passports I hold, or where my family are, or where my personality was and is being shaped? Do they want to know where I identify with or just to confirm their biases? My intellectual home is Imperial College London.

3.1. I had a good tutorial group. Group 2E, I believe. Juan Boon Tan, Augustina Ephraim, Nature Da, Connor Gilder, and Donal Connolly made our first-year group projects a pleasant experience. The camaraderie made me believe in friendship again after a difficult period at boarding school. Thanks, my fellow chemical engineers. Assuming I pass my *viva*, at least three of us will end up becoming doctors; Doctor Krishnan must be proud of us.

3.2. In my final year, my design group spent so much time together that we were like a big family. The library that never closes was of course our family home. I miss working with Abeer Mian, Jian Heseri, Jacob Ho, Calvin Lui, Timothy Kong, Jill Tombs, Dan Wong, Anggraeni Susilo Putri Gunawan, Charles Lim, and Doctor Andreas Kogelbauer. Thank you for that enjoyably busy Spring 2012.

3.3. I am grateful to Doctor Cleo Kontoravdi for introducing me to the modelling of biological systems. In retrospect, Vincent Chan and I did abysmally in that research project. My ideas about the relationship between our model and Alzheimer's disease progression were simply wrong. Well, making mistakes is an important part of learning. Thanks for being a good lab partner, Vincent.

3.4. Every time I walk past Willis Jackson, I smile and think of Alastair Wong, Min-Ho Lee, and Raymond Yang. I am appreciative of their support and friendship. I hope we will remain friends for years to come. I lived in Hammersmith in my second year. It was a particularly happy year and because of that, Hammersmith will always have a homely feel. However, I must admit there is a regret at my arguments with AVO; I wish things had turned out differently. My final year was spent at 7 Brompton Villas and it was as chaotic as the end of my PhD journey. Thankfully, Alex Chaushev, Connor Gilder, Yin Shan Ho, and Bernadette Lee were good housemates. Yes, I had fun being the toilet keeper of the house.

3.5. Onyinye Ezeh is a case of what might have been. I should have chased her harder when I had the chance. I thank her for her good humour, support, and friendliness over the years and wish her a happy marriage.

3.6. I conduct my love affairs philosophically. Anna Reeves knows that more than anyone else. It started with a passion for life worthy of Nietzsche and ended with Wittgenstein's silence: 'Wovon man nicht sprechen kann, darüber muss man schweigen.' If for nothing else, I thank her for broadening my horizons; my love for the German language and yoga both originated from her.

3.7. Speaking of Wittgenstein, I want to thank Pui Him Ip for our philosophical discussions. I wish him good luck with finishing his PhD in divinity.

3.8. I have known Jacky Wong for too long to not devote an item to him. Many thanks for being a good listener to my ravings during my mood swings.

3.9. Wenqian Chen is a good peer who has helped me and offered me good advice many times. On the occasions when I visited London during my PhD years, he was my personal link to Imperial. Thanks mate.

3.10. Additionally I would like to thank the following for the lovely time in South Kensington and putting up with my erratic behaviour: Ronak Thakrar, Tommy Chiu, Simon Au, Evan Venieris, Julian Tay, Kelly Lai, Giulia Ferretti, Luke Johnston, Calvin Lee, Kuok Hao Lai, Kuo Jian Wong, Edwin Goh, Neil Watt, Neal Wannell, Florence Chow, Grace Chan, Weizhao Tan, Jimmy Olet, Phattaraphon Teak Chatthaweesak, Bianca Choi, Piotr Faba, Rong Kai Wong, Edyta Sidorowicz, Jessica Kwannandar, Elias Aliu, Hanyi Zhao, Chao Chen, Hui Xian, Ralf Perpeet, Simon Dowland, Paul Su, and more.

3.11. God is a chemical engineer.

3.12. May the steady-state assumption be with you.

4. I spent my third undergraduate year in the Southern Hemisphere. That year, I philosophised too much and got stuck in my thoughts.

4.1. When I could not sleep in Sydney, I used to take a train to the City; the noises those trains made on their tracks soothed me and kept me grounded in reality. In the City, I just walked aimlessly up and down George Street while ruminating. When I needed peace in the morning, I escaped to Carina Bay with a book.

4.1.1. I am grateful for the hospitality of the Leungs. They made me feel welcome and were very forgiving of my missteps.

4.1.2. Professor Hala Zreiqat kindly let me work in her laboratory during the long Christmas and summer break. Doctor Iman Roohani, then a PhD candidate, and I had a lot of fun playing with bioscaffolds. Iman told me a lot about the PhD lifestyle and I became more convinced that I should go into academia. I am grateful to both of them.

4.1.3. I had the pleasure of studying and working with my classmates, Benton Ng, Tim Adams, Edward Wu, Patrick Manassa, Mohammad Syazwan Bin Kamarudin, Gobinath Pillai Rajarathnam, Aishling Breen, Ann Ling, Feng Huang, Mingzi Hong, Jason Cheng, Alex Donis, Claudia Bertini, Simon Guo, Alyce Garraway, Aya Sasaki, Will Hayes, Neha Faruqui, and more. Thanks for the lovely time.

4.1.4. The friendly and cheerful Kate Boyle helped me with all the administrative issues. The fact that I am still in touch with an administrator after five years merits a special mention. Thanks Kate.

4.1.5. I met Angie Hewett in a ballroom dancing class. Apart from the waltz, I did terribly and stepped on her over and over again. Sorry and thank you! After our last waltz, we did not speak again until halfway through my PhD, after she returned

to England, married and a licensed yoga teacher. Many things have changed since I decided to get a PhD.

4.1.6. I also met the daughter of my mother's best friend at school, Heilok Cheng. She likes wearing lolita and is considering to embark on her own PhD journey. All the best. I am thankful that I am still in touch with this funny girl.

4.2. After Sydney, I moved to La Plata to work in the field of theoretical chemistry. In this unfamiliar city whose language I did not speak well, a sense of alienation drove me deeper into my own thoughts. I stayed in a hostel and met new people every day. In my confused state, I made many acquaintances, talking about football and politics, but I was too detached to bond before they moved on. I wonder if Daniel has achieved his ambition of becoming a singer yet. How are Liliana Ortiz Sánchez and América Alarcón Barreda now? However, there was one family whose company I thoroughly enjoyed. Armando Guachaqueo and I had many conversations about the economy over yerba mate. I enjoyed playing with his son Tobias. He and Ailen must be all grown-up now. I thank all of them for that surreal summer.

4.2.1. The hostel staff were hospitable. Cristian Acosta, Sofia Hawryszko, Juan P. S., and Pavlito Cano took good care of me. My roommate, Jose Medero, and I used Google Translate to form a friendship despite my broken Spanish. He also tried to teach me to swim the butterfly stroke on dry land. I am grateful for our time together.

4.2.2. I thank Doctor Pablo Duchowicz, Doctor Andrew Mercader, and Professor Eduardo Castro for teaching me a new technique: quantitative structure activity relationship analysis. Pablo was especially kind, showing me around La Plata and Buenos Aires, treating me to coffee and meals when I was bored.

4.2.3. Due to the language barrier and the fact that I was there to work, I did not travel much. One day, I will master Spanish and return to South America.

5. After my MS and before my PhD, I boarded a train and travelled across the United States, from the Atlantic to the Pacific. Emotionally, I was too knackered to even think, so I resorted to something receptive. I read about quantum physics, rhetoric, logic, and philosophy in a detached manner. Sometimes, I just sat in a viewing car and watched the landscape pass by for hours. It was a refreshing end to my stint at Columbia.

5.1. My time at Columbia was challenging but rewarding. Compared to my time at Imperial, I had more exposure to the fundamentals of chemical engineering; I also learnt about aspects of biophysics. I must thank Doctor Vanessa Ortiz for teaching me how to program and run computer simulations, Doctor Andre Ribeiro for various Linux tips, and Doctor Ben Stratton and Professor Ben O'Shaughnessy for teaching me about image analysis. Although I did not work with Professor Edward Leonard, he deepened my interest in developmental biology and advised me on many things. He is the grandfather I wish I had.

5.2. I thank the following classmates and colleagues for making my time at Columbia easier than it would otherwise have been: Maxim Stonor, Kevin Lee, Jianyi Ren, Thi Vo, Min-Kang Hsieh, Porakrit Leophairatana, Weiming Wan, Ahmet-Hamdi Cavusoglu, Hakhamanesh Mostafavi, Kolade Adebowale, Mónica Besteiro, Ajinkya Sathe, Su An, Sathish Thiyagarajan, Angela Zheng, Kelly Greenland, and more.

5.3. While at Columbia, I went through a rite of passage. Yuliia Kapeliushna was there for a summer course. We first met in the laundry room in Carlton Arms. She told me about her life in Ukraine, her dreams, and her struggles. It happened while we were walking down Riverside Drive and I was recounting my experiences at her age: I felt old. First time ever. Thank you for the experience.

5.4. Doctor Dessie Zagorcheva is a political scientist. I first met her in Butler Library. Soon, because I frequented that building in the early hours too, I learnt that she was always there. I think this statement is no longer true because she has found another library. Thank you for keeping me company in Butler.

5.5. I also had the pleasure of meeting two legal scholars, Nye Todd and Ben Stanford, and a psychologist, Bryan Sim. Bryan and I had fun struggling to converse in German in Caffe Bene. Caffe Bene was also my haunt when I could neither sleep nor bear going to Butler. This item is a bit random, but my gratitude is sincere.

5.6. I had a dental problem in my first semester. I was transferred back and forth between my dental practice and the university hospital. After much pain and waiting, I met Hashim Alhassany. His attitude was friendly and sympathetic, but the root canal treatment took three sessions and lasted twelve hours in total. By the end of it, we were friends on Facebook. Thanks for being nice to me and filling up my tooth for free.

5.7. At Columbia, I taught my first students. I will always remember Linda Arthur, Oluchi Okoro, and Akie Fujita, who were my very first students. Erik Lovece, Roshan Ramkeesoon, Olivia Romeo, Rebecca Siegelman, Brittany Becker, Christine Shim, Laura Ye, Laura Zhu, Benjamin Franklin Walker, Emma Yee, Karina Montenegro, and many others were all a pleasure to teach. It was difficult at times because I was fresh out of university myself. On the other hand, it was an opportunity to consolidate my understanding of many concepts. I would like to thank my students for being patient with me.

5.7.1. I would like to apologise to my students in Analysis of Chemical Engineering Problems I in Fall 2013. At that time, I was learning to program myself, so I could not help them as much as I wanted to. At least at the beginning of the course, I graded them harshly too. If it helps, I was under tremendous stress due to a funding situation in my research group.

5.7.2. I smoked with a student on Low Steps. Achievement unlocked.

6. My school years were littered with uninspiring teachers. Okay, not all of them.

6.1. When I was ten, I met the first exception. Mister K. Kwok cared more about shaping his students' characters than teaching them mathematics or languages. He was strict and sometimes sarcastic, but he was never unfair. He instilled a strong work ethic in me and taught me to create my own destiny. When I made mistakes, he encouraged me to own up to them. Finally, he wanted me to have a big and forgiving heart. I believe I meet the first standard he set for me all those years ago; the second one, partially; I am still working on the last one. I am forever indebted to him for my development.

6.2. My quest to understand life has taken me to five continents and round the world twice so far. Where and when exactly did it begin? Miss Y. C. Keung was the second exception. Her pedagogic skills and enthusiasm for biology sparked my first academic interest. For the first but certainly not last time, I studied because I enjoyed a subject. The fact that I stopped enjoying it under my subsequent teacher is a testimony to her success. Without her, I probably would have studied law at university and not considered doing a PhD at all. I am eternally grateful to her for introducing me to a whole new world.

6.2.1. My early passions were engulfed by an identity crisis and concerns for future prospects. I just could not figure out how to combine it with abstraction and mathematics until I was at university.

6.3. I did not like Mister Nigel K. Connell. However, he had so much faith in me and was so tolerant of my mistakes. Following my rejection by a prestigious institution in the US, he expressed outrage and said unreservedly that I did not deserve the rejection. If nothing else, I thank him for this incident. I have a feeling that, in a different environment, he could have been as influential as Mister Kwok.

6.4. I used to have a tutor when I was at primary school; she was a university student. I was very rude to her. One day, I upset her so much that she left crying and never came back. I cannot remember her name anymore, but I am so sorry.

6.5. I concede defeat to Mister Joseph Wong. Mathematics is good, sir. Despite my struggles under him, I now build and solve mathematical models for a living. I never disliked him; I was simply frustrated because I failed to integrate by parts in my misspent youth. If it is a consolation for him, I will pursue a part-time degree in mathematics and physics when I have more money.

6.6. My time at boarding school was so pivotal to my development that it deserves another thesis. Therefore, I will not go into any details here. However, when I left, I sent out an email thanking all my teachers out of politeness; it was a hypocritical act for which I now apologise to myself. In particular, I am certainly not thankful to Owen, E. Alchin, Kino, Homewood, Walpole, and Percival; I have no respect for them. To set the record straight, I do not thank my teachers and schoolmates for my holistically

negative experience there; it was an utter waste of money. I also apologise to myself for wanting to attend this school. I would like to make my contempt for this institution crystal clear. Finally, I hereby clarify that I have absolutely no desire to stay in touch with the people I met there. I did not want to join the alumni network, but my parents paid for it despite my protests. I do have fond memories of some people I met there. They are acknowledged in other items. I thank them and would love to stay in touch.

7. My memories of Hong Kong are very vague. Just because I was born there, it does not mean I come from there. By saying that you come from somewhere, you give society the permission to define you in relation to that place. Henceforth, your opinions, ambitions, lifestyle, and behaviour will all be interpreted in its cultural, social, and political context. I object to being wished a happy Chinese New Year without my consent; too many cultures and countries have contributed to my development; that unsolicited greeting ignores many parts of my personality.

7.1. I have fond memories of the time I spent with Wallace Ng, Kenny Lee, Kenneth Chak, Arnold Tang, Chan Zi Wei, Promise Lo, Leon Lai, Gavin Cheng, and Simon Mak. I thank them for those simple days.

7.2. Ivan Au and Ronald Lai are the closest people to a sibling I have ever known. Thank you for being supportive, helpful, caring, and accepting for decades.

7.3. I have not spoken to Bryan Lam for a long time. I remember him as a protective older schoolmate who cared about me. I thank Bryan for standing up for me when I was too confused to do so myself.

7.4. Lawrence Wong and Wyman Wat have known me since I was a less complex character. I thank them for those simple days.

7.5. Professor Henry Wong and Doctor Sam Hau gave me my first research experience, for which I am grateful. I did not enjoy organic synthesis, but I correctly concluded that I am a theorist.

8. The day after Mister Upile told me I had cancer, I moved to Burgess Road. Like Charles Xavier in *Days of Future Past*, I needed someone to lead me, guide me, be patient with me. Emma Gaynor was a student nurse from Ireland. I got to know her while smoking outside the house. Yes, a cancer patient and a nurse smoked together! Throughout that bizarre summer in 2014, her humour, warmth, and kindness consoled me. Every day at work, I looked forward to going home to see her. Emma accompanied me to the biopsy. After waking up from anaesthesia, I asked for her immediately. In my dreamy state, I thought I heard her say jokingly, 'That's my husband!' For the first time in my life, I thought marriage must be wonderful. The diagnosis turned out to be a misdiagnosis: toxoplasmosis, not lymphoma. A couple of weeks after I got the result, Emma returned to Ireland for good. I thank Emma for that summer and making me rethink my life.

8.1. Long before I met Emma, another nurse had comforted me at school. I walked into the medical centre on a day when the world crumbled around me. I did not need to be told that I was wrong or why I was wrong: I already knew both. I needed someone to hold my hand and pull me up. Alison Wertheim was accepting, kind, and gentle: everything that my mother was/is not. She had no answers to my problems, but she reminded me I was not obliged to be in pain. I was on my way out; in the doorway, I turned round and asked for her name. After answering me, Alison told me when she would be in next, asking me to come back. A gradient of something formed between us, drawing me towards her, but I was immobilised. I was immobilised because I could not name or define that something. Before I could even hypothesise, the gradient had degraded. I am eternally grateful to Alison.

8.2. Jennifer Allen took me out of a mad house indifferent to my sufferings. In her arms, I felt completely safe; for just ten seconds, I felt loved. I cannot thank Jenny enough. We are no longer in contact, but Jenny will always be a friend. On his deathbed, Bobby Fischer said, 'Nothing is as healing as the human touch.' At least, I figured it out sooner.

8.3. Is *The Girl with a Pearl Earring* turning towards or away from her viewers? I think she represents what one needs but lacks, and she is turning away from me. Those who have touched me, shaped me, never stayed after inducing my differentiation; they have a high degradation rate constant. Should I feel sad because I am not sure if Mister Kwok's first name is also Kenneth? Or that Alison is not my mother?

8.3.1. I first realised something was missing in my life in Waterloo Station. Sophie Tunstall-Behrens embraced her mother before introducing me to her family. I thank Sophie and her family for their hospitality and showing me what a family should be like. There was so much love in her family.

8.3.2. Almost a decade later, I am no closer to seeing something else in that painting. Perhaps, I just need someone who is there for me personally and permanently. Now that my relationship with VEGFC is over, I should find a girlfriend.

9. Heather Pashley and I conversed about many things. During one of our conversations, I decided that I should write a philosophical novel. Thank you for being a good listener.

9.1. I told her about a eureka moment I had had shortly before finishing school for good. I was walking past the catering staff when I got it: I was under no obligation to be catered for. No, there were no demands on me to dine with those whose ethical standards I questioned. More abstractly, no one said I must play by the rules of a game I disagreed with. Therefore, I went to the other side of the dining hall. While working with Jana Sadlonova, Hannah Ammon, Janice Ammon, and my other colleagues, I found freedom, although in truth, it had always been mine. I thank them for that priceless insight.

9.2. For the last few years, I have tried to convince everyone that VEGFC should be pronounced VEG-F-C rather than VE-G-F-C. I am curious as to what makes someone 'correct' and how 'correctness' affects communication.

9.3. I have been drifting for over a decade now. My PhD journey, chaotic as it sometimes was, was a period of relative stability. It has changed me actively by adding to my character and passively by crystallising it. I have become surer about who I am and what I want since I embarked on it. Towards its end, I decided to get a new name for the person I had become. Although I have been known as Kenneth for as long as I can remember, I now use it because it may be a mentor's first name; Yann is a male variant of Jana, who helped me see my true potential; Wertheim is a tribute to Alison, who protected me from what I wanted. I want to publish, checkmate, and more in their names.

9.4. Now that the epic is over, I need another one. As Kenneth Yann Wertheim, I will continue my quest to understand life and go the distance in it. Here are some specific goals.

9.4.1. Develop a general theory of development, invent human enhancement technologies, and write a philosophical novel. Then, go into cosmology research and moonlight as a painter.

9.4.2. Live in Continental Europe, Africa, and Antarctica. Travel on the Trans-Siberian Railway, the Blue Train, and the Venice-Simplon Orient Express.

9.4.3. Become an octolingual (Arabic, Cantonese, English, French, German, Mandarin, Russian, and Spanish), a FIDE chess master, and a licensed yoga teacher.

9.4.4. Get a degree in mathematics and physics. Less seriously, take some courses about data science, machine learning, IT security, and philosophy. Yes, get a driving license.

10. If you have experimentally validated my theory about VEGFC, please drop me a note. I will buy you lunch then, but I acknowledge and thank you in advance.

To Mister K. Kwok, my teacher; Jennifer Allen, my classmate; Alison Wertheim, my school nurse; and Jana Sadlonova, my colleague. You were my VEGFC.

Chapter 1

Lymphatic System

This thesis is about lymphangiogenesis, the embryonic and post-natal development of new lymphatics by sprouting from veins or/and extending from pre-existing lymphatics (Ji, 2006). In this introductory chapter, we will review the structure and functions of the vertebrate lymphatic system (the lymphatic system henceforth). The aim is to gain an understanding of its complexity, as well as its importance in biomedical applications and basic research. After this chapter, we will review what is known about lymphangiogenesis in the zebrafish and the mouse, two major model organisms in developmental biology. We will identify the missing gaps in our knowledge, pose our research questions, and formulate hypotheses. Then, we will build, solve, and analyse mathematical models in order to test our hypotheses.

This thesis takes the form of a narrative and we will use the plural first-person pronoun to bring the reader into the narrative. It should be read from chapter 1 to chapter 7; when we refer to an earlier part of the narrative, we will use the past tense or the present perfect tense. Although the appendices are stand-alone narratives, they share the acronyms and symbols used in the main body; when an acronym or symbol is defined in the main body, it may be used without definition in the appendices. All acronyms and symbols are defined in the nomenclature. In reference to parts of the thesis, such as figures, tables, equations, simulation results, chapters, sections, and conclusions, we will use the present tense; statements of scientific facts require it too. In reference to our sources, we will use a mixture of tenses. We will use the past tense to describe historical events like measurements; the present perfect tense for studies with connections to our narrative; and the literary present tense to report the narratives in our sources, such as reviews, conclusions, mathematical models, or theories.

1.1 Structure

In contrast to blood vessels which were described in detail in the 6th century BC, lymphatic vessels, sometimes simply called lymphatics, were only discovered in the 17th century (Yang and Oliver, 2014b). In a review article, Schulte-Merker et al. (2011) describe the lymphatic system as complex, highly branched and valved, and blind ending. Lymphatics are present in most organs; exceptions are avascular tissues such as cartilage (Schulte-Merker et al., 2011; Louveau et al., 2015). Louveau et al. (2015) have recently proven the existence of functional lymphatics in the central nervous system. They express the molecular markers characteristic of lymphatic endothelial cells, carry both fluid and immune cells from their surrounding cerebrospinal fluid, and are connected to deep cervical lymph nodes.

In this study, we will divide the lymphatic system into primary and secondary lymphatics. In a review, Margaris and Black (2012) describe their connectivity in the human body. The primary lymphatic vessels drain the tissues they reside in and deliver the resulting lymph into the secondary lymphatic vessels, where it is drained into progressively larger vessels. Eventually, they converge at the right lymph duct or the thoracic duct (Schulte-Merker et al., 2011). The former drains the upper right side of the head and thorax, as well as the right arm, while the latter drains the rest of the body (Margaris and Black, 2012). Both vessels drain into the blood circulation at the subclavian veins (Margaris and Black, 2012). Lymph nodes are distributed at regular intervals along the secondary lymphatic vessels (Margaris and Black, 2012). Figures 1.1 and 1.2 show the lymphatic system's structure and the flow of lymph in it. In the following two subsections, we will look at these two types of lymphatics in greater detail.

1.1.1 Primary Lymphatic Vessels

The primary lymphatic vessels form a network of blind-ended microcapillary ducts (Margaris and Black, 2012). Also known as initial lymphatics, they lack fenestrations, continuous basal membranes, and/or pericytes. Their walls are monolayers of overlapping lymphatic endothelial cells (LECs) (Oliver, 2004; Margaris and Black, 2012). They are not covered by smooth muscle cells (SMCs) either (Stacker et al., 2014).

Since the primary lymphatics do not contract, lymph must enter their lumens passively due to fluctuations in the interstitial pressure (Margaris and Black, 2012). They are attached to their surrounding extracellular matrix (ECM) via anchoring filaments, which prevent them from collapsing at a high interstitial pressure (Schulte-Merker et al., 2011). The LECs forming the capillaries are connected by discontinuous, button-like junctions (Schulte-Merker et al., 2011). The LECs at these junctions overlap to form flap valves which ensure a unidirectional flow from the surrounding interstitium into the capillaries; this mechanism is shown in figure 1.3. An alternative mechanism which involves sliding

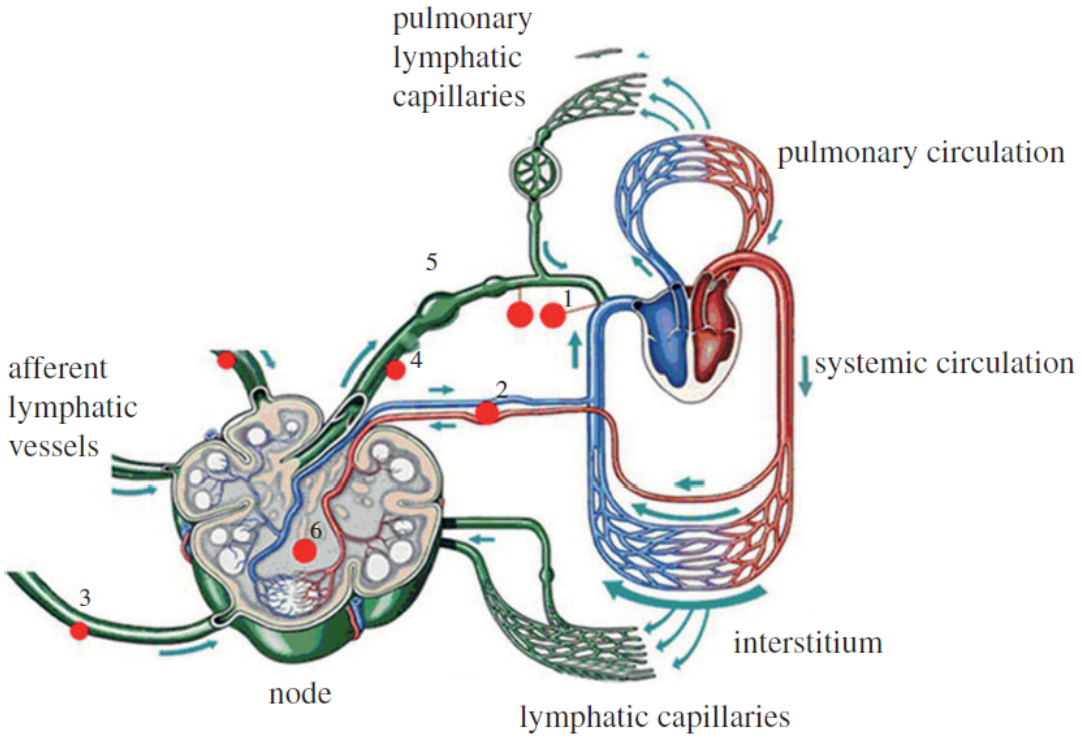

FIGURE 1.1: Schematic of the vertebrate blood and lymphatic circulations (Margaris and Black, 2012); reproduced with permission by the Creative Commons Attribution License.

door valves has been modelled by Heppell et al. (2015). By this theory, when excessive fluid causes the interstitium to expand, the ECM pulls open the lymphatic valves for fluid entry.

1.1.2 Secondary Lymphatic Vessels

The secondary lymphatic vessels are differentiated from their primary siblings by their ability to contract (Margaris and Black, 2012). The pumping action that ensues transports the lymph in their lumens against any adverse pressure gradients. This contraction is possible because the secondary lymphatics, also known as collecting lymphatics, have walls which contain endothelial cells, smooth muscle cells, and collagen fibres. The smooth muscle cells can contract, while the muscles, arteries, and organs nearby add to the contracting force.

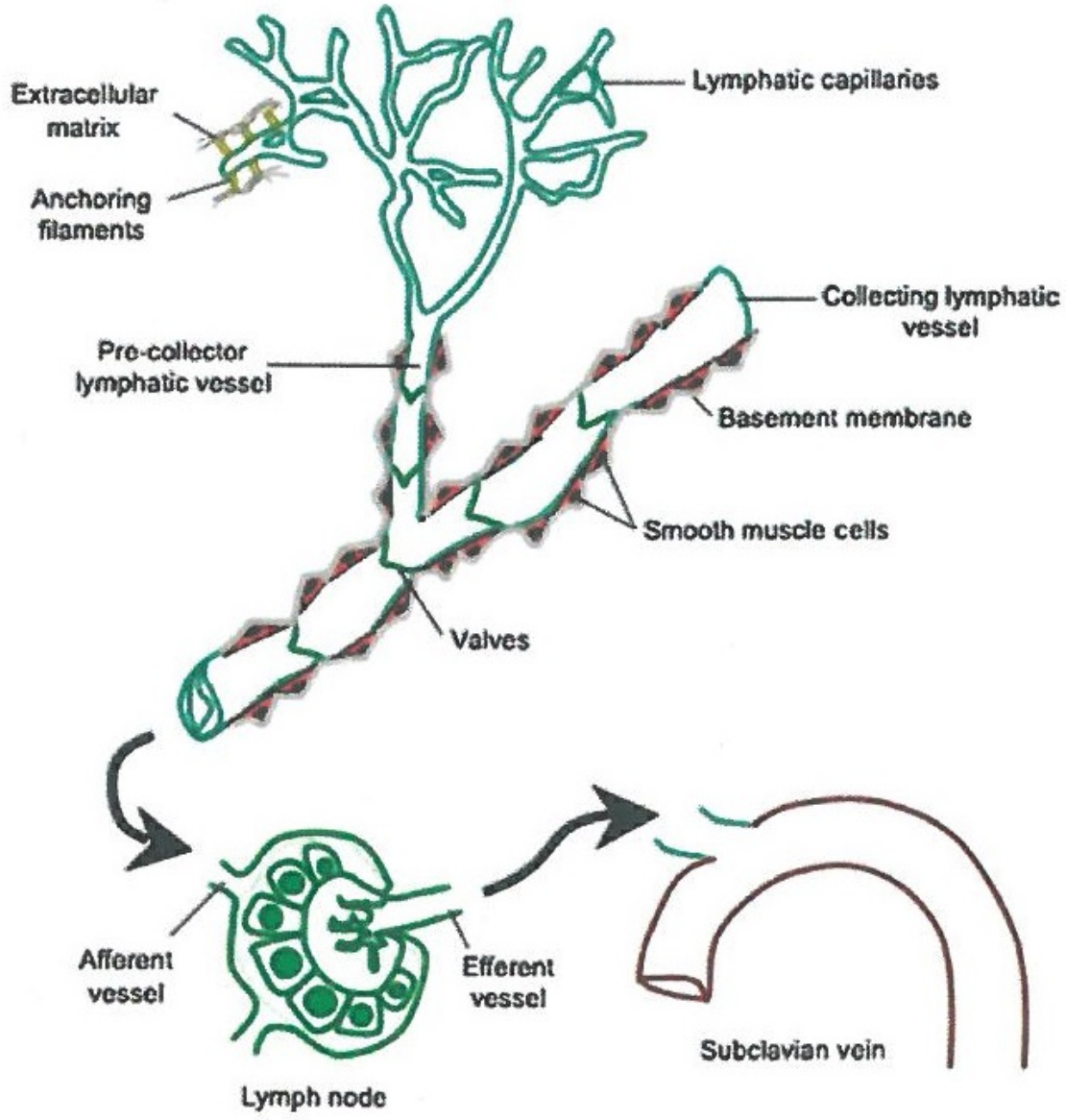

FIGURE 1.2: Schematic of the vertebrate lymphatic system (Maby-El Hajjami and Petrova, 2008); reproduced with permission.

The properties and functions of the valves in the secondary lymphatics are as follows (Schulte-Merker et al., 2011). The intraluminal valves, each of which has two semilunar leaflets, ensure a unidirectional flow. A lymphangion is defined as the vessel segment between two successive intraluminal valves. The length of a lymphangion depends on its surrounding tissue type. The basement membranes surrounding the vessels and the continuous zipperlike junctions among the lining LECs prevent leakage. The contrast between the valves in the two types of vessels is illustrated in figure 1.4.

In a review article, Drayton et al. (2006) discuss the structure and function of a lymph node. Each lymph node is fed by multiple afferent lymphatic vessels, but it drains into one efferent vessel only. Structurally, it can be divided into three parts. Its cortex encapsulates the paracortex which encapsulates the medulla. Immune cells reside in

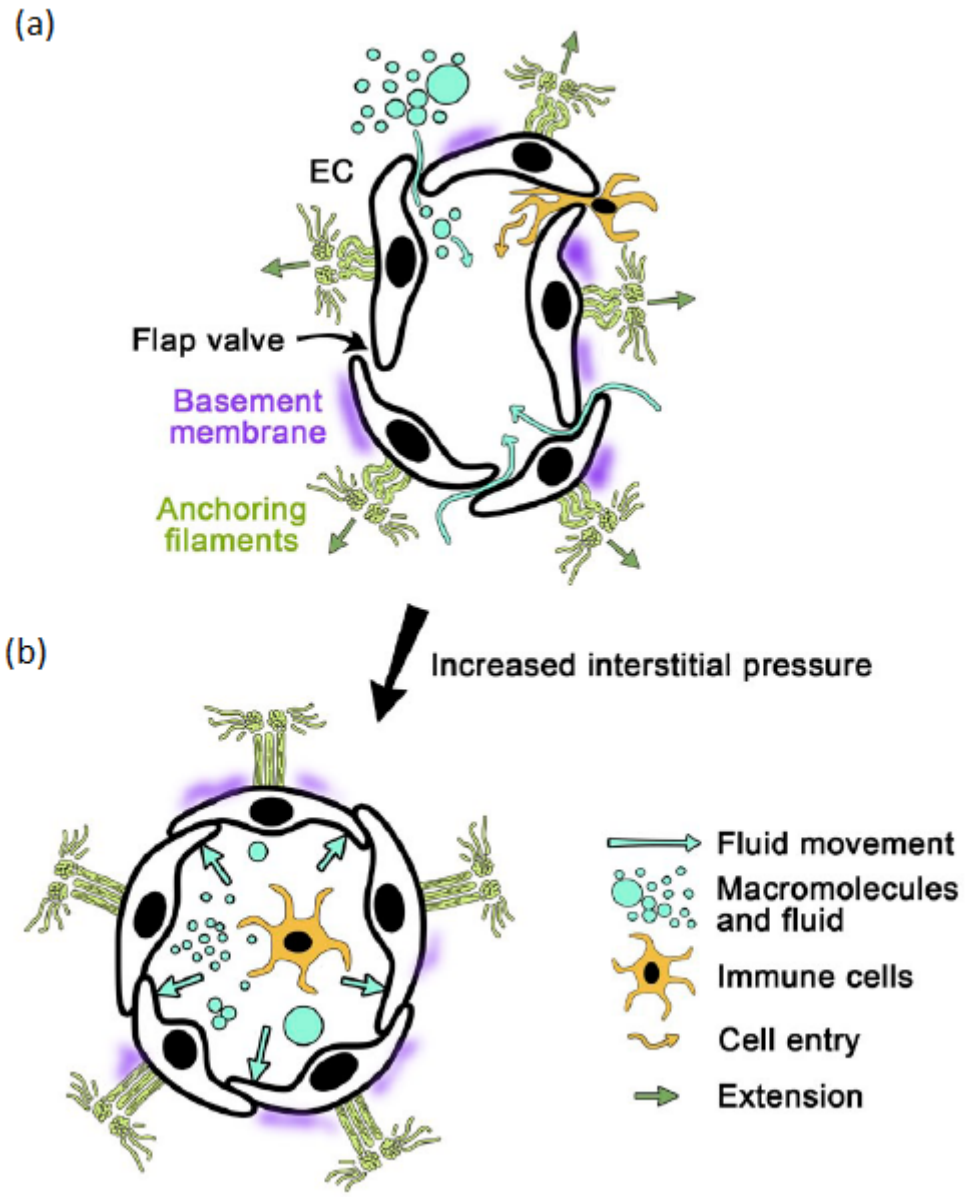

FIGURE 1.3: Flap valves of a primary lymphatic vessel (Schulte-Merker et al., 2011); reproduced with permission. (a) shows that various interstitial components enter the vessel via the gaps between the lining lymphatic endothelial cells. EC stands for endothelial cell. (b) shows that the flap valves prevent backflow into the surrounding interstitium. The filaments anchor the cells to their extracellular matrix to prevent vessel collapse when the interstitial pressure is high.

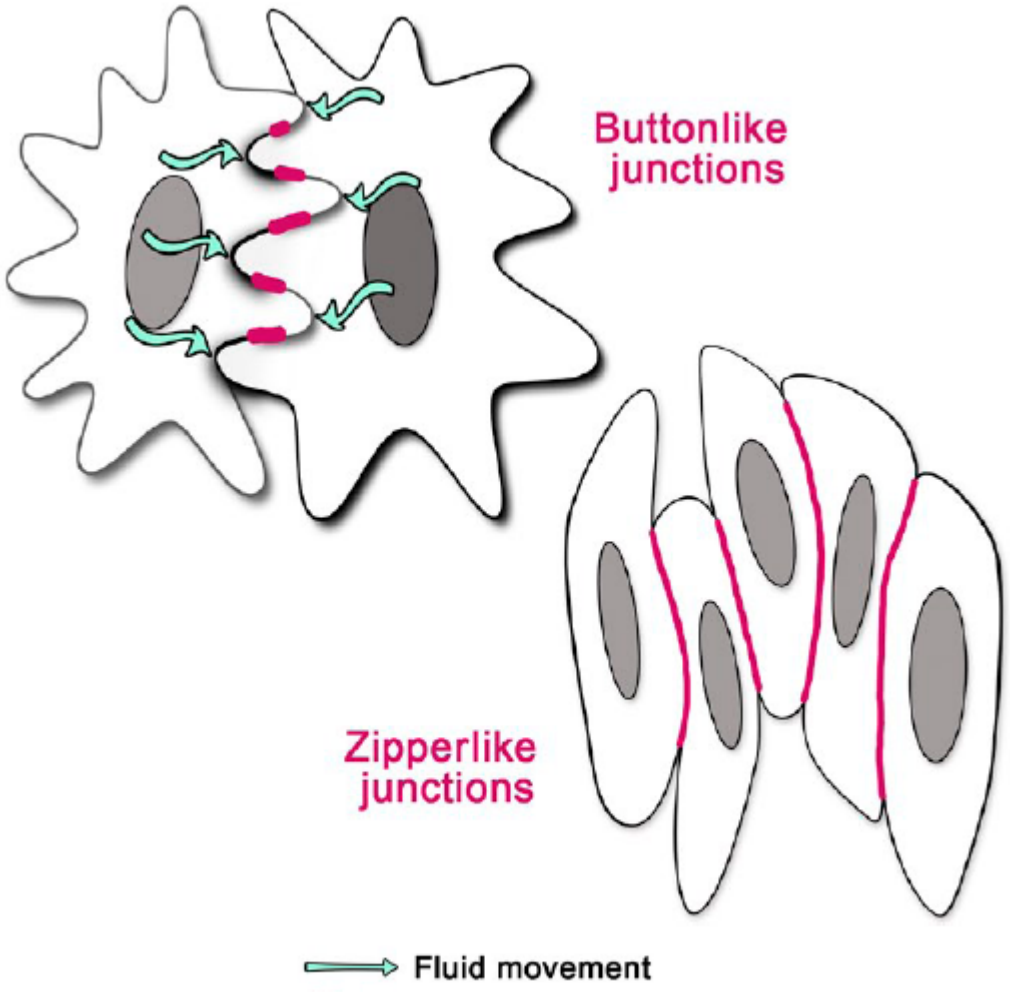

FIGURE 1.4: Different types of intercellular junctions for different types of lymphatic vessels (Schulte-Merker et al., 2011); reproduced with permission. The primary lymphatic vessels have button-like junctions while the secondary lymphatic vessels have zipperlike junctions.

these nodes. When lymph passes through a node, its composition changes since immune cell modifications occur there.

A vertebrate has other lymphoid organs; they play key roles in its immune responses to infectious agents (Drayton et al., 2006). The spleen detects blood-borne pathogens and protects the vertebrate against them; tonsils and Peyer's patches collect antigens directly from its mucosal surfaces; the thymus shapes its T cell repertoire and removes self-reactive T cells from its lymph.

1.2 Functions

A vertebrate relies on its lymphatic system for many purposes.

Its major role is to drain any excessive interstitial fluid and proteins, together with tissue waste products, from the interstitium back into the blood circulation (Margaris and Black, 2012). Therefore, it maintains interstitial fluid homeostasis. A related function is to absorb intestinal lipids (Schulte-Merker et al., 2011). When this draining process fails, a condition known as lymphoedema ensues. This condition is characterised by swelling and pain due to the accumulation of interstitial fluid (Margaris and Black, 2012).

It is also an integral part of the vertebrate's immune responses to infectious agents, so it is related to inflammation, autoimmunity, and cancer (Oliver, 2004). According to Wiig et al. (2010), the lymph nodes contain antigen presenting cells which filter soluble antigens, while dendritic cells travel and present particulate antigens to the lymphoid organs after phagocytosis. The LECs lining the lymphatic vessels release chemokines which bind to their cognate receptors on the dendritic cells. This binding induces the dendritic cells to migrate through the lymphatic system. When the vertebrate is exposed to an inflammatory agent, antigen uptake causes the dendritic cells to migrate to the lymphoid organs and lymph nodes (Oliver, 2004).

The lymphatic system is a major route for cancer metastasis (Stacker et al., 2014). Tumour cells and their microenvironments can produce growth factors to promote lymphangiogenesis, the formation of new lymphatic vessels from existing vessels, and the enlargement of any existing lymphatics nearby. Therefore, when the vertebrate develops cancers, the cancer cells can metastasise through its lymphatic vessels. Furthermore, these events correlate with cancer progression. Therefore, the lymphatic system provides both prognostic and therapeutic targets.

1.3 Chapter Summary

This brief review establishes the complexity and importance of the vertebrate lymphatic system. The facts that its components span multiple length scales, branch in an intricate manner, and have different structural features are obstacles to attempts to understand or manipulate the system. On the other hand, it plays many important roles ranging from fluid homeostasis to immunity. It is also of interest to cancer research in diagnostic and therapeutic terms.

A topic calling for special attention is lymphatic development. Development is more than a fundamental problem because an understanding of lymphangiogenesis will allow engineers to regenerate damaged lymphatic structures, enhance a patient's immune responses, and design strategies for cancer diagnosis and treatment. To answer this call,

we will develop a mathematical model to elucidate lymphangiogenesis. In chapter 2, we will review lymphangiogenesis and lay out the goals of this thesis.

Chapter 2

Lymphatic Development

Compared to the development of blood vessels, the study of lymphatic development has a relatively short history (Yang and Oliver, 2014b). The first major breakthrough dates back to the early 20th century when Florence Sabin injected dye into pig embryos, leading to a conceptual model of lymphatic development (Sabin, 1902). In this model, endothelial cells bud from veins to form lymphatic capillaries. Specifically, a pair of jugular lymph sacs first appears near the junction of the subclavian and anterior cardinal veins of a vertebrate, before spreading out to its head, neck, arms, and thorax. Later, more sacs originate from the other veins and the resulting lymphatics spread to the rest of the vertebrate. In an alternative model, proposed by Huntington and McClure (1910), the lymphatics of a vertebrate arise from its mesenchyme before connecting to its veins.

In their review, Schulte-Merker et al. (2011) conclude that Sabin's venous proposal is consistent with the reviewed lineage tracing analyses of mouse embryos and studies of zebrafish; it is also considered to be conserved across vertebrates. In the mouse, the lymphatic vascular network begins to develop from its cardinal vein and intersomitic vessels at around 9.5 days post-fertilisation (DPF) (Yang and Oliver, 2014b). In the subsequent steps, the venous endothelial cells (VECs) in these vessels transdifferentiate into LEC progenitors, leave the vessels, and express progressively more lymphatic markers and fewer blood vascular markers. Over twenty genes are involved in the process and they are conserved across vertebrates (Schulte-Merker et al., 2011).

We will provide more background information about lymphatic development in this chapter. We will begin by reviewing the developmental steps that generate the mouse and zebrafish lymphatic systems. We will explain why the zebrafish is a better model organism for our study. Armed with this body of knowledge, we will pose our research questions and hypotheses.

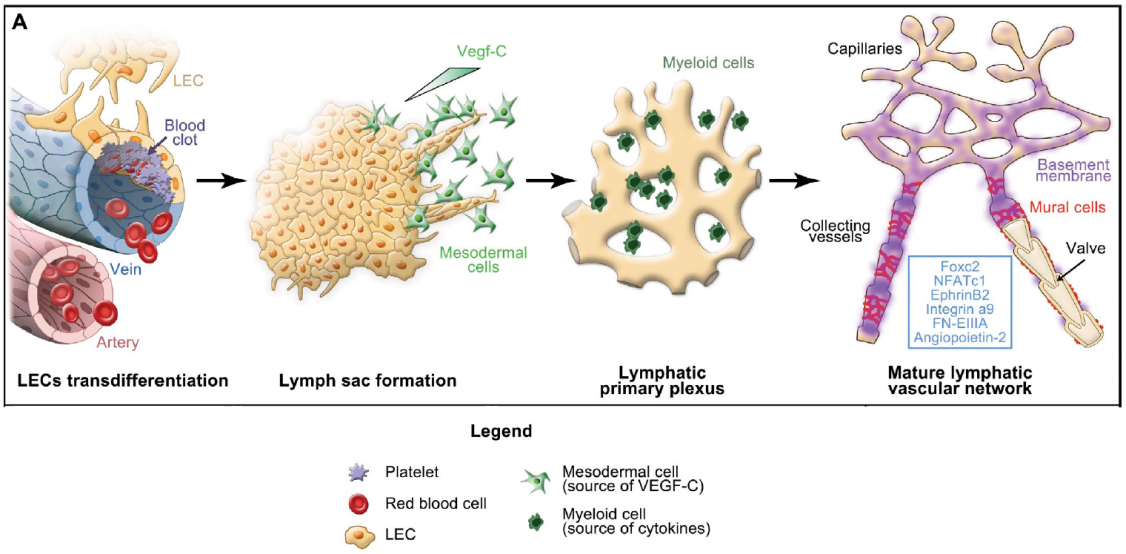

FIGURE 2.1: Developmental steps that generate the mammalian lymphatic system (Schulte-Merker et al., 2011); reproduced with permission. After specifying to the lymphatic phenotype, the progenitors of lymphatic endothelial cells sprout from the vein towards the VEGFC-producing mesodermal cells to form a number of lymph sacs. Further sprouting from the sacs produces the lymphatic plexus. The myeloid cells in contact with the plexus also produce cytokines to regulate lymphatic vascular morphogenesis. The plexus is then remodelled to form specialised structures like collecting vessels, precollecting vessels, and capillaries. The genes in the blue box are important for collecting vessel development. FOXC stands for forkhead box protein C2; NFATc1, nuclear factor of activated T-cells, cytoplasmic, calcineurin-dependent 1; FN-EIIIA, fibronectin containing the EIIIA domain; LEC, lymphatic endothelial cell; VEGFC, vascular endothelial growth factor C.

2.1 Mouse

The mammalian programme of lymphatic development can be divided into four major steps. They are illustrated in figure 2.1. In the following subsections, we will review these steps in the mouse embryo in greater detail.

2.1.1 Transdifferentiation of Venous Endothelial Cells into Lymphatic Endothelial Cell Progenitors

In the mouse embryo, the first progenitors of LECs are specified in the dorsolateral walls of the paired anterior cardinal veins at around 9.5 DPF (Koltowska et al., 2013). The venous endothelial cells (VECs) in these veins express the lymphatic vessel endothelial hyaluronan receptor 1 (LYVE1); only the subset of VECs in the dorsolateral walls expresses the transcriptional factor named prospero homeobox protein 1 (PROX1) (Oliver, 2004). While LYVE1 is not necessary for the VECs to acquire lymphatic competence, PROX1 confers a lymphatic identity on them by activating the expression of lymphatic markers (Oliver, 2004). An example is the vascular endothelial growth factor receptor

3 (VEGFR3), a type of receptor tyrosine kinase which activates multiple intracellular pathways critical for lymphatic specification (Yu et al., 2014). These PROX1-expressing VECs are fully committed to the lymphatic fate and can therefore be considered LEC progenitors (Oliver, 2004). PROX1 is also needed for the ongoing maintenance of lymphatic identity in the mouse's adulthood (Yu et al., 2014), but it is not needed for the aforementioned endothelial cells to bud from the veins (Yang and Oliver, 2014a).

PROX1 expression is in turn induced by another transcription factor named sex-determining region Y box 18 (SOX18) which binds to the promoter region of PROX1 (Schulte-Merker et al., 2011). During lymphatic fate specification, SOX18 is expressed in both the arteries and veins in the embryo, but PROX1 expression is not induced in the arteries (Yu et al., 2014). Even within the veins, SOX18 is highly enriched in the subset of venous endothelial cells destined to become LEC progenitors (Chen et al., 2014). Additional mechanisms are needed to explain this asymmetry. For example, extracellular-signal-regulated kinase (ERK) signalling, also known as mitogen-activated protein kinases (MAPK) signalling, activates SOX18 in the veins (Yang and Oliver, 2014a). An asymmetry in this signalling event may result in the asymmetric SOX18 activity and PROX1 expression. SOX18 is only expressed in the early stage of the developmental programme (Yu et al., 2014), so it is unnecessary for the ongoing maintenance of lymphatic identity.

The chicken ovalbumin upstream promoter transcription factor II (COUP-TFII) is highly expressed in the mesenchymal tissue and blood vascular endothelium of the embryo (Yang and Oliver, 2014b). Within the blood vasculature, its expression is restricted to the veins where its activity is regulated epigenetically by the Brahma-related gene 1 (BRG1), a chromatin-remodelling enzyme (Yang and Oliver, 2014b). COUP-TFII has several functions in the mouse embryo (Yang and Oliver, 2014b). First, it inhibits the activity of Notch (a family of transmembrane proteins) in order to block the arterial transcription programme in the veins. Second, COUP-TFII is a venous cofactor that can bind to the promoter region of PROX1, where it cooperates with SOX18 to activate the expression of PROX1. It means that VECs require COUP-TFII to transdifferentiate into LEC progenitors, which require COUP-TFII to maintain PROX1 expression. However, COUP-TFII is not needed to maintain normal lymphatic functions once the mouse reaches adulthood. Third, it is essential for the prenatal sprouting of lymphatic capillaries because it directly regulates the transcription of neuropilin-2 (NRP2).

In summary, PROX1, COUP-TFII, and Notch constitute feedback loops which regulate the specification of early arterial, venous, and lymphatic cell fates in the mouse embryo.

The organ-based lymphatics of the mouse develop differently from this mechanism. For example, the cardiac lymphatics have a heterogeneous origin according to Klotz et al. (2015). Both the extra-cardiac veins and yolk sac haemogenic endothelium contribute cells to the cardiac lymphatics. PROX1 is necessary and sufficient to drive lymphatic specification in both sources.

2.1.2 Sprouting of Lymphatic Endothelial Cell Progenitors

Lymphangiogenesis is the embryonic and post-natal development and proliferation of new lymphatics by sprouting from veins or/and *de novo* from lymphangioblasts by extending from any pre-existing vessels (Ji, 2006). From around 10 DPF, LEC progenitors exit from multiple sites of the venous vasculature (Koltowska et al., 2013). Sprouting leads to a total of eight lymph sacs along the anterior-posterior axis of the embryo, including pairs of jugular, subclavian, and posterior lymph sacs on its left and right sides, the cisterna chyli, and the retroperitoneal lymph sac (Chen et al., 2014). These sacs contain most of the LEC progenitors fated to become the LECs in the primitive lymphatic plexus. They shrink as the embryo develops (Chen et al., 2014). Some extra LEC progenitors are provided directly by the veins (Chen et al., 2014).

In a review, Yang and Oliver (2014b) explain that only a subpopulation of the LEC progenitors in the veins exit and sprout out. The progenitors that do sprout out take on distinct spindle morphologies, up-regulate their rate of proliferation, and express LEC markers such as podoplanin (PDPN) and NRP2 (Yang and Oliver, 2014a; Koltowska et al., 2013; Chen et al., 2014). Those that remain in the veins are fated to develop into the lymphovenous valves at the junction of the jugular and subclavian veins (Yang and Oliver, 2014b). Instead of acquiring the features characteristic of LECs, they express markers such as the forkhead box protein C2 (FOXC2) and integrin alpha-9 (ITGA9). They intercalate with a subpopulation of the VECs in the veins to form the lymphovenous valves.

The vascular endothelial growth factor C (VEGFC), a lymphangiogenic growth factor provided by the lateral mesoderm of the embryo, is critical in LEC progenitor sprouting (Schulte-Merker et al., 2011). Its importance is underscored by the fact that VEGFC$^{-/-}$ mice do not develop any lymphatic structures because their LEC progenitors fail to leave their veins (Pichol-Thievend et al., 2014). VEGFC binds to and activates VEGFR3; VEGFR3 in turn activates the protein kinase B (AKT) and ERK intracellular pathways to promote endothelial cell proliferation, migration, and survival (Mäkinen et al., 2001). VEGFR3 is a receptor tyrosine kinase (Schulte-Merker et al., 2011). In the mouse embryo, it is initially expressed by both VECs and LEC progenitors, but after 10.5 DPF, it is mostly restricted to the latter (Schulte-Merker et al., 2011). Mechanistically, it is the tyrosine kinase activity of VEGFR3 rather than its VEGFC-binding domain that is necessary for LEC progenitor sprouting (Yang and Oliver, 2014a). VEGFC can also activate the vascular endothelial growth factor receptor 2 (VEGFR2) after proteolysis; VEGFR2 is only expressed by LEC progenitors and it only promotes lymphatic vessel enlargement, not sprouting (Schulte-Merker et al., 2011). The vascular endothelial growth factor D (VEGFD) is another ligand which can activate VEGFR3 (Mäkinen et al., 2001).

Since the ECM is an obstacle to cell migration, it is unsurprising that the production of ECM components like laminin or collagen IV by LEC progenitors is down-regulated from around 10.5 DPF (Oliver, 2004).

2.1.3 Lymphatic Vascular Remodelling and Maturation

From 15.5 DPF onwards, the primitive lymphatic plexus further specialises into lymphatic capillaries, precollectors, and collecting lymphatic vessels (Schulte-Merker et al., 2011).

In a review, Bazigou et al. (2014) describe the junctions among the LECs on the lymphatic capillaries as the vessels' entry sites. These junctions, known as buttons, are discontinuously arranged around the LEC membranes to create valve-like gaps of around 3 µm in diameter. When there are more buttons, for example during diseases, the capillaries become leakier.

The collecting lymphatic vessels' formation is marked by a transient up-regulation of FOXC2 (Schulte-Merker et al., 2011). Where their intraluminal valves form, PROX1, FOXC2, and a transcription factor called GATA2 are up-regulated (Koltowska et al., 2013). While the valves continue to express FOXC2 and PROX1 strongly until and throughout the mouse's adulthood, the lymphangions between successive valves express less PROX1, VEGFR3, LYVE1, and CCL21, secrete basement membrane proteins, and acquire smooth muscle cell coverage (Schulte-Merker et al., 2011). In the valve-forming LECs, GATA2 regulates the expression of PROX1 and FOXC2 and controls a genetic network linking PROX1, ITGA9, and Ephrin-B2 (Koltowska et al., 2013; Bazigou et al., 2014). As reviewed by Vittet (2014), the initiation of valve formation coincides with the onset of lymph flow. This flow induces FOXC2 expression by the LECs at the future valve sites. FOXC2 cooperates with PROX1 to regulate gene expression and signalling pathways to establish the valves' territories, constrict the collecting lymphatic vessels, and form the valves' leaflets. There are other relevant signalling pathways. Examples are Ephrin-Eph signalling (Koltowska et al., 2013), ANG/TIE signalling (Koltowska et al., 2013), and reelin signalling (Yang and Oliver, 2014a). The receptors for various ECM components are involved in collecting lymphatic vessel maturation, such as integrin signalling which promotes LEC proliferation, survival, and migration (Yang and Oliver, 2014a).

2.1.4 Separation from Blood Vessels

In a healthy mammal, the lymphatic and blood vasculatures should be disconnected. An exception is the junction of its jugular and subclavian veins. At this location, lymph is returned to the blood circulation through two pairs of lymphovenous valves (Schulte-Merker et al., 2011; Chen et al., 2014).

In the mouse embryo, platelets aggregate where the veins meet the lymph sacs to seal off the two vasculatures (Schulte-Merker et al., 2011). The molecular details are as follows (Schulte-Merker et al., 2011). The O-glycosylated mucoprotein podoplanin, expressed by the LEC progenitors in the sacs, binds to the C-type lectin domain family 2 receptor (CLEC2), expressed by the platelets. Their binding induces the intracellular signalling cascades mediated by the spleen tyrosine kinase (SYK), the sarcoma-homology-2-domain-containing leukocyte protein of 76 kDa (SLP-76), and the phospholipase Cγ2 (PLCγ2). The final products are blood clots; they seal off the two vasculatures. T-synthase is a glycosyltransferase which catalyses the O-glycosylation of podoplanin to stabilise the latter (Chen et al., 2014).

2.2 Zebrafish

Although we want to build mathematical models, run computer simulations, and propose theories, we want to make predictions that can easily be validated experimentally, so the ease of experimental studies must be taken into consideration. Many developmental mechanisms are conserved across vertebrates, such as the venous origin of the lymphatic vasculature and the gene products governing lymphangiogenesis (Schulte-Merker et al., 2011). This property allows us to study a simple vertebrate and apply our conclusions to more complex ones. The zebrafish (*Danio rerio*) is a better model organism than the mouse because of the following reasons.

1. The lymphatic vasculature in its trunk is spatially periodic as illustrated in figure 2.2. The developmental steps that generate it are also spatially periodic in addition to being simple and well-defined (van Impel and Schulte-Merker, 2014). We will go through the developmental steps in greater detail in the following subsections.

2. There is a wealth of information about its genetics and developmental biology, such as the reviews written by Gore et al. (2012) and van Impel and Schulte-Merker (2014).

3. Because of the small size of the zebrafish embryo, diffusion alone can supply sufficient oxygen in the first few days of its development (Gore et al., 2012). Since its blood circulation only starts at 30 hours post-fertilisation (HPF) (Iida et al., 2010), we can study the effects of vascular defects on other aspects of its development.

4. The embryo develops rapidly. For example, the major lymphatic vessel, the thoracic duct (TD), is fully formed by 5 DPF (van Impel and Schulte-Merker, 2014). Also, it reaches sexual maturity roughly 3 months post-fertilisation

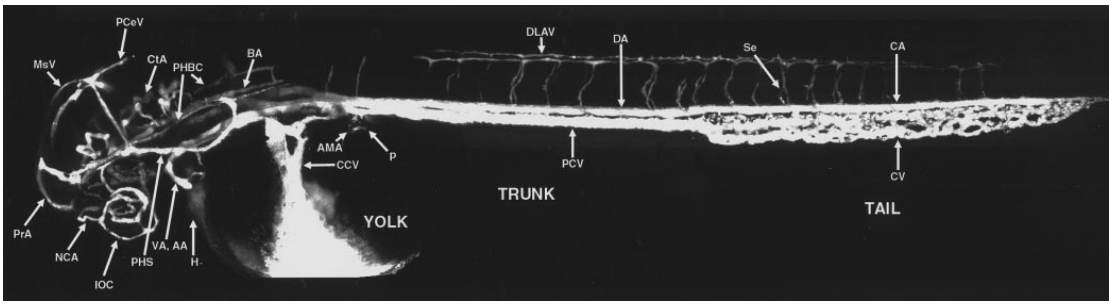

FIGURE 2.2: Schematic of the zebrafish embryo at around 2 days post-fertilisation (Isogai et al., 2001); reproduced with permission. DA is the dorsal aorta; PCV, the posterior cardinal vein; DLAV, one of the paired dorsal longitudinal anastomotic vessels; Se, an intersegmental vessel; CA, the caudal artery; CV, the caudal vein. We are interested in the trunk, so the structures in and near the head are not relevant.

(Nasiadka and Clark, 2012). We can perform quick experiments on zebrafish embryos.

5. The embryo is transparent and does not develop *in utero*: we can easily manipulate zebrafish embryos and optically image their internal structures at a high resolution (Gore et al., 2012).

In the mouse, lymphatic sprouting occurs after the formation of veins. In the zebrafish, however, venous and lymphatic sprouts emerge from the cardinal veins simultaneously. Therefore, we will review the lymphangiogenic process in the zebrafish trunk together with the angiogenic process therein. The whole process is illustrated in figure 2.3. We will go through the individual steps in the following subsections.

2.2.1 Formation of Blood Vessels

At 32 HPF, most of the blood vasculature in the zebrafish embryo is fully formed, including the dorsal aorta (DA), the posterior cardinal vein (PCV), a set of intersegmental arteries (aISVs), and a pair of dorsal longitudinal anastomotic vessels (DLAVs) (Koltowska et al., 2013). The spatial layout of these structures at this stage is shown in figure 2.3(a).

The DA and the PCV form by vasculogenesis, the co-migration and coalescence of the angioblast progenitor cells from the lateral mesoderm to form vessels *de novo* (Isogai et al., 2003). Beginning at around 0.8 DPF, around thirty pairs of primary sprouts emerge bilaterally from the DA at each vertical myoseptal boundary of the embryo. They elongate dorsally towards the dorsolateral roof of the neural tube. There, they branch rostrally towards the embryo's head and caudally towards its tail. Finally, they interconnect to form two paired dorsal longitudinal anastomotic vessels (DLAVs) (Isogai et al., 2003; van Impel and Schulte-Merker, 2014). The DA and the DLAVs are linked by the aISVs.

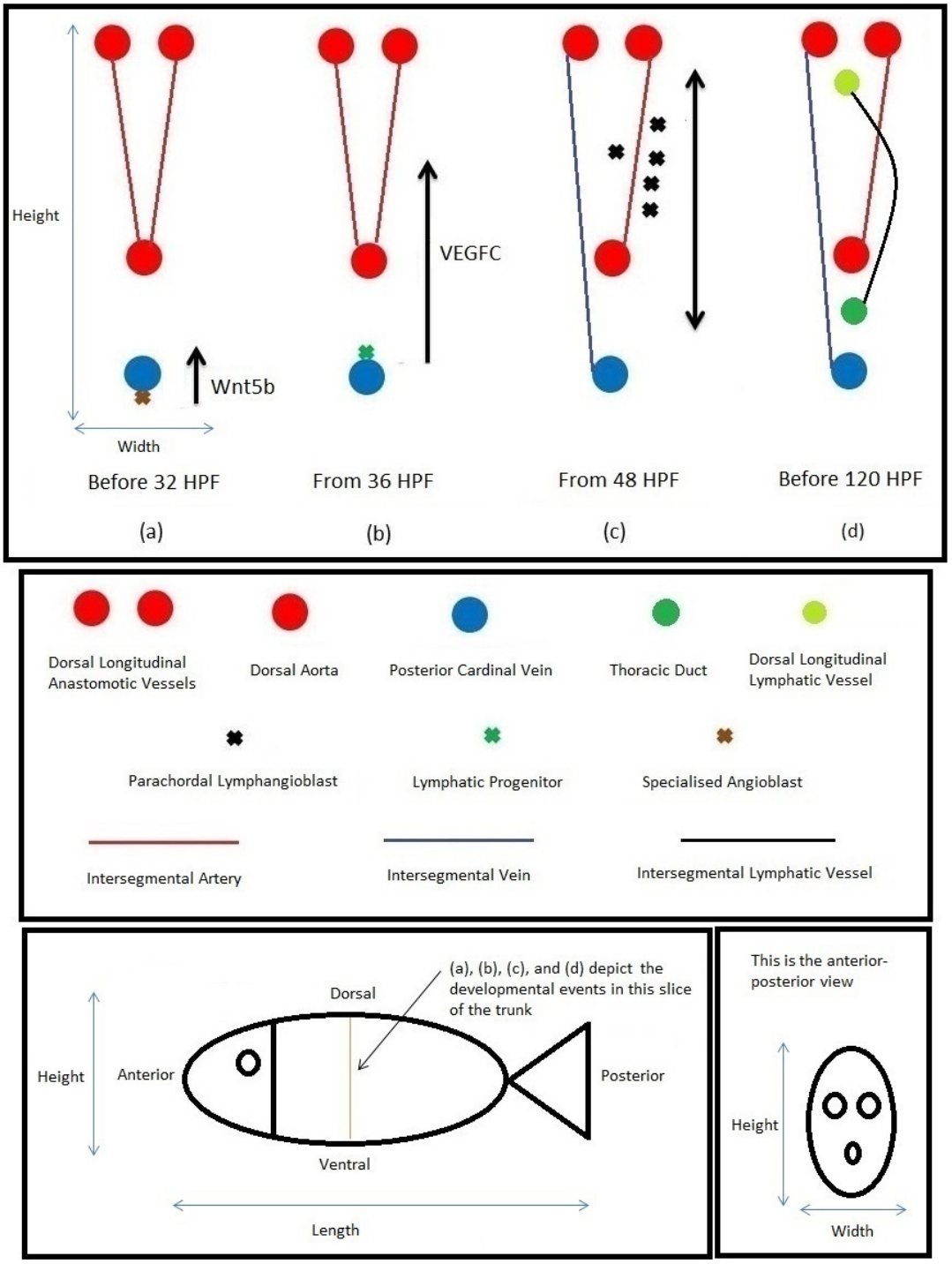

FIGURE 2.3: Developmental steps that generate the lymphatic vasculature in the zebrafish trunk. (a), (b), (c), and (d) show a slice of the trunk cut along the ventral-dorsal axis. The developmental events in the slice are depicted in the anterior-posterior view. This particular slice of the trunk has a pair of intersegmental arteries (aISVs) and a pair of lymphatic sprouts, one of which fuses with an aISV to from an intersegmental vein (vISV). There are thirty slices like this one in the trunk. When the parachordal lymphangioblasts (PLs) reach where the thoracic duct and the dorsal longitudinal lymphatic vessels lie in the ventral-dorsal slice depicted, they migrate anteriorly and posteriorly to connect with the PLs from the remaining twenty-nine slices.

2.2.2 Transdifferentiation

Lymphangiogenesis begins in the ventral wall of the PCV, where Wnt5b, secreted by the endoderm, commits specialised angioblasts to the lymphatic fate by 24 HPF; this step has been observed by Nicenboim et al. (2015). Nicenboim et al. (2015) have shown that the resulting LEC progenitors translocate to the dorsal side of the PCV by 30 HPF. This step is shown in figure 2.3(a), where the upward-pointing arrow represents the translocation step.

Nicenboim et al. (2015) have also shown that the specialised angioblasts come from the lateral plate mesoderm and they can divide asymmetrically to produce arterial, venous, and lymphatic cells. In a review, Koltowska et al. (2013) argue that the angioblasts need PROX1 homologues to commit to the lymphatic fate. On the other hand, while a mouse embryo without PROX1 is completely devoid of lymphatic vessels, a zebrafish embryo with similar impairments can form up to 70 % of its TD (Pichol-Thievend et al., 2014). In the zebrafish embryo, COUP-TFII is also essential for lymphatic development, but the role of SOX18 is unclear (Koltowska et al., 2013).

2.2.3 Sprouting of Lymphatic Endothelial Cell Progenitors

At around 36 HPF, the LEC progenitors emerge from the PCV as thirty pairs of secondary sprouts and migrate dorsally (van Impel and Schulte-Merker, 2014). This step is shown in figure 2.3(b), where the upward-pointing arrow represents the progenitors' sprouting.

Hogan et al. (2009) have demonstrated that this sprouting is only possible when the LEC progenitors are stimulated by VEGFC through VEGFR3. In the zebrafish embryo, VEGFC is expressed in the DA, the aISVs, and the hypochord, while VEGFR3 is expressed by VECs and LEC progenitors (van Impel and Schulte-Merker, 2014). VEGFC is believed to utilise autocrine and paracrine signalling (Mulligan and Weinstein, 2014).

2.2.4 Formation of Intersegmental Veins

At approximately 48 HPF, half of the secondary sprouts are already fused with their adjacent aISVs to form a set of intersegmental veins (vISVs) (van Impel and Schulte-Merker, 2014). At first, the vISVs remain connected to the DA. These connections thin and disappear completely soon, leaving the vISVs connected to the PCV and the DLAVs only (van Impel and Schulte-Merker, 2014). The spatial layout of the vessels after these steps is shown in figure 2.3(c).

2.2.5 Formation of Parachordal Lymphangioblast String

In the same time window between 36 and 48 HPF, the remaining secondary sprouts migrate to a region named horizontal myoseptum; it divides the dorsal and ventral halves of the embryo. After reaching the horizontal myoseptum, the sprouts disconnect from the PCV (van Impel and Schulte-Merker, 2014). They form a pool of cells called parachordal lymphangioblasts (PLs); they are the precursors of most of the LECs in the trunk (van Impel and Schulte-Merker, 2014). The PLs form a string-like structure which is functionally equivalent to the mouse embryo's lymph sacs, but proper lymph sacs are absent in the zebrafish embryo (Koltowska et al., 2013). The PLs stay in the horizontal myoseptum until around 60 HPF (Cha et al., 2012; Koltowska et al., 2013). In figure 2.3(c), the leftmost PL is in the horizontal myoseptum.

In this time window, the horizontal myoseptum expresses the ligand named chemokine (C-X-C motif) ligand 12a (Cxcl12a), which binds to the receptor named chemokine (C-X-C motif) receptor 4 (Cxcr4), expressed on the LEC progenitors forming the sprouts; this binding ensures that the dorsally migrating sprouts turn laterally when they reach the horizontal myoseptum. This guidance mechanism has been shown by Cha et al. (2012). Cxcr4 is a G-protein-coupled receptor (Kucia et al., 2004). When it is activated by its ligands, it in turn activates multiple intracellular signalling events, including calcium efflux, ERK signalling, and AKT signalling (Kucia et al., 2004). The functional responses of the cells expressing it are motility, chemotactic responses, adhesion, and secretion of growth factors and proteases (Kucia et al., 2004). Further guidance cues for the sprouts are thought to be provided by the motor neuron axons positioned along the horizontal myoseptum (Cha et al., 2012).

2.2.6 Migration from Parachordal Lymphangioblast String

Then, the PLs continue to express Cxcr4 as they migrate both ventrally and dorsally along their adjacent aISVs; the aISVs express the ligand Cxcl12b. This step has been confirmed by Cha et al. (2012). In figure 2.3(c), the four PLs on the aISV's right hand side are the migrating PLs; the up-down arrow represents their migration in opposite directions.

2.2.7 Functional Lymphatic System

By 120 HPF, the TD is formed between the DA and the PCV, the dorsal longitudinal lymphatic vessel (DLLV) below the DLAVs (van Impel and Schulte-Merker, 2014). They are both formed by the PLs. At this stage, the PCV expresses Cxcl12a and the DA expresses Cxcl12b, thus ensuring the ventrally migrating PLs stop between the two blood vessels. Cha et al. (2012) have again demonstrated this guidance mechanism.

Once they reach where the DLLV and TD should lie in a ventral-dorsal slice, the PLs migrate anteriorly and posteriorly to connect with the PLs from the other ventral-dorsal slices in the embryo's trunk, thus ensuring the two lymphatic vessels are continuous (van Impel and Schulte-Merker, 2014). The DLLV and TD are connected via a set of intersegmental lymphatic vessels (ISLVs) (van Impel and Schulte-Merker, 2014). Bussmann et al. (2010) have found that 97 % of the ISLVs are adjacent to the aISVs.

The trunk lymphatic system is functional by 5 DPF in the sense that it is capable of taking up substances from the interstitium and returning lymph to the blood circulation (Schulte-Merker et al., 2011). The spatial layout of it is shown in figure 2.3(d).

2.2.8 Further Development

The embryo has other lymphatic vessels too. As reviewed by Mulligan and Weinstein (2014), some LECs leave the ISLVs and migrate rostrally and caudally along the horizontal myoseptum to form the parachordal lymphatic vessel between 5 and 7 DPF. Some LECs migrate ventrally from this vessel along the intercostal vessels, forming the intercostal lymphatic vessels by 15 DPF (Mulligan and Weinstein, 2014). The facial lymphatics, lateral lymphatics, and intestinal lymphatics all connect to the TD (Koltowska et al., 2013). There is also a lymphatic system in the tail fin (van Impel and Schulte-Merker, 2014). These steps are not shown in figure 2.3.

2.2.9 Differences from the Mouse

It is noteworthy that CLEC2, podoplanin, lymph sacs, and lymph valves are all absent in the zebrafish (Chen et al., 2014). However, as argued by van Impel and Schulte-Merker (2014), the genetic programmes regulating lymphangiogenesis in the zebrafish and mouse have more similarities than differences, while the stark contrast on the cellular level may be down to cell-cell and cell-ECM interactions.

2.3 Research Questions and Hypotheses

In this section, we will pose the research questions of this thesis. Due to the reasons stated in section 2.2, we will study the zebrafish embryo.

First, we will summarise what we know about the regulators of lymphatic development in the zebrafish embryo. Nicenboim et al. (2015) have shown that Wnt5b is responsible for the lymphatic specification of the specialised angioblasts in the ventral wall of the

PCV. Hogan et al. (2009) have shown that the resulting LEC progenitors bud off from the PCV when they are stimulated by VEGFC in a process that requires the collagen-and-calcium-binding-epidermal-growth-factor-domain-containing protein 1 (CCBE1). Cha et al. (2012) have demonstrated that they migrate dorsally, turn laterally at the horizontal myoseptum under the guidance of Cxcl12a, and form the PL string there. The PLs leave the horizontal myoseptum and migrate along the aISVs because, as Cha et al. (2012) have found out, the aISVs express Cxcl12b. The aISVs express VEGFC too (Mulligan and Weinstein, 2014; van Impel and Schulte-Merker, 2014).

Second, we will identify the gaps in our knowledge. Although we know that VEGFC causes the LEC progenitors in the PCV to sprout out, and Cxcl12a guides them into the horizontal myoseptum, it is unclear what directs them from the PCV to the horizontal myoseptum. In other words, VEGFC is the start signal and Cxcl12a is the stop signal, but what keeps the cells on track? Furthermore, the LEC progenitors that exit the veins in the mouse embryo undergo changes in cell shape, proliferation rate, and express lymphatic markers during their migration (Chen et al., 2014). Although podoplanin is absent in the zebrafish according to Chen et al. (2014), the zebrafish is likely to share some of the other changes in the mouse due to their similar genetic programmes (van Impel and Schulte-Merker, 2014); the PCV-derived LEC progenitors in the zebrafish embryo are likely to differentiate after their exit too. The question is what induces their differentiation in a position-dependent manner.

Third, we will hypothesise about these gaps. Mäkinen et al. (2001) have demonstrated that VEGFC promotes LEC survival, proliferation, and migration. Therefore, VEGFC is a growth factor for LECs and their progenitors in general. This is consistent with our understanding that VEGFC stimulates the sprouting of LEC progenitors from the mouse's and zebrafish's veins. We hypothesise that VEGFC is also a morphogen for the migrating LEC progenitors in the zebrafish embryo. As reviewed by Pichol-Thievend et al. (2014), VEGFC-VEGFR3 signalling activates ERK signalling, while Deng et al. (2013) have shown that ERK signalling is necessary for lymphatic fate specification, providing a basis for our hypothesis. Because VEGFC promotes survival and proliferation in LECs in general, we further speculate that VEGFC guides the migrating LEC progenitors in the zebrafish embryo by chemoattraction. By a morphogen, we mean a chemical that provides positional information to a developing embryo through a concentration gradient; the cells in the embryo express genes differentially depending on their positions in the gradient. Appendix A is a detailed review of morphogens. By a chemoattractant, we mean a chemical that provides directional information to these cells; they migrate up a concentration gradient of the chemoattractant.

It is important to stay objective and not be blinded by our hypotheses. In the following chapters, we will build mathematical models to describe the concentration

dynamics of VEGFC in the zebrafish embryo. However, VEGFC is only a candidate morphogen and chemoattractant. Using our models, we will seek to capture generic mechanisms which are relevant to other candidates too.

2.4 Chapter Summary

In this chapter, we reviewed what is known about lymphatic development in the mouse and zebrafish. The zebrafish has some clear advantages over the mouse as a model organism for our investigation. The PCV-derived LEC progenitors' migration to the horizontal myoseptum is an uncertain step in the zebrafish embryo; it occurs between 36 and 48 HPF. Specifically, it is unclear what directs the migrating LEC progenitors and what causes them to differentiate during migration. We hypothesised that VEGFC, an important regulator of the cells' sprouting from the PCV, is also a morphogen and chemoattractant for them. To test our hypotheses, we will model the concentration dynamics of VEGFC in the zebrafish embryo mathematically. However, VEGFC is only a candidate, so we will aim to capture generic mechanisms with our modelling work.

Chapter 3

Interstitial Flow

We will build a mathematical model to test our hypotheses. In this chapter, we will construct the interstitial flow component of the model. First, we will review how the interstitial flow in an embryo can regulate the lymphangiogenic processes therein. Then, we will build an idealised geometry of the zebrafish embryo's trunk. After a comparison between Darcy's law and Brinkman's equation, we will model the interstitial flow in the trunk using Brinkman's equation and the principle of mass conservation. We will end the chapter by parametrising the interstitial flow model component.

3.1 Morphogenetic Functions

In this thesis, the interstitial space of an organism is defined as the two-phase environment surrounding its cells. The two phases are an interstitial medium (extracellular matrix, ECM) and the interstitial fluid flowing through this medium.

As reviewed by Swartz and Fleury (2007), interstitial fluid makes up 20 % of the human body mass. Its flow is driven by the hydrostatic and osmotic pressure differences between the blood vessels, the interstitial space, and the lymphatics. The pumping secondary lymphatics and their nearby tissues provide additional driving forces. As reviewed by Breslin (2014), after the lymphatic system absorbs the interstitial fluid, it is returned to the blood circulation at the lymph nodes and the subclavian veins. The interstitial flow velocities in different adult tissues range from 0.1 to 2 $\mu m\ s^{-1}$; this range is lower than that for blood flow (Swartz and Fleury, 2007). As explained by Rutkowski and Swartz (2007), this difference is due to the resistance of the extracellular matrices.

The interstitial flow in an embryo can regulate its morphogenesis in a few ways (Rutkowski and Swartz, 2007). First, it applies shear stresses and pressure forces on

the cells in the embryo, and tethering forces on the cell-ECM connections, thereby inducing intracellular changes. Second, it can shift the distributions of morphogens, chemokines, and proteases in the embryo. For example, by skewing a concentration profile in one direction, the flow allows the cells to receive chemical cues released by themselves, a phenomenon known as autologous gradient generation. Since some chemical cues are sequestered by the ECM, the interstitial flow can affect their concentration profiles by shifting the distributions of their releasing proteases too.

Boardman and Swartz (2003) studied lymphatic regeneration in a collagen implant in a mouse tail undergoing skin regeneration. During the experiment, channels formed in the collagen in the interstitial flow's direction. Then, LECs migrated along these channels and organised into a functional lymphatic network. Based on these observations, Boardman and Swartz (2003) have proposed a mechanism: matrix metalloproteinases (MMPs) travel in the flow's direction, they preferentially degrade the collagen in this direction, the resulting channels skew the flow further in this direction, and VEGFC is preferentially transported down the channels to induce LEC proliferation and migration along them.

Coffindaffer-Wilson et al. (2011b) have shown that the zebrafish's lymphatic development is contingent on a normal interstitial flow. An abnormally high and an abnormally low flow both impair the TD's formation: the PLs in the horizontal myoseptum fail to exit between 2 and 3 DPF. This impairment is due to the transport of biochemicals, not biomechanical stimuli.

Helm et al. (2005) studied capillary morphogenesis *in vitro*. The take-home message of the paper is a contrast between the roles of diffusion and convection in morphogenesis. Diffusion from a source of morphogens and proteases leads to decreasing, symmetric, and autocrine distributions of these chemicals. An asymmetric fluid flow (convection) can create transcellular gradients of the chemicals increasing in the flow's direction. This idea has been explored theoretically by Fleury et al. (2006). Their simulation results show that the pericellular gradients of cell-secreted and matrix-binding proteins are steepened compared to their non-matrix-binding counterparts.

Song and Munn (2011) stimulated endothelial cells with a blood flow, a transverse interstitial flow, and the vascular endothelial growth factor (VEGF). In the experiments, endothelial cell sprouting via the nitric oxide pathway was inhibited by the shear stresses from the blood flow; this sprouting was enhanced by the interstitial flow, but it occurred against the flow's direction; vessel dilation was enhanced in the flow's direction; this sprouting was enhanced by positive VEGF gradients; negative VEGF gradients resulted in vessel dilation instead. Although Song and Munn (2011) studied blood vessel development, it is possible that lymphangiogenesis is regulated by similar mechanisms.

The phasic contractions that drive a lymph flow can be explained in terms of the integration of physical forces and biochemical factors (Kunert et al., 2015). The proposed mathematical model is based on the following observed facts. First, the muscle cells lining a lymphatic vessel are sensitive to calcium ion dynamics. Neurotransmitters or other stimulants can depolarise the membranes of these cells, triggering an influx of calcium ions and hence muscle contractions. Furthermore, the muscle cells have stretch-activated ion channels which open to calcium ions in response to mechanical stresses. Second, the LECs forming the lymphatic vessel can produce nitric oxide (NO) in response to the fluid flow in its lumen; NO modulates the release and uptake of calcium ions, as well as the enzymes responsible for muscle contractions. Third, NO dynamics are faster than the lymphatic vessel's pumping dynamics, connecting the first two observations. The proposed model describes the following mechanism. The vessel contracts to enhance the lymph flow; an increased flow means higher shear stresses on the LECs, activating endothelial NOS (eNOS) production and subsequently, NO production; NO blunts or reverses the muscle cells' calcium-ion-dependent contractions, lowering the lymph flow, its shear stresses, and the production rate of NO while the existing NO degrades quickly; the calcium ion level is restored for the next cycle. The simulation results show that the concentrations of calcium ions and NO oscillate spatiotemporally to form feedback loops, which result in phasic contractions to drive the lymph flow. This control system is robust over a range of fluid pressures.

3.2 Idealised Geometry

According to van Impel and Schulte-Merker (2014), the blood and lymphatic vasculatures in the zebrafish trunk are spatially periodic along the anterior-posterior axis. Exceptions are the three sets of intersegmental vessels, the aISVs, vISVs, and ISLVs, which appear at certain points on the anterior-posterior axis only. They break the symmetry by extending along the ventral-dorsal axis. The secondary sprouts of LEC progenitors emerge from the PCV next to the aISVs, forming the vISVs; the ISLVs are adjacent to the aISVs too (Isogai et al., 2003). Therefore, the three sets of intersegmental vessels coalign in thirty ventral-dorsal slices of the zebrafish trunk (Isogai et al., 2003). These slices are regularly spaced along the anterior-posterior axis; two successive slices are about 75 µm apart (Coffindaffer-Wilson et al., 2011a). As reviewed in chapter 2, in our time frame of interest, between 36 and 48 HPF, the LEC progenitors migrate dorsally, meaning there are not any cells in the vicinity of each slice. Taken together, there are two implications for our study. First, the lymphangiogenic events we are interested in occur in these thirty slices. Second, each slice can be considered independently from the rest. Therefore, we will model just one

TABLE 3.1: Dimensions of the idealised geometry and its internal structures. PCV abbreviates posterior cardinal vein; DA, dorsal aorta; DLAV, dorsal longitudinal anastomotic vessel; LEC, lymphatic endothelial cell; HPF, hours post-fertilisation. Note that 'LEC progenitor' and 'LEC' are used interchangeably in reference to the solid circle inside the idealised geometry.

Quantity Measured	Time	Measurement	Reference
Total Height	96 HPF	434 μm	McGee et al. (2012)
Total Width	72 HPF	43 μm	Hermans et al. (2010)
PCV Diameter	96 HPF	20 μm	Coffindaffer-Wilson et al. (2011a)
DA Diameter	96 HPF	12 μm	Coffindaffer-Wilson et al. (2011a)
DLAV Diameter	96 HPF	13 μm	Coffindaffer-Wilson et al. (2011a)
PCV-DA Distance	96 HPF	51 μm	Coffindaffer-Wilson et al. (2011a)
DA-DLAV Distance	96 HPF	151 μm	Coffindaffer-Wilson et al. (2011a)
LEC Diameter	-	10 μm	Yaniv et al. (2006)

ventral-dorsal slice with a pair of secondary sprouts from the PCV, the slice shown in figure 2.3. The anterior-posterior and ventral-dorsal axes are defined in figure 2.3 too.

However, we will simplify the slice in figure 2.3. We will not model the aISVs because our interest is the period from 36 to 48 HPF, the period when the PCV-derived LEC progenitors migrate to the horizontal myoseptum and differentiate during migration. These events are not dependent on the aISVs (Bussmann et al., 2010). Additionally, there are a pair of DLAVs in the slice, but the distance between them is small. Representing them as two separate tubes requires a high-resolution grid, so we will model one DLAV only and double the flux into this vessel.

Based on the above assumptions, we will construct the idealised geometry in figure 3.1. The solid circle represents an LEC progenitor on its way to the horizontal myoseptum; it is located halfway between the DA and the PCV. Our model does not consider cell migration, so the grey circle is stationary. For the purpose of model development, we will divide the geometry into two domains, the LEC progenitor and the interstitial space, which is the the whole geometry minus the LEC progenitor. We are unsure where exactly the LEC progenitor differentiates into a mature LEC, so we will use 'LEC progenitor' and 'LEC' interchangeably to refer to the solid circle. The blood vasculature in the zebrafish is fully established by 32 HPF and its lymphatic vasculature forms in association with the blood vasculature (Koltowska et al., 2013). Furthermore, the embryo's volume does not change significantly from 2 DPF onwards (Okuda et al., 2012). As a result, we will not consider any volumetric changes of the geometry and its internal structures.

The dimensions of the geometry and its internal structures are summarised in table 3.1.

Henceforth, we will refer to the structure in figure 3.1 as the model zebrafish trunk.

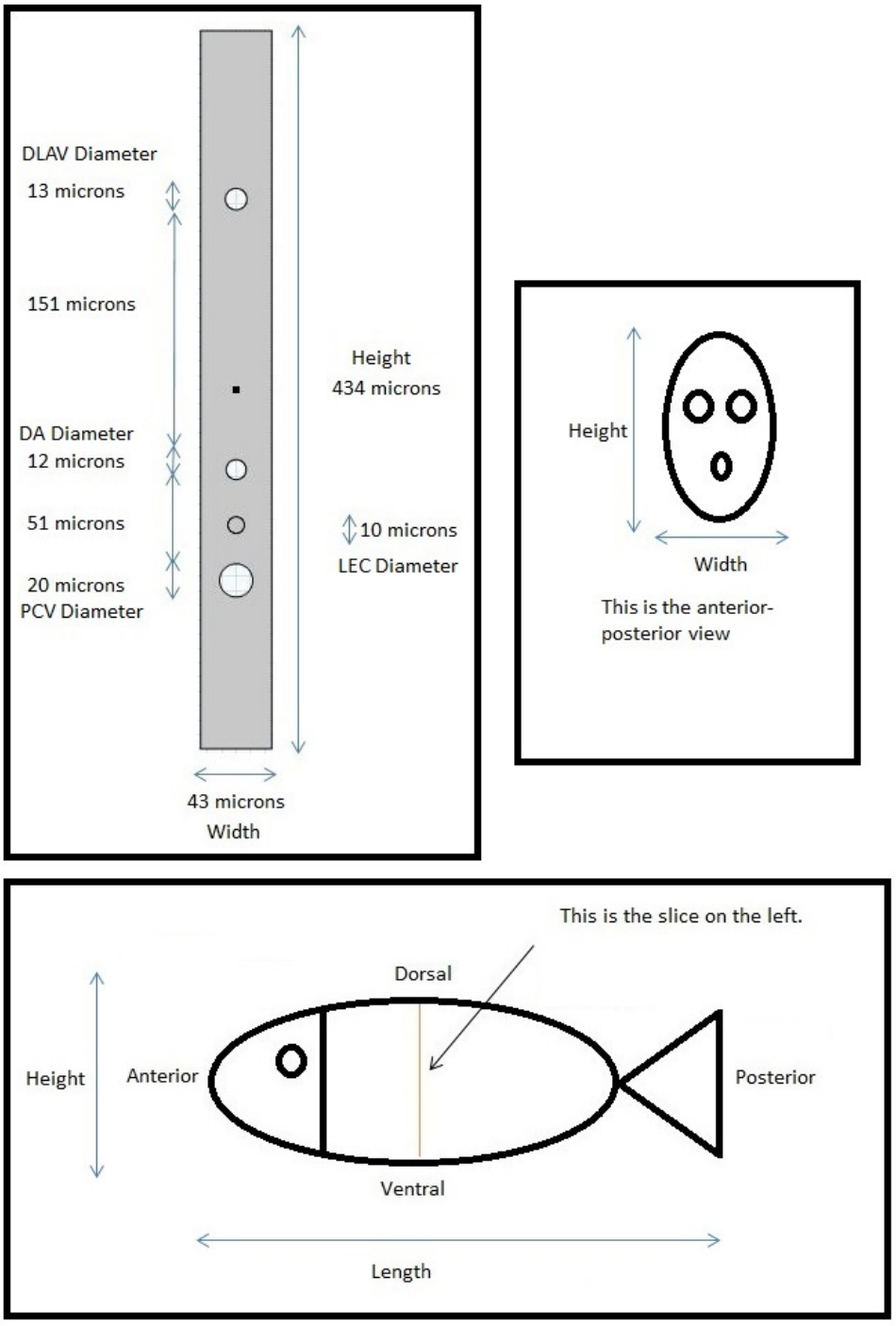

FIGURE 3.1: Idealised geometry of a ventral-dorsal slice of the zebrafish trunk between 36 and 48 hours post-fertilisation. This figure shows the idealised geometry in the anterior-posterior view. This slice is one of the thirty slices with secondary sprouts from the posterior cardinal vein (PCV). The empty circles are, from top to bottom, the dorsal longitudinal anastomotic vessel (DLAV), the dorsal aorta (DA), and the PCV. The solid circle is a lymphatic endothelial cell (LEC) progenitor derived from the PCV; it is halfway between the dorsal aorta and the posterior cardinal vein. The dot in the middle of the figure indicates the horizontal myoseptum, which is the destination of the LEC progenitor. In this study, we consider it to be stationary. Note that 'LEC progenitor' and 'LEC' are used interchangeably in reference to the solid circle. This geometry is called the model zebrafish trunk in this thesis.

3.3 Model Building

The interstitial flow in an organism is driven by the pressure differences between its blood vasculature, interstitial space, and lymphatic vasculature (Swartz and Fleury, 2007). Our model zebrafish trunk does not have a lymphatic vasculature, but the blood circulation in the zebrafish begins by 30 HPF (Iida et al., 2010). There should be an interstitial flow at the beginning of our time frame from 36 to 48 HPF, so we need to model the interstitial flow in the model zebrafish trunk. However, we will not consider the direct effects of the flow on the LEC. In general, cells are sensitive to the shear stresses from a fluid flow; the shear stresses induce intracellular and functional changes in them (Shi and Tarbell, 2011; Ng et al., 2004). However, we are interested in the concentration dynamics of VEGFC on the tissue level; the intracellular details we need to calculate the LEC's responses to the interstitial flow are beyond the scope of this study.

The mathematical model relies on several assumptions. First, like Coffindaffer-Wilson et al. (2011b), we will assume that the DA has the highest blood pressure in the zebrafish, meaning the DA is the sole inlet of fluid in the model zebrafish trunk; its high pressure forces blood plasma into the interstitial space by paracellular transport. Second, we will assume a constant density for the resulting interstitial fluid. Third, we will only model the interstitial flow in the interstitial space domain; the LEC domain is separated from the interstitial fluid by its cell membrane. Fourth, we will assume there are no sources or sinks of fluid in the interstitial space. Fifth, images show that the DA, PCV, and DLAVs have diameters comparable to that of a single endothelial cell (Coffindaffer-Wilson et al., 2011a), so we can reasonably treat them as leaky capillaries with the same permeability (Jain, 1987). Sixth, we will ignore the pulsating nature of the blood circulation. Finally, we will assume that the interstitial flow is at a steady state.

The conservation of fluid mass in the interstitial space is described by the equation

$$\frac{\partial \rho}{\partial t} = -\boldsymbol{\nabla} \cdot (\rho \boldsymbol{u}) + q, \tag{3.1}$$

where ρ is the interstitial fluid's density (kg m^{-3}), t is time (s), $\boldsymbol{u}$ is the interstitial flow's velocity (m s^{-1}), and q is the sum total of all fluid sources and sinks (kg m^{-3} s^{-1}). Essentially, it means that any changes to the fluid mass in the interstitial space are due to inflow, outflow, sources, and sinks. Due to our assumptions that there are no sources or sinks, that ρ is constant, and that the interstitial flow is at a steady state, we can transform equation (3.1) into the equation

$$\boldsymbol{\nabla} \cdot \boldsymbol{u} = 0. \tag{3.2}$$

The other part of the interstitial space, the ECM, is a porous medium. Therefore, the interstitial flow can be described by Darcy's law, a formulation of the principle of momentum conservation. Neglecting gravity, Darcy's law is described by the equation

$$\boldsymbol{u} = -\frac{\kappa}{\mu}\boldsymbol{\nabla} P, \tag{3.3}$$

where κ is the specific hydraulic conductivity (permeability) of the ECM (m^2), a medium property; μ, the dynamic viscosity (kg m^{-1} s^{-1}) of the interstitial fluid; and P, the pressure field (kg m^{-1} s^{-2}) in the interstitial space.

However, Darcy's law is only appropriate for porous media like the ECM. In the next chapter, we will expand the model to include some of the biochemical reactions that degrade the ECM to form channels. Darcy's law cannot model these channels accurately. By contrast, Brinkman's equation can model both phases. It is modelled by the equation

$$\boldsymbol{\nabla} P = -\frac{\mu}{\kappa}\boldsymbol{u} + \mu\boldsymbol{\nabla}^2\boldsymbol{u}, \tag{3.4}$$

where the first term on the right hand side is the Darcy's law contribution, while the second term is the Stokes flow contribution. In the ECM where κ is small, the Darcy's law term dwarfs the Stokes flow term. In a pore of pure interstitial fluid, a large κ reduces Brinkman's equation to Stokes equation, the governing equation for Stokes flow.

To solve this mathematical model, we need some boundary conditions. The fluxes out of the DA and into the PCV and DLAV can be modelled by an equation (Jain, 1987); it is a linear relation between a transvascular flux and the transvascular pressure drop driving it. We will define $\boldsymbol{x}$ (m) as the position vector in the model zebrafish trunk and $\boldsymbol{n}$ as the normal vector. The normal vector points outwards, so it points out of the interstitial space and into the blood vessels. Our definition also means a mass flux into the interstitial space domain is positive.

We will use L_{DA} (kg^{-1} m^2 s) to represent the DA vascular permeability and P^{DA} (kg m^{-1} s^{-2}) to represent the pressure inside the DA. Mathematically, the mass flux from the DA surface ($\partial\Omega_{DA}$) into the interstitial space is modelled by the equation

$$-\boldsymbol{n}\cdot(\rho\boldsymbol{u}) = \rho L_{DA}(P^{DA} - P) \qquad \boldsymbol{x} \in \partial\Omega_{DA}. \tag{3.5}$$

After defining their vascular permeabilities as L_{PCV} and L_{DLAV} (kg^{-1} m^2 s), and their intraluminal pressures as P^{PCV} and P^{DLAV} (kg m^{-1} s^{-2}), we can derive the boundary

conditions on the PCV and DLAV surfaces, $\partial\Omega_{PCV}$ and $\partial\Omega_{DLAV}$, along the same lines, leading to the equations,

$$-\boldsymbol{n}\cdot(\rho\boldsymbol{u}) = L_{PCV}(P^{PCV} - P) \qquad \boldsymbol{x} \in \partial\Omega_{PCV} \text{ and} \tag{3.6}$$

$$-\boldsymbol{n}\cdot(\rho\boldsymbol{u}) = 2L_{DLAV}(P^{DLAV} - P) \qquad \boldsymbol{x} \in \partial\Omega_{DLAV}. \tag{3.7}$$

The multiplicative factor of 2 in equation (3.7) is there because we are representing two paired DLAVs as one vessel.

Finally, We will impose no-slip boundary conditions on the four outer boundaries of the model zebrafish trunk, collectively labelled $\partial\Omega_{x,y}$, and the LEC surface, seen from the interstitial space domain, $\partial\Omega_{LEC/IS+}$. They are represented by the equation

$$\boldsymbol{u} = 0 \qquad \boldsymbol{x} \in \partial\Omega_{x,y} \text{ and } \partial\Omega_{LEC/IS+}. \tag{3.8}$$

3.4 Parametrisation

The parameters of the interstitial flow component of the mathematical model are the intraluminal pressures, the vascular permeabilities, and the properties of the interstitial fluid and the ECM. Table 3.2 summarises these parameters whose origins will be explained in this section.

Hu et al. (2000) have found the relation between the zebrafish embryo's DA pressure and its wet body weight. Their results indicate that the wet body weight is 0.714 mg (7.14×10^{-7} kg) at 48 HPF. The relation gives the corresponding peak-systolic (0.2433 mmHg or 32.437 kg m^{-1} s^{-2}) and end-diastolic (0.1255 mmHg or 16.732 kg m^{-1} s^{-2}) pressures. Ignoring the pulsating nature of the blood flow, we will average them to obtain an estimated DA pressure: 0.1844 mmHg (24.585 kg m^{-1} s^{-2}) relative to the pressure outside the embryo. Intuitively, we expect the DA pressure to drop away from the zebrafish's heart. This drop brings our modelling approach into question: is it appropriate to model a two-dimensional slice only, considering it does not account for this pressure drop? This treatment is reasonable because the pressure drop occurs along the DA. On the other hand, the lymphangiogenic events we are interested in occur normal to the DA, along the ventral-dorsal axis. Even if we want to study the effects of this pressure drop on the modelled events, we can perform a sensitivity analysis on this parameter.

The PCV and the DLAV are parts of the closed and pumped blood circulatory system, so they must have higher pressures than the interstitial space. However, in the absence

TABLE 3.2: Parameters of the interstitial flow component of the mathematical model. DA abbreviates dorsal aorta; PCV, posterior cardinal vein; DLAV, dorsal longitudinal anastomotic vessel; IF, interstitial fluid.

Parameter	Definition	Value	Reference
P^{DA}	DA Pressure	24.585 kg m^{-1} s^{-2}	Hu et al. (2000)
P^{DLAV}	DLAV Pressure	0 kg m^{-1} s^{-2}	Assumed
P^{PCV}	PCV Pressure	0 kg m^{-1} s^{-2}	Assumed
L_{DA}	DA Permeability	734.196 kg^{-1} m^2 s	Jain (1987)
L_{DLAV}	DLAV Permeability	734.196 kg^{-1} m^2 s	Jain (1987)
L_{PCV}	PCV Permeability	734.196 kg^{-1} m^2 s	Jain (1987)
μ	IF Dynamic Viscosity	0.0012 kg m^{-1} s^{-1}	Swartz and Fleury (2007)
ρ	IF Density	1025 kg m^{-3}	Frcitas (1998)

of data about how the blood pressure varies in the circulatory system, back-of-the-envelope estimates are unlikely to be accurate. We will therefore assume that the DA pressure dominates in the embryo, thus setting the pressures in the PCV and the DLAV at zero. We will do the same for the interstitial space.

We have already decided to use one vascular permeability for the three blood vessels. We will rely on Jain (1987) for this parameter. Measurements pertaining to species ranging from the Guinea pig to the frog are stated in the paper. Although the zebrafish is not among these species, we can use the permeability for frog skeletal muscles, 7.2×10^6 cm s^{-1} cmH_2O^{-1} (734.196 kg^{-1} m^2 s). The justification is that the frog and zebrafish are both cold-blooded.

The specific hydraulic conductivity of the ECM depends on the ECM's composition. We cannot use a constant value for this parameter. In the next chapter, we will incorporate some of the biochemical reactions that remodel the ECM into our model. We will consider this parameter in the next chapter.

In general, interstitial fluid contains roughly 40 % of the protein concentration of blood plasma (Swartz and Fleury, 2007). Their similarities in composition allow us to use the parameters for blood plasma. At 37 °C (310.15 K), the dynamic viscosity of blood plasma is 1.2 cP or 0.0012 kg m^{-1} s^{-1} (Swartz and Fleury, 2007) and its density is 1025 kg m^{-3} (Frcitas, 1998).

3.5 Chapter Summary

In this chapter, we reviewed how the interstitial flow of an organism regulates its lymphatic development. We also constructed an idealised geometry of the zebrafish embryo's trunk. Then, we used Brinkman's equation to model the interstitial flow in it. We ended after parametrisation because this interstitial flow model is only a

component of a larger mathematical model to be completed in the next chapter. Solution of this component will give us the pressure and velocity profiles in the model zebrafish trunk only. On their own, they will not help us understand lymphatic development. Furthermore, we have not decided how to model the specific hydraulic conductivity of the ECM yet, so we cannot solve it at this stage anyway.

Chapter 4

Coupled Phenomena

In this chapter, we will complete the mathematical model. First, we will review the biochemical reactions integral to lymphangiogenesis, the ECM remodelling and VEGFC proteolytic reactions. Then, we will model the transport of and reactions among the participating molecular species in the model zebrafish trunk. We will do so using a set of reaction-diffusion-convection equations. We will link this model component to the interstitial flow component through the convection terms and the specific hydraulic conductivity of the ECM. Finally, we will parametrise the full model, nondimensionalise it, and simplify it.

4.1 Extracellular Matrix Remodelling

In chapter 3, we defined the interstitial space of an organism as a two-phase environment. Also in that chapter, we considered the interstitial fluid in the model zebrafish trunk. Now, we will consider the other phase, the ECM. Its major structural components include different kinds of collagens and glycosaminoglycans (Lutter and Makinen, 2014). Collagens make up more than two-thirds of the ECM protein contents in many soft tissues (Swartz and Fleury, 2007). According to Prockop and Kivirikko (1995), collagen type I is the most abundant protein in the human. More importantly for our study, LECs are mainly surrounded by fibrillar type I collagen in general (Wiig et al., 2010; Paupert et al., 2011). For a general discussion of the properties and functions of ECM components, please consult appendix B.

In their review, Lutter and Makinen (2014) explain how lymphangiogenesis is affected by the ECM it takes place in. First, the ECM confers structural support and stability to the embedded cells, tissues, and organs, but it is also a barrier to cell migration. Second, many ECM components can bind to a myriad of cell-surface receptors, thus inducing intracellular changes. Third, these components can bind to various growth

factors too. This binding regulates the growth factors negatively by sequestering them and positively by creating concentration gradients.

We will model the third function because when VEGFC is transported in the zebrafish's interstitial space, it interacts with the ECM. We will model the ECM as pure collagen I; this simplification is justified because LECs are generally surrounded by fibrillar type I collagen (collagen I henceforth). VEGFC binds to heparan sulfate (Lutter and Makinen, 2014), but we do not know if it binds to collagen I. Without modelling heparan sulfate explicitly, we can model VEGFC's interactions with the ECM by assuming that VEGFC binds to collagen I reversibly in an 1:1 stoichiometric ratio.

The ECM is not inert and undergoes constant remodelling. For example, MMPs can degrade ECM components: LECs secrete the matrix metalloproteinase 9 (MMP9) to render their surroundings more conducive to migration (Helm et al., 2007); LECs can produce and activate another protease called matrix metalloproteinase 2 (MMP2) to regulate lymphangiogenesis (Bruyère et al., 2008). In their paper, commenting on Bruyère et al. (2008), Detry et al. (2012) argue that MMP2 is more important than MMP9. This theory explains lymphangiogenesis in terms of LEC migration through interstitial collagen I and a collagenolytic pathway driven by MMP2 (Detry et al., 2012). In a review paper, Noel and Sounni (2013) review that MMP2 is synthesised as an inactive precursor zymogen called proMMP, which is activated by a cell-membrane-associated MMP called membrane type I matrix metalloproteinase (MT1-MMP); MT1-MMP can degrade collagen I directly too. Noel and Sounni (2013) go on to describe the anti-angiogenic effects of ECM degradation. Collagen type IV degrades into arresten, canstatin, and tumstatin; type V collagen, restin; type XVIII collagen, endostatin and neostatin. However, collagen type I is not known to generate any anti-lymphangiogenic products after degradation. We will model the production and activation of MMP2 in the LEC domain of our model zebrafish trunk, and the degradation of collagen I by MMP2 in the interstitial space domain. On the other hand, we will not model degraded collagen I explicitly because it is neither known to stimulate nor inhibit lymphangiogenesis. The interstitial flow may affect the ECM's composition too. Its influence can be mechanical and direct, or biochemical and through stimulating the LEC to remodel the ECM. However, we will assume that the dynamics between MMP2 and collagen I dominate the input from the flow, so we will not model the latter.

Karagiannis and Popel (2004) have proposed a conceptual model of the MMP2-related events described in the last paragraph. In this conceptual model, a species called tissue inhibitor of metalloproteinases 2 (TIMP2) and MT1-MMP cooperatively activate proMMP2 to form MMP2 in LECs. In reality, MT1-MMP is restricted to the LECs' surfaces, but we will simplify the mathematics by dispersing our LEC domain's MT1-MMP throughout the domain. Furthermore, we will assume that the copy

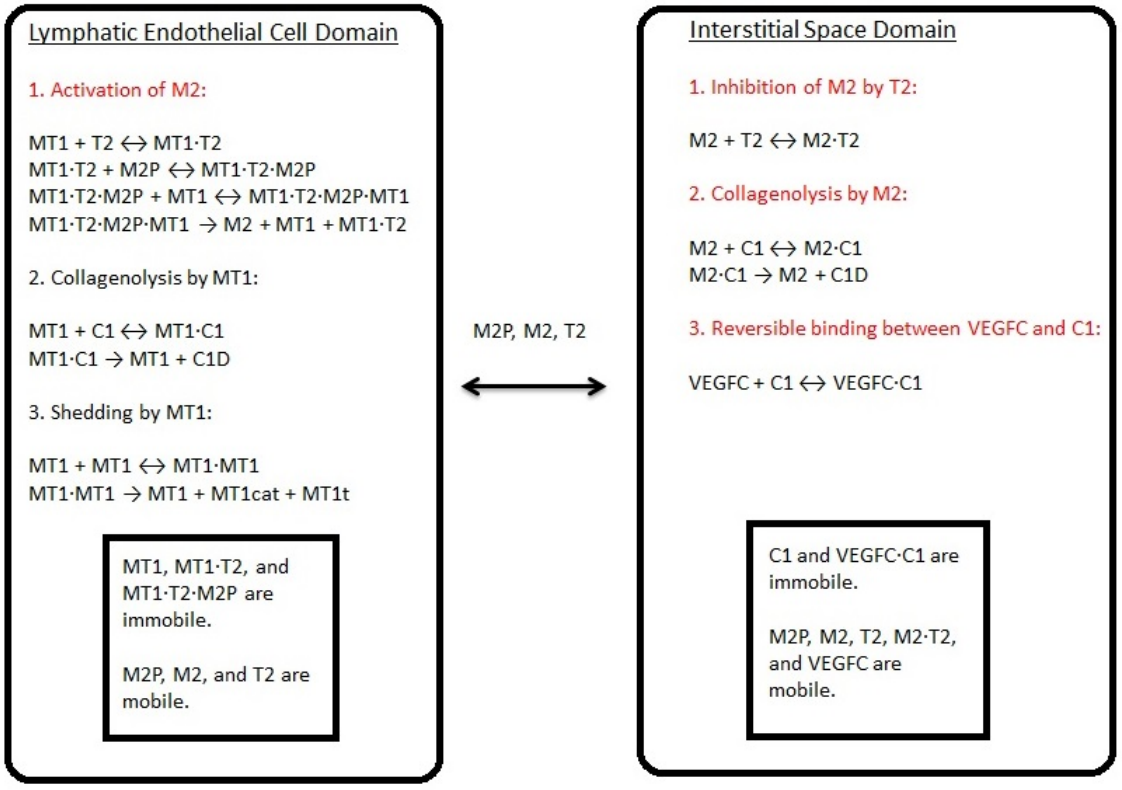

FIGURE 4.1: Biochemical reaction network underlying the mathematical model. M2P abbreviates proMMP2; M2, MMP2; T2; TIMP2; C1, collagen I; MT1, MT1-MMP. A dot between two species means they are complexed together in one molecule. Only proMMP2, MMP2, and TIMP2 are present in both domains and can cross the boundary between them. A mobile species undergoes diffusion and/or convection; an immobile one does not. Only the red events are represented by the mathematical model developed in this thesis.

number of MT1-MMP in the LEC domain is constant, meaning its production rate equals its shedding rate. We can then ignore shedding altogether because the shedded species do not interact with the modelled species. Although proMMP2 and TIMP2 are synthesised and MMP2 is activated in the LEC domain, they can all diffuse into the interstitial space domain. In the interstitial space domain, MMP2 degrades collagen I irreversibly and binds to TIMP2 reversibly. MT1-MMP has its own collagenolytic activity too, but it is localised to the LEC domain, a stationary circle devoid of collagen I. Therefore, we do not need to model the collagenolytic action of MT1-MMP. Karagiannis and Popel (2006) have converted this conceptual model into a mathematical model; it is an inspiration for our study.

The biochemical events we will model are summarised schematically in the reaction map in figure 4.1.

4.2 VEGFC Proteolytic Processing

VEGFC is synthesised as a preproprotein called proVEGFC; it has an N-terminal signal sequence followed by an N-terminal propeptide, then a VEGF homology, and finally a cysteine-rich C-terminal segment (Joukov et al., 1996, 1997; Siegfried et al., 2003). This preproprotein is cleaved intracellularly and extracellularly before it is active and can be considered VEGFC (Joukov et al., 1997). Intracellular processing turns the preproprotein into a tetramer with a molecular weight of 120 kDa (Joukov et al., 1997). The tetramer is secreted from its synthesising cell before binding to VEGFR3 on an LEC. On the cell surface, it is cooperatively cleaved by CCBE1 and a species known as a disintegrin and metalloprotease with thrombospondin motifs-3 (ADAMTS3) (Jeltsch et al., 2014). For more details about the proteolytic processing of VEGFC, please consult appendix C.

Our investigation is concerned with the spatiotemporal dynamics of VEGFC on the tissue level, so we are not interested in the cellular-level events described in the last paragraph. We will not model any cleavage events of VEGFC and VEGFC-VEGFR3 binding. In this investigation, we consider VEGFC in its tetrameric form only and it is limited to the interstitial space domain.

4.3 Model Building

In this section, we will convert the biochemical reaction network in figure 4.1 into its mathematical form. We will start by considering the mobile species in the interstitial space domain; we will use a set of reaction-diffusion-convection equations to model their spatiotemporal dynamics. After considering the diffusion terms of these equations in greater detail, we will use simpler equations to model the immobile species in the interstitial space domain, as well as the species in the LEC domain. Then, we will work out the functional forms of the reaction terms in the equations. Then, we will define our boundary and initial conditions. Finally, we will link this model component to the interstitial flow component developed in chapter 3.

4.3.1 Reaction-Diffusion-Convection Equations

We will use the equation used by Karagiannis and Popel (2006) to model the mobile species in the interstitial space domain. In this equation, C_i (mol m^{-3}) represents the molar concentration of species i in the overall volume (ECM plus interstitial fluid); t (s), time; D_i^{eff} (m^2 s^{-1}), the effective diffusivity of species i; ω, the volume fraction where diffusion occurs; $\boldsymbol{u}$ (m s^{-1}), the velocity provided by the interstitial flow

component; R_i^{IS} (mol m^{-3} s^{-1}), the net production rate of species i. These equations have the form

$$\frac{\partial C_i}{\partial t} = \boldsymbol{\nabla} \cdot (D_i^{eff} \boldsymbol{\nabla}(\frac{C_i}{\omega}) - \boldsymbol{u} C_i) + R_i^{IS}. \tag{4.1}$$

In equation (4.1), the diffusion term depends on $\frac{C_i}{\omega}$ rather than C_i, the fluid phase concentration rather than the overall mixture concentration of species i. It seems to give a flux in the fluid phase, not the overall volume, raising a concern that mass is not balanced. As we will explain in the next subsection, we will use the expression developed by Ogston et al. (1973) for D_i^{eff}. It describes how spherical molecules diffuse in a solution of randomly oriented, straight, and cylindrical fibrils; its basis is the probability of a molecule avoiding the fibrils surrounding it. The use of this expression means our diffusion term links the concentration gradient of species i in the fluid phase to its flux in the overall volume.

The convective term depends on C_i, the overall mixture concentration of species i. At a glance, it suggests that collagen I does not block the interstitial flow. However, the effects of collagen I are already included in the permeability (κ) in Brinkman's equation.

4.3.2 Diffusion Terms

Diffusion does not occur in collagen I fibrils or the fluid associated with them. The volume into which a molecular species can diffuse should be based on the specific 'wet' weight of collagen I (Levick, 1987). Denoting the partial specific volume of hydrated collagen I by v_{C1h} (m^3 kg^{-1}) and the combined mass concentration of free and VEGFC-bound collagen I by $[Cl]_m$ (kg m^{-3}), we will reproduce the relation given by Levick (1987) as the equation

$$\omega = 1 - v_{C1h}[Cl]_m. \tag{4.2}$$

In regions devoid of collagen I, $\omega = 1$, so the mixture concentration reduces to the fluid phase concentration.

The effective diffusivity can be calculated by an equation given by Ogston et al. (1973). Labelling the diffusivity of species i in pure interstitial fluid by D_i^{∞} (m^2 s^{-1}), the volume fraction of dry collagen I fibrils (without associated water molecules) by ν, the radius of a collagen I fibril by r_f (m), and the Stokes-Einstein radius of species i by $r_{s,i}$ (m), we can model the effective diffusivity of species i by the equation

$$D_i^{eff} = D_i^{\infty} exp(\frac{-\sqrt{\nu} r_{s,i}}{r_f}). \tag{4.3}$$

With v_{C1} (m^3 kg^{-1}) being the partial specific volume of dry collagen I, the dry volume fraction of collagen I is modelled by the equation (Levick, 1987)

$$\nu = v_{C1}[Cl]_m. \tag{4.4}$$

In regions devoid of collagen I, $\nu = 0$, so D_i^{eff} reduces to D_i^{∞}, meaning the flux in the fluid phase is the same as that in the overall volume.

With the Boltzmann constant being k_B ($1.380648813 \times 10^{-23}$ kg m^2 s^{-2} K^{-1}) and temperature being T (K), the Stokes-Einstein radius of species i is modelled by the equation (Einstein, 1905)

$$r_{s,i} = \frac{k_B T}{6\pi\mu D_i^{\infty}}. \tag{4.5}$$

4.3.3 Other Equations

For the immobile species in the interstitial space domain, we will use a set of ordinary differential equations (ODEs) to model their dynamics. They are of the form

$$\frac{\partial C_i}{\partial t} = R_i^{IS}. \tag{4.6}$$

We will now turn to the LEC domain where there is neither collagen I nor an interstitial flow. With R_i^{LEC} (mol m^{-3} s^{-1}) being the net production rate of species i in the LEC domain, the mobile species' dynamics there are governed by a set of reaction-diffusion equations of the form

$$\frac{\partial C_i}{\partial t} = D_i^{\infty} \boldsymbol{\nabla}^2 C_i + R_i^{LEC}. \tag{4.7}$$

In the LEC domain again, we will use a set of ODEs for the immobile species. They have the form

$$\frac{\partial C_i}{\partial t} = R_i^{LEC}. \tag{4.8}$$

4.3.4 Reaction Terms

Most of the reaction terms, R_i^{IS} and R_i^{LEC}, can be worked out from figure 4.1 by applying mass action kinetics. It assumes that the rate of a reaction is the product of a rate constant and the concentrations of the participating reactants.

An exception is the enzymatic degradation of collagen I by MMP2, to which we will apply Michaelis-Menten kinetics, the standard model for enzymatic reactions. Consistent with Michaelis-Menten kinetics, we will assume that MMP2·Collagen I is at a steady state. This approach was also used and has already been justified by Karagiannis and Popel (2004). Again following Karagiannis and Popel (2004), we will simplify the last two steps of the MMP2 activation mechanism. We will assume that the quarternary complex is at a steady state, thereby approximating the two steps as a single second-order kinetic process.

Additionally, we need to model some biochemical reactions not shown in figure 4.1. First, proMMP2 and TIMP2 are produced in the LEC domain. Second, the molecules in the interstitial space domain are subjected to attacks from enzymes (Gutfreund, 1993). An exception is VEGFC-bound collagen I; we will assume that sequestration by collagen I protects VEGFC from enzymatic attacks.

We will model neither the synthesis of collagen I nor its natural degradation.

The first assumption is that the embryo produces collagen I transiently to reach a 'normal' level of C_{C1} before 36 HPF. Pashley et al. (2004) have proven experimentally that collagen fibrils are mainly degraded by MMPs and bacteria. In their experiments, when both agents were inhibited, collagen degradation did not occur after 250 days. Since the zebrafish reaches sexual maturity roughly 3 months post-fertilisation (Nasiadka and Clark, 2012), it is fair to neglect the 'natural' means of degradation like oxidation. Unless MMPs or bacteria are present, the 'normal' state is in equilibrium.

The second assumption is that in the time window of interest, collagen I is not produced to compensate for its degradation by MMP2. As explained in section 4.1, MMP2 is the major enzyme that degrades collagen I. Therefore, in our model, the sudden burst of MMP2 production when $t = 0$ s (36 HPF) disturbs the 'normal' state of equilibrium. In the zebrafish, an MMP2-induced departure from the 'normal' state may be slowed down by collagen I production. However, in the model, it is absorbed into the degradation term. In the zebrafish, once MMP2 production ceases, collagen I may be produced in order to bring the 'normal' state back. However, MMP2 is produced in our time frame of interest, so this recovery is not our concern and we will not model it.

TABLE 4.1: Reaction terms in the interstitial space domain. M2 and T2 complex reversibly. VEGFC binds to C1 reversibly. M2 degrades C1 catalytically. M2P, M2, T2, $M2 \cdot T2$, and VEGFC degrade in the interstitial space. $k^{on}_{VC,C1}$ and $k^{off}_{VC,C1}$ are the binding and unbinding rate constants of VC and C1; $k^{on}_{M2,T2}$ and $k^{off}_{M2,T2}$, the binding and unbinding rate constants of M2 and T2; $k^{cat}_{M2,C1}$, the turnover number in the degradation of C1 by M2; $K_M^{M2,C1}$, the Michaelis-Menten constant in the degradation of C1 by M2; k_i^{deg}, the degradation rate constant of species i. M2P abbreviates proMMP2; M2, MMP2; T2, TIMP2; VC, VEGFC; C1, collagen I.

Reaction Term	Form	Equation
R^{IS}_{M2P}	$-k^{deg}_{M2P}C_{M2P}$	(4.1)
R^{IS}_{M2}	$-k^{on}_{M2,T2}C_{M2}C_{T2}+k^{off}_{M2,T2}C_{M2\cdot T2}-k^{deg}_{M2}C_{M2}$	(4.1)
R^{IS}_{T2}	$-k^{on}_{M2,T2}C_{M2}C_{T2}+k^{off}_{M2,T2}C_{M2\cdot T2}-k^{deg}_{T2}C_{T2}$	(4.1)
$R^{IS}_{M2\cdot T2}$	$k^{on}_{M2,T2}C_{M2}C_{T2}-k^{off}_{M2,T2}C_{M2\cdot T2}-k^{deg}_{M2\cdot T2}C_{M2\cdot T2}$	(4.1)
R^{IS}_{VC}	$-k^{on}_{VC,C1}C_{VC}C_{C1}+k^{off}_{VC,C1}C_{VC\cdot C1}-k^{deg}_{VC}C_{VC}$	(4.1)
R^{IS}_{C1}	$-\frac{k^{cat}_{M2,C1}C_{M2}C_{C1}}{K_M^{M2,C1}+C_{C1}}-k^{on}_{VC,C1}C_{VC}C_{C1}+k^{off}_{VC,C1}C_{VC\cdot C1}$	(4.6)
$R^{IS}_{VC\cdot C1}$	$k^{on}_{VC,C1}C_{VC}C_{C1}-k^{off}_{VC,C1}C_{VC\cdot C1}$	(4.6)

The steady state of C_{C1} is zero. It is physiologically irrelevant as collagen I is a major ECM component (Swartz and Fleury, 2007; Prockop and Kivirikko, 1995), but we are not interested in the steady state.

The reaction terms are given in tables 4.1 and 4.2.

4.3.5 Boundary and Initial Conditions

To solve the mathematical model, we need some boundary and initial conditions.

On the four outer boundaries of the model zebrafish trunk and the vessel surfaces, we will impose no-flux boundary conditions on the mobile species. This choice is justified as follows. We are unaware of any experimental observations of the zebrafish losing the modelled molecules through its 'skin'; it means ignoring this hypothetical mechanism will not make our model less descriptive. Similarly, the modelled molecules are not known to enter the zebrafish's blood vessels. Even if they do, we do not understand how they are filtered by the lining cells. For example, the cells may have binding receptors. Anyway, the molecules are lost or degraded once they leave the zebrafish or enter its vessels.

However, there is an exception. We will model an influx of VEGFC from the DA surface into the interstitial space domain. In the zebrafish embryo, VEGFC is expressed in the DA, aISVs, and hypochord (van Impel and Schulte-Merker, 2014). Our model zebrafish trunk does not have any aISVs, while the DA and hypochord are near each other (Eriksson and Löfberg, 2000). The region with the highest pressure in

TABLE 4.2: Reaction terms in the lymphatic endothelial cell domain. M2P and T2 are produced at constant rates. T2 binds to MT1 reversibly. M2P binds to MT1·T2 reversibly. MT1 activates the M2P in $MT1 \cdot T2 \cdot M2P$ to form M2 and release $MT1 \cdot T2$. P_{M2P} and P_{T2} are the production rates of M2P and T2; $k^{on}_{MT1,T2}$ and $k^{off}_{MT1,T2}$, the binding and unbinding rate constants of MT1 and T2; $k^{on}_{MT1 \cdot T2,M2P}$ and $k^{off}_{MT1 \cdot T2,M2P}$, the binding and unbinding rate constants of MT1 · T2 and M2P; k^{eff}_{act}, the activation rate constant of M2. M2P abbreviates proMMP2; M2, MMP2; T2, TIMP2; MT1, MT1-MMP.

Reaction Term	Form	Equation
R^{LEC}_{M2P}	P_{M2P}-$k^{on}_{MT1 \cdot T2,M2P} C_{MT1 \cdot T2} C_{M2P}$ $+k^{off}_{MT1 \cdot T2,M2P} C_{MT1 \cdot T2 \cdot M2P}$	(4.7)
R^{LEC}_{M2}	$k^{eff}_{act} C_{MT1 \cdot T2 \cdot M2P} C_{MT1}$	(4.7)
R^{LEC}_{T2}	P_{T2}-$k^{on}_{MT1,T2} C_{MT1} C_{T2}$+$k^{off}_{MT1,T2} C_{MT1 \cdot T2}$	(4.7)
R^{LEC}_{MT1}	-$k^{on}_{MT1,T2} C_{MT1} C_{T2}$+$k^{off}_{MT1,T2} C_{MT1 \cdot T2}$	(4.8)
$R^{LEC}_{MT1 \cdot T2}$	$k^{on}_{MT1,T2} C_{MT1} C_{T2}$-$k^{off}_{MT1,T2} C_{MT1 \cdot T2}$ $-k^{on}_{MT1 \cdot T2,M2P} C_{MT1 \cdot T2} C_{M2P}$ $+k^{off}_{MT1 \cdot T2,M2P} C_{MT1 \cdot T2 \cdot M2P}$ $+k^{eff}_{act} C_{MT1 \cdot T2 \cdot M2P} C_{MT1}$	(4.8)
$R^{LEC}_{MT1 \cdot T2 \cdot M2P}$	$k^{on}_{MT1 \cdot T2,M2P} C_{MT1 \cdot T2} C_{M2P}$ $-k^{off}_{MT1 \cdot T2,M2P} C_{MT1 \cdot T2 \cdot M2P}$ $-k^{eff}_{act} C_{MT1 \cdot T2 \cdot M2P} C_{MT1}$	(4.8)

our idealised geometry is around the DA as established in chapter 3. We will place the source of VEGFC on the DA's surface. This arrangement retains the essences of VEGFC transport in the zebrafish embryo and keeps the model simple simultaneously. We must remind ourselves that VEGFC does not come from the blood inside the DA. Furthermore, the production of VEGFC by one part of the wall is independent of its production by another part of the wall, so the production rate does not change along the DA.

On the four outer boundaries, the no-flux boundary conditions for proMMP2, MMP2, TIMP2, MMP2·TIMP2, and VEGFC are of the form

$$\boldsymbol{n} \cdot [D_i^{eff} \boldsymbol{\nabla}(\frac{C_i}{\omega}) - \boldsymbol{u} C_i] = 0 \qquad \boldsymbol{x} \in \partial\Omega_{x,y}. \tag{4.9}$$

On the PCV and the DLAV, they are modelled by the equations,

$$\boldsymbol{n} \cdot [D_i^{eff} \boldsymbol{\nabla}(\frac{C_i}{\omega}) - \boldsymbol{u} C_i] = 0 \qquad \boldsymbol{x} \in \partial\Omega_{PCV} \text{ and} \tag{4.10}$$

$$\boldsymbol{n} \cdot [D_i^{eff} \boldsymbol{\nabla}(\frac{C_i}{\omega}) - \boldsymbol{u} C_i] = 0 \qquad \boldsymbol{x} \in \partial\Omega_{DLAV}. \tag{4.11}$$

On the DA, the boundary conditions for the mobile species except VEGFC are of the form

$$\boldsymbol{n} \cdot [D_i^{eff} \boldsymbol{\nabla}(\frac{C_i}{\omega}) - \boldsymbol{u} C_i] = 0 \qquad \boldsymbol{x} \in \partial\Omega_{DA}. \tag{4.12}$$

With R_{VC}^{DA} (mol m^{-2} s^{-1}) being the release rate of VEGFC from the DA surface, the constant flux of VEGFC is modelled by the equation

$$-\boldsymbol{n} \cdot [-D_{VC}^{eff} \boldsymbol{\nabla}(\frac{C_{VC}}{\omega}) + \boldsymbol{u} C_{VC}] = R_{VC}^{DA} \qquad \boldsymbol{x} \in \partial\Omega_{DA}. \tag{4.13}$$

On the LEC's surface, we will impose continuity conditions on the species which can cross the boundary between the two domains. They include proMMP2, MMP2, and TIMP2. We will denote the LEC surface seen from the interstitial space by $\partial\Omega_{LEC/IS+}$. Seen from the LEC domain, the surface is denoted by $\partial\Omega_{LEC/IS-}$. These continuity conditions are represented by the general equations,

$$\boldsymbol{n} \cdot [D_i^{eff} \boldsymbol{\nabla}(\frac{C_i}{\omega}) - \boldsymbol{u} C_i]|_{\partial\Omega_{LEC/IS+}} = -\boldsymbol{n} \cdot (D_i^{\infty} \boldsymbol{\nabla} C_i)|_{\partial\Omega_{LEC/IS-}} \text{ and} \tag{4.14}$$

$$C_i|_{\partial\Omega_{LEC/IS+}} = C_i|_{\partial\Omega_{LEC/IS-}}. \tag{4.15}$$

On the LEC surface seen from the interstitial space domain, we will apply no-flux conditions on MMP2·TIMP2 and VEGFC. These conditions are represented by the general equation

$$\boldsymbol{n} \cdot [D_i^{eff} \boldsymbol{\nabla}(\frac{C_i}{\omega}) - \boldsymbol{u} C_i] = 0 \qquad \boldsymbol{x} \in \partial\Omega_{LEC/IS+}. \tag{4.16}$$

In the LEC domain, we will assume that only MT1-MMP is present when $t = 0$ s; in the interstitial space domain, we will assume that only collagen I is present when $t = 0$ s. We will label the initial concentrations of these species by $C_{MT1,0}$ and $C_{C1,0}$ respectively.

4.3.6 Specific Hydraulic Conductivity

Next, we will connect the concentration dynamics to the interstitial flow modelled in chapter 3. The link is the specific hydraulic conductivity in equation (3.4). As the collagen I in the interstitial space domain changes, this parameter also changes, thereby affecting the interstitial flow.

We will define κ' (kg^{-1} m^3 s) as the hydraulic conductivity of the ECM in the interstitial space domain. In the model zebrafish trunk, the ECM is pure collagen I. We will define $[Collagen\ I]$ as the mass fraction of collagen I (both free and VEGFC-bound) in the interstitial space domain. Using experimental data (Levick, 1987), we can relate the two by the equation

$$log\kappa' = -2.70log[Collagen\ I] - 14.18. \tag{4.17}$$

With M_{C1} (kg mol^{-1}) being the molar mass of collagen I, $[Collagen\ I]$ is given by the relation

$$[Collagen\ I] = \frac{M_{C1}(C_{C1} + C_{VC \cdot C1})}{1000\ \text{kg m}^{-3}}. \tag{4.18}$$

Equation (4.18) assumes a density of 1000 kg m^{-3} for the interstitial space domain. It is also assumed that the combined mass of the interstitial fluid and the ECM in the domain is conserved. In other words, when collagen I degrades, the products remain in the interstitial space, so the mass of a region is fixed at 1000 kg m^{-3} multiplied by the volume of the region. The experiments cited by Levick (1987) were carried out using a reference fluid with a dynamic viscosity of 1 cP or 0.001 kg m^{-1} s^{-1}. We can therefore convert the hydraulic conductivity to the specific hydraulic conductivity:
$\kappa = \kappa' \times 0.001$ kg m^{-1} s^{-1}.

4.4 Parametrisation

We can categorise our model parameters into three types, those in the interstitial flow component, the transport parameters in the reaction-diffusion-convection equation and its simplified forms, and the kinetic parameters in the reaction-diffusion-convection equation and its simplified forms. Most of the interstitial flow parameters have already been discussed (see chapter 3). The only addition is M_{C1} in equation (4.18). Karagiannis and Popel (2006) used a molecular weight of around 300 kDa for a collagen I fibril, which is equivalent to a molar mass of 300 kg mol^{-1}.

4.4.1 Transport Parameters

In order to calculate ω using equation (4.2) and D_i^{eff} using equation (4.3), we need several parameters. We will assume a temperature of 298 K. A collagen I fibril is approximately 300 nm long and 4 nm in diameter, so r_f is 2 nm or 2×10^{-9} m (Karagiannis and Popel, 2006). We can also use the D_i^{∞} values provided by

TABLE 4.3: Transport parameters in the reaction-diffusion-convection equation and its simplified forms. M2P abbreviates proMMP2; M2, MMP2; T2, TIMP2; VC, VEGFC; C1, collagen I.

Parameter	Definition	Value	Reference
D^{∞}_{VC}	Diffusivity of VC	5.01×10^{-11} m^2 s^{-1}	Berk et al. (1993)
D^{∞}_{M2}	Diffusivity of M2	8.5×10^{-11} m^2 s^{-1}	Karagiannis and Popel (2006)
D^{∞}_{M2P}	Diffusivity of M2P	8×10^{-11} m^2 s^{-1}	Karagiannis and Popel (2006)
$D^{\infty}_{M2{\cdot}T2}$	Diffusivity of M2·T2	7.5×10^{-11} m^2 s^{-1}	Karagiannis and Popel (2006)
D^{∞}_{T2}	Diffusivity of T2	1.10×10^{-10} m^2 s^{-1}	Karagiannis and Popel (2006)
r_f	Radius of a C1 Fibril	2×10^{-9} m	Karagiannis and Popel (2006)
v_{C1}	Specific Volume of Dry C1	7.5×10^{-4} m^3 kg^{-1}	Levick (1987)
v_{C1h}	Specific Volume of Hydrated C1	1.89×10^{-3} m^3 kg^{-1}	Levick (1987)
T	Temperature	298 K	Assumed

Karagiannis and Popel (2006) and Berk et al. (1993). The partial specific volume of dry collagen I and that of hydrated collagen I, v_{C1} and v_{C1h}, are 7.5×10^{-4} and 1.89×10^{-3} m^3 kg^{-1} (Levick, 1987). These parameters are summarised in table 4.3.

4.4.2 Kinetic Parameters

We will rely on Karagiannis and Popel (2006) and Karagiannis and Popel (2004) for most of the kinetic parameters about ECM remodelling. They are based on experimental studies.

As explained in section 4.1, there are no data about VEGFC-collagen I interactions. We must rely on surrogates, such as the experimentally estimated parameters used by Köhn-Luque et al. (2013). They pertain to the interactions of VEGF (related to but different from VEGFC) with various ECM molecules like fibronectin and heparan sulphate proteoglycans.

We will use the general degradation rate constant used by Hashambhoy et al. (2011).

For the production rates of proMMP2 and TIMP2, we will use the secretion rates of general MMPs and general tissue inhibitors of metalloproteinases (TIMPs) pertaining to endothelial cells (Vempati et al., 2010). These estimates are in molecules per cell per hour, so we will convert them to mol m^{-3} s^{-1} using the known LEC diameter of 10 µm. We are unaware of any data about VEGFC production. Therefore, we will use the secretion rate of VEGF pertaining to endothelial cells (Hashambhoy et al., 2011).

TABLE 4.4: Kinetic parameters in the reaction-diffusion-convection equation and its simplified forms. M2P abbreviates proMMP2; M2, MMP2; T2, TIMP2; VC, VEGFC; C1, collagen I; MT1, MT1-MMP. $k_{i,j}^{on}$ means the binding rate constant of species i and j; $k_{i,j}^{off}$, their unbinding rate constant; k_{act}^{eff}, the activation rate constant of M2; $k_{M2,C1}^{cat}$, the turnover number in the degradation of C1 by M2; $K_M^{M2,C1}$, the Michaelis-Menten constant in the degradation of C1 by M2; k_i^{deg}, the degradation rate constant of species i; P_i, the production rate of species i; R_{VC}^{DA}, the production rate of VC on the surface of the dorsal aorta.

Parameter	Value	Reference
$k_{VC,C1}^{on}$	3.60×10^{1} mol^{-1} m^3 s^{-1}	Köhn-Luque et al. (2013)
$k_{VC,C1}^{off}$	3.60×10^{-3} s^{-1}	Köhn-Luque et al. (2013)
$k_{M2,T2}^{on}$	5.90×10^{3} mol^{-1} m^3 s^{-1}	Karagiannis and Popel (2004)
$k_{M2,T2}^{off}$	6.30 s^{-1}	Karagiannis and Popel (2004)
$k_{MT1,T2}^{on}$	3.54×10^{3} mol^{-1} m^3 s^{-1}	Toth et al. (2002)
$k_{MT1,T2}^{off}$	2×10^{-4} s^{-1}	Toth et al. (2002)
$k_{MT1{\cdot}T2,M2P}^{on}$	0.14×10^{3} mol^{-1} m^3 s^{-1}	Karagiannis and Popel (2004)
$k_{MT1{\cdot}T2,M2P}^{off}$	4.70×10^{-3} s^{-1}	Karagiannis and Popel (2004)
k_{act}^{eff}	2.80 mol^{-1} m^3 s^{-1}	Karagiannis and Popel (2004)
$k_{M2,C1}^{cat}$	4.50×10^{-3} s^{-1}	Karagiannis and Popel (2004)
$K_M^{M2,C1}$	8.50×10^{-3} mol m^{-3}	Karagiannis and Popel (2004)
k_{VC}^{deg}	10^{-4} s^{-1}	Hashambhoy et al. (2011)
k_{M2}^{deg}	10^{-4} s^{-1}	Hashambhoy et al. (2011)
k_{M2P}^{deg}	10^{-4} s^{-1}	Hashambhoy et al. (2011)
$k_{M2{\cdot}T2}^{deg}$	10^{-4} s^{-1}	Hashambhoy et al. (2011)
k_{T2}^{deg}	10^{-4} s^{-1}	Hashambhoy et al. (2011)
P_{M2P}	2.64×10^{-5} mol m^{-3} s^{-1}	Vempati et al. (2010)
P_{T2}	1.54×10^{-7} mol m^{-3} s^{-1}	Vempati et al. (2010)
R_{VC}^{DA}	1.65×10^{-15} mol m^{-2} s^{-1}	Hashambhoy et al. (2011)

These parameters are summarised in table 4.4.

Finally, we need to initialise the concentrations of MT1-MMP in the LEC domain and collagen I in the interstitial space domain. $C_{MT1,0}$ is unavailable for endothelial cells. However, Karagiannis and Popel (2006) used a value based on other cell types, 180000 molecules per cell or 5.71×10^{-4} mol m^{-3}. The concentrations of collagen I in adult tissues range from 1.76×10^{-1} to 5.29×10^{-1} mol m^{-3} (Levick, 1987; Karagiannis and Popel, 2006). We will use the midpoint of this range, so $C_{C1,0}$ is 3.50×10^{-1} mol m^{-3} for adult tissues. For frog embryos and larvae, the range is from 4.51×10^{-4} to 2.73×10^{-3} mol m^{-3} (Edds Jr, 1958). We will use the midpoint of this range, 1.59×10^{-3} mol m^{-3}, for embryonic tissues.

4.5 Nondimensionalisation

Nondimensionalisation reduces the number of parameters in a mathematical model, provides insights into the model in terms of its key parameters and characteristic properties, and identifies opportunities for approximation like limiting cases. In this section, we will nondimensionalise our mathematical model.

We need the characteristic scales of the model in order to nondimensionalise it. The nondimensionalised spatial coordinates are nondimensionalised by the length scale, L, so $\tilde{\boldsymbol{x}} = \frac{\boldsymbol{x}}{L}$; we will use the largest dimension of the model zebrafish trunk, 434 μm (4.34×10^{-4} m). In this thesis, a tilde means the variable underneath it is nondimensionalised. We will use the maximum pressure, P^{DA} (0.1844 mmHg or 24.585 kg m^{-1} s^{-2}), to nondimensionalise the pressure field, so $\tilde{P} = \frac{P}{P^{DA}}$. Because the time frame we are modelling is from 36 to 48 HPF, we will use a time scale, τ, of 12 hours (43200 s); after nondimensionalisation, $\tilde{t} = \frac{t}{\tau}$. After nondimensionalising the velocity field, $\tilde{\boldsymbol{u}} = \frac{\boldsymbol{u}}{U}$. For the concentrations, $\tilde{C}_i = \frac{C_i}{C_{i,s}}$. Since we are not modelling collagen I synthesis, its initial concentration is also its highest possible concentration. We will use it as the concentration scale for collagen I, so $C_{C1,s} = C_{C1,0}$. We will use the adult value, so $C_{C1,s} = 3.50 \times 10^{-4}$ M (3.50×10^{-1} mol m^{-3}). The total concentration of MT1-MMP and its two complexes is conserved. The three concentrations always add up to $C_{MT1,0}$ (5.71×10^{-7} M or 5.71×10^{-4} mol m^{-3}), so we will use this value as the concentration scales $C_{MT1,s}$, $C_{MT1{\cdot}T2,s}$, and $C_{MT1{\cdot}T2{\cdot}M2P,s}$.

In the next subsections, we will determine the velocity scale, U (m s^{-1}), and the remaining concentration scales while nondimensionalising the model. All the characteristic scales of the model are summarised in table 4.5. The dimensionless parameters are in tables 4.6 and 4.7.

TABLE 4.5: Characteristic scales of the mathematical model. M2P abbreviates proMMP2; M2, MMP2; T2, TIMP2; VC, VEGFC; C1, collagen I; MT1, MT1-MMP.

Scale	Description	Value
$C_{C1,s}$	Concentration scale for C1	3.50×10^{-1} mol m^{-3}
$C_{VC,s}$	Concentration scale for VC	1.64×10^{-7} mol m^{-3}
$C_{VC\cdot C1,s}$	Concentration scale for VC·C1	8.93×10^{-2} mol m^{-3}
$C_{M2,s}$	Concentration scale for M2	3.94×10^{-2} mol m^{-3}
$C_{M2P,s}$	Concentration scale for M2P	1.14 mol m^{-3}
$C_{M2\cdot T2,s}$	Concentration scale for M2·T2	6.68×10^{4} mol m^{-3}
$C_{MT1,s}$	Concentration scale for MT1	5.71×10^{-4} mol m^{-3}
$C_{MT1\cdot T2,s}$	Concentration scale for MT1·T2	5.71×10^{-4} mol m^{-3}
$C_{MT1\cdot T2\cdot M2P,s}$	Concentration scale for MT1·T2·M2P	5.71×10^{-4} mol m^{-3}
$C_{T2,s}$	Concentration scale for T2	6.65×10^{-3} mol m^{-3}
L	Length scale	4.34×10^{-4} m
P^{DA}	Pressure scale and DA pressure	24.585 kg m^{-1} s^{-2}
τ	Time scale	43200 s
U	Velocity scale	1.371×10^{-10} m s^{-1}

TABLE 4.6: Dimensionless parameters in the nondimensionalised interstitial flow equations and the reaction-diffusion-convection equation. DA abbreviates dorsal aorta; PCV, posterior cardinal vein; DLAV, dorsal longitudinal anastomotic vessel; M2P, proMMP2; M2, MMP2; T2, TIMP2; VC, VEGFC; C1, collagen I.

Parameter	Form	Value
α	Constant	-2.70
η_1	$\frac{\mu U L}{P^{DA}\beta(M_{C1}C_{C1,s})^{\alpha}}$	1
η_2	$\frac{C_{VC\cdot C1,s}}{C_{C1,s}}$	0.255
η_3	$\frac{\mu U}{L P^{DA}}$	1.542×10^{-11}
η_{DA}	$\frac{L_{DA}P^{DA}}{U}$	1.317×10^{14}
η_{PCV}	$\frac{L_{PCV}P^{DA}}{U}$	1.317×10^{14}
η_{DLAV}	$\frac{2L_{DLAV}P^{DA}}{U}$	2.634×10^{14}
$\lambda_{1,VC}$	$\frac{D^{\infty}_{VC}\tau}{L^2}$	1.15×10^{1}
$\lambda_{1,M2}$	$\frac{D^{\infty}_{M2}\tau}{L^2}$	1.95×10^{1}
$\lambda_{1,M2P}$	$\frac{D^{\infty}_{M2P}\tau}{L^2}$	1.83×10^{1}
$\lambda_{1,M2\cdot T2}$	$\frac{D^{\infty}_{M2\cdot T2}\tau}{L^2}$	1.72×10^{1}
$\lambda_{1,T2}$	$\frac{D^{\infty}_{T2}\tau}{L^2}$	2.52×10^{1}
$\lambda_{2,VC}$	$\frac{k_B T}{6\pi\mu D^{\infty}_{VC} r_f}$	1.81
$\lambda_{2,M2}$	$\frac{k_B T}{6\pi\mu D^{\infty}_{M2} r_f}$	1.07
$\lambda_{2,M2P}$	$\frac{k_B T}{6\pi\mu D^{\infty}_{M2P} r_f}$	1.14
$\lambda_{2,M2\cdot T2}$	$\frac{k_B T}{6\pi\mu D^{\infty}_{M2\cdot T2} r_f}$	1.21
$\lambda_{2,T2}$	$\frac{k_B T}{6\pi\mu D^{\infty}_{T2} r_f}$	8.26×10^{-1}
λ_3	$v_{C1}M_{C1}C_{C1,s}$	7.88×10^{-2}
λ_4	$v_{C1}M_{C1}C_{VC\cdot C1,s}$	2.01×10^{-2}
λ_5	$v_{C1h}M_{C1}C_{C1,s}$	1.98×10^{-1}
λ_6	$v_{C1h}M_{C1}C_{VC\cdot C1,s}$	5.06×10^{-2}
λ_7	$\frac{U\tau}{L}$	1.36×10^{-2}

TABLE 4.7: Dimensionless parameters in the nondimensionalised reaction terms. λ_{28} is not really dimensionless and is in mol m^{-3}, but the term $\frac{\lambda_{28}\tilde{C}_{M2}\tilde{C}_{C1}}{K_M^{M2,C1}+C_{C1,s}\tilde{C}_{C1}}$ is dimensionless because the denominator is also in mol m^{-3}. M2P abbreviates proMMP2; M2, MMP2; T2, TIMP2; VC, VEGFC; C1, collagen I; MT1, MT1-MMP; DA, dorsal aorta.

Parameter	Form	Value
λ_8	$\frac{P_{M2P}\tau}{C_{M2P,s}}$	1
λ_9	$k^{on}_{MT1\cdot T2,M2P}\tau C_{MT1\cdot T2,s}$	3.45×10^{3}
λ_{10}	$\frac{k^{off}_{MT1\cdot T2,M2P}\tau C_{MT1\cdot T2\cdot M2P,s}}{C_{M2P,s}}$	1.02×10^{-1}
λ_{11}	$k^{deg}_{M2P}\tau$	4.32
λ_{12}	$\frac{k^{eff}_{act}\tau C_{MT1\cdot T2\cdot M2P,s}C_{MT1,s}}{C_{M2,s}}$	1
λ_{13}	$k^{on}_{M2,T2}\tau C_{T2,s}$	1.69×10^{6}
λ_{14}	$\frac{k^{off}_{M2,T2}\tau C_{M2\cdot T2,s}}{C_{M2,s}}$	4.61×10^{11}
λ_{15}	$k^{deg}_{M2}\tau$	4.32
λ_{16}	$\frac{P_{T2}\tau}{C_{T2,s}}$	1
λ_{17}	$k^{on}_{MT1,T2}\tau C_{MT1,s}$	8.73×10^{4}
λ_{18}	$\frac{k^{off}_{MT1,T2}\tau C_{MT1\cdot T2,s}}{C_{T2,s}}$	7.42×10^{-1}
λ_{19}	$k^{on}_{M2,T2}\tau C_{M2,s}$	1×10^{7}
λ_{20}	$\frac{k^{off}_{M2,T2}\tau C_{M2\cdot T2,s}}{C_{T2,s}}$	2.73×10^{12}
λ_{21}	$k^{deg}_{T2}\tau$	4.32
λ_{22}	$\frac{k^{on}_{M2,T2}\tau C_{M2,s}C_{T2,s}}{C_{M2\cdot T2,s}}$	1
λ_{23}	$k^{off}_{M2,T2}\tau$	2.72×10^{5}
λ_{24}	$k^{deg}_{M2\cdot T2}\tau$	4.32
λ_{25}	$k^{on}_{VC,C1}\tau C_{C1,s}$	5.44×10^{5}
λ_{26}	$\frac{k^{off}_{VC,C1}\tau C_{VC\cdot C1,s}}{C_{VC,s}}$	8.47×10^{7}
λ_{27}	$k^{deg}_{VC}\tau$	4.32
λ^{DA}_{VC}	$\frac{R^{DA}_{VC}\tau}{C_{VC,s}L}$	1
λ_{28}	$k^{cat}_{M2,C1}\tau C_{M2,s}$	7.66×10^{-3}
λ_{29}	$k^{on}_{VC,C1}\tau C_{VC,s}$	2.55×10^{-1}
λ_{30}	$\frac{k^{off}_{VC,C1}\tau C_{VC\cdot C1,s}}{C_{C1,s}}$	3.97×10^{1}
λ_{31}	$\frac{k^{on}_{VC,C1}\tau C_{VC,s}C_{C1,s}}{C_{VC\cdot C1,s}}$	1
λ_{32}	$k^{off}_{VC,C1}\tau$	1.56×10^{2}
λ_{33}	$k^{on}_{MT1,T2}\tau C_{T2,s}$	1.02×10^{6}
λ_{34}	$\frac{k^{off}_{MT1,T2}\tau C_{MT1\cdot T2,s}}{C_{MT1,s}}$	8.64
λ_{35}	$\frac{k^{on}_{MT1,T2}\tau C_{MT1,s}C_{T2,s}}{C_{MT1\cdot T2,s}}$	1.02×10^{6}
λ_{36}	$k^{off}_{MT1,T2}\tau$	8.64
λ_{37}	$k^{on}_{MT1\cdot T2,M2P}\tau C_{M2P,s}$	6.89×10^{6}
λ_{38}	$\frac{k^{off}_{MT1\cdot T2,M2P}\tau C_{MT1\cdot T2\cdot M2P,s}}{C_{MT1\cdot T2,s}}$	2.03×10^{2}
λ_{39}	$\frac{k^{eff}_{act}\tau C_{MT1\cdot T2\cdot M2P,s}C_{MT1,s}}{C_{MT1\cdot T2,s}}$	6.91×10^{1}
λ_{40}	$\frac{k^{on}_{MT1\cdot T2,M2P}\tau C_{MT1\cdot T2,s}C_{M2P,s}}{C_{MT1\cdot T2\cdot M2P,s}}$	6.89×10^{6}
λ_{41}	$k^{off}_{MT1\cdot T2,M2P}\tau$	2.03×10^{2}
λ_{42}	$k^{eff}_{act}\tau C_{MT1,s}$	6.91×10^{1}

4.5.1 Interstitial Flow Component

We will combine equations (4.17) and (4.18) in order to express κ' as a function of C_{C1} and $C_{VC{\cdot}C1}$. Knowing that $\kappa = \kappa' \times 0.001$ kg m^{-1} s^{-1}, we can easily convert the result to κ. After defining the constants β (6.61×10^{-21} m^2) and α (-2.70), we can write κ as $\beta[\frac{M_{C1}(C_{C1}+C_{VC{\cdot}C1})}{1000\ \text{kg m}^{-3}}]^{\alpha}$. Substituting this expression into equation (3.4) and nondimensionalising the variables will give the nondimensionalised Brinkman's equation

$$\tilde{\boldsymbol{\nabla}}\tilde{P} = -\frac{\mu U L}{P^{DA}\beta(M_{C1}C_{C1,s})^{\alpha}}\frac{\tilde{\boldsymbol{u}}}{(\tilde{C}_{C1} + \frac{C_{VC{\cdot}C1,s}}{C_{C1,s}}\tilde{C}_{VC{\cdot}C1})^{\alpha}} + \frac{\mu U}{LP^{DA}}\tilde{\boldsymbol{\nabla}}^2\tilde{\boldsymbol{u}}. \tag{4.19}$$

We will lump the parameters into three dimensionless groups defined by the equations, $\eta_1 = \frac{\mu U L}{P^{DA}\beta(M_{C1}C_{C1,s})^{\alpha}}$, $\eta_2 = \frac{C_{VC{\cdot}C1,s}}{C_{C1,s}}$, and $\eta_3 = \frac{\mu U}{LP^{DA}}$. To determine the scale of $\boldsymbol{u}$, we can use either η_1 or η_3. If $\eta_1 = 1$, $U = 1.371 \times 10^{-10}$ m s^{-1}; if $\eta_3 = 1$, $U = 8.891$ m s^{-1}. The velocity for an interstitial flow is reported to range from 0.1 to 2 μm s^{-1} (Swartz and Fleury, 2007), so the former is more reasonable. It means that $\eta_3 = 1.542 \times 10^{-11}$; it characterises the flow speed in the ECM (Darcy's law) rather than any pores that may form therein (Brinkman's equation). After expressing equation (4.19) in terms of these dimensionless groups,

$$\tilde{\boldsymbol{\nabla}}\tilde{P} = -\frac{\tilde{\boldsymbol{u}}}{(\tilde{C}_{C1} + \eta_2\tilde{C}_{VC{\cdot}C1})^{\alpha}} + \eta_3\tilde{\boldsymbol{\nabla}}^2\tilde{\boldsymbol{u}}. \tag{4.20}$$

We will finish this component by nondimensionalising equation (3.2) and the boundary conditions. If $\eta_{DA} = \frac{L_{DA}P^{DA}}{U}$, $\eta_{PCV} = \frac{L_{PCV}P^{DA}}{U}$, and $\eta_{DLAV} = \frac{2L_{DLAV}P^{DA}}{U}$, then

$$\tilde{\boldsymbol{\nabla}} \cdot \tilde{\boldsymbol{u}} = 0, \tag{4.21}$$

$$-\boldsymbol{n} \cdot \tilde{\boldsymbol{u}} = \eta_{DA}(1 - \tilde{P}) \qquad \tilde{\boldsymbol{x}} \in \partial\Omega_{DA}, \tag{4.22}$$

$$-\boldsymbol{n} \cdot \tilde{\boldsymbol{u}} = \eta_{PCV}(\frac{P^{PCV}}{P^{DA}} - \tilde{P}) \qquad \tilde{\boldsymbol{x}} \in \partial\Omega_{PCV}, \tag{4.23}$$

$$-\boldsymbol{n} \cdot \tilde{\boldsymbol{u}} = \eta_{DLAV}(\frac{P^{DLAV}}{P^{DA}} - \tilde{P}) \qquad \tilde{\boldsymbol{x}} \in \partial\Omega_{DLAV}, \text{ and} \tag{4.24}$$

$$\tilde{\boldsymbol{u}} = 0 \qquad \tilde{\boldsymbol{x}} \in \partial\Omega_{x,y} \text{ and } \partial\Omega_{LEC/IS+}. \tag{4.25}$$

4.5.2 Reaction-Diffusion-Convection Equation and its Simplified Forms

We will turn our attention to the equations governing the concentration fields next. Our first targets are equations (4.1) and (4.6). They govern the concentration dynamics in the interstitial space domain.

After defining $\tilde{D}_i^{eff}$ as $\frac{D_i^{eff}\tau}{L^2}$, λ_7 as $\frac{U\tau}{L}$, and $\tilde{R}_i^{IS}$ as $\frac{R_i^{IS}\tau}{C_{i,s}}$, we will nondimensionalise equation (4.1). As a result,

$$\frac{\partial \tilde{C}_i}{\partial \tilde{t}} = \tilde{\boldsymbol{\nabla}} \cdot [\tilde{D}_i^{eff} \tilde{\boldsymbol{\nabla}} (\frac{\tilde{C}_i}{\omega}) - \lambda_7 \tilde{\boldsymbol{u}} \tilde{C}_i] + \tilde{R}_i^{IS}. \tag{4.26}$$

After stating that $\lambda_5 = v_{C1h} M_{C1} C_{C1,s}$ and $\lambda_6 = v_{C1h} M_{C1} C_{VC\cdot C1,s}$, we will write ω in terms of the dimensionless parameters. As a result,

$$\omega = 1 - \lambda_5 \tilde{C}_{C1} - \lambda_6 \tilde{C}_{VC\cdot C1}. \tag{4.27}$$

If $\lambda_{1,i} = \frac{D_i^{\infty}\tau}{L^2}$, $\lambda_{2,i} = \frac{k_B T}{6\pi\mu D_i^{\infty} r_f}$, $\lambda_3 = v_{C1} M_{C1} C_{C1,s}$, and $\lambda_4 = v_{C1} M_{C1} C_{VC\cdot C1,s}$, $\tilde{D}_i^{eff}$ can be written in the simplified form

$$\tilde{D}_i^{eff} = \lambda_{1,i} exp(-\lambda_{2,i} \sqrt{\lambda_3 \tilde{C}_{C1} + \lambda_4 \tilde{C}_{VC\cdot C1}}). \tag{4.28}$$

Crossing out the diffusion and convection terms of equation (4.26) will give us the nondimensionalised equation (4.6). Following this operation,

$$\frac{\partial \tilde{C}_i}{\partial \tilde{t}} = \tilde{R}_i^{IS}. \tag{4.29}$$

We define that $\tilde{R}_i^{LEC} = \frac{R_i^{LEC}\tau}{C_{i,s}}$. This definition allows the nondimensionalisation of the governing equations for the LEC domain, equations (4.7) and (4.8). Following this nondimensionalisation,

$$\frac{\partial \tilde{C}_i}{\partial \tilde{t}} = \lambda_{1,i} \tilde{\boldsymbol{\nabla}}^2 \tilde{C}_i + \tilde{R}_i^{LEC} \text{ and} \tag{4.30}$$

$$\frac{\partial \tilde{C}_i}{\partial \tilde{t}} = \tilde{R}_i^{LEC}. \tag{4.31}$$

We will then nondimensionalise the boundary and initial conditions of these partial and ordinary differential equations (PDEs and ODEs).

Equations (4.9) to (4.11), which apply to proMMP2, MMP2, TIMP2, MMP2·TIMP2, and VEGFC, have the nondimensionalised forms,

$$\boldsymbol{n} \cdot [\tilde{D}_i^{eff} \tilde{\boldsymbol{\nabla}} (\frac{\tilde{C}_i}{\omega}) - \lambda_7 \tilde{\boldsymbol{u}} \tilde{C}_i] = 0 \qquad \tilde{\boldsymbol{x}} \in \partial\Omega_{x,y}, \tag{4.32}$$

$$\boldsymbol{n} \cdot [\tilde{D}_i^{eff} \tilde{\boldsymbol{\nabla}} (\frac{\tilde{C}_i}{\omega}) - \lambda_7 \tilde{\boldsymbol{u}} \tilde{C}_i] = 0 \qquad \tilde{\boldsymbol{x}} \in \partial\Omega_{PCV}, \text{ and} \tag{4.33}$$

$$\boldsymbol{n} \cdot [\tilde{D}_i^{eff} \tilde{\boldsymbol{\nabla}} (\frac{\tilde{C}_i}{\omega}) - \lambda_7 \tilde{\boldsymbol{u}} \tilde{C}_i] = 0 \qquad \tilde{\boldsymbol{x}} \in \partial\Omega_{DLAV}. \tag{4.34}$$

The boundary conditions for proMMP2, MMP2, TIMP2, and MMP2·TIMP2 on the DA's surface, represented by equation (4.12), have the nondimensionalised form

$$\boldsymbol{n} \cdot [\tilde{D}_i^{eff} \tilde{\boldsymbol{\nabla}} (\frac{\tilde{C}_i}{\omega}) - \lambda_7 \tilde{\boldsymbol{u}} \tilde{C}_i] = 0 \qquad \tilde{\boldsymbol{x}} \in \partial\Omega_{DA}. \tag{4.35}$$

The dimensionless production rate of VEGFC is represented by the equation $\lambda_{VC}^{DA} = \frac{R_{VC}^{DA} \tau}{C_{VC,s} L}$. Setting that $\lambda_{VC}^{DA} = 1$ will give the concentration scale $C_{VC,s}$ at 1.64×10^{-7} mol m^{-3}; it characterises the amount of VEGFC produced in the time frame of interest. Equation (4.13) has the nondimensionalised form

$$-\boldsymbol{n} \cdot [-\tilde{D}_i^{eff} \tilde{\boldsymbol{\nabla}} (\frac{\tilde{C}_i}{\omega}) + \lambda_7 \tilde{\boldsymbol{u}} \tilde{C}_i] = \lambda_{VC}^{DA} \qquad \tilde{\boldsymbol{x}} \in \partial\Omega_{DA}. \tag{4.36}$$

The boundary conditions on the LEC's surface, equations (4.14) to (4.16), have the nondimensionalised forms,

$$\boldsymbol{n} \cdot [\tilde{D}_i^{eff} \tilde{\boldsymbol{\nabla}} (\frac{\tilde{C}_i}{\omega}) - \lambda_7 \tilde{\boldsymbol{u}} \tilde{C}_i]|_{\partial\Omega_{LEC/IS+}} = -\boldsymbol{n} \cdot (\lambda_{1,i} \tilde{\boldsymbol{\nabla}} \tilde{C}_i)|_{\partial\Omega_{LEC/IS-}}, \tag{4.37}$$

$$\tilde{C}_i|_{\partial\Omega_{LEC/IS+}} = \tilde{C}_i|_{\partial\Omega_{LEC/IS-}}, \text{ and} \tag{4.38}$$

$$\boldsymbol{n} \cdot [\tilde{D}_i^{eff} \tilde{\boldsymbol{\nabla}} (\frac{\tilde{C}_i}{\omega}) - \lambda_7 \tilde{\boldsymbol{u}} \tilde{C}_i] = 0 \qquad \tilde{\boldsymbol{x}} \in \partial\Omega_{LEC/IS+}. \tag{4.39}$$

The continuity condition defined by equations (4.37) and (4.38) applies to proMMP2, MMP2, and TIMP2. The no-flux condition defined by equation (4.39) applies to MMP2·TIMP2 and VEGFC.

After nondimensionalisation, the initial concentrations of MT1-MMP in the LEC domain and collagen I in the interstitial space domain are both 1.

4.5.3 Reaction Terms

Finally, we need to express the reaction terms, $\tilde{R}_i^{IS}$ and $\tilde{R}_i^{LEC}$, in terms of the nondimensionalised concentrations. For this purpose, we need the remaining concentration scales.

Setting the dimensionless production term of proMMP2 to unity, meaning $\frac{P_{M2P}\tau}{C_{M2P,s}} = 1$, will give us $C_{M2P,s}$ at 1.14 mol m^{-3}; it characterises the amount of proMMP2 produced in the time frame of interest.

Doing the same for the MMP2 production term, it follows that $\frac{k_{act}^{eff}\tau C_{MT1\cdot T2\cdot M2P,s}C_{MT1,s}}{C_{M2,s}} = 1$ and $C_{M2,s} = 3.94 \times 10^{-2}$ mol m^{-3}; it characterises the amount of MMP2 produced in the time frame of interest if both C_{MT1} and $C_{MT1\cdot T2\cdot M2P}$ equal their scales.

If the TIMP2 production term is set to unity, $\frac{P_{T2}\tau}{C_{T2,s}} = 1$, then $C_{T2,s} = 6.65 \times 10^{-3}$ mol m^{-3}, characterising the amount of TIMP2 produced in the time frame of interest.

If the binding term of MMP2 and TIMP2 is set to unity, $\frac{k_{M2,T2}^{on}\tau C_{M2,s}C_{T2,s}}{C_{M2\cdot T2,s}} = 1$, then $C_{M2\cdot T2,s} = 6.68 \times 10^{4}$ mol m^{-3}; it characterises the number of binding events in the time frame of interest if C_{M2} and C_{T2} equal their scales.

Similarly with the binding term of VEGFC and collagen I, if $\frac{k_{VC,C1}^{on}\tau C_{VC,s}C_{C1,s}}{C_{VC\cdot C1,s}} = 1$, $C_{VC\cdot C1,s} = 8.93 \times 10^{-2}$ mol m^{-3}; it characterises the number of binding events in the time frame of interest if C_{VC} and C_{C1} equal their scales.

With all the scales determined, the reaction terms can easily be worked out. They are summarised in table 4.8.

4.5.4 Model Features

We can gain insights into the model by examining the relative sizes of the dimensionless parameters.

First, we will examine equation (4.20). The Darcy's law term is ten orders of magnitude larger than the Stokes flow term; it is tempting to ignore the latter. Indeed, we should do so in a stationary study for $\tilde{t} = 0$. However, we are interested in the model's dynamic behaviour, including collagen I degradation and the formation of pores of pure interstitial fluid. In these pores, $\tilde{C}_{C1} = 0$ and $\tilde{C}_{VC\cdot C1} = 0$. Without the Stokes flow term, the model is not well-defined in the pores, so we must keep both terms.

TABLE 4.8: Nondimensionalised reaction terms in the interstitial space and lymphatic endothelial cell domains. M2P abbreviates proMMP2; M2, MMP2; T2, TIMP2; VC, VEGFC; C1, collagen I; MT1, MT1-MMP; IS, interstitial space; LEC, lymphatic endothelial cell.

Reaction Term	Form	Equation
$\tilde{R}^{IS}_{M2P}$	$-\lambda_{11}\tilde{C}_{M2P}$	(4.26)
$\tilde{R}^{IS}_{M2}$	$-\lambda_{13}\tilde{C}_{M2}\tilde{C}_{T2}+\lambda_{14}\tilde{C}_{M2\cdot T2}-\lambda_{15}\tilde{C}_{M2}$	(4.26)
$\tilde{R}^{IS}_{T2}$	$-\lambda_{19}\tilde{C}_{M2}\tilde{C}_{T2}+\lambda_{20}\tilde{C}_{M2\cdot T2}-\lambda_{21}\tilde{C}_{T2}$	(4.26)
$\tilde{R}^{IS}_{M2\cdot T2}$	$\tilde{C}_{M2}\tilde{C}_{T2}-\lambda_{23}\tilde{C}_{M2\cdot T2}-\lambda_{24}\tilde{C}_{M2\cdot T2}$	(4.26)
$\tilde{R}^{IS}_{VC}$	$-\lambda_{25}\tilde{C}_{VC}\tilde{C}_{C1}+\lambda_{26}\tilde{C}_{VC\cdot C1}-\lambda_{27}\tilde{C}_{VC}$	(4.26)
$\tilde{R}^{IS}_{C1}$	$\frac{-\lambda_{28}\tilde{C}_{M2}\tilde{C}_{C1}}{K_M^{M2,C1}+C_{C1,s}\tilde{C}_{C1}}-\lambda_{29}\tilde{C}_{VC}\tilde{C}_{C1}+\lambda_{30}\tilde{C}_{VC\cdot C1}$	(4.29)
$\tilde{R}^{IS}_{VC\cdot C1}$	$\tilde{C}_{VC}\tilde{C}_{C1}-\lambda_{32}\tilde{C}_{VC\cdot C1}$	(4.29)
$\tilde{R}^{LEC}_{M2P}$	$1-\lambda_9\tilde{C}_{MT1\cdot T2}\tilde{C}_{M2P}+\lambda_{10}\tilde{C}_{MT1\cdot T2\cdot M2P}$	(4.30)
$\tilde{R}^{LEC}_{M2}$	$\tilde{C}_{MT1\cdot T2\cdot M2P}\tilde{C}_{MT1}$	(4.30)
$\tilde{R}^{LEC}_{T2}$	$1-\lambda_{17}\tilde{C}_{MT1}\tilde{C}_{T2}+\lambda_{18}\tilde{C}_{MT1\cdot T2}$	(4.30)
$\tilde{R}^{LEC}_{MT1}$	$-\lambda_{33}\tilde{C}_{MT1}\tilde{C}_{T2}+\lambda_{34}\tilde{C}_{MT1\cdot T2}$	(4.31)
$\tilde{R}^{LEC}_{MT1\cdot T2}$	$\lambda_{35}\tilde{C}_{MT1}\tilde{C}_{T2}-\lambda_{36}\tilde{C}_{MT1\cdot T2}$ $-\lambda_{37}\tilde{C}_{MT1\cdot T2}\tilde{C}_{M2P}+\lambda_{38}\tilde{C}_{MT1\cdot T2\cdot M2P}$ $+\lambda_{39}\tilde{C}_{MT1\cdot T2\cdot M2P}\tilde{C}_{MT1}$	(4.31)
$\tilde{R}^{LEC}_{MT1\cdot T2\cdot M2P}$	$\lambda_{40}\tilde{C}_{MT1\cdot T2}\tilde{C}_{M2P}-\lambda_{41}\tilde{C}_{MT1\cdot T2\cdot M2P}$ $-\lambda_{42}\tilde{C}_{MT1\cdot T2\cdot M2P}\tilde{C}_{MT1}$	(4.31)

Second, we will consider the reaction terms in the LEC domain. In $\tilde{R}^{LEC}_{MT1}$, λ_{33} is orders of magnitude bigger than λ_{34}. In $\tilde{R}^{LEC}_{MT1\cdot T2}$, λ_{37} is orders of magnitude bigger than λ_{38} and λ_{39}. In $\tilde{R}^{LEC}_{MT1\cdot T2\cdot M2P}$, λ_{40} is orders of magnitude bigger than λ_{41} and λ_{42}. Because the model does not have a MT1-MMP production term, it describes a quick conversion of the initial supply of MT1-MMP into MT1-MMP·TIMP2·proMMP2, leaving very little MT1-MMP and MT1-MMP·TIMP2. Because proMMP2 and TIMP2 are continuously supplied, the model describes an accumulation of these species following the saturation of MT1-MMP. On the other hand, the scarcity of MT1-MMP means a low $\tilde{R}^{LEC}_{M2}$ once the initial supply of MT1-MMP is used up. We can of course separate the two time scales (before and after the saturation of MT1-MMP), but we are interested in both phases, so we will not cross out any terms here.

Third, we will consider the equations in the interstitial space domain. In $\tilde{R}^{IS}_{M2}$, $\tilde{R}^{IS}_{T2}$, and $\tilde{R}^{IS}_{M2\cdot T2}$, the kinetic parameters except the degradation ones are all orders of magnitude larger than the transport parameters in their corresponding equations. Physically, it means the binding and unbinding rates of MMP2 and TIMP2 are transport-controlled. Also, in each of the three reaction terms, the unbinding rate constant is five orders of magnitude larger than the binding rate constant, suggesting MMP2 is not saturated by TIMP2. In $\tilde{R}^{IS}_{VC}$, for the same reasons, the binding and unbinding rates of VEGFC and collagen I are transport-controlled, and VEGFC is not saturated by collagen I. In $\tilde{R}^{IS}_{C1}$, when $\tilde{C}_{C1}$ is close to unity, the three terms are similar.

Clearly, a fast reaction rate means nothing unless the reactants can meet in space, so both kinetic and transport terms must remain in our equations. Although the unbinding rate constants are orders of magnitude larger than the binding ones, the unbinding terms equal zero without the binding ones. Taken together, we will not cross out any terms here.

4.6 Simplification

The nondimensionalised model provides some opportunities for simplification.

First, η_{DA}, η_{PCV}, and η_{DLAV} stand out in table 4.6: they are orders of magnitude bigger than everything else. They describe how permeable the blood vessels are, so the latter are very leaky. We can simplify our boundary conditions accordingly.

Second, some of our transport parameters (κ, $\tilde{D}_i^{eff}$, and ω) depend on the amount of unbound and VEGFC-bound collagen I present. Since the initial supply of collagen I is in the unbound state, and the unbinding rate constants of VEGFC and collagen I are orders of magnitude larger than the binding rate constants, we may be able to ignore $\tilde{C}_{VC{\cdot}C1}$ in our transport terms.

In the following subsections, we will carry out these simplifications.

4.6.1 Leaky Blood Vessels

First, the boundary conditions representing the transvascular fluxes of interstitial fluid, equations (4.22) to (4.24), can be simplified. The dimensionless vascular permeabilities are all orders of magnitude larger than unity: $\eta_{DA} = 1.317 \times 10^{14}$, $\eta_{PCV} = 1.317 \times 10^{14}$, and $\eta_{DLAV} = 2.634 \times 10^{14}$. In physiological terms, the blood vessels are very leaky. Therefore, we will ignore any transvascular pressure drops and replace the fluxes with constant pressures. This simplification means

$$\tilde{P}^s = \frac{1}{\eta_3} \qquad \tilde{\boldsymbol{x}} \in \partial\Omega_{DA}, \tag{4.40}$$

$$\tilde{P}^s = 0 \qquad \tilde{\boldsymbol{x}} \in \partial\Omega_{PCV}, \text{ and} \tag{4.41}$$

$$\tilde{P}^s = 0 \qquad \tilde{\boldsymbol{x}} \in \partial\Omega_{DLAV}. \tag{4.42}$$

4.6.2 Specific Hydraulic Conductivity

Second, we can linearise the term $\frac{\tilde{\boldsymbol{u}}}{(\tilde{C}_{C1}+\eta_2\tilde{C}_{VC\cdot C1})^{\alpha}}$ in equation (4.20). It factorises to give $\tilde{\boldsymbol{u}}\tilde{C}_{C1}^{-\alpha}(1+\frac{\eta_2\tilde{C}_{VC\cdot C1}}{\tilde{C}_{C1}})^{-\alpha}$, which can be expanded as a Taylor series at the point where $\frac{\eta_2\tilde{C}_{VC\cdot C1}}{\tilde{C}_{C1}}=0$. This expansion leads to the series

$$\tilde{\boldsymbol{u}}\tilde{C}_{C1}^{-\alpha}[1-\alpha\frac{\eta_2\tilde{C}_{VC\cdot C1}}{\tilde{C}_{C1}}+\frac{\alpha(\alpha+1)}{2}(\frac{\eta_2\tilde{C}_{VC\cdot C1}}{\tilde{C}_{C1}})^2 - \frac{\alpha(\alpha+1)(\alpha+2)}{6}(\frac{\eta_2\tilde{C}_{VC\cdot C1}}{\tilde{C}_{C1}})^3+\ldots]. \quad (4.43)$$

This expansion assumes that $\left|\frac{\eta_2\tilde{C}_{VC\cdot C1}}{\tilde{C}_{C1}}\right| \ll 1$ in the interstitial space domain. The binding rate constant of VEGFC and collagen I in $\tilde{R}^{IS}_{VC\cdot C1}$, λ_{31}, is 1; the unbinding rate constant of the same process, λ_{32}, is 1.56×10^2. The initial concentration of free collagen I is unity, but it is zero for VEGFC-bound collagen I. It follows that $\tilde{C}_{VC\cdot C1}$ must be orders of magnitude smaller than $\tilde{C}_{C1}$ all the time. We also know that $\eta_2=0.255$. Taken together, the required assumption is a reasonable one to make. By the same argument, the terms beyond unity in the square brackets can be neglected, so

$$\tilde{\boldsymbol{\nabla}}\tilde{P}\approx-\tilde{\boldsymbol{u}}\tilde{C}_{C1}^{-\alpha}+\eta_3\tilde{\boldsymbol{\nabla}}^2\tilde{\boldsymbol{u}}. \quad (4.44)$$

To facilitate the model's numerical solution, we will divide equation (4.44) by η_3 and define the simulated pressure by the equation $\tilde{P}^s=\frac{\tilde{P}}{\eta_3}$. After this simplification of equation (4.20),

$$\tilde{\boldsymbol{\nabla}}\tilde{P}^s=-\frac{\tilde{\boldsymbol{u}}\tilde{C}_{C1}^{-\alpha}}{\eta_3}+\tilde{\boldsymbol{\nabla}}^2\tilde{\boldsymbol{u}}. \quad (4.45)$$

4.6.3 Diffusion Term

Third, we will linearise the diffusion term in equation (4.26): $\tilde{D}_i^{eff}\tilde{\boldsymbol{\nabla}}(\frac{\tilde{C}_i}{\omega})$.

We will start with the term $\frac{1}{\omega}$, which can be expressed as $(1-\lambda_5\tilde{C}_{C1}-\lambda_6\tilde{C}_{VC\cdot C1})^{-1}$. From Abramowitz and Stegun (1964), we know that $(1+x)^{-1}\approx1-x+x^2-x^3+x^4-\ldots$ when x is in the vicinity of zero. Applying this result,

$$[1+(-\lambda_5\tilde{C}_{C1}-\lambda_6\tilde{C}_{VC\cdot C1})]^{-1} \approx 1-(-\lambda_5\tilde{C}_{C1}-\lambda_6\tilde{C}_{VC\cdot C1})+(-\lambda_5\tilde{C}_{C1}-\lambda_6\tilde{C}_{VC\cdot C1})^2+\ldots. \quad (4.46)$$

This expansion assumes that $\left|\lambda_5\tilde{C}_{C1}+\lambda_6\tilde{C}_{VC\cdot C1}\right| \ll 1$ in the interstitial space domain. Since $\lambda_5 = 1.98\times10^{-1}$ and $\tilde{C}_{C1} \leq 1$, we can conclude that $\lambda_5\tilde{C}_{C1} \ll 1$. With respect to the second term, we know that $\lambda_6 = 5.06\times10^{-2}$ and $\tilde{C}_{VC\cdot C1} \ll \tilde{C}_{C1}$, so it is orders of magnitude less than unity. The assumption is a valid one. The terms beyond $\lambda_5\tilde{C}_{C1}$ are negligible for the same reasons. As a result, $\frac{1}{\omega} \approx 1+\lambda_5\tilde{C}_{C1}$.

We will simplify the effective diffusivity along similar lines. When x is near zero, $e^x \approx 1+x+\frac{x^2}{2!}+\frac{x^3}{3!}+\ldots.$ We will apply this result to the exponential term in the equation $\tilde{D}_i^{eff} = \lambda_{1,i}exp(-\lambda_{2,i}\sqrt{\lambda_3\tilde{C}_{C1}+\lambda_4\tilde{C}_{VC\cdot C1}})$. It follows that

$$exp(-\lambda_{2,i}\sqrt{\lambda_3\tilde{C}_{C1}+\lambda_4\tilde{C}_{VC\cdot C1}}) \approx 1-\lambda_{2,i}\sqrt{\lambda_3\tilde{C}_{C1}+\lambda_4\tilde{C}_{VC\cdot C1}} + \frac{\lambda_{2,i}^2(\lambda_3\tilde{C}_{C1}+\lambda_4\tilde{C}_{VC\cdot C1})}{2!}+\ldots. \quad (4.47)$$

As usual, this expansion requires the magnitude of the exponent to be much smaller than one. Since $\lambda_3 = 7.88\times10^{-2}$ and $\tilde{C}_{C1} \leq 1$, the first term in the square root is much smaller than one; because $\lambda_4 = 2.01\times10^{-2}$ and $\tilde{C}_{VC\cdot C1} \ll \tilde{C}_{C1}$, the same is true for the second term. Overall, the square root is on the order of 1×10^{-1} or smaller. The prefactor of the square root, $\lambda_{2,i}$, is on the order of unity. Therefore, the expansion is justified. The terms beyond $-\lambda_{2,i}\sqrt{\lambda_3\tilde{C}_{C1}+\lambda_4\tilde{C}_{VC\cdot C1}}$ in the expansion are negligible for the same reasons. The simplified diffusivity is $\lambda_{1,i}(1-\lambda_{2,i}\sqrt{\lambda_3\tilde{C}_{C1}+\lambda_4\tilde{C}_{VC\cdot C1}})$.

The square root in $\lambda_{1,i}(1-\lambda_{2,i}\sqrt{\lambda_3\tilde{C}_{C1}+\lambda_4\tilde{C}_{VC\cdot C1}})$ can be simplified even further. Rewriting it as $\sqrt{\lambda_3\tilde{C}_{C1}}(1+\frac{\lambda_4\tilde{C}_{VC\cdot C1}}{\lambda_3\tilde{C}_{C1}})^{1/2}$ and knowing that $\left|\frac{\lambda_4\tilde{C}_{VC\cdot C1}}{\lambda_3\tilde{C}_{C1}}\right| \ll 1$, we can expand it as a Taylor series at the point where $\frac{\lambda_4\tilde{C}_{VC\cdot C1}}{\lambda_3\tilde{C}_{C1}} = 0$:

$$\sqrt{\lambda_3\tilde{C}_{C1}}[1+\frac{1}{2}(\frac{\lambda_4\tilde{C}_{VC\cdot C1}}{\lambda_3\tilde{C}_{C1}})-\frac{1}{8}(\frac{\lambda_4\tilde{C}_{VC\cdot C1}}{\lambda_3\tilde{C}_{C1}})^2+\ldots]. \quad (4.48)$$

The terms beyond unity are negligible, so the approximate effective diffusivity is $\lambda_{1,i}(1-\lambda_{2,i}\sqrt{\lambda_3\tilde{C}_{C1}})$.

The simplified equation (4.26) has the form

$$\frac{\partial\tilde{C}_i}{\partial\tilde{t}} = \tilde{\boldsymbol{\nabla}}\cdot[\lambda_{1,i}(1-\lambda_{2,i}\sqrt{\lambda_3\tilde{C}_{C1}})\tilde{\boldsymbol{\nabla}}(\tilde{C}_i+\lambda_5\tilde{C}_{C1}\tilde{C}_i)-\lambda_7\tilde{\boldsymbol{u}}\tilde{C}_i]+\tilde{R}_i. \quad (4.49)$$

The simplified expressions, $\frac{1}{\omega} = 1 + \lambda_5 \tilde{C}_{C1}$ and $\tilde{D}_i^{eff} = \lambda_{1,i}(1 - \lambda_{2,i}\sqrt{\lambda_3 \tilde{C}_{C1}})$, also apply to the boundary conditions.

4.7 Chapter Summary

In this chapter, we completed the mathematical model by adding the biochemistry of ECM remodelling and VEGFC-ECM binding, as well as the transport phenomena of the participating molecular species. These biophysical and biochemical phenomena are represented by a set of ordinary and partial differential equations in the model. They are connected to the interstitial flow component developed in chapter 3; the links are the specific hydraulic conductivity of the ECM and the convection terms. Following parametrisation, we nondimensionalised and simplified the full mathematical model. We will refer to the embryo represented by the final version of our mathematical model as the primary system. The mathematical model of the primary system is summarised in appendix D. We will simulate the system and its modified forms in chapter 5.

Chapter 5

Computer Simulations

In this chapter, we will use the mathematical model developed in chapters 3 and 4 to simulate the dynamics of VEGFC, MMP2, and collagen I in the primary system. The mathematical model representing it is summarised in appendix D. It is analytically intractable, so we must solve it and its modified versions numerically. We will use COMSOL Multiphysics for these computer simulations. It is a software package which solves PDEs by the finite element method (FEM). Appendix E is a review of some common numerical methods used to solve PDEs. Using the simulation results, we will try to answer the research questions raised in section 2.3.

5.1 COMSOL Multiphysics Settings

In this section, we will explain how COMSOL Multiphysics will be used to simulate the primary system. The solution of its mathematical model involves two stages. First, the interstitial flow equations, (D.1) and (D.2), will be solved alone for the initial velocity field. Second, we will solve the time-dependent equations (D.3) to (D.7), (D.10) to (D.11), and (D.12) to (D.17), together with equations (D.1) and (D.2).

We will adopt a fully coupled approach to solve the model. It means that at each stage, the relevant equations will be solved together in one step. Since our equations are all non-linear, their discretisation will result in a system of non-linear algebraic equations. In the first stage, the non-linear equations will be solved by an 'automatic highly non-linear (Newton)' solver; the second stage will be tackled by the 'constant (Newton)' solver. The former has a minimum damping factor of 1×10^{-8} and the damping factor cannot change more than tenfold in one iteration. It terminates when the estimated relative error is less than 0.001. The latter has a constant damping factor of 0.9 and terminates when the estimated relative error is less than 0.01. However, if COMSOL detects a linear problem, it will use the 'PARDISO' solver with

a pivoting perturbation of 1×10^{-8}. This solver handles systems of linear equations directly rather than iteratively. A direct method solves a linear system in a finite number of steps; an iterative method forms a sequence of approximations which converge to the exact solution.

The second stage is time-dependent, running from when $\tilde{t} = 0$ to when $\tilde{t} = 1$. We will use the BDF (backward differentiation formula) method to determine the time steps adaptively. At each time point, the solutions from the previous one or two time steps are used to estimate the time derivatives of the next time step, while the derivatives' stability determines the step size. The maximum step size is tentatively 0.02, but we will optimise this criterion after optimising the mesh.

When $\tilde{t} = 0$, there are not any mobile species and they take time to permeate the model zebrafish trunk. Their concentrations are likely to change drastically in the first few time steps, so these time steps require tight control. Since $U = 1.371 \times 10^{-4}$ μm s^{-1}, it takes a particle 7.29×10^3 s to transverse 1 μm by convection. Because $D_{T2}^{\infty} = 110$ μm^2 s^{-1} and D_{T2}^{∞} is the highest diffusivity in our model, we know that the equivalent time is 9.09×10^{-3} s for diffusion. Nondimensionalising the shorter travelling time, 9.09×10^{-3} s becomes 2.10×10^{-7}. Therefore, we will use an initial time step of 1×10^{-7}. Our choice of 1 μm is unrelated to the mesh size in the COMSOL implementation of our model. This choice is appropriate because the LEC diameter is 10 μm and we are not interested in the subcellular length scale. By using an initial time step smaller than the time required to transverse a subcellular distance, we will capture the dynamics of interest to us. In short, this restriction on the initial time step is motivated by the scope of our interest, not numerical stability.

We will perform a convergence study to determine the appropriate mesh size for the primary system. In COMSOL Multiphysics version 5.2, there are several predefined mesh settings. We will solve the mathematical model with the 'fine', 'finer', 'extra fine', and 'extremely fine' mesh settings on a desktop computer with an Intel(R) Core(TM) i5-3570 CPU at 3.40 GHz and 16 GB of RAM. Figure 5.1 is the resulting convergence plot. The velocity range of interstitial flows is from 0.1 to 2 μm s^{-1} (Swartz and Fleury, 2007). The second data point in the plot is 0.0173 μm s^{-1}, so the 'finer' mesh setting is sufficient to capture the relevant biological information. With this setting, there are 33562 elements ranging from 1.98×10^{-5} to 0.037 in nondimensionalised length.

We will optimise the maximum step size next. The equations governing $\tilde{\boldsymbol{u}}$, equations (D.1) and (D.2), are static. $\tilde{C}_{C1}$, which is controlled by an ordinary differential equation in time, equation (D.10), is more suitable for this convergence study. We will use the 'finer' mesh setting for this convergence study. Our results show that a maximum time step of 0.02 corresponds to a minimum $\tilde{C}_{C1}$ of 0.9991 when $\tilde{t} = 1$; a maximum time step of 0.01, a minimum $\tilde{C}_{C1}$ of 0.99909 when $\tilde{t} = 1$; the difference is 0.001 % only. Furthermore, the biologically relevant range of $\tilde{C}_{C1}$ is from 0.01 to 1

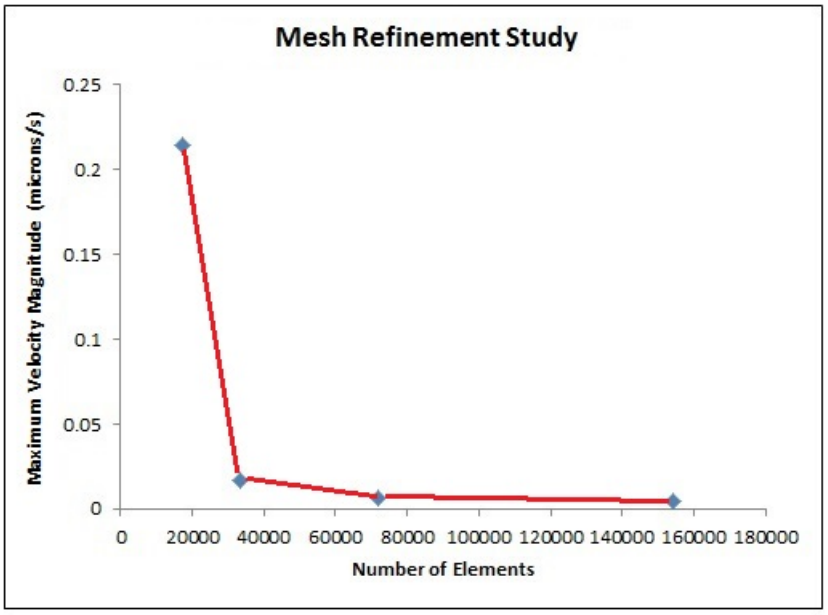

FIGURE 5.1: Convergence plot for the mesh refinement study. It shows how the maximum velocity magnitude when $\tilde{t} = 1$ changes with the number of mesh elements. The data points are the numerical results obtained with, from left to right, the 'fine', 'finer', 'extra fine', and 'extremely fine' mesh settings in COMSOL Multiphysics version 5.2.

(Edds Jr, 1958; Levick, 1987; Karagiannis and Popel, 2006). Taken together, we can safely assume that a maximum time step of 0.02 is appropriate.

Our model zebrafish trunk is symmetric about the y-axis. The line of symmetry runs vertically through it and passes the centres of the blood vessels and LEC. We can simulate half the structure only to save computational costs. To do so in COMSOL Multiphysics version 5.2, we will remove from the structure everything to the right of the line of symmetry. Then, we will set the normal components of the velocity and molecular fluxes to zero at the symmetry boundary.

5.2 Simulation Results

The primary system and its modified versions were simulated in COMSOL Multiphysics using the settings described in section 5.1. In this section, we will study the simulation results; they can be classified into three categories.

The first category is defined by an initial $\tilde{C}_{C1}$ of 1. The primary system summarised in appendix D is the base case. The numerical experiments are concerned with the production rate of VEGFC (λ_{VC}^{DA}), VEGFC-collagen I interactions (λ_{25}, λ_{26}, λ_{29}, λ_{30}, λ_{31}, and λ_{32}), the production rate of TIMP2 (λ_{16}), and the production of MMP2. With respect to MMP2, we will compare the primary system's activation mechanism with a constant source.

The second category is defined by an initial $\tilde{C}_{C1}$ of 0.1. Neither MMP2 nor TIMP2 is produced in the base case. Then, we will consider numerical experiments with VEGFC-collagen I interactions (λ_{25}, λ_{26}, λ_{29}, λ_{30}, λ_{31}, and λ_{32}), the pressure field's boundary conditions given by equations (D.18) to (D.20), a constant source of MMP2, and the geometry's aspect ratio.

The third category is defined by an initial $\tilde{C}_{C1}$ of 0.01. Neither MMP2 nor TIMP2 is produced in the base case. We will study a numerical experiment concerned with VEGFC-collagen I interactions (λ_{25}, λ_{26}, λ_{29}, λ_{30}, λ_{31}, and λ_{32}).

5.2.1 Diffusion and Sequestration Act Together

We will begin with the primary system.

The Péclet number of a transport process, Pe, measures the relative importance of convection and diffusion in the process. For our mathematical model, it is $\frac{UL}{D_i^\infty}$ or $\frac{\lambda_7}{\lambda_{1,i}}$. This expression is based on the characteristic velocity scale, but the velocity magnitude varies in space. A better option is $|\tilde{\boldsymbol{u}}|Pe$. The simulation results of the primary system indicate that when $\tilde{t} = 1$, the maximum value of $|\tilde{\boldsymbol{u}}|Pe$ is 0.14909 for VEGFC. VEGFC has the smallest $\lambda_{1,i}$ and highest $|\tilde{\boldsymbol{u}}|Pe$ among the modelled mobile species. We can therefore generalise and conclude that diffusion is the dominant transport phenomenon in the primary system.

The spatiotemporal dynamics of $\tilde{C}_{VC}$ in the primary system are shown in figure 5.2. At all time points, $\tilde{C}_{VC}$ peaks at the DA and decreases away from it. This symmetric distribution around the source is consistent with diffusion being the dominant mode of transport. As time passes, VEGFC achieves a wider reach by diffusion, so the transport of VEGFC does not equilibrate on this time scale. Because VEGFC is constantly produced, its baseline concentration increases with time.

Based on the dynamics of $\tilde{C}_{VC}$, VEGFC is unlikely to be a chemotactic factor for the LEC in the model zebrafish trunk. Its concentration increases from the PCV to the DA and then decreases to the horizontal myoseptum. If VEGFC is a chemoattractant, it can guide the LEC to the DA, but not further to the horizontal myoseptum. If it is a chemorepellent, it cannot guide the LEC dorsally at all.

On the other hand, the dynamics support the idea that VEGFC is a morphogen for the LEC. The LEC is in a VEGFC gradient which increases from the PCV to the DA at all time points. When $\tilde{t} = 1$, $\tilde{C}_{VC}$ rises from around 0.0001 at the dorsal end of the PCV to 0.0034 at the ventral end of the DA, roughly a thirtyfold increase over 25 µm. Informally and as a rule of thumb, a morphogen only needs a threefold change in its concentration over 30 µm to induce a cellular response (Gurdon and Bourillot, 2001). According to this criterion, the simulated VEGFC concentration profile allows VEGFC

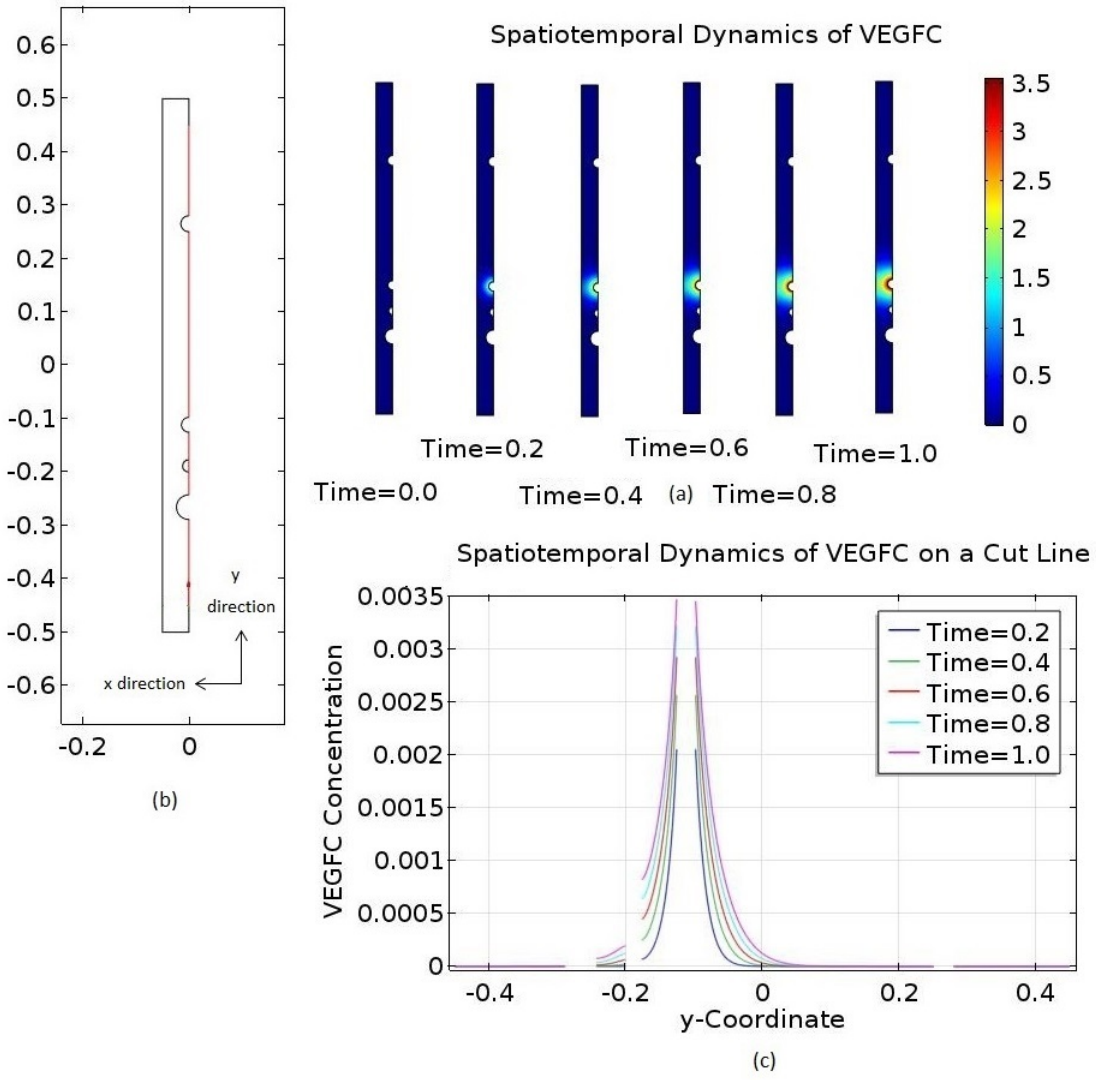

FIGURE 5.2: Spatiotemporal dynamics of VEGFC in the primary system. (a) shows the full concentration profiles of VEGFC at different time points. (b) defines the coordinate system of the model zebrafish trunk and a cut line along the y-axis. The cut line, which is in red, lies where $\tilde{x} = 0$ and runs from where $\tilde{y} = -0.45$ to where $\tilde{y} = 0.45$. (c) shows the concentration profiles of VEGFC on this cut line at different time points. The gaps are, from left to right, the posterior cardinal vein, the lymphatic endothelial cell, the dorsal aorta, and the dorsal longitudinal anastomotic vessel.

to be a morphogen for the LEC in the primary system. An argument against this idea is the absolute amount of VEGFC. The simulated $\tilde{C}_{VC}$ is on the order of 1×10^{-13} M, well below the viable concentration range of known morphogens, 1×10^{-9} to 1×10^{-11} M (Gurdon and Bourillot, 2001). Assuming sequestered VEGFC cannot function like free VEGFC, there is insufficient VEGFC in the primary system. However, our VEGFC production rate and VEGFC-collagen I binding/unbinding rate constants are crude estimates. Figure 5.3(a) shows the $\tilde{C}_{VC}$ dynamics in the case where λ_{VC}^{DA} is tenfold higher: the baseline of $\tilde{C}_{VC}$ is also tenfold higher while its profile shape remains unchanged.

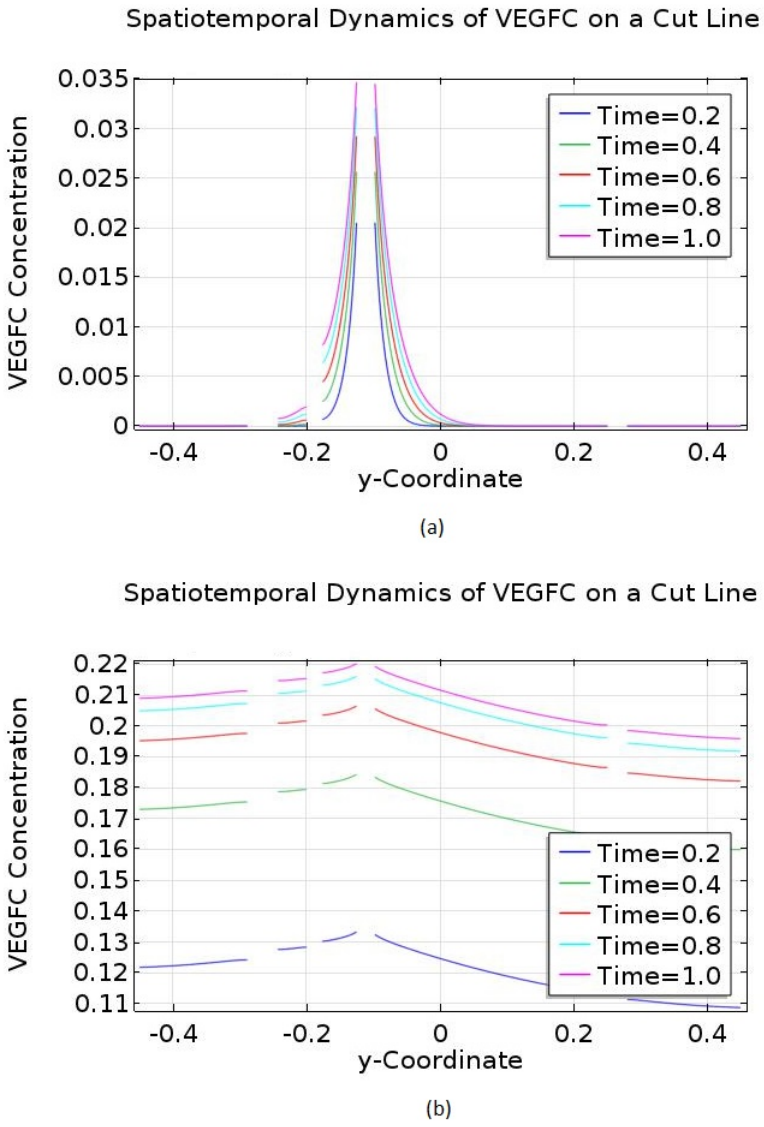

FIGURE 5.3: Spatiotemporal dynamics of VEGFC in two numerical experiments on the primary system. Both sets of results are shown on the cut line between (0, -0.45) and (0, 0.45). (a) shows the simulated dynamics after a tenfold increase in the production rate of VEGFC. (b) shows the dynamics simulated without VEGFC-collagen I interactions.

Figure 5.3(b) shows the dynamics of a system where $\lambda_{25} = 0$, $\lambda_{26} = 0$, $\lambda_{29} = 0$, $\lambda_{30} = 0$, $\lambda_{31} = 0$, and $\lambda_{32} = 0$. Biophysically, it means the interactions between VEGFC and collagen I are off in this system. Although the peak of $\tilde{C}_{VC}$ remains at the DA and its baseline still increases with time, the gradients are now too flat for VEGFC to be a morphogen.

To conclude, in a diffusion-dominant zebrafish embryo like the primary system, VEGFC may act as a morphogen, but it cannot be a chemotactic factor. For it to be a morphogen, it must bind to the ECM in the embryo to steepen its concentration

gradients. Sufficient VEGFC must be produced too because its production rate controls its concentration baseline.

5.2.2 MMP2 Acts Uniformly when Diffusion Dominates

We will turn our attention to the simulated dynamics of $\tilde{C}_{M2}$ in the primary system. As shown in figure 5.4(a), MT1-MMP gets depleted very quickly in the LEC domain. MMP2 activation requires MT1-MMP to break up MT1-MMP·TIMP2·proMMP2, so there is an initial burst of MMP2 output followed by a prolonged period of low production. Such dynamics are illustrated by figure 5.4(b). In figure 5.4(c), MMP2 is almost homogeneously distributed, meaning its diffusion can be considered to be in equilibrium on this time scale. Since MMP2 degrades collagen I, the latter has a nearly homogeneous distribution in figure 5.4(d) too. The extent of this degradation is less than 0.1 % and therefore negligible.

Separately, also in the primary system, the homogeneity of MMP2 means MMP2-TIMP2 binding only affects the baseline of $\tilde{C}_{M2}$, not its spatial profile. The diffusion of TIMP2 is in equilibrium on the time scale we are interested in.

However, endothelial cells produce MT1-MMP and TIMP2 adaptively; they may produce more MT1-MMP and less TIMP2 when the existing stock of MT1-MMP is depleted (Noel and Sounni, 2013; Sternlicht and Werb, 2001). Without modelling these mechanisms explicitly, Karagiannis and Popel (2006) have experimented with different combinations of MT1-MMP and TIMP2 production rates in a similar system, observing different MMP2 dynamics. Relevantly for our study, according to Karagiannis and Popel (2006), an LEC has the ability to produce more MMP2 than figure 5.4 suggests. It is also the case we are interested in. The primary system almost certainly produces less MMP2 than the zebrafish embryo it represents; there are many LECs in the latter. As a result, it is of no scientific value to explore a lower MMP2 production rate. What we want to know is whether an increase in the production rate of MMP2 can affect its spatial distribution.

We do not need to model the adaptive mechanisms to answer this question. In fact, we can dispense with the activation mechanism of MMP2 in the LEC domain; we only need a constant MMP2 production rate that exceeds the primary system's output. We can also ignore TIMP2 because it only affects the baseline of $\tilde{C}_{M2}$. The simplified primary system ignores proMMP2, TIMP2, MT1-MMP, and their complexes. Mathematically, only the equations governing the interstitial flow, $\tilde{C}_{M2}$, $\tilde{C}_{VC}$, $\tilde{C}_{C1}$, and $\tilde{C}_{VC\cdot C1}$ remain. Furthermore, $\tilde{R}_{M2}^{LEC} = 10$ and $\tilde{R}_{M2}^{IS} = -\lambda_{15}\tilde{C}_{M2}$ in the simplified model. In figure 5.4(b), the maximum $\tilde{R}_{M2}^{LEC}$ is around 0.2, so the simplified primary system has a significantly higher MMP2 output. The dynamics of this modified primary system are shown in figure 5.5. The extent of degradation is significant at almost 20 %. However, the spatial distributions of MMP2 and collagen I remain almost homogeneous.

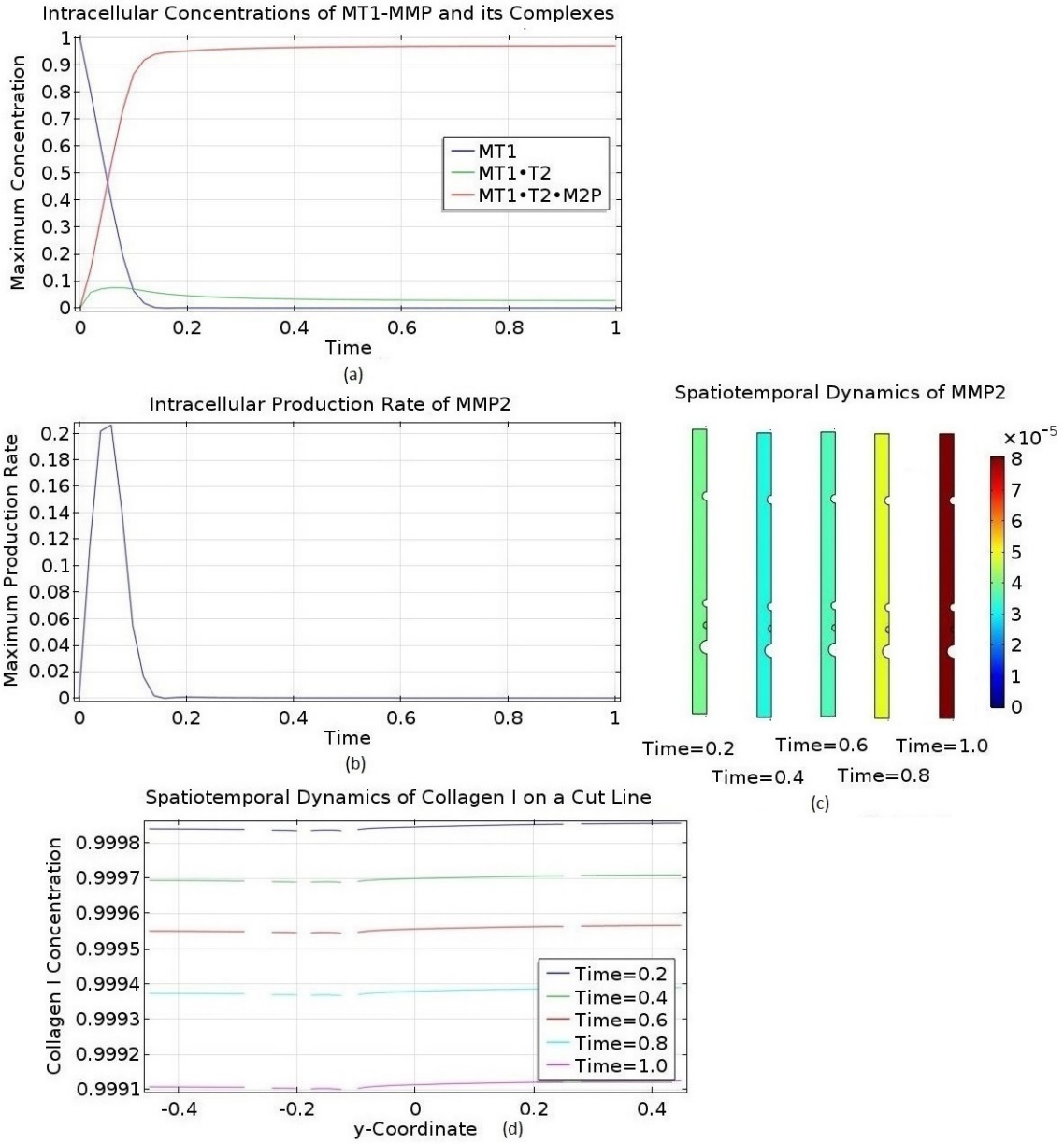

FIGURE 5.4: Behaviour of MMP2 in the primary system. (a) shows the temporal dynamics of MT1-MMP and its complexes inside the lymphatic endothelial cell (LEC) domain. For each species and at each time point, the maximum concentration in the LEC domain is plotted. (b) shows the production rate of MMP2 in the LEC domain, $\tilde{C}_{MT1 \cdot T2 \cdot M2P} \tilde{C}_{MT1}$. The maximum production rate in the cell is plotted at each time point. (c) shows the concentration profiles of MMP2 at selected time points. (d) shows the spatiotemporal dynamics of collagen I on the cut line between (0, -0.45) and (0, 0.45). MT1 abbreviates MT1-MMP; T2, TIMP2; M2P, proMMP2.

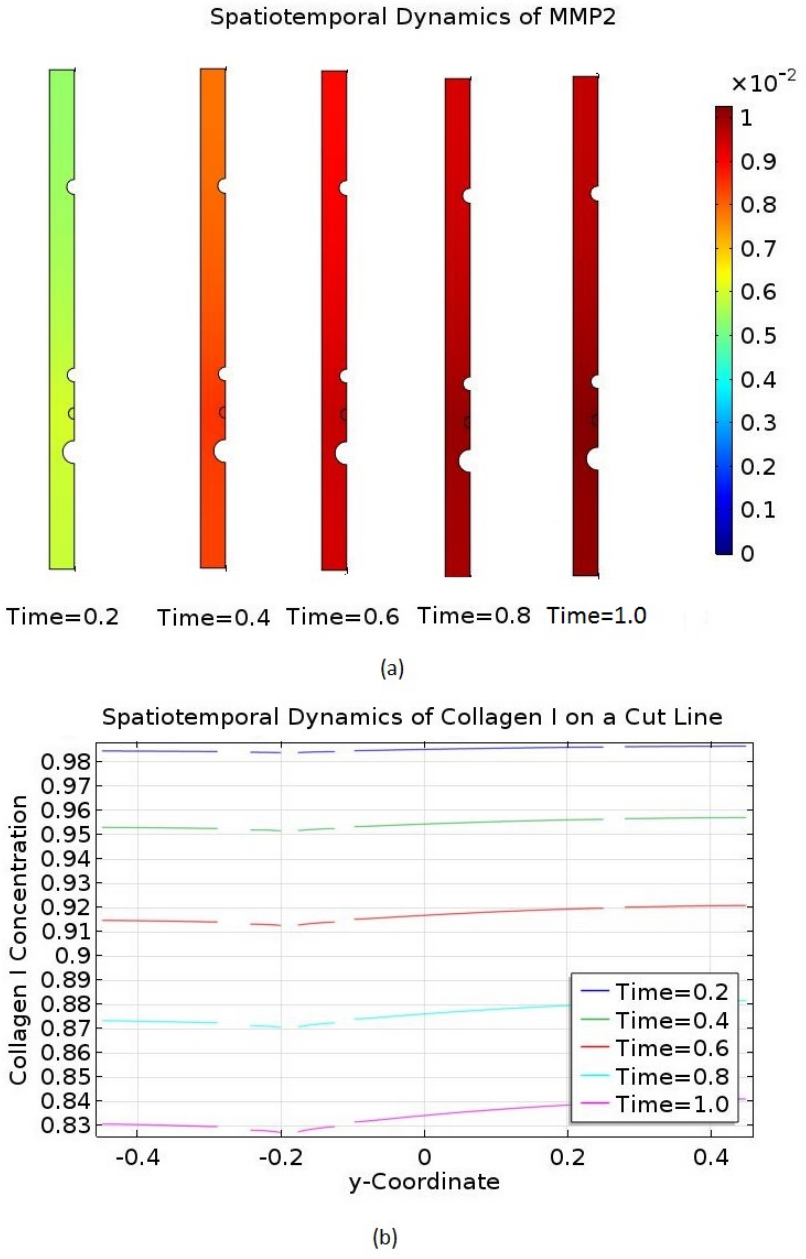

FIGURE 5.5: Behaviour of MMP2 in a modified primary system: it produces MMP2 at a constant rate and the output is higher than that of the primary system; it does not produce TIMP2. (a) shows the concentration profiles of MMP2 at selected time points. (b) shows the spatiotemporal dynamics of collagen I on the cut line between (0, -0.45) and (0, 0.45).

To conclude, in the zebrafish embryo, MMP2 diffusion is in equilibrium on our time scale of interest. When diffusion is the dominant mode of transport, as in the primary system, MMP2 permeates the entire embryo and degrades collagen I almost homogeneously. This conclusion is in agreement with Karagiannis and Popel (2006). In their conceptual model, MMP2 (mobile) remodels the entirety of an ECM to make it conducive to cell migration; MT1-MMP (cell-bound) degrades the collagen I surrounding a cell, thereby triggering its migration. In other words, the action of MMP2 is global, while the action of MT1-MMP is local. Another conclusion is concerned with TIMP2: its diffusion in the zebrafish embryo is also in equilibrium on our time scale of interest. In the primary system, TIMP2 is uniformly distributed and it only changes the baseline concentration of MMP2, not its spatial distribution.

5.2.3 Convection and Asymmetry

The primary system's characteristic scale for C_{C1} is 3.50×10^{-1} mol m^{-3}, the upper end of the biologically relevant range from 1.59×10^{-3} mol m^{-3} to 3.50×10^{-1} mol m^{-3}. The simulation results we will consider in this subsection pertain to a modified primary system where $\tilde{C}_{C1} = 0.1$ initially. As discussed in subsection 5.2.2, in a diffusion-dominant embryo, collagen I degradation by MMP2 and MMP2-TIMP2 binding do not affect the spatial profile of $\tilde{C}_{C1}$ significantly. Their effects on the baseline of $\tilde{C}_{C1}$ can simply be modelled by a lower initial $\tilde{C}_{C1}$, just like the modified primary system here. In other words, the dynamics of MMP2 and TIMP2 occur before and result in the initial condition of this modified system. The modified system does not produce MMP2 and TIMP2.

The mathematical model of this system only contains the interstitial flow equations and the governing equations of $\tilde{C}_{VC}$, $\tilde{C}_{C1}$, and $\tilde{C}_{VC\cdot C1}$. The reduction in the initial value of $\tilde{C}_{C1}$ means the transport and kinetic properties of this system differ from those of the primary system. In the zebrafish embryo, however, there are ECM components other than collagen I. For example, the sequestration of VEGFC by heparan sulfate is independent of collagen I. The kinetic terms must be controlled. Compared to the primary system, $\tilde{C}_{C1}$ is uniformly lower by an order of magnitude. Therefore, to compensate for this shortfall, the VEGFC-collagen I binding terms are an order of magnitude higher in this modified system. Mathematically, $\tilde{R}^{IS}_{VC} = -10\lambda_{25}\tilde{C}_{VC}\tilde{C}_{C1} + \lambda_{26}\tilde{C}_{VC\cdot C1} - \lambda_{27}\tilde{C}_{VC}$, $\tilde{R}^{IS}_{C1} = -10\lambda_{29}\tilde{C}_{VC}\tilde{C}_{C1} + \lambda_{30}\tilde{C}_{VC\cdot C1}$, and $\tilde{R}^{IS}_{VC\cdot C1} = 10\tilde{C}_{VC}\tilde{C}_{C1} - \lambda_{32}\tilde{C}_{VC\cdot C1}$.

The simulation results are summarised in figure 5.6. From figure 5.6(a), we can infer that convection marginally dominates diffusion in the centre, but diffusion still dominates in the periphery. Figures 5.6(b) and 5.6(c) are very similar to their counterparts in figure 5.2. Our comments on the primary system apply to this modified system too.

Next, we will consider a further modified system where VEGFC does not interact with collagen I. Its model only contains the interstitial flow equations and the reaction-diffusion-convection equation governing $\tilde{C}_{VC}$. Also, $\tilde{R}^{IS}_{VC} = -\lambda_{27}\tilde{C}_{VC}$ and $\tilde{C}_{C1} = 0.1$. Figure 5.6(d) shows the spatiotemporal dynamics of $\tilde{C}_{VC}$ in this modified system. The interstitial flow in the system pushes most of its VEGFC to the periphery. The baseline of $\tilde{C}_{VC}$ is two orders of magnitude higher than the case in figure 5.6(c). However, according to the rule of thumb of Gurdon and Bourillot (2001), the VEGFC gradient is not steep enough to be a morphogen gradient for the LEC. Its directionality does not allow VEGFC to guide the migrating LEC to the horizontal myoseptum either. Furthermore, although it makes sense that VEGFC goes with the flow, its accumulation downstream does not appear to be physical. Even though the embryo's lymphatic system is under development, there must be another way to remove

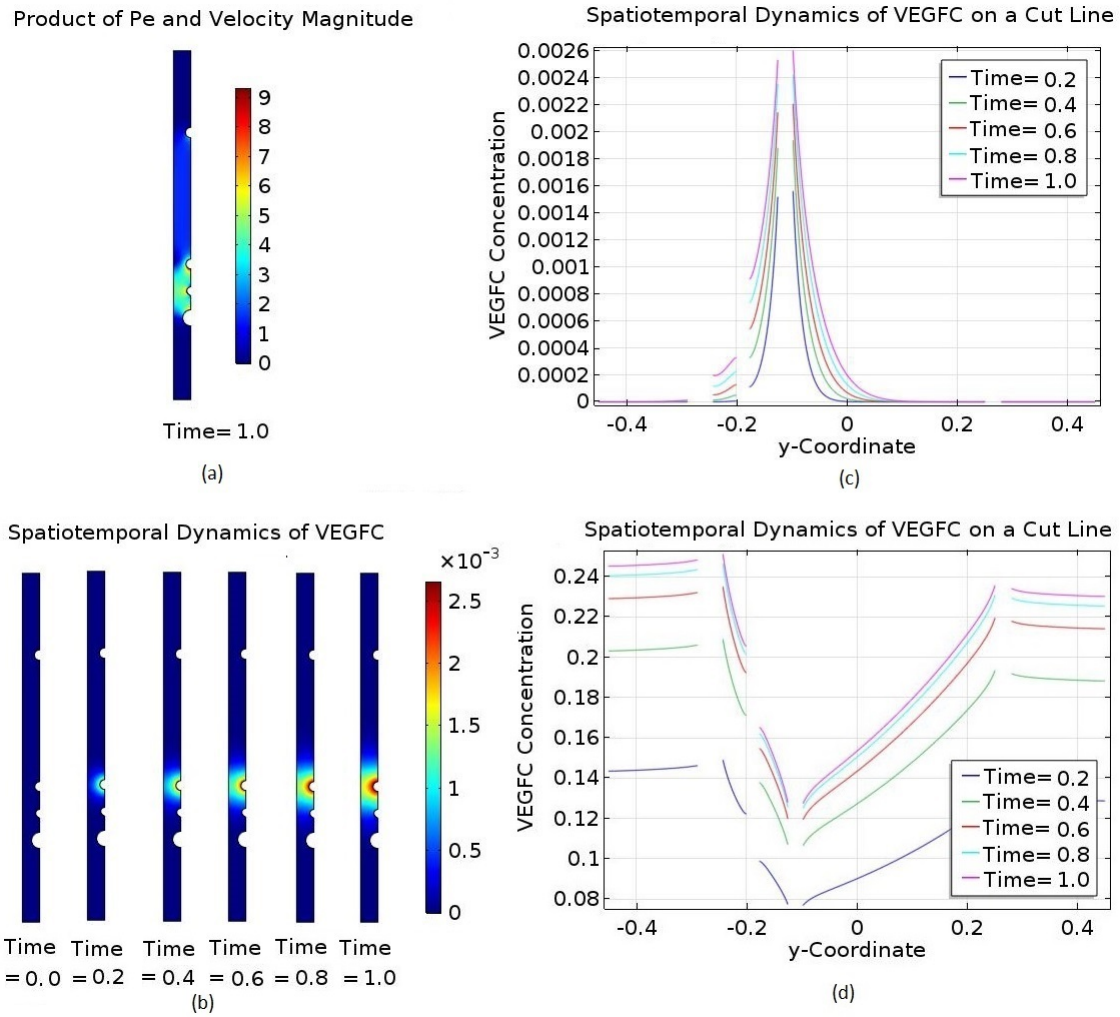

FIGURE 5.6: Spatiotemporal dynamics of VEGFC in two modified primary systems. In both systems, convection is dominant, $\tilde{C}_{C1} = 0.1$ initially, and MMP2 and TIMP2 are not produced. VEGFC binds to collagen I in the first system only. (a) shows that convection is marginally dominant in the central region of the first modified system, but diffusion still dominates in the periphery. The Péclet number is based on $\lambda_{1,VC}$, but the conclusion is general. (b) shows the concentration profiles of VEGFC at selected time points in the first system. (c) plots the data of (b) on the cut line between (0, -0.45) and (0, 0.45). (d) shows the spatiotemporal dynamics of VEGFC in the second modified system (no VEGFC-collagen I interactions) on the same cut line.

excessive fluid and any solutes in the fluid from the interstitial space. For example, they may be excreted directly through the anus. Our model zebrafish trunk is a slice of the trunk, so our model cannot capture any transport phenomena along the anterior-posterior axis, such as the proposed excretion method. Based on the evidence available and physical intuition, the scenario shown in figure 5.6(d) can neither be achieved by the zebrafish embryo nor influence lymphangiogenesis.

Commenting on the system where VEGFC does not bind to collagen I, we hypothesise that the pressure field is the key regulator of VEGFC dynamics. To test this hypothesis, we will consider the dynamics of yet another modified system. It is

identical to the modified system where VEGFC does not interact with collagen I except it has a steeper and asymmetric pressure field. We will modify the boundary conditions of the pressure field according to the equations,

$$\tilde{P}^s = \frac{1}{\eta_3} \qquad \tilde{\boldsymbol{x}} \in \partial\Omega_{DA}, \tag{5.1}$$

$$\tilde{P}^s = \frac{-0.5}{\eta_3} \qquad \tilde{\boldsymbol{x}} \in \partial\Omega_{PCV}, \text{ and} \tag{5.2}$$

$$\tilde{P}^s = \frac{0.8}{\eta_3} \qquad \tilde{\boldsymbol{x}} \in \partial\Omega_{DLAV}. \tag{5.3}$$

Figure 5.7 illustrates the resulting dynamics of $\tilde{C}_{VC}$. The $\tilde{C}_{VC}$ gradient from the DA to the PCV is steeper due to the steepened pressure gradient; it is now a threefold gradient; VEGFC may act as a morphogen for the LEC according to the rule of thumb of Gurdon and Bourillot (2001). The pressure drop from the DA to the PCV is larger than that from the DA to the DLAV, so the interstitial flow is faster ventrally to the DA. Because VEGFC goes with the interstitial flow, its concentration gradient is asymmetric. However, it can only guide the LEC to the horizontal myoseptum if it is a chemorepellent. We know that VEGFC generally promotes survival, proliferation, and migration in LECs, so it is unlikely to repel them. Nevertheless, the pressure field in this system is arbitrary. In a pressure field decreasing in the opposite direction, VEGFC can chemoattract the LEC to its destination.

How can we justify tweaking the pressure field in this arbitrary manner? The pressure field in the primary system is a rough estimate anyway; it ignores the pulsating nature of the blood flow in the zebrafish embryo. In the zebrafish embryo, the pressure field is likely to vary with time, symmetric at one time and asymmetric at another, steeper at one moment and gentler at another. It is conceivable that the pressure fields discussed are all relevant at different developmental stages. The objection is over their consistency. It is hard to imagine how a consistent pressure field is maintained throughout the time window of interest. As a result, the scenario in figure 5.7 is more relevant for synthetic systems, such as bioreactors for tissue engineering.

To conclude, there is a tension between convection and VEGFC sequestration by the ECM in the zebrafish embryo. Even when convection is marginally dominant, the interstitial flow cannot influence VEGFC when the latter is sequestered by the ECM. When VEGFC is influenced by the flow, the pressure field in the embryo controls its spatiotemporal dynamics. The field's steepness determines if VEGFC can be a morphogen for the LECs migrating therein; its directionality determines if VEGFC can guide their migration by chemotaxis. However, the pressure field in the embryo is

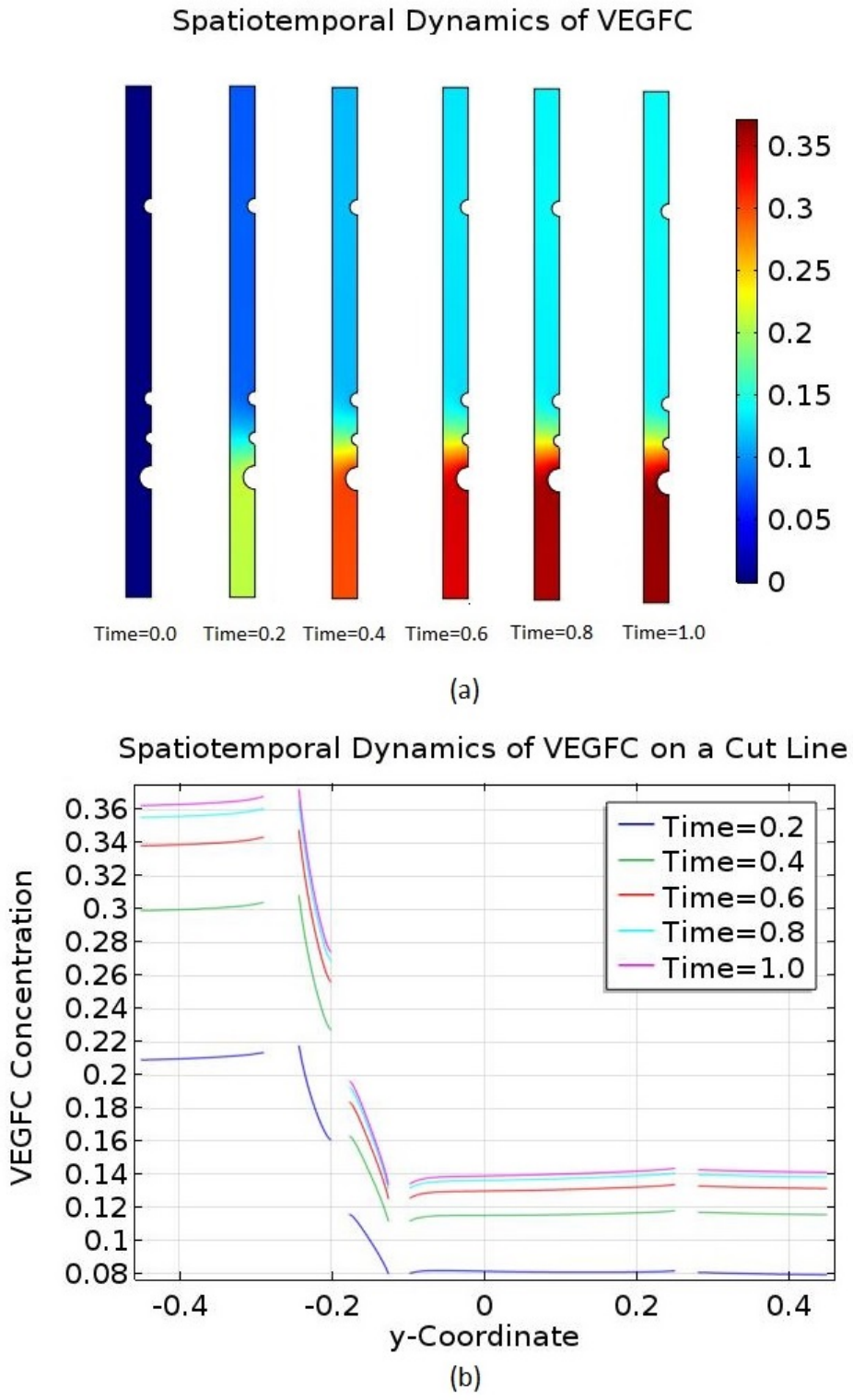

FIGURE 5.7: Spatiotemporal dynamics of VEGFC in a modified primary system: convection is dominant, $\tilde{C}_{C1} = 0.1$, MMP2 and TIMP2 are not produced, VEGFC-collagen I interactions are off, and the pressure field is asymmetric. (a) is a collection of VEGFC concentration profiles at selected time points. (b) shows the spatiotemporal dynamics of VEGFC on the cut line between (0, -0.45) and (0, 0.45).

unlikely to be consistent throughout the time frame of interest. As a regulator of lymphangiogenesis, it is not robust. It is more useful for bioengineering applications.

5.2.4 Channelisation

In subsection 5.2.2, we concluded that MMP2 is almost homogeneously distributed in the primary system, a diffusion-dominant zebrafish embryo. In subsection 5.2.3, we showed that by degrading collagen I uniformly in the embryo, MMP2 can enhance convection. However, we have not considered the behaviour of MMP2 *after* convection overrides diffusion yet. Inspecting the asymmetric profiles in figure 5.7, we suspect that MMP2 is not homogeneously distributed in a convection-dominant zebrafish embryo. We will consider a modified version of the system shown in figure 5.7. The modification is the addition of a constant MMP2 source. Although TIMP2 is unlikely to be homogeneous either, it has the same source as and a similar diffusion coefficient to MMP2. As before, MMP2-TIMP2 binding only affects the baseline of $\tilde{C}_{M2}$, so TIMP2 is not produced by this modified system.

The mathematical model of this modified system includes the interstitial flow equations and the governing equations of $\tilde{C}_{M2}$, $\tilde{C}_{VC}$, and $\tilde{C}_{C1}$. Furthermore, $\tilde{R}^{LEC}_{M2} = 10$, $\tilde{R}^{IS}_{M2} = -\lambda_{15}\tilde{C}_{M2}$, $\tilde{R}^{IS}_{VC} = -\lambda_{27}\tilde{C}_{VC}$, and $\tilde{R}^{IS}_{C1} = \frac{-\lambda_{28}\tilde{C}_{M2}\tilde{C}_{C1}}{K_M^{M2,C1}+C_{C1,s}\tilde{C}_{C1}}$. The pressure field is given by equations (5.1), (5.2), and (5.3).

Figure 5.8 summarises the results of this numerical experiment. In short, there is a positive feedback loop. Due to the asymmetric interstitial flow, MMP2 is concentrated at the ventral end; this asymmetry in $\tilde{C}_{M2}$ translates to a higher degradation rate of collagen I at the ventral end; the interstitial flow is thus strengthened in that direction to complete the feedback loop. The impact of this loop on VEGFC is shown in figure 5.8(d). Its concentration gradient steepens as time passes because it goes with the ever increasing interstitial flow. This loop enhances any morphogenetic and chemotactic properties VEGFC may have.

The model zebrafish trunk is too thin for any spatial effects to show up along the x-axis, but its dimensions are estimates only. Figure 5.9 shows the results of repeating the last numerical experiment in a triply widened geometry. In this geometry, $\tilde{x}$ goes from -0.15 (outer boundary) to 0 (line of symmetry). In figure 5.9(a), between the DA and PCV, we can clearly see a $\tilde{C}_{C1}$ gradient along the x-axis. Focusing on the cut line between (-0.15, -0.23) and (0, -0.23), which lies between the LEC and PCV, figures 5.9(b) and 5.9(c) illustrate that a channel with scarce collagen I and abundant VEGFC gradually forms near the line of symmetry.

To conclude, an asymmetric interstitial flow and MMP2 form a positive feedback loop in a convection-dominant zebrafish embryo. There are two consequences. First, the concentration gradient of VEGFC steepens along the ventral-dorsal axis, potentially

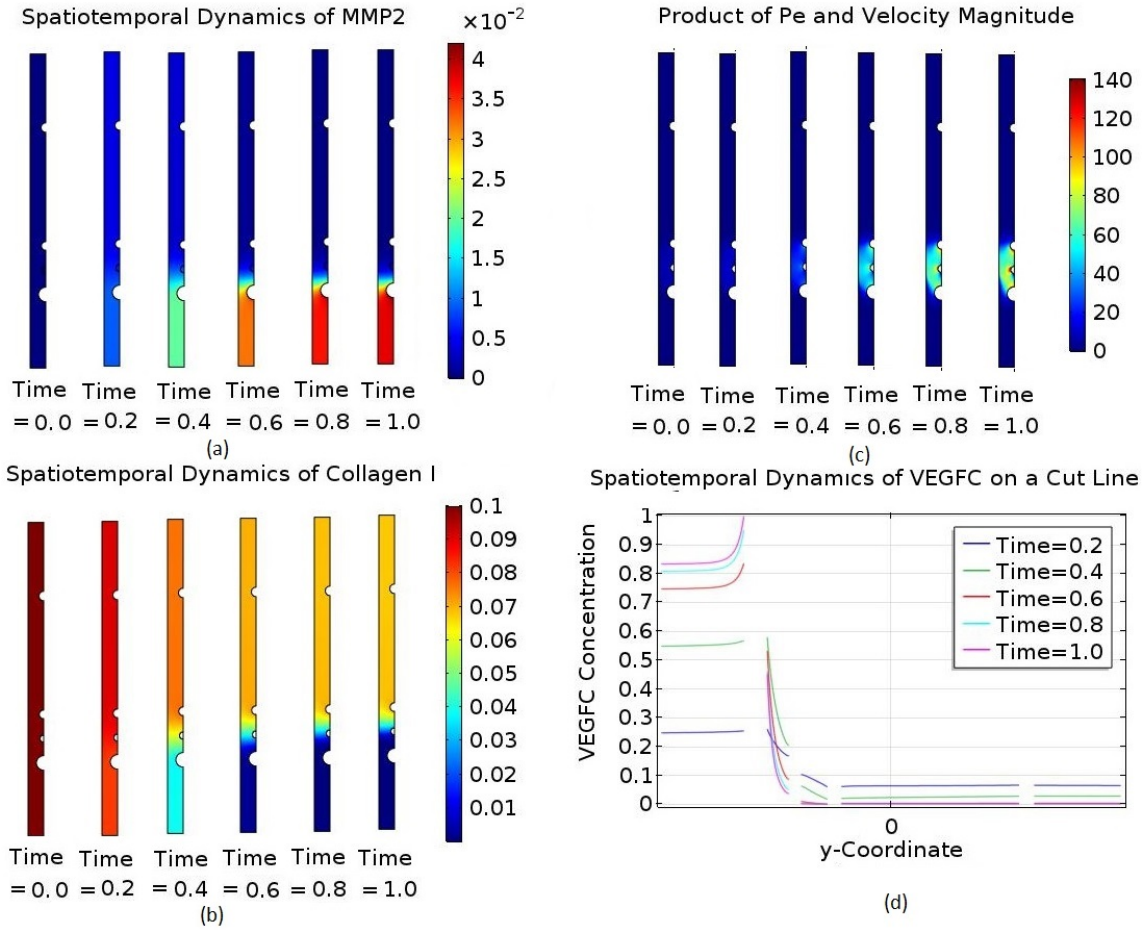

FIGURE 5.8: Positive feedback loop in a modified primary system: convection is dominant, $\tilde{C}_{C1} = 0.1$ initially, TIMP2 is not produced, MMP2 is produced at a constant rate, VEGFC-collagen I interactions are off, and the pressure field is asymmetric. (a) shows the spatiotemporal dynamics of MMP2. (b) shows the spatiotemporal dynamics of collagen I. (c) shows that convection becomes increasingly dominant in the region ventral to the DA. The Péclet number is based on $\lambda_{1,VC}$, but the conclusion is general. (d) shows the spatiotemporal dynamics of VEGFC on the cut line between (0, -0.45) and (0, 0.45).

making VEGFC a better morphogen and chemotactic factor. Second, a channel of scarce collagen I and abundant VEGFC forms near the blood vessels' plane along the ventral-dorsal axis. VEGFC is a growth factor for endothelial cells in general and collagen I a physical barrier to cell migration. Therefore, channelisation ensures that the migrating LECs move along the ventral-dorsal axis and in the same plane as the blood vessels. In short, it ensures that the lymphatic and blood vessels co-align. The role of MMP2 in channelisation is global. It changes the distributions of both VEGFC and collagen I on the tissue level to create an environment conducive to LEC migration. The migrating LECs degrade collagen I locally using their cell-bound MT1-MMP (Karagiannis and Popel, 2006). A similar mechanism has been proposed by Boardman and Swartz (2003) to explain lymphatic regeneration in the adult mouse's tail, but the mechanism has neither been modelled nor applied to the zebrafish embryo.

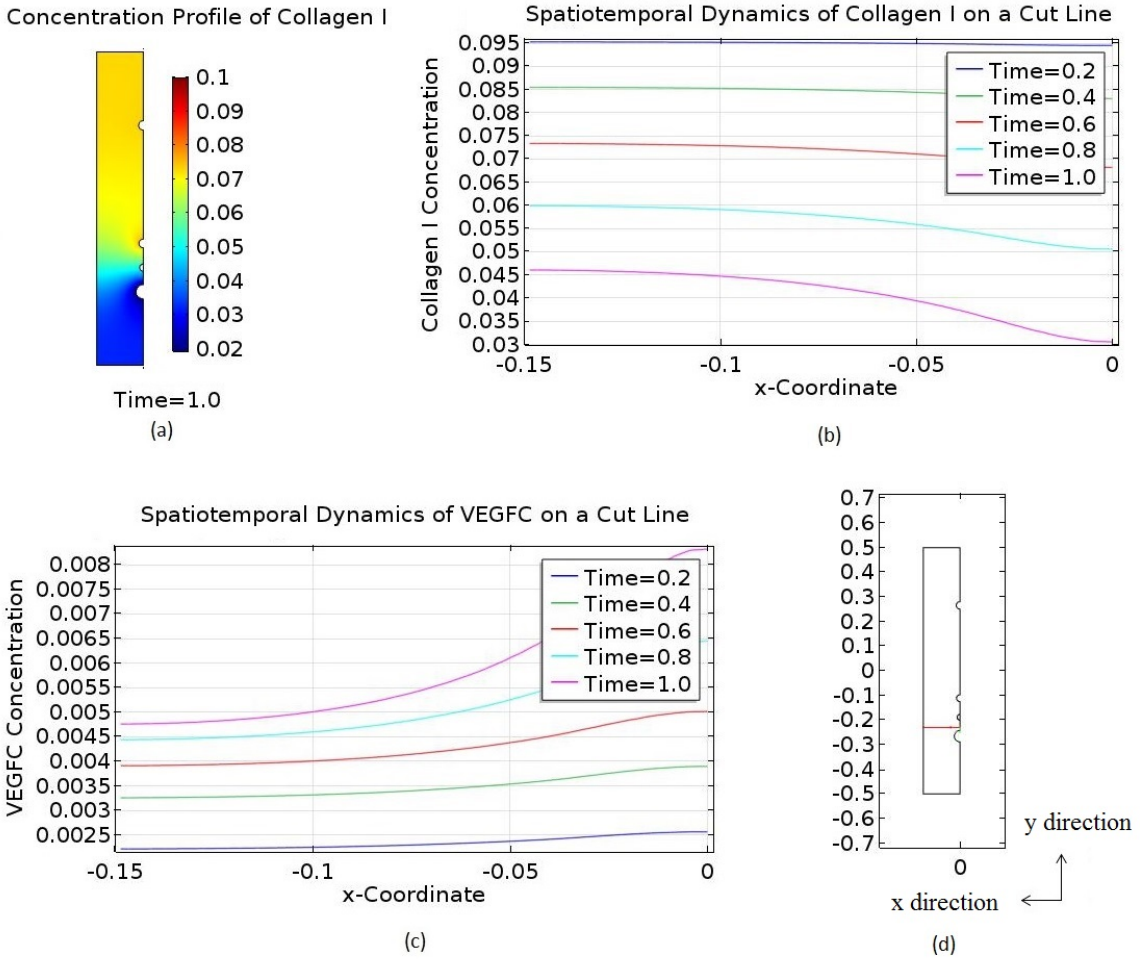

FIGURE 5.9: Channelisation in a modified primary system: its geometry is triply widened compared to the primary system, convection is dominant, $\tilde{C}_{C1} = 0.1$ initially, TIMP2 is not produced, MMP2 is produced at a constant rate, VEGFC-collagen I interactions are off, and the pressure field is asymmetric. (a) is the concentration profile of collagen I when $\tilde{t} = 1$. (b) shows the spatiotemporal dynamics of collagen I on the cut line between (-0.15, -0.23) and (0, -0.23). This cut line is between the posterior cardinal vein and lymphatic endothelial cell. (c) shows the spatiotemporal dynamics of VEGFC on the same cut line. (d) shows the aforementioned cut line.

5.2.5 Concentration Gradients Vanish Without Sequestration

This subsection is concerned with a modified primary system whose initial $\tilde{C}_{C1}$ is 0.01. With so little collagen I to begin with, there is no point in modelling its degradation, so the modified system does not produce MMP2. Without MMP2, there is no point in considering TIMP2, so the system does not produce TIMP2 either. It has the same pressure field as the primary system.

The mathematical model of this system consists of the interstitial flow equations and the governing equations of $\tilde{C}_{VC}$, $\tilde{C}_{C1}$, and $\tilde{C}_{VC\cdot C1}$. Its kinetic properties are controlled by increasing the VEGFC-collagen I binding terms by two orders of magnitude. Because of these changes, $\tilde{R}^{IS}_{VC} = -100\lambda_{25}\tilde{C}_{VC}\tilde{C}_{C1} + \lambda_{26}\tilde{C}_{VC\cdot C1} - \lambda_{27}\tilde{C}_{VC}$, $\tilde{R}^{IS}_{C1} = -100\lambda_{29}\tilde{C}_{VC}\tilde{C}_{C1} + \lambda_{30}\tilde{C}_{VC\cdot C1}$, and $\tilde{R}^{IS}_{VC\cdot C1} = 100\tilde{C}_{VC}\tilde{C}_{C1} - \lambda_{32}\tilde{C}_{VC\cdot C1}$. In $\lambda_{1,VC}(1 - \lambda_{2,VC}\sqrt{\lambda_3\tilde{C}_{C1}})$, the term inside the brackets is at least 0.94, so we will approximate the effective diffusivity of VEGFC as $\lambda_{1,VC}$ in this modified system.

Figures 5.10(a) and 5.10(b) summarise the dynamics of this modified system. The $|\tilde{\boldsymbol{u}}|Pe$ profile shows that convection is orders of magnitude more important than diffusion in the central region. Therefore, the interstitial flow flushes VEGFC to the periphery, resulting in boundary layers. These gradients cannot influence the LEC in the central region. How important are the interactions between VEGFC and collagen I in this system? For comparison, we will consider a further modified system. In its mathematical model, there are only the interstitial flow equations and the governing equation of $\tilde{C}_{VC}$; $\tilde{R}^{IS}_{VC} = -\lambda_{27}\tilde{C}_{VC}$ and $\tilde{C}_{C1} = 0.01$. Figure 5.10(c) shows the spatiotemporal dynamics of VEGFC in this system. The central regions of figures 5.10(b) and 5.10(c) are the same, proving that sequestration by collagen I cannot protect VEGFC from such a powerful interstitial flow.

To conclude, when there is insufficient collagen I in the zebrafish embryo, VEGFC cannot form a suitable concentration gradient to influence the migrating LECs. In other words, it can neither be a morphogen nor a chemotactic factor for them. It is because the interstitial flow clears the embryo's central region of VEGFC. When the interstitial flow is strong enough, sequestration by collagen I cannot protect VEGFC from going with the flow. However, the zebrafish embryo has other ECM components in addition to collagen I. The two modified systems considered in this subsection are probably unrepresentative of the embryo in that they are unrealistically permeable.

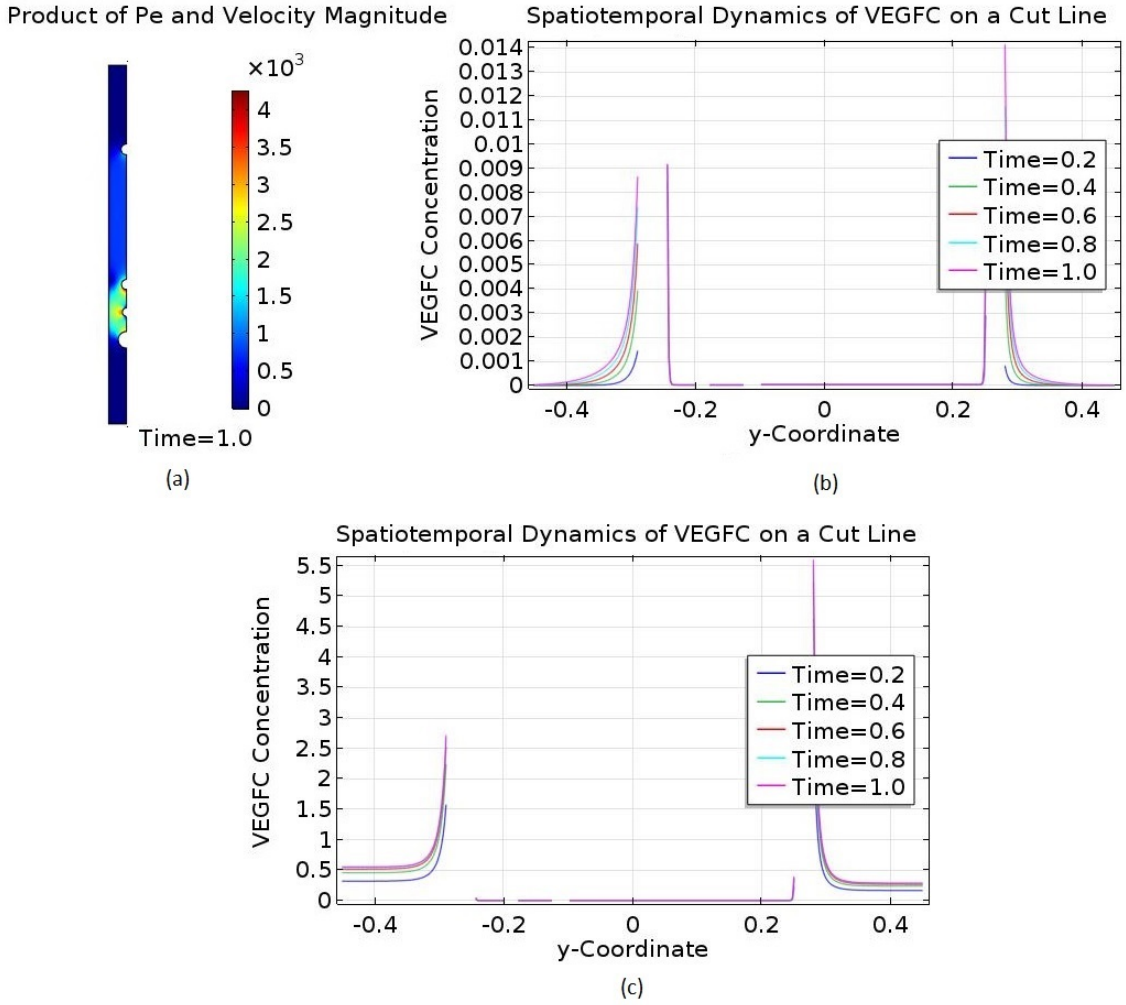

FIGURE 5.10: Concentration gradients cannot form with insufficient collagen I. In these two modified primary systems, $\tilde{C}_{C1} = 0.01$ initially, MMP2 and TIMP2 are not produced, and the pressure fields are symmetric around the dorsal aorta (same as the primary system); VEGFC binds to collagen I in the first modified system only. (a) illustrates that the central region of the first system is overwhelmingly dominated by convection although diffusion dominates in the periphery. The Péclet number is based on $\lambda_{1,VC}$, but the conclusion is general. (b) shows the dynamics of VEGFC on the cut line between (0, -0.45) and (0, 0.45) in the first system; VEGFC binds to collagen I. (c) shows the dynamics of VEGFC in the second system (no VEGFC-collagen I interactions) on the same cut line.

5.3 Discussion

The primary system, our proposed model of the VEGFC dynamics in the zebrafish embryo, has many parameters. The values used have different sources. Many of them are not *in vivo* values and many more do not pertain to the zebrafish embryo. Some of them are simply unavailable, such as the production rate of VEGFC, for which a reported VEGF production rate is used as a surrogate. To complicate matters, the conditions in the embryo are dynamic, so the parameters should not be static. Our simulations do not reflect the actual zebrafish embryo. Nonetheless, they are scenarios within the realms of possibility. In this section, we will integrate these simulation results into a coherent framework.

5.3.1 VEGFC

In three of the simulated scenarios, VEGFC is well-positioned to act as a morphogen or chemotactic factor for the LECs migrating from the PCV to the horizontal myoseptum. We remind ourselves that this happens between 36 and 48 HPF in the zebrafish embryo's trunk.

Scenario 1 is a diffusion-dominant embryo where VEGFC is sequestered by the ECM. In this scenario, VEGFC has a concentration profile that peaks at and decreases symmetrically from its source, the DA. The gradient between the PCV and the DA is a perfect morphogen gradient for the migrating LECs. However, the symmetric profile means VEGFC is unlikely to be their chemotactic factor. In general, the combination of diffusion and sequestration creates short-range, steep, and symmetric gradients of mobile species.

Scenario 2 is an embryo marginally dominated by convection; its ECM binds to VEGFC too. In this scenario, VEGFC is protected from the interstitial flow and behaves like it does in scenario 1.

Scenario 3 is also an embryo marginally dominated by convection, but VEGFC does not bind to the ECM. In this case, the pressure field is the key regulator of VEGFC concentration dynamics. A sufficiently steep pressure field translates to a viable morphogen gradient; an asymmetric pressure field gives a directionality to the gradient, thus allowing VEGFC to guide cell migration by chemotaxis. In general, a steep and asymmetric pressure field creates steep, asymmetric, and embryo-wide concentration gradients of mobile species. The prerequisites are convection being marginally dominant and a non-binding ECM. However, a caveat is that the pressure field inside the zebrafish embryo is likely to be chaotic. It is hard for the pressure field to be tweaked to suit the embryo's needs, so it is not a robust regulator of

lymphangiogenesis. This scenario is more relevant for bioengineering applications like bioreactors for tissue engineering.

5.3.2 Collagen I and MMP2

In the zebrafish embryo, collagen I concentration is the key variable that determines the dominant mode of transport and hence, the scenario it is in. In fact, when there is insufficient collagen I, concentration gradients cannot form at all. The embryo can switch back and forth among different scenarios by remodelling its ECM. It can even get the most out of a scenario by remodelling its ECM.

When diffusion is dominant, the distribution of MMP2 in the embryo is almost homogeneous. Therefore, it degrades collagen I almost uniformly until convection takes over. This mechanism allows the embryo to move from scenario 1 to scenarios 2 and 3.

In scenario 3, an asymmetric interstitial flow and the collagenolytic action of MMP2 form a positive feedback mechanism. It steepens and enhances the asymmetry of the VEGFC concentration gradient in the embryo. The two effects can potentially make VEGFC a more effective morphogen and chemotactic factor respectively. The mechanism can also create channels of abundant VEGFC and scarce collagen I to guide the migrating LECs to where they should be. Channelisation has been proposed by Boardman and Swartz (2003) to explain their experimental results about lymphatic regeneration in the adult mouse's tail, suggesting it is a versatile mechanism.

In scenarios 2 and 3, although our model cannot demonstrate this feature, the embryo can lower MMP2 production and increase collagen I production, thus tilting the balance in diffusion's favour. For example, it can start in scenario 3 where embryo-wide morphogen gradients divide it into segments of different cell types. Then, it can switch to scenario 1 where local gradients fine-tune the development of each segment.

We emphasise that these scenarios occur on the tissue level, so the action of MMP2 is global. It remodels the entire ECM and changes the global distributions of VEGFC and collagen I. Then, the LECs degrade collagen I locally using MT1-MMP as they migrate in the embryo (Karagiannis and Popel, 2006).

We note that our model only considers the abundance of collagen I in the ECM. However, the size distribution and spatial arrangement of collagen I fibrils in the ECM, as well as the fibrils' inner structures, also affect the ECM's mechanical properties (Ottani et al., 2001). Our model does not consider these molecular details.

5.3.3 MT1-MMP and TIMP2

The abundance of MMP2 is in turned controlled by MT1-MMP and TIMP2 inside the LECs. Karagiannis and Popel (2006) have shown that the relative concentrations of MT1-MMP, TIMP2, and proMMP2 determine the production/activation rate of MMP2 in a cell. Using the primary system, we reproduced the case where MT1-MMP is saturated by the other two. However, LECs generally produce MMP2 to aid their migration, so the saturated case is irrelevant to our time window between 36 and 48 HPF, during which LEC migration occurs. Karagiannis and Popel (2006) have already modelled how a general LEC can boost its MMP2 output. We applied this result to simplify the primary system. In many of its modified versions, a constant MMP2 source replaces the activation mechanism in the LEC domain. On the tissue level, TIMP2 is distributed like MMP2, so MMP2-TIMP2 binding only affects the baseline concentration of MMP2; TIMP2 is unimportant and absent from most modified primary systems. These simplifications make six of the ten species and complexes in the primary system redundant.

5.3.4 Answers to our Research Questions

Now, we can answer the research questions raised in section 2.3. Developmental processes are shaped by evolution. The fact that VEGFC is distributed like a morphogen in multiple representations of the zebrafish embryo suggests that it is actually one. On the other hand, even if VEGFC is a chemoattractant or chemorepellent, it can only perform its function in an asymmetric pressure field in scenario 3. The pressure field is also a poor regulator because it is likely to change drastically over time. A different molecular species is probably required to guide the PCV-derived LECs to the horizontal myoseptum. However, to validate our predictions, we need to comprehend the intracellular responses of an LEC to a concentration gradient of VEGFC; this can only be done experimentally.

5.3.5 Generalisations and Extensions

We have demonstrated many ways in which VEGFC can be a morphogen for the migrating LECs. We have also shown that stringent conditions must be satisfied for VEGFC to be a chemoattractant. However, the evidence available can support alternative hypotheses too, meaning the demonstrated mechanisms are generic. Other candidate morphogens and chemoattractants may behave like VEGFC does in the simulated scenarios, so the proposed mechanisms can regulate their spatiotemporal dynamics too. For example, Cxcl12a is expressed in the horizontal myoseptum and there is no evidence that it is localised. If it is mobile and interacts with the ECM like

VEGFC does in scenario 1, it can form a gradient rising towards the horizontal myoseptum. In this gradient, Cxcl12a is well-positioned to chemoattract the PCV-derived LECs to the horizontal myoseptum. It can even work in conjunction with VEGFC; VEGFC acts as a morphogen and Cxcl12a acts as a chemoattractant. More generally, the scenarios and mechanisms presented are frameworks within which embryonic development, tissue regeneration, and other biological phenomena can be understood.

The mathematical model *per se* is an innovation too. To the best of our knowledge, this is the first mathematical model that considers an interstitial flow, a remodelling ECM, and the sequestration of a mobile species by the ECM holistically. By changing the model geometry, its biochemical reaction network, and the model parameters, one can simulate the dynamics of a wide range of biological phenomena. By changing the geometry, one can study lymphangiogenesis in another organism. By changing the biochemical reaction network and model parameters, one can study a different event in the zebrafish.

The model can be improved upon in four ways. First, it took 1300 seconds to simulate the primary system on the desktop computer described in section 5.1. The other simulations took similar amounts of time. Because the model can be solved so cheaply, it can be extended to consider more realistic geometries, larger domains, and three dimensions. In three dimensions, we can model the transport of fluid and molecular species along the anterior-posterior axis, such as their excretion through the embryo's anus. Second, the model parameters are very uncertain, especially the binding and unbinding rate constants of VEGFC and collagen I. They are important parameters of this model, but they are currently unavailable. Knowledge of them will enhance the model's predictive power significantly. Third, as explained, it will be interesting to consider the dynamics of Cxcl12a as well. Fourth, we can add more ECM components and ECM-remodelling species to make the dynamics richer.

5.4 Chapter Summary

In this chapter, we considered the primary system and its modified versions to understand the spatiotemporal dynamics of VEGFC in the zebrafish embryo. According to the simulation results, it behaves very differently depending on the dominant transport phenomenon, its interactions with the ECM, and the pressure field. By remodelling the ECM, the embryo can generate a wide repertoire of VEGFC patterns. Our simulation results suggest that VEGFC is a morphogen for the PCV-derived LECs, but it cannot guide them to the horizontal myoseptum by chemotaxis. However, we made our predictions based on circumstantial evidence; they must be validated experimentally. Our proposed mechanisms are generic; they can be

used to explain lymphangiogenesis in terms of other molecular species, such as Cxcl12a. More generally, these mechanisms and the mathematical model *per se* can help researchers study other biological phenomena, be they natural or synthetic. We also suggested several improvements for the model.

Chapter 6

Turing Patterns

In 1952, the mathematician Alan Turing postulated that spatially heterogeneous patterns of chemicals can arise from a homogeneous distribution (Turing, 1952). This symmetry-breaking mechanism depends on the instability of the homogeneous distribution. This instability in turn requires the chemicals to diffuse at different rates and interact with each other non-linearly.

In the primary system, the two major diffusing species, VEGFC and MMP2, diffuse at different rates. However, as we will see in this chapter, they do not interact in a manner typical of Turing's mechanism. Another deviation is the presence of collagen I, an immobile binding substrate which interacts with VEGFC and MMP2 biochemically and controls their diffusion rates. We want to answer a simple question: can VEGFC patterns emerge in the model zebrafish trunk through Turing's mechanism?

We will begin this chapter with a review of pattern formation in biology. Then, we will modify the primary system in accordance with our needs. We will identify the Turing space of the modified system (secondary system henceforth), the region of the parametric space where Turing's mechanism works. We will simulate the emergence of VEGFC patterns in different geometries too. Finally, we will discuss our results in relation to lymphangiogenesis.

6.1 Biological Pattern Formation

In this section, we will review the major theories about biological pattern formation.

6.1.1 Alan Turing and Lewis Wolpert

Turing's mechanism and positional information are the two major theories of pattern formation in biology. Our discussion is based on the comparative and speculative study by Green and Sharpe (2015).

In 1952, Alan Turing postulated that certain chemicals can instruct different cell fates in a concentration-dependent manner (Turing, 1952). Turing coined the term 'morphogen' for this type of chemical. According to his theory, when there is more than one morphogen, and the transport and kinetic parameters are in certain combinations, random fluctuations to a homogeneous distribution of the morphogens can create heterogeneous patterns. This symmetry-breaking mechanism is driven by diffusion and may have a domain-size dependence. As a result, it may happen spontaneously as a domain grows beyond a certain size. Possible outcomes include travelling waves, oscillations, and stable periodic patterns. Periodic patterns are most relevant to embryonic development. For example, the stripes and spots on animal skins are periodic. A specific instance of Turing's mechanism has been proposed by Gierer and Meinhardt (1972). It involves a fast diffusing inhibitor and a slowly diffusing activator; the activator stimulates the production of both species while the inhibitor inhibits the activator's production only. If a Turing pattern is stable and the parameters are global, all its periods are produced independently and identically. In other words, the mechanism is position-independent and the pattern is periodic. Stationary Turing patterns were first observed *in vitro* in 1990 (Castets et al., 1990).

In 1969, Lewis Wolpert proposed an alternative mechanism (Wolpert, 1969). It is less concerned with symmetry breaking than the development of complex patterns from existing asymmetries. The mechanism works as follows. A pre-existing morphogen gradient divides a developing tissue into different domains. The cells in different domains differentiate differently, thereby generating a complex pattern of gene expression. Contrary to Turing's mechanism, Wolpert's mechanism does not require the pattern to match the morphogen gradient. The morphogen gradient simply serves as a coordinate system in the developing tissue, providing positional information to the cells therein. The intermediate interpretation step can theoretically lead to any patterns from the morphogen gradient. Because the interpretation step is carried out intracellularly, the morphogen gradient can be used in other tissues and species. For example, the Hox genes define the anterior-posterior axes of all animals (Akam, 1989b).

In their paper, Green and Sharpe (2015) discuss the disadvantages of Turing's mechanism. First, its dependence on global parameters leads to rigid patterns; this feature is at odds with the ability of biological patterns to scale with their domain sizes. Second, it is sensitive to noises and initial conditions. Third, biological patterns tend to develop from one into another, not from homogeneity. Initially, biologists favoured Wolpert's mechanism over Turing's due to experimental results, for example,

about chick wing buds and *Drosophila* (Saunders and Gasseling, 1968; Akam, 1989a). Recently, there has been a revival in using Turing's mechanism to explain pattern formation in different contexts, such as mammalian hard palates (Economou et al., 2012), limb digits (Raspopovic et al., 2014), germ layer specification (Müller et al., 2012; Schier, 2009), and left-right patterning (Shiratori and Hamada, 2006).

However, the two ideas do not contradict each other. Green and Sharpe (2015) describe three ways in which they can work together. First, Wolpert's theory assumes a pre-existing asymmetry without explaining how it is created. In an embryo spanning half the wavelength of a Turing pattern, the Turing pattern is a monotonic gradient; it is perfect for providing positional information to the embryo's constituent cells. Second, the two patterning mechanisms can work concurrently. For example, a periodic Turing pattern can pattern regular structures like digits, while a morphogen gradient spanning all the digits can create differences among the digits. Third, Turing's mechanism can be a downstream process of Wolpert's mechanism. If a Turing pattern develops within and under the influence of a morphogen gradient, its wavelength may vary spatially.

In a book chapter, Marciniak-Czochra (2015) states Turing's mechanism in relation to a homogeneous steady state as follows. When two chemical species with different diffusion rates react with each other, the homogeneous steady state may become unstable and give way to a non-trivial spatial structure.

6.2 Secondary System

We will perform our Turing pattern analysis on a simplified version of the primary system described in appendix D. Let us call it the secondary system. We will write down the dimensional form of its mathematical model before explaining its differences from the primary system. In the interstitial space domain,

$$\frac{\partial C_{M2}}{\partial t} = \frac{\partial}{\partial x}\left[D_{M2}^{eff}\frac{\partial}{\partial x}\left(\frac{C_{M2}}{\omega}\right)\right] + \frac{P_{M2}C_{VC}C_{C1}}{C_{VC,s}C_{C1,s}} - k_{M2}^{deg}C_{M2}, \tag{6.1}$$

$$\frac{\partial C_{VC}}{\partial t} = \frac{\partial}{\partial x}\left[D_{VC}^{eff}\frac{\partial}{\partial x}\left(\frac{C_{VC}}{\omega}\right)\right] + \frac{P_{VC}C_{C1}}{C_{C1,s}} - k_{VC}^{deg}C_{VC} - k_{VC,C1}^{on}C_{VC}C_{C1} + k_{VC,C1}^{off}C_{VC\cdot C1}, \tag{6.2}$$

$$\frac{\partial C_{C1}}{\partial t} = P_{C1} - k_{M2,C1}^{cat}C_{M2} - k_{VC,C1}^{on}C_{VC}C_{C1} + k_{VC,C1}^{off}C_{VC\cdot C1}, \text{ and} \tag{6.3}$$

$$\frac{\partial C_{VC\cdot C1}}{\partial t} = k^{on}_{VC,C1} C_{VC} C_{C1} - k^{off}_{VC,C1} C_{VC\cdot C1}. \tag{6.4}$$

As in subsection 4.3.2,

$$\omega = 1 - v_{C1h} M_{C1} C_{C1} - v_{C1h} M_{C1} C_{VC\cdot C1} \text{ and} \tag{6.5}$$

$$D_i^{eff} = D_i^{\infty} exp\Big(\frac{-k_B T}{6\pi\mu D_i^{\infty} r_f} \sqrt{v_{C1} M_{C1} C_{C1} + v_{C1} M_{C1} C_{VC\cdot C1}}\Big). \tag{6.6}$$

The boundary conditions where $x = 0$ and $x = L$ are given by the equations,

$$\frac{\partial}{\partial x}\Big(\frac{C_{M2}}{\omega}\Big) = 0 \text{ and} \tag{6.7}$$

$$\frac{\partial}{\partial x}\Big(\frac{C_{VC}}{\omega}\Big) = 0. \tag{6.8}$$

We are interested in the effects of noises on the homogeneous steady state of this model. Therefore, the initial concentrations are simply the concentrations at the homogeneous steady state plus noises.

6.2.1 Differences from the Primary System

This model is considerably simpler than the one representing the primary system; the equations of the latter are given in appendix D.

First, it has one dimension only; we do not need to consider two dimensions to decide whether the system can produce Turing patterns.

Second, Turing's mechanism does not consider any external perturbations to a homogeneous steady state. We must limit ourselves to the diffusion-dominant regime where $C_{C1} + C_{VC\cdot C1} > 1 \times 10^{-4}$ M (1×10^{-1} mol m^{-3}), so there are no convection terms in the model of the secondary system. As explained in chapter 5, this concentration range is physiologically relevant. There is no longer a specialised LEC domain where MMP2 is produced. Instead, it is produced throughout the interstitial space domain. This arrangement is justified because the LECs in the trunk move around. Likewise, VEGFC is produced throughout the interstitial space domain, not on the DA's surface only. This arrangement is justified by the embryo-spanning and VEGFC-producing aISVs (van Impel and Schulte-Merker, 2014). The aISVs are absent from the primary system because they are not important for the lymphangiogenic

events between 36 and 48 HPF. These assumptions mean the secondary system represents the zebrafish trunk after the PCV-derived LECs invade the whole trunk and when it is at a homogeneous steady state (after 48 HPF).

Third, MMP2 is not produced by the intracellular mechanism that involves MT1-MMP, proMMP2, and TIMP2. Depending on the relative concentrations of the three species, MT1-MMP may degrade collagen I directly, activate proMMP2, or be inactivated by TIMP2 (Karagiannis and Popel, 2006). We are interested in the second case which can be approximated by just one MMP2 production term. The emergence of VEGFC patterns occurs on the tissue level, so it is reasonable to ignore an intracellular detail. Although TIMP2 binds to MMP2 in the interstitial space, we have learnt that it only changes the baseline concentration of the latter; it is reasonable to ignore TIMP2 in the interstitial space domain too. Therefore, MT1-MMP, proMMP2, TIMP2, and their complexes are absent from the secondary system.

Fourth, the Michaelis-Menten term in the primary system's model, $\frac{-k_{M2,C1}^{cat} C_{M2} C_{C1}}{K_M^{M2,C1} + C_{C1}}$, gives way to a linear term, $-k_{M2,C1}^{cat} C_{M2}$. Earlier, we specified that $C_{C1} + C_{VC \cdot C1} > 1 \times 10^{-4}$ M (1×10^{-1} mol m^{-3}). We now tighten this constraint and stipulate that $C_{C1} > 1 \times 10^{-4}$ M (1×10^{-1} mol m^{-3}). This tightening is justified because as explained in subsection 4.6.2, the unbinding of VEGFC from collagen I is much faster than their binding, so $C_{C1} \gg C_{VC \cdot C1}$. Since $K_M^{M2,C1} = 8.50 \times 10^{-3}$ mol m^{-3}, $C_{C1} \gg K_M^{M2,C1}$, justifying the simplification.

On the other hand, the production rates of MMP2 and VEGFC are now adaptive to the dynamics of collagen I and VEGFC. Before this chapter, we were interested in the concentration dynamics in the zebrafish trunk between 36 and 48 HPF. Now, we are interested in the steady state after the transient dynamics. The production rates are independent of C_{VC} and C_{C1} in the primary system, simplifying its dynamics. However, this independence is not an apt assumption for the secondary system: the production rates' relations to C_{VC} and C_{C1} are important for the steady state's stability.

First, the production rate of MMP2 is proportional to $C_{VC} C_{C1}$.

Huang and Sui (2012) used immunohistochemistry to study the ovarian tissues of patients with epithelial ovarian cancer; there is a positive correlation between C_{VC} and C_{M2} in their data. In their experiments, Bauer et al. (2005) induced a threefold increase in the level of fibroblast-secreted VEGFC and noticed a threefold increase in the level of endothelial-cell-bound MT1-MMP. Together, these two observations suggest that VEGFC boosts MMP2 production through the activation mechanism that involves MT1-MMP, proMMP2, and TIMP2.

It has been observed that collagen I and collagen IV can both enhance MMP2 activation without regulating the transcription of proMMP2, TIMP2, and MT1-MMP

(Maquoi et al., 2000). In the experiments, the extent of MMP2 activation responded non-linearly to an increasing C_{C1}; it went up, peaked, and then decreased slowly (Maquoi et al., 2000). A potential mechanism is that collagen I and collagen IV bring MT1-MMP, proMMP2, and TIMP2 closer together to speed up the activation of MMP2 (Maquoi et al., 2000). Therefore, collagen I and VEGFC favour MMP2 production through the same activation mechanism. We speculate that when collagen I is in excess, it saturates MT1-MMP, thereby shutting down MMP2 activation. However, we will assume that MT1-MMP is not limiting in the secondary system and ignore the non-linear relation between MMP2 activation and C_{C1}.

The product of C_{VC} and C_{C1} reflects that VEGFC and collagen I affect the same mechanism. P_{M2} is the maximum production rate of MMP2; it is achieved when C_{VC} and C_{C1} take their maximum values, which are determined by the model parameters.

Second, the production rate of VEGFC is proportional to C_{C1}. Jeltsch et al. (2014) have found that CCBE1 enhances the secretion and proteolytic cleavage of VEGFC, while CCBE1 is likely to act by binding to ECM components like collagen I (Bos et al., 2011). Without knowing the mechanistic details, it is impossible to model the effects of collagen I on VEGFC production. Our simple production term captures what we know, that collagen I favours VEGFC production. P_{VC} is the maximum VEGFC production rate achieved when C_{C1} is at its maximum value, which is defined by the model parameters.

There is also a constant source of collagen I in the secondary system. Based on our discussion in this subsection so far, the secondary system represents the zebrafish trunk at some point after 48 HPF, after the LECs invade the whole trunk and when it is at a homogeneous steady state. As explained in subsection 4.3.4, we assume that collagen I is produced to establish the 'normal' C_{C1} before 36 HPF. From 36 HPF onwards, as the LECs migrate, they degrade collagen I; this step is represented by the primary system. Once the LECs arrive at their destinations after 48 HPF, collagen I degradation is likely to slow down, allowing C_{C1} to be restored to its 'normal' level; this restoration step is not represented by the primary system because at its steady state, $C_{C1} = 0$ mol m^{-3}, a biologically irrelevant situation (Swartz and Fleury, 2007; Prockop and Kivirikko, 1995). By contrast, the constant P_{C1} gives the secondary system a relevant steady state for our Turing pattern analysis.

Like the production rates, the diffusion rates are more complicated in the secondary system than in the primary system; they follow equations (4.1) to (4.5) without the simplifications described in section 4.6. Turing's mechanism results from diffusion-driven instability, so it is not sensible to use the simplified form for this study.

6.2.2 Parametrisation and Nondimensionalisation

Most of the parameters are the same as those for the primary system.

For P_{M2}, we will use the value of P_{M2P} in table 4.4. There are many steps in the conversion of proMMP2 to MMP2. Furthermore, there is no reason why P_{M2P} should be capped at 2.64×10^{-5} mol m^{-3} s^{-1}. However, it is a reasonable value. We will explore the parametric space in its vicinity.

For P_{VC}, we will use the value of R_{VC}^{DA} in table 4.4. Assuming a cell diameter of 1×10^{-5} m, we will convert it from 1.65×10^{-15} mol m^{-2} s^{-1} to 9.90×10^{-10} mol m^{-3} s^{-1}. Once again, there is no reason why it should be capped at this value. However, it is a reasonable value. We will explore the parametric space in its vicinity.

We will determine P_{C1} while scaling the model. We will use the same length scale as the primary system, meaning 4.34×10^{-4} m. We will use a time scale (τ) of 10000 s, the time scale of natural degradation. For the concentration scale of collagen I, $C_{C1,s}$, we will use 5.29×10^{-1} mol m^{-3}, the highest measured value of C_{C1} that we know (Levick, 1987; Karagiannis and Popel, 2006). This ensures that the secondary system is diffusion-dominant. For our remaining concentration scales, $C_{i,s}$'s, we will use the concentrations at the homogeneous steady state where $C_{C1} = 5.29 \times 10^{-1}$ mol m^{-3}. After replacing C_i's with $C_{i,s}$'s and crossing out the derivatives, equations (6.1) to (6.4) become a set of algebraic equations. It can be solved to give the concentration scales and P_{C1}:

$$C_{M2,s} = \frac{P_{M2}}{k_{M2}^{deg}}, \tag{6.9}$$

$$C_{VC,s} = \frac{P_{VC}}{k_{VC}^{deg}}, \tag{6.10}$$

$$P_{C1} = k_{M2,C1}^{cat} C_{M2,s}, \text{ and} \tag{6.11}$$

$$C_{VC\cdot C1,s} = \frac{k_{VC,C1}^{on} C_{VC,s} C_{C1,s}}{k_{VC,C1}^{off}}. \tag{6.12}$$

Numerically, $C_{VC,s} = 9.90 \times 10^{-6}$ mol m^{-3}, $C_{M2,s} = 2.64 \times 10^{-1}$ mol m^{-3}, $P_{C1} = 1.19 \times 10^{-3}$ mol m^{-3} s^{-1}, and $C_{VC\cdot C1,s} = 5.24 \times 10^{-2}$ mol m^{-3}. The scales characterising the secondary system are summarised in table 6.1.

We will use a lower value of P_{C1}, 6×10^{-4} mol m^{-3} s^{-1}, to ensure that $C_{C1} < C_{C1,s}$ at the homogeneous steady state. Because the production rates of VEGFC and MMP2

TABLE 6.1: Characteristic scales of the secondary system. M2 abbreviates MMP2; VC, VEGFC; C1, collagen I.

Scale	Description	Value
$C_{C1,s}$	Concentration scale for C1	5.29×10^{-1} mol m^{-3}
$C_{M2,s}$	Concentration scale for M2	2.64×10^{-1} mol m^{-3}
$C_{VC,s}$	Concentration scale for VC	9.90×10^{-6} mol m^{-3}
$C_{VC\cdot C1,s}$	Concentration scale for VC·C1	5.24×10^{-2} mol m^{-3}
L	Length scale	4.34×10^{-4} m
τ	Time scale	10000 s

both increase with C_{C1} linearly, $C_{VC} < C_{VC,s}$, $C_{M2} < C_{M2,s}$, and $C_{VC\cdot C1} < C_{VC\cdot C1,s}$ at the homogeneous steady state too. These inequalities make sure that the steady state concentrations stay within the concentration scales. As discussed in the last subsection, we limit ourselves to the regime where $C_{C1} > 1 \times 10^{-1}$ mol m^{-3}. At the homogeneous steady state where $P_{C1} = 6 \times 10^{-4}$ mol m^{-3} s^{-1}, C_{C1} must satisfy this constraint.

Using the parameters and scales determined in this subsection, we can nondimensionalise equations (6.1) to (6.4). After nondimensionalisation,

$$\frac{\partial \tilde{C}_{M2}}{\partial \tilde{t}} = \frac{\partial}{\partial \tilde{x}}\Big[a_{1,M2} exp\Big(-a_{2,M2}\sqrt{a_3\tilde{C}_{C1} + \frac{a_3 b_4}{b_5}\tilde{C}_{VC\cdot C1}}\Big)\frac{\partial}{\partial \tilde{x}}\Big(\frac{\tilde{C}_{M2}}{1 - a_4\tilde{C}_{C1} - \frac{a_4 b_4}{b_5}\tilde{C}_{VC\cdot C1}}\Big)\Big] + \tilde{C}_{VC}\tilde{C}_{C1} - \tilde{C}_{M2}, \quad (6.13)$$

$$\frac{\partial \tilde{C}_{VC}}{\partial \tilde{t}} = \frac{\partial}{\partial \tilde{x}}\Big[a_{1,VC} exp\Big(-a_{2,VC}\sqrt{a_3\tilde{C}_{C1} + \frac{a_3 b_4}{b_5}\tilde{C}_{VC\cdot C1}}\Big)\frac{\partial}{\partial \tilde{x}}\Big(\frac{\tilde{C}_{VC}}{1 - a_4\tilde{C}_{C1} - \frac{a_4 b_4}{b_5}\tilde{C}_{VC\cdot C1}}\Big)\Big] + \tilde{C}_{C1} - \tilde{C}_{VC} - b_1(\tilde{C}_{VC}\tilde{C}_{C1} - \tilde{C}_{VC\cdot C1}), \quad (6.14)$$

$$\frac{\partial \tilde{C}_{C1}}{\partial \tilde{t}} = b_2 - b_3\tilde{C}_{M2} - b_4(\tilde{C}_{VC}\tilde{C}_{C1} - \tilde{C}_{VC\cdot C1}), \text{ and} \quad (6.15)$$

$$\frac{\partial \tilde{C}_{VC\cdot C1}}{\partial \tilde{t}} = b_5(\tilde{C}_{VC}\tilde{C}_{C1} - \tilde{C}_{VC\cdot C1}). \quad (6.16)$$

The boundary conditions where $\tilde{x} = 0$ and $\tilde{x} = 1$ are given by the equations,

$$\frac{\partial}{\partial \tilde{x}}\Big(\frac{\tilde{C}_{M2}}{1 - a_4\tilde{C}_{C1} - \frac{a_4 b_4}{b_5}\tilde{C}_{VC\cdot C1}}\Big) = 0 \text{ and} \quad (6.17)$$

TABLE 6.2: Dimensionless parameters in the nondimensionalised model of the secondary system. M2 abbreviates MMP2; VC, VEGFC; C1, collagen I.

Parameter	Form	Value
b_1	$k^{on}_{VC,C1}\tau C_{C1,s}$	1.90×10^5
b_2	$\frac{P_{C1}\tau}{C_{C1,s}}$	1.13×10^1
b_3	$\frac{k^{cat}_{M2,C1}\tau P_{M2}}{k^{deg}_{M2} C_{C1,s}}$	2.25×10^1
b_4	$\frac{k^{on}_{VC,C1}\tau P_{VC}}{k^{deg}_{VC}}$	3.56
b_5	$k^{off}_{VC,C1}\tau$	3.60×10^1
$a_{1,M2}$	$\frac{D^{\infty}_{M2}\tau}{L^2}$	4.51
$a_{1,VC}$	$\frac{D^{\infty}_{VC}\tau}{L^2}$	2.66
$a_{2,M2}$	$\frac{k_B T}{6\pi\mu D^{\infty}_{M2} r_f}$	1.07
$a_{2,VC}$	$\frac{k_B T}{6\pi\mu D^{\infty}_{VC} r_f}$	1.81
a_3	$v_{C1} M_{C1} C_{C1,s}$	1.19×10^{-1}
a_4	$v_{C1h} M_{C1} C_{C1,s}$	3.00×10^{-1}

$$\frac{\partial}{\partial \tilde{x}}\left(\frac{\tilde{C}_{VC}}{1 - a_4\tilde{C}_{C1} - \frac{a_4 b_4}{b_5}\tilde{C}_{VC\cdot C1}}\right) = 0. \tag{6.18}$$

There are fewer dimensionless kinetic parameters than dimensional ones because $k^{deg}_{M2}\tau = k^{deg}_{VC}\tau = 1$. The dimensionless parameters are summarised in table 6.2.

6.3 Turing Pattern Analysis

The secondary system, whose mathematical model is provided in appendix F, differs from the classic instance of Turing's mechanism (Gierer and Meinhardt, 1972) in three ways. First, VEGFC and MMP2 do not form a self-activator-self-inhibitor pair as defined by Gierer and Meinhardt (1972). While VEGFC stimulates the production of MMP2, it does not stimulate its own production; MMP2 does not inhibit VEGFC production either, but by degrading collagen I, MMP2 can inhibit the production of both species indirectly. Second, VEGFC binds to collagen I, an immobile substrate, reversibly. Third, the diffusion rates of both VEGFC and MMP2 depend on the concentration of collagen I. In this section, we will find out if the secondary system can generate Turing patterns of VEGFC. Murray (1993) describes the mechanics of this analysis in his book.

6.3.1 Homogeneous Steady State

We will set the derivatives in equations (6.13) to (6.16) to zero. The result is a system of algebraic equations. If the steady state concentration of species i is represented by

$\tilde{C}_{i,ss}$,

$$0 = \tilde{C}_{VC,ss}\tilde{C}_{C1,ss} - \tilde{C}_{M2,ss}, \tag{6.19}$$

$$0 = \tilde{C}_{C1,ss} - \tilde{C}_{VC,ss} - b_1(\tilde{C}_{VC,ss}\tilde{C}_{C1,ss} - \tilde{C}_{VC\cdot C1,ss}), \tag{6.20}$$

$$0 = b_2 - b_3\tilde{C}_{M2,ss} - b_4(\tilde{C}_{VC,ss}\tilde{C}_{C1,ss} - \tilde{C}_{VC\cdot C1,ss}), \text{ and} \tag{6.21}$$

$$0 = \tilde{C}_{VC,ss}\tilde{C}_{C1,ss} - \tilde{C}_{VC\cdot C1,ss}. \tag{6.22}$$

It follows that $\tilde{C}_{M2,ss} = \frac{b_2}{b_3}$, $\tilde{C}_{VC,ss} = \sqrt{\frac{b_2}{b_3}}$, $\tilde{C}_{C1,ss} = \sqrt{\frac{b_2}{b_3}}$, and $\tilde{C}_{VC\cdot C1,ss} = \frac{b_2}{b_3}$. Since b_2 and b_3 are non-negative, the steady state concentrations cannot be negative and non-physical. However, we must impose a couple of constraints. First, as discussed in subsection 6.2.2, $C_{C1,ss} > 1 \times 10^{-1}$ mol m^{-3}. Second, to keep the concentrations within their scales, we stipulate that $b_2 < b_3$.

6.3.2 Homogeneous Perturbation

Turing's mechanism relies on diffusion-driven instability. If the mechanism works for a homogeneous steady state, the latter must be stable in response to small perturbations in time only; when diffusion is present, it must be unstable in response to small spatial perturbations (Murray, 1993). In other words, diffusion picks out a spatial pattern from the perturbations and amplifies it.

After crossing out the diffusion terms in equations (6.13) to (6.16), a system of ODEs remains. A linear stability analysis involves expanding the right hand side of each equation as a Taylor series at the homogeneous steady state. As implied by the name of this analysis, the non-linear terms in the series are ignored. Denoting the perturbation to $\tilde{C}_{i,ss}$ by $\Delta\tilde{C}_i$ such that $\tilde{C}_i = \tilde{C}_{i,ss} + \Delta\tilde{C}_i$,

$$\frac{\partial}{\partial\tilde{t}}\begin{pmatrix}\Delta\tilde{C}_{M2}\\ \Delta\tilde{C}_{VC}\\ \Delta\tilde{C}_{C1}\\ \Delta\tilde{C}_{VC\cdot C1}\end{pmatrix} = \begin{pmatrix}-1 & \tilde{C}_{C1,ss} & \tilde{C}_{VC,ss} & 0\\ 0 & -1-b_1\tilde{C}_{C1,ss} & 1-b_1\tilde{C}_{VC,ss} & b_1\\ -b_3 & -b_4\tilde{C}_{C1,ss} & -b_4\tilde{C}_{VC,ss} & b_4\\ 0 & b_5\tilde{C}_{C1,ss} & b_5\tilde{C}_{VC,ss} & -b_5\end{pmatrix}\begin{pmatrix}\Delta\tilde{C}_{M2}\\ \Delta\tilde{C}_{VC}\\ \Delta\tilde{C}_{C1}\\ \Delta\tilde{C}_{VC\cdot C1}\end{pmatrix}. \tag{6.23}$$

We will denote the Jacobian matrix by A. The solution to equation (6.23) has an exponential form. Each of the four perturbations has the form $ce^{\sigma\tilde{t}}$; c is a constant. Substituting this solution into equation (6.23) and rearranging, we find that

$$\begin{pmatrix} -1-\sigma & \tilde{C}_{C1,ss} & \tilde{C}_{VC,ss} & 0 \\ 0 & -1-b_1\tilde{C}_{C1,ss}-\sigma & 1-b_1\tilde{C}_{VC,ss} & b_1 \\ -b_3 & -b_4\tilde{C}_{C1,ss} & -b_4\tilde{C}_{VC,ss}-\sigma & b_4 \\ 0 & b_5\tilde{C}_{C1,ss} & b_5\tilde{C}_{VC,ss} & -b_5-\sigma \end{pmatrix} \begin{pmatrix} \Delta\tilde{C}_{M2} \\ \Delta\tilde{C}_{VC} \\ \Delta\tilde{C}_{C1} \\ \Delta\tilde{C}_{VC\cdot C1} \end{pmatrix} = 0. \quad (6.24)$$

In order to get a non-trivial solution, we need that $\left|A-\sigma I\right| = 0$; σ is the eigenvalue of A. Since this relation is a quartic equation, there are four solutions of σ. If they all have negative real parts, the perturbations decay with time, meaning the secondary system is stable with respect to them. From this linear stability analysis, we obtain the third constraint on the Turing space: the eigenvalues of A must have negative real parts.

6.3.3 Heterogeneous Perturbation

Next, we need to bring diffusion back to the system. We need to linearise the diffusion terms in equations (6.13) and (6.14). The two terms have the form $\frac{\partial}{\partial\tilde{x}}\left[a_{1,i}exp\Big(-a_{2,i}\sqrt{a_3\tilde{C}_{C1}+\frac{a_3b_4}{b_5}\tilde{C}_{VC\cdot C1}}\Big)\frac{\partial}{\partial\tilde{x}}\Big(\frac{\tilde{C}_i}{1-a_4\tilde{C}_{C1}-\frac{a_4b_4}{b_5}\tilde{C}_{VC\cdot C1}}\Big)\right]$. Expanding in two Taylor series at the homogeneous steady state, we find that

$$\begin{aligned} a_{1,i}exp\Big(-a_{2,i}\sqrt{a_3\tilde{C}_{C1}+\frac{a_3b_4}{b_5}\tilde{C}_{VC\cdot C1}}\Big) &\approx a_{1,i}exp\Big(-a_{2,i}\sqrt{a_3\tilde{C}_{C1,ss}+\frac{a_3b_4}{b_5}\tilde{C}_{VC\cdot C1,ss}}\Big) \\ &+ a_{1,i}exp\Big(-a_{2,i}\sqrt{a_3\tilde{C}_{C1,ss}+\frac{a_3b_4}{b_5}\tilde{C}_{VC\cdot C1,ss}}\Big)\Big[\frac{-a_{2,i}a_3}{2\sqrt{a_3\tilde{C}_{C1,ss}+\frac{a_3b_4}{b_5}\tilde{C}_{VC\cdot C1,ss}}}\Big]\Delta\tilde{C}_{C1} \\ &+ a_{1,i}exp\Big(-a_{2,i}\sqrt{a_3\tilde{C}_{C1,ss}+\frac{a_3b_4}{b_5}\tilde{C}_{VC\cdot C1,ss}}\Big)\Big[\frac{-a_{2,i}a_3b_4}{2b_5\sqrt{a_3\tilde{C}_{C1,ss}+\frac{a_3b_4}{b_5}\tilde{C}_{VC\cdot C1,ss}}}\Big]\Delta\tilde{C}_{VC\cdot C1} \end{aligned}$$

and (6.25)

$$\begin{aligned} \frac{\tilde{C}_i}{1-a_4\tilde{C}_{C1}-\frac{a_4b_4}{b_5}\tilde{C}_{VC\cdot C1}} &\approx \frac{\tilde{C}_{i,ss}}{1-a_4\tilde{C}_{C1,ss}-\frac{a_4b_4}{b_5}\tilde{C}_{VC\cdot C1,ss}}+\frac{\Delta\tilde{C}_i}{1-a_4\tilde{C}_{C1,ss}-\frac{a_4b_4}{b_5}\tilde{C}_{VC\cdot C1,ss}} \\ &+\frac{\tilde{C}_{i,ss}a_4\Delta\tilde{C}_{C1}}{(1-a_4\tilde{C}_{C1,ss}-\frac{a_4b_4}{b_5}\tilde{C}_{VC\cdot C1,ss})^2}+\frac{\tilde{C}_{i,ss}a_4b_4\Delta\tilde{C}_{VC\cdot C1}}{b_5(1-a_4\tilde{C}_{C1,ss}-\frac{a_4b_4}{b_5}\tilde{C}_{VC\cdot C1,ss})^2}. \quad (6.26) \end{aligned}$$

We will substitute equations (6.25) and (6.26) into the general diffusion term. After ignoring the non-linear terms,

$$\begin{aligned}
&\frac{\partial}{\partial\tilde{x}}\Big[a_{1,i}exp\Big(-a_{2,i}\sqrt{a_3\tilde{C}_{C1}+\frac{a_3b_4}{b_5}\tilde{C}_{VC\cdot C1}}\Big)\frac{\partial}{\partial\tilde{x}}\Big(\frac{\tilde{C}_i}{1-a_4\tilde{C}_{C1}-\frac{a_4b_4}{b_5}\tilde{C}_{VC\cdot C1}}\Big)\Big] \\
&\qquad\approx \frac{a_{1,i}exp\Big(-a_{2,i}\sqrt{a_3\tilde{C}_{C1,ss}+\frac{a_3b_4}{b_5}\tilde{C}_{VC\cdot C1,ss}}\Big)}{1-a_4\tilde{C}_{C1,ss}-\frac{a_4b_4}{b_5}\tilde{C}_{VC\cdot C1,ss}}\frac{\partial^2\Delta\tilde{C}_i}{\partial\tilde{x}^2} \\
&\qquad+\frac{a_{1,i}exp\Big(-a_{2,i}\sqrt{a_3\tilde{C}_{C1,ss}+\frac{a_3b_4}{b_5}\tilde{C}_{VC\cdot C1,ss}}\Big)a_4\tilde{C}_{i,ss}}{(1-a_4\tilde{C}_{C1,ss}-\frac{a_4b_4}{b_5}\tilde{C}_{VC\cdot C1,ss})^2}\frac{\partial^2\Delta\tilde{C}_{C1}}{\partial\tilde{x}^2} \\
&\qquad+\frac{a_{1,i}exp\Big(-a_{2,i}\sqrt{a_3\tilde{C}_{C1,ss}+\frac{a_3b_4}{b_5}\tilde{C}_{VC\cdot C1,ss}}\Big)a_4b_4\tilde{C}_{i,ss}}{(1-a_4\tilde{C}_{C1,ss}-\frac{a_4b_4}{b_5}\tilde{C}_{VC\cdot C1,ss})^2b_5}\frac{\partial^2\Delta\tilde{C}_{VC\cdot C1}}{\partial\tilde{x}^2}. \qquad (6.27)
\end{aligned}$$

We can simplify by defining that

$$d_{1,i}=\frac{a_{1,i}exp\Big(-a_{2,i}\sqrt{a_3\tilde{C}_{C1,ss}+\frac{a_3b_4}{b_5}\tilde{C}_{VC\cdot C1,ss}}\Big)}{1-a_4\tilde{C}_{C1,ss}-\frac{a_4b_4}{b_5}\tilde{C}_{VC\cdot C1,ss}}, \qquad (6.28)$$

$$d_{2,i}=\frac{a_{1,i}exp\Big(-a_{2,i}\sqrt{a_3\tilde{C}_{C1,ss}+\frac{a_3b_4}{b_5}\tilde{C}_{VC\cdot C1,ss}}\Big)a_4\tilde{C}_{i,ss}}{(1-a_4\tilde{C}_{C1,ss}-\frac{a_4b_4}{b_5}\tilde{C}_{VC\cdot C1,ss})^2}, \text{ and} \qquad (6.29)$$

$$d_{3,i}=\frac{a_{1,i}exp\Big(-a_{2,i}\sqrt{a_3\tilde{C}_{C1,ss}+\frac{a_3b_4}{b_5}\tilde{C}_{VC\cdot C1,ss}}\Big)a_4b_4\tilde{C}_{i,ss}}{(1-a_4\tilde{C}_{C1,ss}-\frac{a_4b_4}{b_5}\tilde{C}_{VC\cdot C1,ss})^2b_5}. \qquad (6.30)$$

Addition of the linearised diffusion terms to the right hand side of equation (6.23) gives us the linearised secondary system. In matrix form,

$$\begin{aligned}
\frac{\partial}{\partial\tilde{t}}\begin{pmatrix}\Delta\tilde{C}_{M2}\\ \Delta\tilde{C}_{VC}\\ \Delta\tilde{C}_{C1}\\ \Delta\tilde{C}_{VC\cdot C1}\end{pmatrix}&=\begin{pmatrix}d_{1,M2}&0&d_{2,M2}&d_{3,M2}\\ 0&d_{1,VC}&d_{2,VC}&d_{3,VC}\\ 0&0&0&0\\ 0&0&0&0\end{pmatrix}\begin{pmatrix}\frac{\partial^2\Delta\tilde{C}_{M2}}{\partial\tilde{x}^2}\\ \frac{\partial^2\Delta\tilde{C}_{VC}}{\partial\tilde{x}^2}\\ \frac{\partial^2\Delta\tilde{C}_{C1}}{\partial\tilde{x}^2}\\ \frac{\partial^2\Delta\tilde{C}_{VC\cdot C1}}{\partial\tilde{x}^2}\end{pmatrix} \\
&+\begin{pmatrix}-1&\tilde{C}_{C1,ss}&\tilde{C}_{VC,ss}&0\\ 0&-1-b_1\tilde{C}_{C1,ss}&1-b_1\tilde{C}_{VC,ss}&b_1\\ -b_3&-b_4\tilde{C}_{C1,ss}&-b_4\tilde{C}_{VC,ss}&b_4\\ 0&b_5\tilde{C}_{C1,ss}&b_5\tilde{C}_{VC,ss}&-b_5\end{pmatrix}\begin{pmatrix}\Delta\tilde{C}_{M2}\\ \Delta\tilde{C}_{VC}\\ \Delta\tilde{C}_{C1}\\ \Delta\tilde{C}_{VC\cdot C1}\end{pmatrix}. \qquad (6.31)
\end{aligned}$$

The spatial eigenvalue problem associated with equation (6.31) has a Fourier series as its solution: $\sum_{n\in\mathbb{Z}} \left[\boldsymbol{c}_n^c cos(n\pi\tilde{x}) + \boldsymbol{c}_n^s sin(n\pi\tilde{x})\right]$; $\boldsymbol{c}_n^c$'s and $\boldsymbol{c}_n^s$'s are constant vectors. However, this solution must satisfy the linearised boundary conditions: equations (6.17) and (6.18) after linearisation. At the homogeneous steady state, $\left|a_4\tilde{C}_{C1} + \frac{a_4 b_4}{b_5}\tilde{C}_{VC\cdot C1}\right| < 1$, so $\tilde{C}_{M2}(1 - a_4\tilde{C}_{C1} - \frac{a_4 b_4}{b_5}\tilde{C}_{VC\cdot C1})^{-1} \approx \tilde{C}_{M2}(1 + a_4\tilde{C}_{C1} + \frac{a_4 b_4}{b_5}\tilde{C}_{VC\cdot C1} + \dots)$ in equation (6.17). Keeping the linear term only, $\frac{\partial \tilde{C}_{M2}}{\partial \tilde{x}} = 0$ where $\tilde{x} = 0$ and $\tilde{x} = 1$. Similarly, $\frac{\partial \tilde{C}_{VC}}{\partial \tilde{x}} = 0$ where $\tilde{x} = 0$ and $\tilde{x} = 1$. Only the cosine terms in the Fourier series satisfy these boundary conditions, so the solution is $\sum_{n\in\mathbb{Z}} \boldsymbol{c}_n^c cos(n\pi\tilde{x})$.

The solution to equation (6.31), a vector containing the four $\Delta\tilde{C}_i$'s, is the product of the Fourier cosine series and an exponential term: $\sum_{n\in\mathbb{Z}} e^{\sigma\tilde{t}}\boldsymbol{c}_n^c cos(n\pi\tilde{x})$; σ is a variable. We will abbreviate this solution to $\sum_{n\in\mathbb{Z}} e^{\sigma\tilde{t}}\boldsymbol{w}_n$, where $\boldsymbol{w}_n = \boldsymbol{c}_n^c cos(n\pi\tilde{x})$. Each $\boldsymbol{w}_n$ is a Fourier mode at the wavenumber k, which is $n\pi$. After substituting the solution into equation (6.31),

$$(B - \sigma I)\boldsymbol{w}_n = 0 \text{ and} \tag{6.32}$$

$$B = \begin{pmatrix} -1 - k^2 d_{1,M2} & \tilde{C}_{C1,ss} & \tilde{C}_{VC,ss} - k^2 d_{2,M2} & -k^2 d_{3,M2} \\ 0 & -1 - b_1\tilde{C}_{C1,ss} - k^2 d_{1,VC} & 1 - b_1\tilde{C}_{VC,ss} - k^2 d_{2,VC} & b_1 - k^2 d_{3,VC} \\ -b_3 & -b_4\tilde{C}_{C1,ss} & -b_4\tilde{C}_{VC,ss} & b_4 \\ 0 & b_5\tilde{C}_{C1,ss} & b_5\tilde{C}_{VC,ss} & -b_5 \end{pmatrix}. \tag{6.33}$$

Equation (6.32) holds for each value of n and hence k. In order to get a non-trivial solution, we need that $\left|B - \sigma I\right| = 0$. This relation is a quartic equation of σ in k^2; the four solutions of σ are the eigenvalues of B. At a k value, if at least one of them has a positive real part, that Fourier mode grows with time, meaning it is an unstable noise component for the homogeneous steady state. Since the eigenvalues vary with n^2 or k^2, we do not need to consider the negative n or k values. From this linear stability analysis, we obtain the fourth constraint on the Turing space: at least one eigenvalue of B must have a positive real part at at least one k value.

6.3.4 Dispersion Relation

At each point in the parametric space, the eigenvalues of B vary with the wavenumber, k. At each value of k, there are four eigenvalues, one of whose real parts is larger than or equal to the other three. The relation between this real part, $Re(\sigma_{max})$, and k^2 is the dispersion relation for that point in the parametric space.

If Turing's mechanism works at that point, the dispersion relation there must have a maximum. The Fourier mode corresponding to this maximum grows faster than the other noise components, leading to a periodic pattern with a wavelength of $\frac{2\pi}{k}$. The nondimensionalised length of our domain is 1, so a visible pattern must have a smaller wavelength. On the other hand, the nondimensionalised LEC diameter is 0.023, so a pattern with a smaller wavelength cannot be resolved by an LEC. Placing the fifth constraint on the Turing space, we stipulate that the maximum of a dispersion relation must be in the relevant range of Fourier modes ($0.023 < \frac{2\pi}{k} < 1$ or $2 < n < 87$).

We want to have a finite number of unstable Fourier modes only. If the third constraint is satisfied, the dispersion relation must be negative when $n = 0$. If the fourth and fifth constraints are satisfied too, the dispersion relation must cross the x-axis on the left hand side of its maximum, which lies in the relevant range. Therefore, we place the sixth constraint on the Turing space: a dispersion relation must cross the x-axis to the right of its maximum.

6.3.5 Turing Space: Parametric Distributions

The secondary system, defined by equations (6.13) to (6.16), is analytically intractable. We will study a finite number of parametric points.

Table 6.2 defines the reference point in the parametric space: these parameters are literature-based estimates. The kinetic parameters, b_i's, can be changed independently of each other. On the other hand, the first four transport parameters, $a_{1,j}$'s and $a_{2,j}$'s, depend on three dimensional parameters, D^{∞}_{M2}, D^{∞}_{VC}, and μ, only. The last two transport parameters, a_3 and a_4, are fixed.

Starting at the reference point, we will vary each of b_1, b_2, b_3, b_4, b_5, D^{∞}_{M2}, D^{∞}_{VC}, and μ by two orders of magnitude in each direction. For example, we will consider b_1 at 1.90×10^3, 1.90×10^4, 1.90×10^5 (reference point), 1.90×10^6, and 1.90×10^7. The variation choices are random because we simply want to generate a sample of parametric combinations centred around the reference point.

In total, there are 5^9 or 1953125 combinations of parameters. We will call each combination a Turing point candidate. To qualify as a Turing point, a point in the Turing space, a candidate must satisfy the constraints established in this section. There are six of them.

1. $C_{C1} + C_{VC\cdot C1} > 1 \times 10^{-1}$ mol m^{-3}. This inequality ensures that there is sufficient collagen I to justify our model assumptions. For example, the secondary system must be diffusion-dominant.
2. $b_2 < b_3$. This inequality ensures that the steady state concentrations are within their scales.

3. The eigenvalues of A must have negative real parts. A is the Jacobian matrix of the secondary system's reaction terms. This constraint ensures that the system is stable in response to homogeneous perturbations.

4. At least one of the eigenvalues of B must have a positive real part at at least one k value. B is A plus the linearised diffusion terms of the secondary system. This constraint ensures that the system is unstable in response to heterogeneous perturbations.

5. Its dispersion relation is at its maximum in the relevant range of wavenumbers ($2 < n < 87$). The existence of a maximum means the associated Fourier mode grows faster than the other noise components. Its existence in this range means its wavelength is smaller than the domain size but larger than the LEC diameter.

6. The dispersion relation must turn negative after reaching the maximum. This property means only a finite number of Fourier modes can grow from the noises in the secondary system.

We will use a Python program, provided in appendix G, to identify the Turing space. Because the model is analytically intractable, our program can assess a finite number of k^2 values only (n from 0 to 87). It will therefore miss several cases. First, the dispersion relation may stay negative in the assessed range and turn positive beyond it. Second, even if the dispersion relation is positive in parts of the assessed range, its maximum may lie beyond the range. Third, the dispersion relation may drop from its maximum to a negative value and then cross the x-axis again. Fourth, the dispersion relation may decrease from its maximum and only cross the x-axis beyond the assessed range. Fifth, the dispersion relation may have two or more identical maxima, which may lie outside the assessed range. We are not interested in the Fourier modes beyond the assessed range anyway, so the first and fourth cases do not concern us. Without considering all the Fourier modes, we cannot eliminate the second, third, and fifth cases. We must bear these possibilities in mind when we analyse our results. If we encounter the second case, the predicted wavelength of our Turing pattern will be wrong. If we encounter the third case, we may have an infinite number of unstable Fourier modes. If we encounter the fifth case, we cannot predict the wavelength. Furthermore, since our program considers the first maximum (smallest n) only, the dispersion relation may stay positive after the last maximum (largest n), thus leading to an infinite number of unstable Fourier modes.

The first three constraints depend on the kinetic parameters, b_i's, only. There are 5^5 or 3125 combinations of kinetic parameters in total. Only 537 of them satisfy the first three constraints, so there are only 537×5^3 or 67125 Turing point candidates left. Only 52174 of them satisfy the fourth constraint by being unstable with respect to heterogeneous perturbations. Among them, 94 satisfy the fifth and sixth constraints,

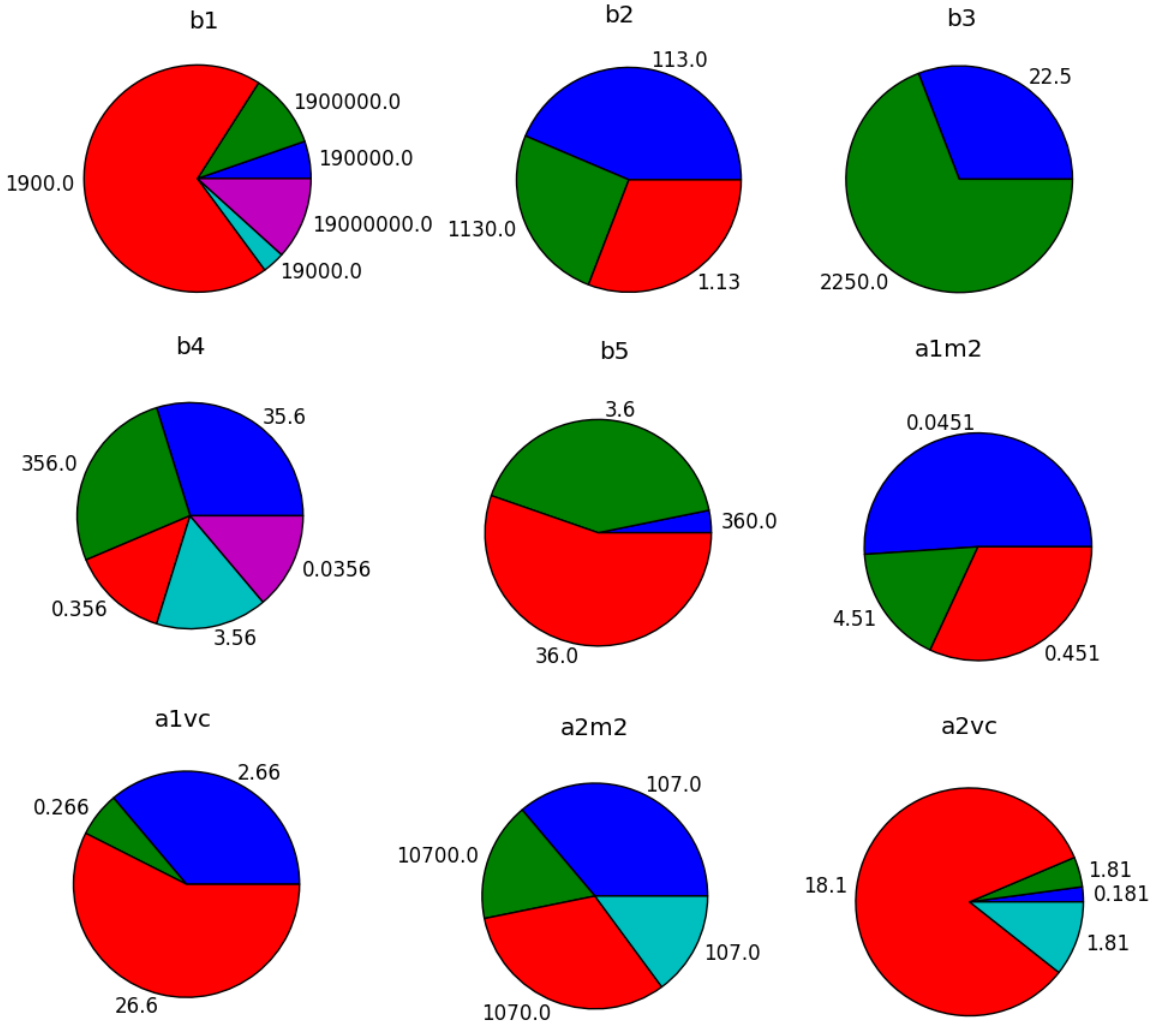

FIGURE 6.1: Distributions of parameters in the secondary system's Turing space. The parameters are defined as follows: $b_1 = k^{on}_{VC,C1}\tau C_{C1,s}$, $b_2 = \frac{P_{C1}\tau}{C_{C1,s}}$, $b_3 = \frac{k^{cat}_{M2,C1}\tau P_{M2}}{k^{deg}_{M2}C_{C1,s}}$, $b_4 = \frac{k^{on}_{VC,C1}\tau P_{VC}}{k^{deg}_{VC}}$, $b_5 = k^{off}_{VC,C1}\tau$, $a_{1,M2} = \frac{D^{\infty}_{M2}\tau}{L^2}$, $a_{1,VC} = \frac{D^{\infty}_{VC}\tau}{L^2}$, $a_{2,M2} = \frac{k_BT}{6\pi\mu D^{\infty}_{M2}r_f}$, and $a_{2,VC} = \frac{k_BT}{6\pi\mu D^{\infty}_{VC}r_f}$.

while 32 satisfy the fifth constraint only. These 94 parametric combinations form a sample of the Turing space.

We will study how the parameters are distributed in this sample of 94 Turing points; these distributions are shown in figure 6.1. The b_1 distribution is heavily biased towards the lower end, suggesting a smaller-than-estimated $k^{on}_{VC,C1}$ favours Turing's mechanism. Although the b_2 distribution contains the reference value, as well as smaller and larger values, it is biased towards the largest two; it suggests a larger-than-estimated P_{C1} favours Turing's mechanism. The b_3 distribution contains the reference value and the largest value; the latter is significantly more common, suggesting a higher-than-estimated $k^{cat}_{M2,C1}$ or P_{M2} is favourable. The b_4 distribution contains all five values and is roughly even. Although b_4 is controlled by both $k^{on}_{VC,C1}$

and P_{VC}, the b_1 distribution suggests that a smaller-than-estimated $k^{on}_{VC,C1}$ favours Turing's mechanism. Therefore, we conclude that the mechanism is not sensitive to P_{VC}. The b_5 distribution is dominated by the reference value, although it also contains the two adjacent values; we conclude that the estimated $k^{off}_{VC,C1}$ is favourable for Turing's mechanism.

There is some information which cannot be inferred from figure 6.1. First, the four transport parameters are not independent, so we cannot understand them by studying their independent distributions. Second, figure 6.1 tells us nothing about the correlations among the kinetic parameters. For example, when a Turing point has a b_1 value of 1900, b_3 may always be 22.5. Third, we are still ignorant of how the form of a dispersion relation depends on its parameters. Fourth, figure 6.1 is about a finite number of Turing points, so our comments in the last paragraph are just inklings about the Turing space, not definitive conclusions.

6.3.6 Turing Space: Dispersion Relations

The 94 Turing points lie at different distances from the reference point. Considering the reference point has its basis in the literature, the Turing points closest to it deserve special attention. We will define S as the distance between a Turing point and the reference point. Labelling the parametric values at the reference point by a^{ref}'s and b^{ref}'s, we can calculate S using the equation

$$\begin{aligned} S^2 = &\left(\frac{b_1 - b_1^{ref}}{b_1^{ref}}\right)^2 + \left(\frac{b_2 - b_2^{ref}}{b_2^{ref}}\right)^2 + \left(\frac{b_3 - b_3^{ref}}{b_3^{ref}}\right)^2 + \left(\frac{b_4 - b_4^{ref}}{b_4^{ref}}\right)^2 \\ &+ \left(\frac{b_5 - b_5^{ref}}{b_5^{ref}}\right)^2 + \left(\frac{a_{1,M2} - a_{1,M2}^{ref}}{a_{1,M2}^{ref}}\right)^2 + \left(\frac{a_{1,VC} - a_{1,VC}^{ref}}{a_{1,VC}^{ref}}\right)^2 \\ &+ \left(\frac{a_{2,M2} - a_{2,M2}^{ref}}{a_{2,M2}^{ref}}\right)^2 + \left(\frac{a_{2,VC} - a_{2,VC}^{ref}}{a_{2,VC}^{ref}}\right)^2. \end{aligned} \tag{6.34}$$

We will calculate S for each Turing point and select the ten points with the smallest S values. The ranking algorithm, implemented in Python, is in appendix G. The results are tabulated in table 6.3. In each case, VEGFC diffuses faster than MMP2.

We will compare three pairs of dispersion relations from table 6.3: 2 and 3, 4 and 9, and 6 and 8. In each pair, the kinetic parameters, b_i's, are the same for both points. Examining $a_{1,M2}$ and $a_{1,VC}$, we notice that they scale with D^{∞}_{M2} and D^{∞}_{VC} respectively; $a_{2,M2}$ and $a_{2,VC}$ scale inversely with μD^{∞}_{M2} and μD^{∞}_{VC} respectively. In short, μ appears in the volume exclusion terms only; the direct effects of viscosity on diffusion are not modelled. Assuming D_i^{∞} is inversely proportional to μ, $a_{2,j}$'s are

TABLE 6.3: The ten Turing points closest to the reference point in the secondary system's parametric space. The parameters are defined as follows: $b_1 = k^{on}_{VC,C1}\tau C_{C1,s}$, $b_2 = \frac{P_{C1}\tau}{C_{C1,s}}$, $b_3 = \frac{k^{cat}_{M2,C1}\tau P_{M2}}{k^{deg}_{M2}C_{C1,s}}$, $b_4 = \frac{k^{on}_{VC,C1}\tau P_{VC}}{k^{deg}_{VC}}$, $b_5 = k^{off}_{VC,C1}\tau$, $a_{1,M2} = \frac{D^{\infty}_{M2}\tau}{L^2}$, $a_{1,VC} = \frac{D^{\infty}_{VC}\tau}{L^2}$, $a_{2,M2} = \frac{k_BT}{6\pi\mu D^{\infty}_{M2}r_f}$, and $a_{2,VC} = \frac{k_BT}{6\pi\mu D^{\infty}_{VC}r_f}$. S is the distance between a Turing point and the reference point. The last column gives the wavelength of the fastest growing Fourier mode for each Turing point.

b_1	b_2	b_3	b_4	b_5	$a_{1,M2}$	$a_{1,VC}$	$a_{2,M2}$	$a_{2,VC}$	S	Wavelength
1.9×10^6	1.13	22.5	35.6	3.6	0.0451	2.66	107	1.81	99.8279	0.400
1.9×10^6	1.13	22.5	35.6	3.6	0.451	2.66	107	18.1	100.2319	0.038
1.9×10^6	1.13	22.5	35.6	3.6	4.51	26.6	107	18.1	100.6311	0.125
1.9×10^5	1.13	22.5	356	36	0.451	2.66	107	18.1	140.3019	0.111
1.9×10^6	1.13	22.5	356	36	0.0451	2.66	107	1.81	140.3025	0.400
1.9×10^4	1.13	22.5	356	36	0.451	2.66	107	18.1	140.3048	0.400
1.9×10^7	1.13	22.5	35.6	3.6	0.0451	2.66	107	1.81	140.3054	0.133
1.9×10^4	1.13	22.5	356	36	0.0451	0.266	107	18.1	140.3083	0.125
1.9×10^5	1.13	22.5	356	36	4.51	26.6	107	18.1	140.5874	0.333
1.9×10^3	113	2250	3.56	36	0.451	2.66	107	18.1	140.5909	0.250

invariant under a change in μ, while $a_{1,j}$'s change by the same factor as but inversely to μ. Effectively, only μ changes in each selected pair. The comparison plots are shown in figure 6.2. In each case, a decrease in μ or equivalently an increase in D^{∞}_{M2} and D^{∞}_{VC} gives a more 'compressed' dispersion relation. Physically, when MMP2 and VEGFC diffuse faster, fewer noise components are unstable and the unstable components have longer wavelengths. This is favourable for Turing's mechanism because when fewer noise components are unstable, the resulting pattern is more regular.

The dispersion relations of the remaining Turing points from table 6.3 are given in figure 6.3.

The dispersion relations, calculated using the Python program in appendix G, contain round-off errors. In a flat dispersion relation like figure 6.3(a), the smallness of the eigenvalues means they are highly sensitive to these errors; the predicted dominant wavenumber may be inaccurate. By contrast, the dispersion relation in figure 6.3(d) has the sharpest peak in figures 6.2 and 6.3. In the next subsection, we will consider this parametric point (last point in table 6.3) further.

6.3.7 Turing Space: Bifurcation

In subsection 6.2.2, we commented that the values of P_{M2} and P_{VC} are uncertain. P_{M2} and P_{VC} control b_3 and b_4 respectively. Therefore, b_3 and b_4 are our bifurcation parameters. When a system bifurcates, its qualitative behaviour changes because of changes to its parameter values. As discussed in the last subsection, the dispersion relation at the last Turing point in table 6.3 is robust, so we will perturb b_3 and b_4 independently from this point. The Python programs used are in appendix G.

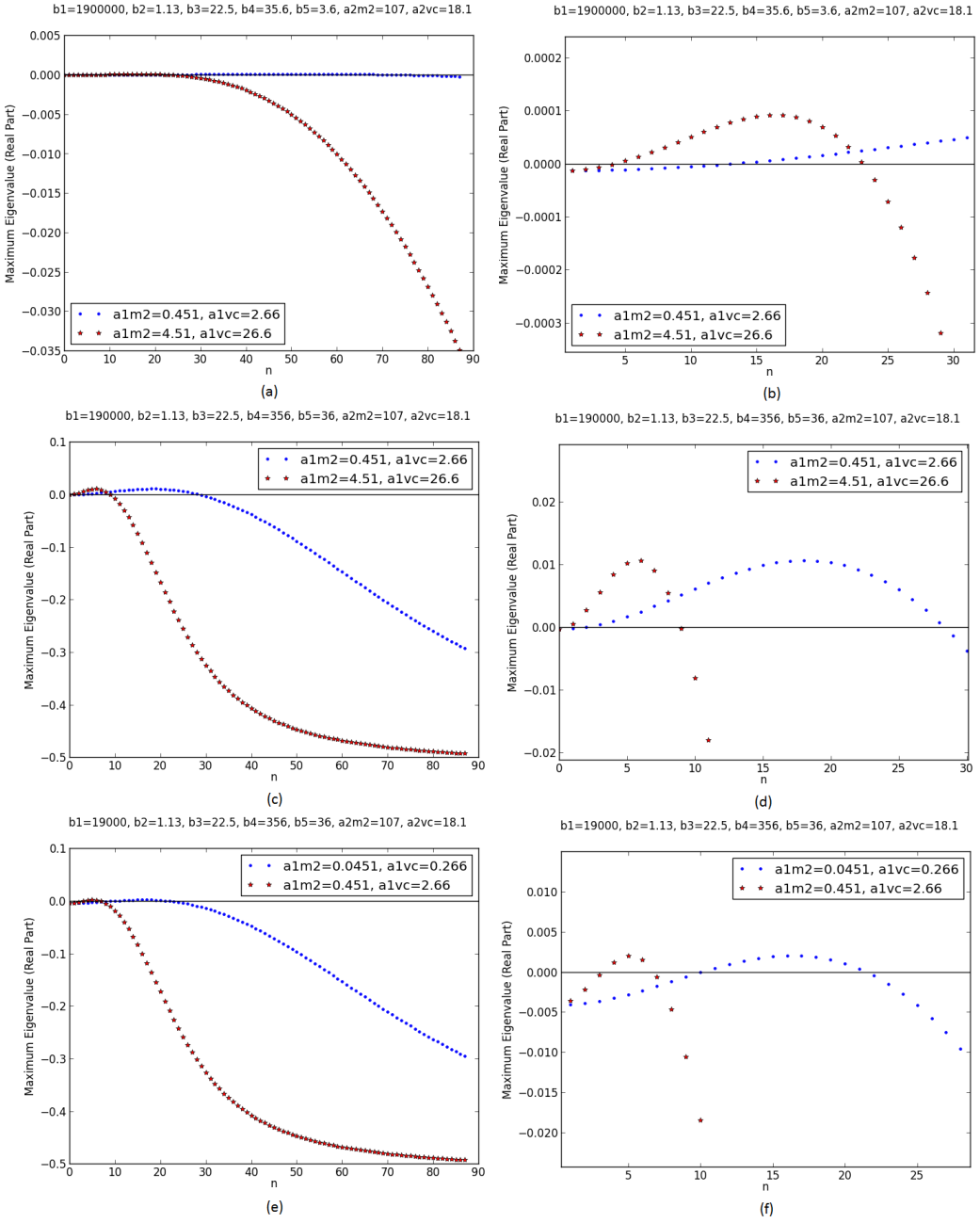

FIGURE 6.2: Comparison plots of the dispersion relations at selected Turing points. They are selected from the ten Turing points closest to the secondary system's reference point. In each pair, the kinetic parameters are the same, but μ changes and leads to differences in the transport parameters. The plots on the right are parts of their counterparts on the left. On the x-axes, n is the integer in the wavenumber ($k = n\pi$). For (a) and (b), $b_1 = 1.9 \times 10^6$, $b_2 = 1.13$, $b_3 = 22.5$, $b_4 = 35.6$, $b_5 = 3.6$, $a_{2,M2} = 107$, and $a_{2,VC} = 18.1$; for the blue trend, $a_{1,M2} = 0.451$ and $a_{1,VC} = 2.66$; for the red trend, $a_{1,M2} = 4.51$ and $a_{1,VC} = 26.6$. For (c) and (d), $b_1 = 1.9 \times 10^5$, $b_2 = 1.13$, $b_3 = 22.5$, $b_4 = 356$, $b_5 = 36$, $a_{2,M2} = 107$, and $a_{2,VC} = 18.1$; for the blue trend, $a_{1,M2} = 0.451$ and $a_{1,VC} = 2.66$; for the red trend, $a_{1,M2} = 4.51$ and $a_{1,VC} = 26.6$. For (e) and (f), $b_1 = 1.9 \times 10^4$, $b_2 = 1.13$, $b_3 = 22.5$, $b_4 = 356$, $b_5 = 36$, $a_{2,M2} = 107$, and $a_{2,VC} = 18.1$; for the blue trend, $a_{1,M2} = 0.0451$ and $a_{1,VC} = 0.266$; for the red trend, $a_{1,M2} = 0.451$ and $a_{1,VC} = 2.66$. Larger versions of these plots are provided in appendix H.

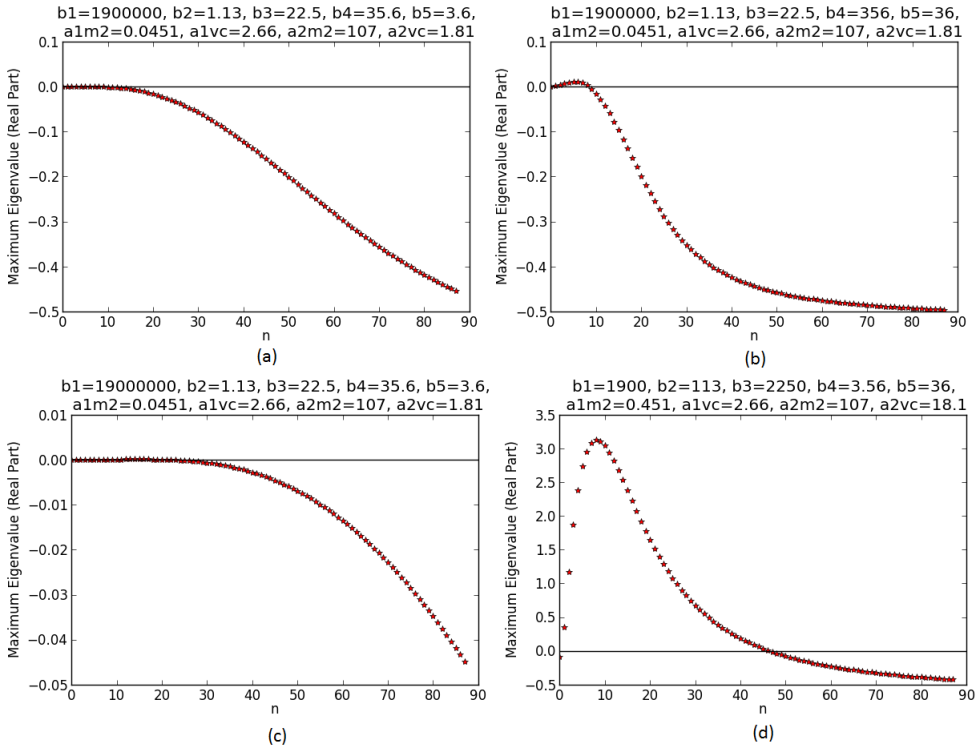

FIGURE 6.3: Dispersion relations at selected Turing points. They are selected from the ten Turing points closest to the secondary system's reference point. On the x-axes, n is the integer in the wavenumber ($k = n\pi$). For (a), $b_1 = 1.9 \times 10^6$, $b_2 = 1.13$, $b_3 = 22.5$, $b_4 = 35.6$, $b_5 = 3.6$, $a_{1,M2} = 0.0451$, $a_{1,VC} = 2.66$, $a_{2,M2} = 107$, and $a_{2,VC} = 1.81$. For (b), $b_1 = 1.9 \times 10^6$, $b_2 = 1.13$, $b_3 = 22.5$, $b_4 = 356$, $b_5 = 36$, $a_{1,M2} = 0.0451$, $a_{1,VC} = 2.66$, $a_{2,M2} = 107$, and $a_{2,VC} = 1.81$. For (c), $b_1 = 1.9 \times 10^7$, $b_2 = 1.13$, $b_3 = 22.5$, $b_4 = 35.6$, $b_5 = 3.6$, $a_{1,M2} = 0.0451$, $a_{1,VC} = 2.66$, $a_{2,M2} = 107$, and $a_{2,VC} = 1.81$. For (d), $b_1 = 1.9 \times 10^3$, $b_2 = 113$, $b_3 = 2250$, $b_4 = 3.56$, $b_5 = 36$, $a_{1,M2} = 0.451$, $a_{1,VC} = 2.66$, $a_{2,M2} = 107$, and $a_{2,VC} = 18.1$. Larger versions of these plots are provided in appendix H.

Figure 6.4(a) shows the dispersion relations in a wide range of b_3 values. Table 6.4 summarises how well they fit within the constraints from subsection 6.3.5. The trends are not consistent, so we can only conclude that b_3 is a very sensitive parameter. It should be noted that $b_3 = \frac{k^{cat}_{M2,C1} \tau P_{M2}}{k^{deg}_{M2} C_{C1,s}}$. Both $k^{cat}_{M2,C1}$ and P_{M2} parametrise the MMP2-catalysed degradation of collagen I, providing a possible explanation for this sensitivity: a change in b_3 affects both MMP2 production and action.

Among the five cases shown in figure 6.4(a), only the case with the largest b_3 gives a Turing point. Therefore, we will limit our analysis to a smaller region around it. Figure 6.4(b) and table 6.5 summarise the results. An increase in b_3 decreases the eigenvalue when the wavenumber is zero. At the largest b_3, it is negative, satisfying the stability requirement with respect to homogeneous perturbations. An increase in b_3 also leads to a sharper peak at a smaller wavenumber and a smaller region of positive eigenvalues.

In summary, b_3 or P_{M2} seems to be a sensitive parameter. When it increases, the secondary system stabilises with respect to homogeneous perturbations. There are

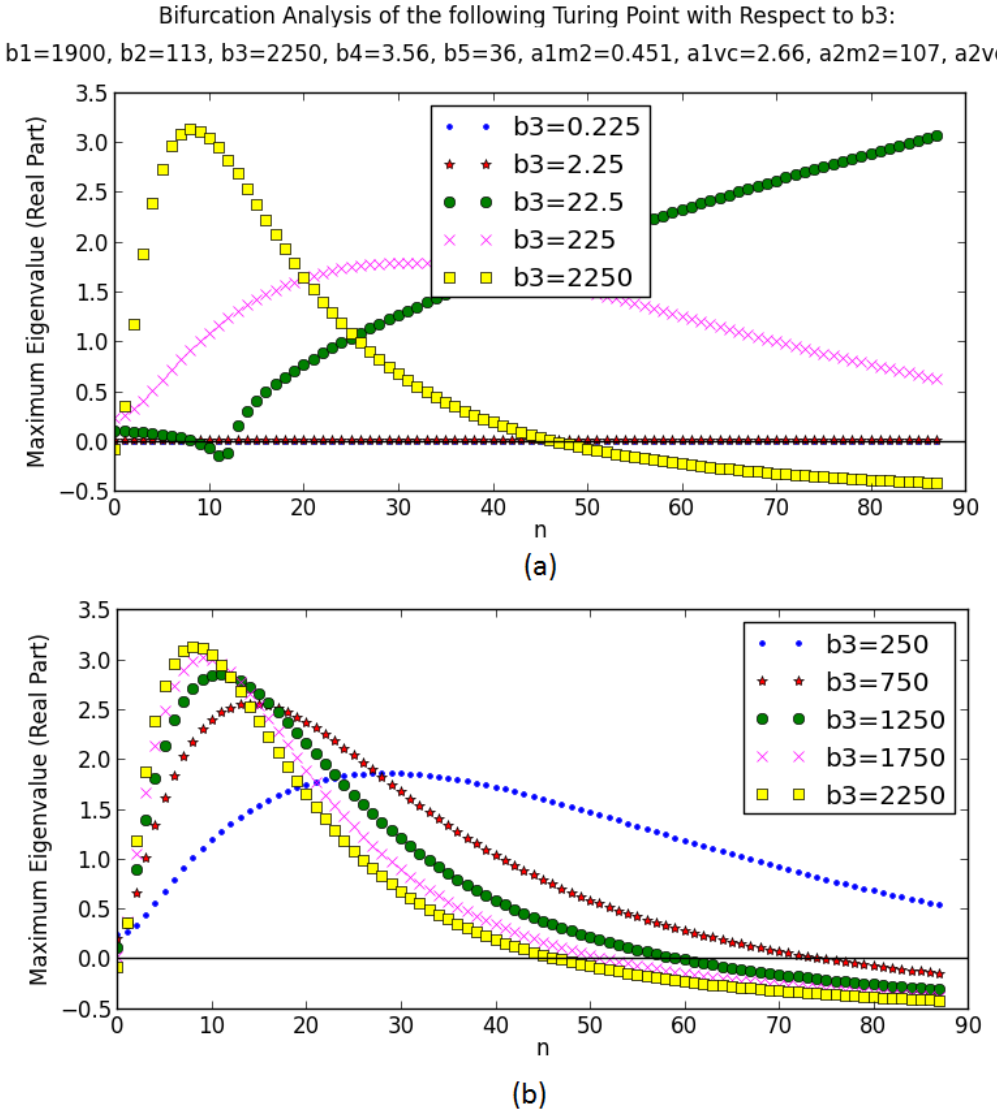

FIGURE 6.4: Bifurcation analysis of a selected Turing point with respect to b_3. It is selected from the ten Turing points closest to the secondary system's reference point. At this Turing point, $b_1 = 1.9 \times 10^3$, $b_2 = 113$, $b_3 = \frac{k^{cat}_{M2,C1} \tau P_{M2}}{k^{deg}_{M2} C_{C1,s}} = 2250$, $b_4 = 3.56$, $b_5 = 36$, $a_{1,M2} = 0.451$, $a_{1,VC} = 2.66$, $a_{2,M2} = 107$, and $a_{2,VC} = 18.1$. On the x-axes, n is the integer in the wavenumber ($k = n\pi$). (a) considers a wider range of b_3 than (b).

TABLE 6.4: Bifurcation analysis of a selected Turing point with respect to b_3 (wide range). It is selected from the ten Turing points closest to the secondary system's reference point. At this Turing point, $b_1 = 1.9 \times 10^3$, $b_2 = 113$, $b_3 = \frac{k^{cat}_{M2,C1}\tau P_{M2}}{k^{deg}_{M2} C_{C1,s}} = 2250$, $b_4 = 3.56$, $b_5 = 36$, $a_{1,M2} = 0.451$, $a_{1,VC} = 2.66$, $a_{2,M2} = 107$, and $a_{2,VC} = 18.1$. The first column lists the b_3 values; the second column states if the steady state concentrations stay within their scales; third, if there is sufficient collagen I at the steady state; fourth, if the steady state is stable in response to homogeneous perturbations; fifth, if the steady state is unstable in response to heterogeneous perturbations; sixth, if the dispersion relation has its maximum in the relevant range of wavenumbers ($2 < n < 87$); seventh, if the dispersion relation's maximum-containing region of positive eigenvalues is bounded by two regions of negative eigenvalues within the assessed region of wavenumbers (n from 0 to 87). *When $b_3 = 2.25$, the dispersion relation stays positive throughout the assessed range of wavenumbers and its fluctuations are minute (an order of -5), so we consider it to be flat and not have a maximum.

b_3	$b_2 < b_3$	Collagen I	Stability	Instability	Maximum	Bounded
0.225	No	Yes	Yes	No	No	No
2.25	No	Yes	No	Yes	No*	No
22.5	No	Yes	No	Yes	No	No
225	Yes	Yes	No	Yes	Yes	No
2250	Yes	Yes	Yes	Yes	Yes	Yes

TABLE 6.5: Bifurcation analysis of a selected Turing point with respect to b_3 (narrow range). It is selected from the ten Turing points closest to the secondary system's reference point. At this Turing point, $b_1 = 1.9 \times 10^3$, $b_2 = 113$, $b_3 = \frac{k^{cat}_{M2,C1}\tau P_{M2}}{k^{deg}_{M2} C_{C1,s}} = 2250$, $b_4 = 3.56$, $b_5 = 36$, $a_{1,M2} = 0.451$, $a_{1,VC} = 2.66$, $a_{2,M2} = 107$, and $a_{2,VC} = 18.1$. The first column lists the b_3 values; the second column states if the steady state concentrations stay within their scales; third, if there is sufficient collagen I at the steady state; fourth, if the steady state is stable in response to homogeneous perturbations; fifth, if the steady state is unstable in response to heterogeneous perturbations; sixth, if the dispersion relation has its maximum in the relevant range of wavenumbers ($2 < n < 87$); seventh, if the dispersion relation's maximum-containing region of positive eigenvalues is bounded by two regions of negative eigenvalues within the assessed region of wavenumbers (n from 0 to 87).

b_3	$b_2 < b_3$	Collagen I	Stability	Instability	Maximum	Bounded
250	Yes	Yes	No	Yes	Yes	No
750	Yes	Yes	No	Yes	Yes	Yes
1250	Yes	Yes	No	Yes	Yes	Yes
1750	Yes	Yes	No	Yes	Yes	Yes
2250	Yes	Yes	Yes	Yes	Yes	Yes

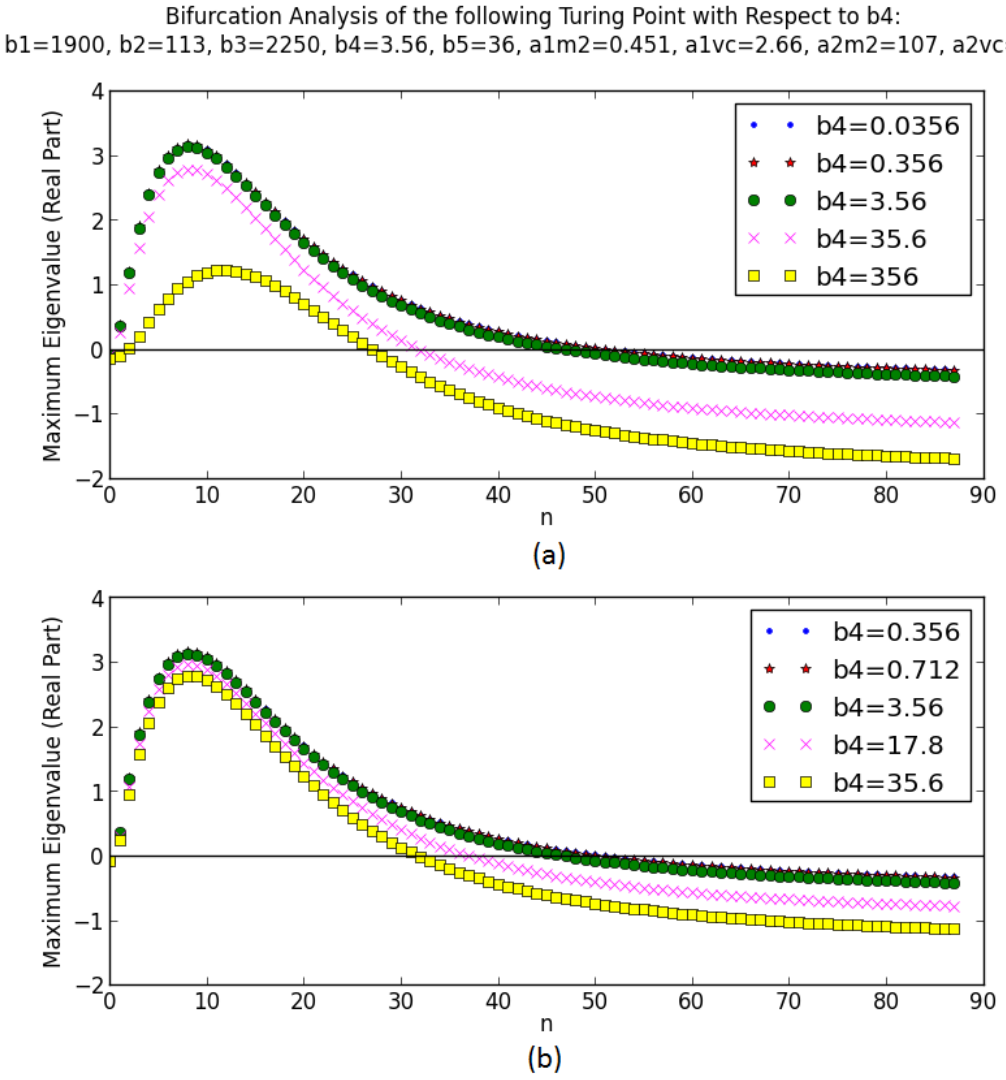

FIGURE 6.5: Bifurcation analysis of a selected Turing point with respect to b_4. It is selected from the ten Turing points closest to the secondary system's reference point. At this Turing point, $b_1 = 1.9 \times 10^3$, $b_2 = 113$, $b_3 = 2250$, $b_4 = \frac{k^{on}_{VC,C1} \tau P_{VC}}{k^{deg}_{VC}} = 3.56$, $b_5 = 36$, $a_{1,M2} = 0.451$, $a_{1,VC} = 2.66$, $a_{2,M2} = 107$, and $a_{2,VC} = 18.1$. On the x-axes, n is the integer in the wavenumber ($k = n\pi$). (a) considers a wider range of b_4 than (b).

fewer unstable Fourier modes with smaller wavenumbers (longer wavelengths) too, meaning the resulting pattern is more regular.

Figure 6.5 shows the dispersion relations for different b_4 values. In all cases, the six constraints are satisfied. Clearly, the secondary system is less sensitive to b_4 than b_3. The trends are clear too: a decrease in b_4 results in a sharper peak at a smaller wavenumber and a smaller region of positive eigenvalues. In other words, it is the opposite of the trend for b_3.

6.4 Computer Simulations

In this section, we will simulate the effects of noises on the homogeneous steady state of the secondary system. The mathematical model is given in appendix F and parametrised at a selected Turing point ($b_1 = 1.9 \times 10^5$, $b_2 = 1.13$, $b_3 = 22.5$, $b_4 = 356$, $b_5 = 36$, $a_{1,M2} = 4.51$, $a_{1,VC} = 26.6$, $a_{2,M2} = 107$, and $a_{2,VC} = 18.1$). Out of the ten Turing points described in table 6.3, the tenth point has the dispersion relation with the sharpest and highest peak, figure 6.3(d). However, it also has more than forty unstable Fourier modes, so we are likely to get a noisy and irregular pattern at this point. The dispersion relations at the fifth and ninth Turing points, as shown in figure 6.6, have fewer than ten unstable Fourier modes apiece. We will simulate at the latter Turing point because the difference between the diffusion rates of MMP2 and VEGFC is smaller at that point. In other words, it is a less stringent constraint on MMP2 and VEGFC.

6.4.1 COMSOL Multiphysics Settings

We will perform our simulations in COMSOL Multiphysics version 5.2. We will run the simulations on a desktop computer with an Intel(R) Core(TM) i5-3570 CPU at 3.40 GHz and 16 GB of RAM.

We will adopt a fully coupled approach, meaning equations (6.13) to (6.16) will be solved together in one step. Since our equations are all non-linear, their discretisation will result in a system of non-linear algebraic equations. This system of equations will be solved by the 'constant (Newton)' solver. This solver has a constant damping factor of 0.9 and terminates when the estimated relative error is less than 0.01. However, the maximum number of iterations is 8: after that, Newton's method terminates even if the estimated relative error is larger than 0.01. However, if COMSOL detects a linear problem, it will use the 'PARDISO' solver with a pivoting perturbation of 1×10^{-8}. This solver handles systems of linear equations directly rather than iteratively. A direct method solves a linear system in a finite number of steps; an iterative method forms a sequence of approximations which converge to the exact solution.

In each simulation and when $\tilde{t} = 0$, the concentrations are their homogeneous steady state values plus noises. The noises are modelled by a random function which depends on the spatial coordinates, the number of which agrees with the number of dimensions. The function is evaluated at each node in the mesh according to a uniform distribution; it is centred at zero with an amplitude of 0.001. A fine mesh mimics the randomness of noises better than a coarse one, so we will use the 'extremely fine' mesh setting: the finest mesh setting available in the software package.

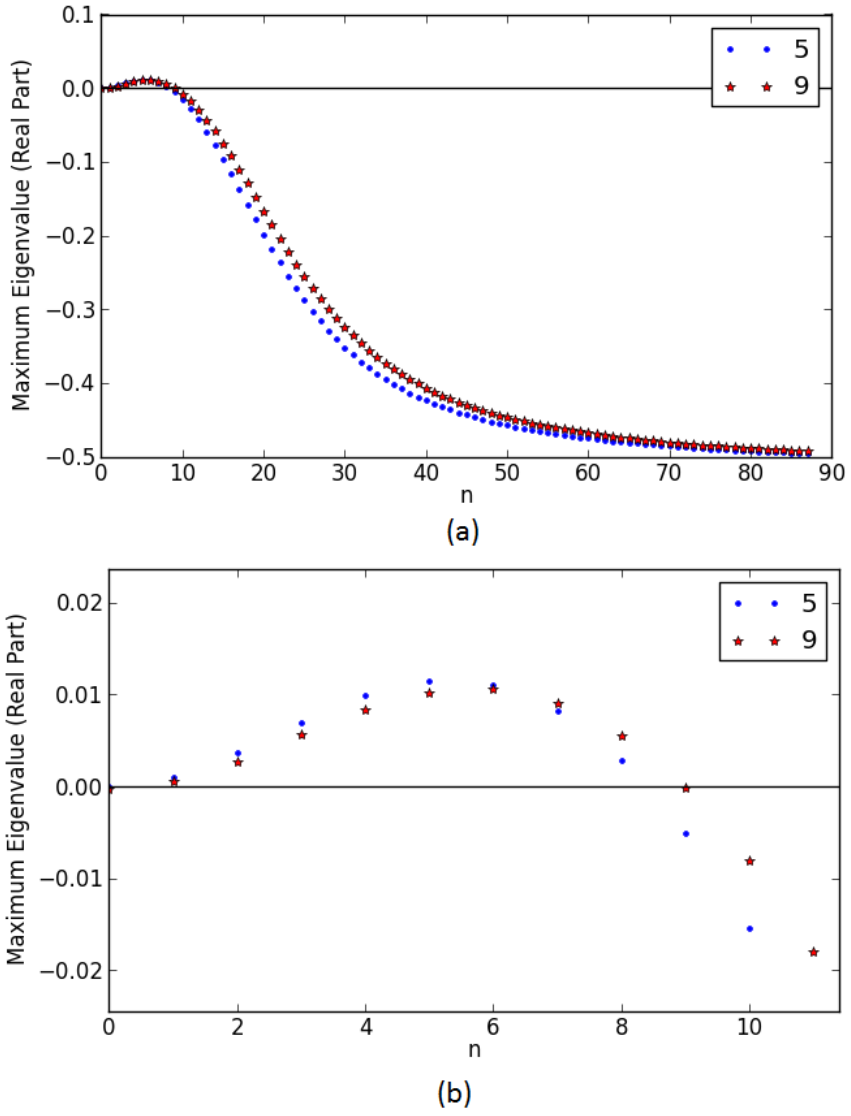

FIGURE 6.6: Dispersion relations at two Turing points. They are selected from the ten Turing points closest to the secondary system's reference point. At point 5, $b_1 = 1.9 \times 10^6$, $b_2 = 1.13$, $b_3 = 22.5$, $b_4 = 356$, $b_5 = 36$, $a_{1,M2} = 0.0451$, $a_{1,VC} = 2.66$, $a_{2,M2} = 107$, and $a_{2,VC} = 1.81$. At point 9, $b_1 = 1.9 \times 10^5$, $b_2 = 1.13$, $b_3 = 22.5$, $b_4 = 356$, $b_5 = 36$, $a_{1,M2} = 4.51$, $a_{1,VC} = 26.6$, $a_{2,M2} = 107$, and $a_{2,VC} = 18.1$. On the x-axes, n is the integer in the wavenumber ($k = n\pi$). (b) is a part of (a).

We will simulate the secondary system as $\tilde{t}$ runs from 0 to 100. We will use the BDF (backward differentiation formula) method to determine the time steps adaptively. At each time point, the solutions from the previous one or two time steps are used to estimate the time derivatives of the next time step, while the derivatives' stability determines the step size. In each simulation, we will divide the $\tilde{t}$ range into 10000 equal intervals. By using a 'strict' setting, we will force each time step to end before or at the end of the interval it begins in. Effectively, the maximum time step is 0.01.

6.4.2 One Dimension

Figures 6.7, 6.8, and 6.9 illustrate the spatiotemporal dynamics of VEGFC concentration in the secondary system. In figure 6.7, most noise components decay quickly. As the unstable noise components grow with time, the concentration profile of VEGFC becomes smoother and its range broadens. In figures 6.8 and 6.9, three peaks emerge and vanish in an oscillatory manner.

Earlier in this chapter, we predicted that the fastest growing Fourier mode has a wavelength of 0.333 (table 6.3); it is consistent with the presence of three peaks because the domain size is 1. We can compare our prediction with the simulation more rigorously using the discrete Fourier transform. In the simulation, the spatial domain is divided into 100 equal intervals separated by 101 nodes. The discrete Fourier transform of the $\tilde{C}_{VC}$ profile at a point in time is $\sum_{n=0}^{100} \tilde{C}_{VC}(n) exp\left(\frac{-2\pi jFn}{101}\right)$, a summation over the nodes; $j = \sqrt{-1}$; F is frequency in space. At each frequency (integers from 0 to 100), the discrete Fourier transform gives a complex number; its magnitude indicates the strength of that frequency component in the spatial $\tilde{C}_{VC}$ profile; its phase provides information about where this component stands in relation to the other components in the profile. We will transform the $\tilde{C}_{VC}$ profile when $\tilde{t} = 96$ in MATLAB R2012a. The result is shown in figure 6.10 where the output magnitude is represented by m. Since the $\tilde{C}_{VC}$ profile is sampled once every 0.01 spatial units, the sampling frequency is 100. By the Nyquist-Shannon sampling theorem, the sampling frequency must be at least twice the highest frequency (Nyquist frequency) in the continuous $\tilde{C}_{VC}$ profile: it ensures that the sample captures all the information in the continuous profile. Therefore, the maximum frequency in figure 6.10 is 50. When $F = 0$, the output is the summation of all 101 sample concentrations, so the peak there simply means the samples do not cancel out. Ignoring this mathematical artefact, the strongest frequency component is 3 as expected.

To explain the oscillatory behaviour and growing concentration range, we must consider the eigenvalues of B more carefully. At the chosen Turing point and dominant wavenumber ($k = 6\pi$), they are -4.2756×10^4, -1.1887, $1.0570 \times 10^{-2} - 0.4510j$, and $1.0570 \times 10^{-2} + 0.4510j$. In the phase space that represents the secondary system, the solution curve of a given initial condition and parametric point is called an orbit. The collection of all orbits at a parametric point constitutes the secondary system's phase portrait there. At the chosen Turing point and dominant wavenumber, the complex conjugates have positive real parts, meaning some orbits spiral out of the steady state. This is in agreement with the observed oscillations and growing concentration range.

On the other hand, when the three peaks are present, they have different widths and heights. In section 6.3, we explained that there is more than one unstable Fourier mode, so there are interruptions to the dominant one. Also, Turing pattern analysis is

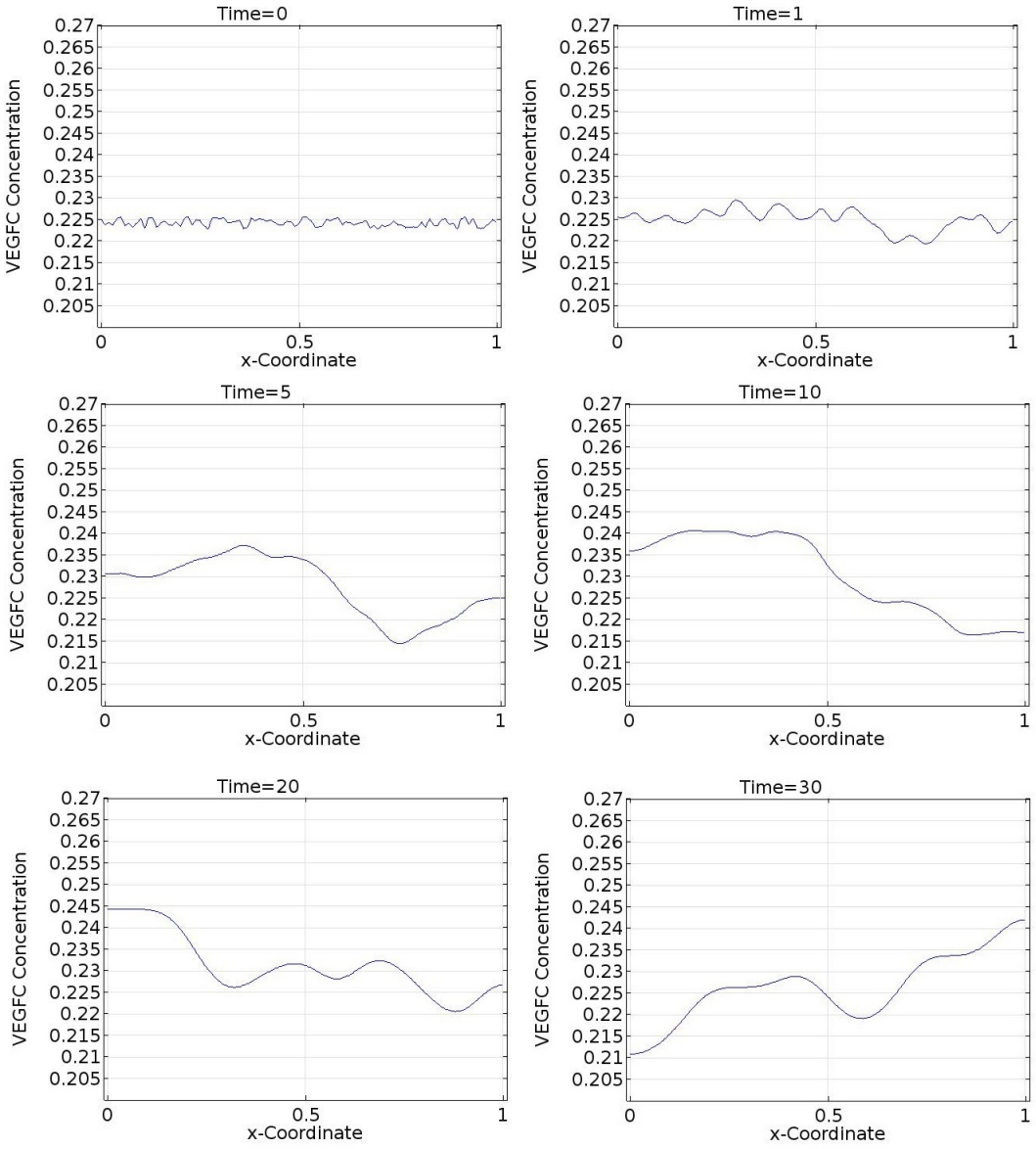

FIGURE 6.7: Spatiotemporal dynamics of VEGFC in the one-dimensional secondary system (Part 1). In this simulation, $b_1 = 1.9 \times 10^5$, $b_2 = 1.13$, $b_3 = 22.5$, $b_4 = 356$, $b_5 = 36$, $a_{1,M2} = 4.51$, $a_{1,VC} = 26.6$, $a_{2,M2} = 107$, and $a_{2,VC} = 18.1$. VEGFC stands for the vascular endothelial growth factor C.

a linear stability analysis. Without considering the non-linear dynamics of the secondary system, we cannot predict the peak amplitudes.

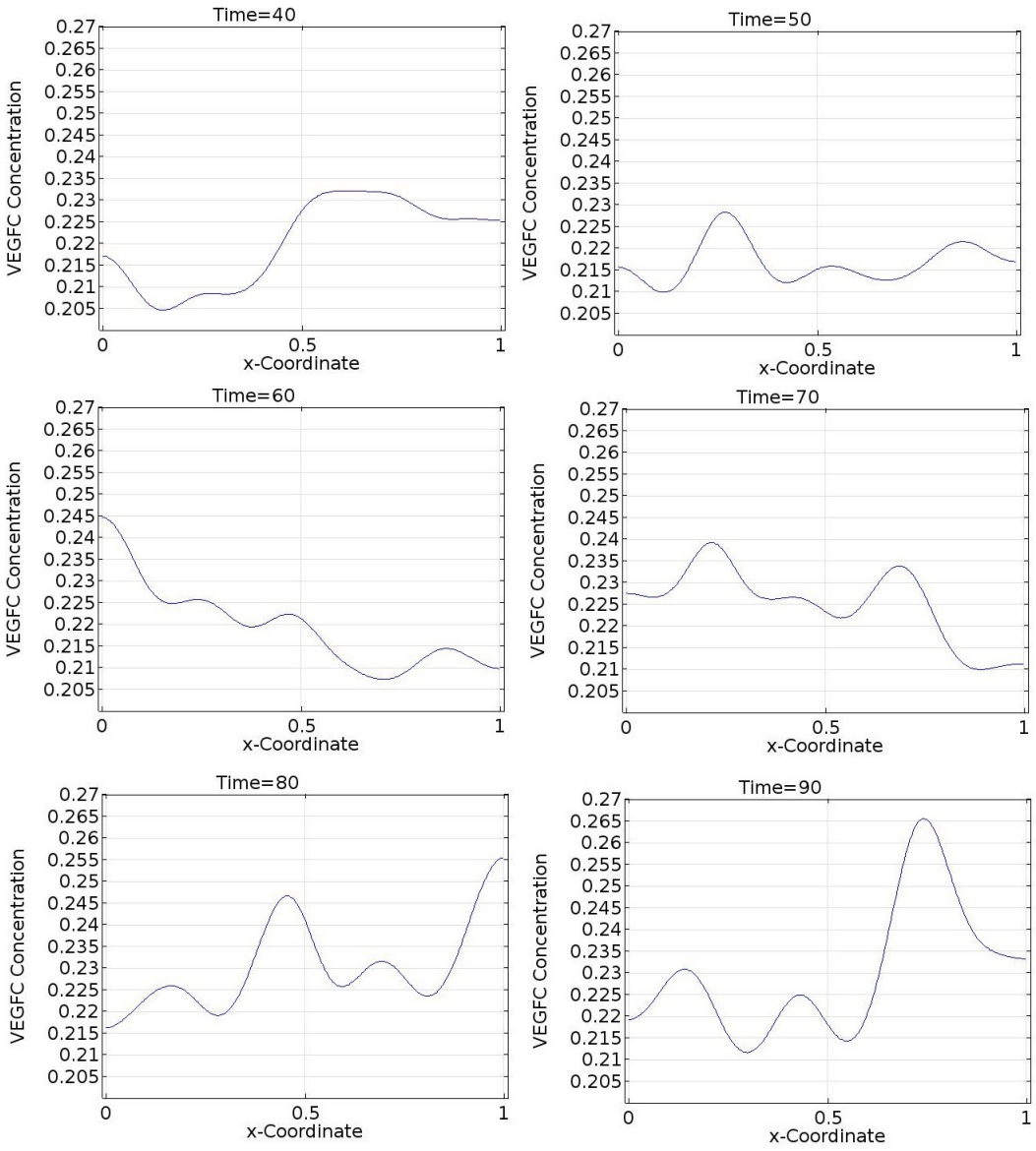

FIGURE 6.8: Spatiotemporal dynamics of VEGFC in the one-dimensional secondary system (Part 2). In this simulation, $b_1 = 1.9 \times 10^5$, $b_2 = 1.13$, $b_3 = 22.5$, $b_4 = 356$, $b_5 = 36$, $a_{1,M2} = 4.51$, $a_{1,VC} = 26.6$, $a_{2,M2} = 107$, and $a_{2,VC} = 18.1$. VEGFC stands for the vascular endothelial growth factor C.

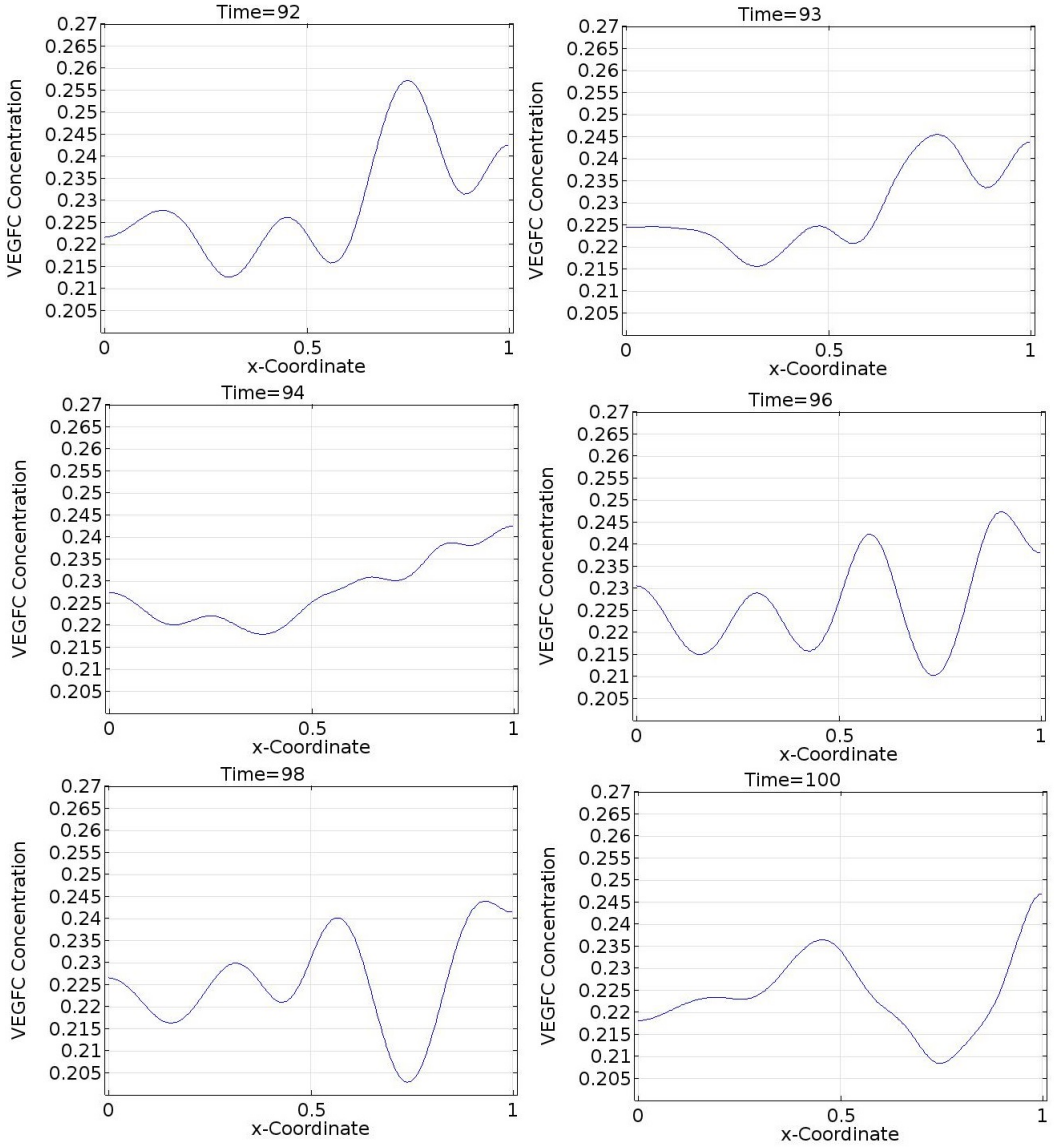

FIGURE 6.9: Spatiotemporal dynamics of VEGFC in the one-dimensional secondary system (Part 3). In this simulation, $b_1 = 1.9 \times 10^5$, $b_2 = 1.13$, $b_3 = 22.5$, $b_4 = 356$, $b_5 = 36$, $a_{1,M2} = 4.51$, $a_{1,VC} = 26.6$, $a_{2,M2} = 107$, and $a_{2,VC} = 18.1$. VEGFC stands for the vascular endothelial growth factor C.

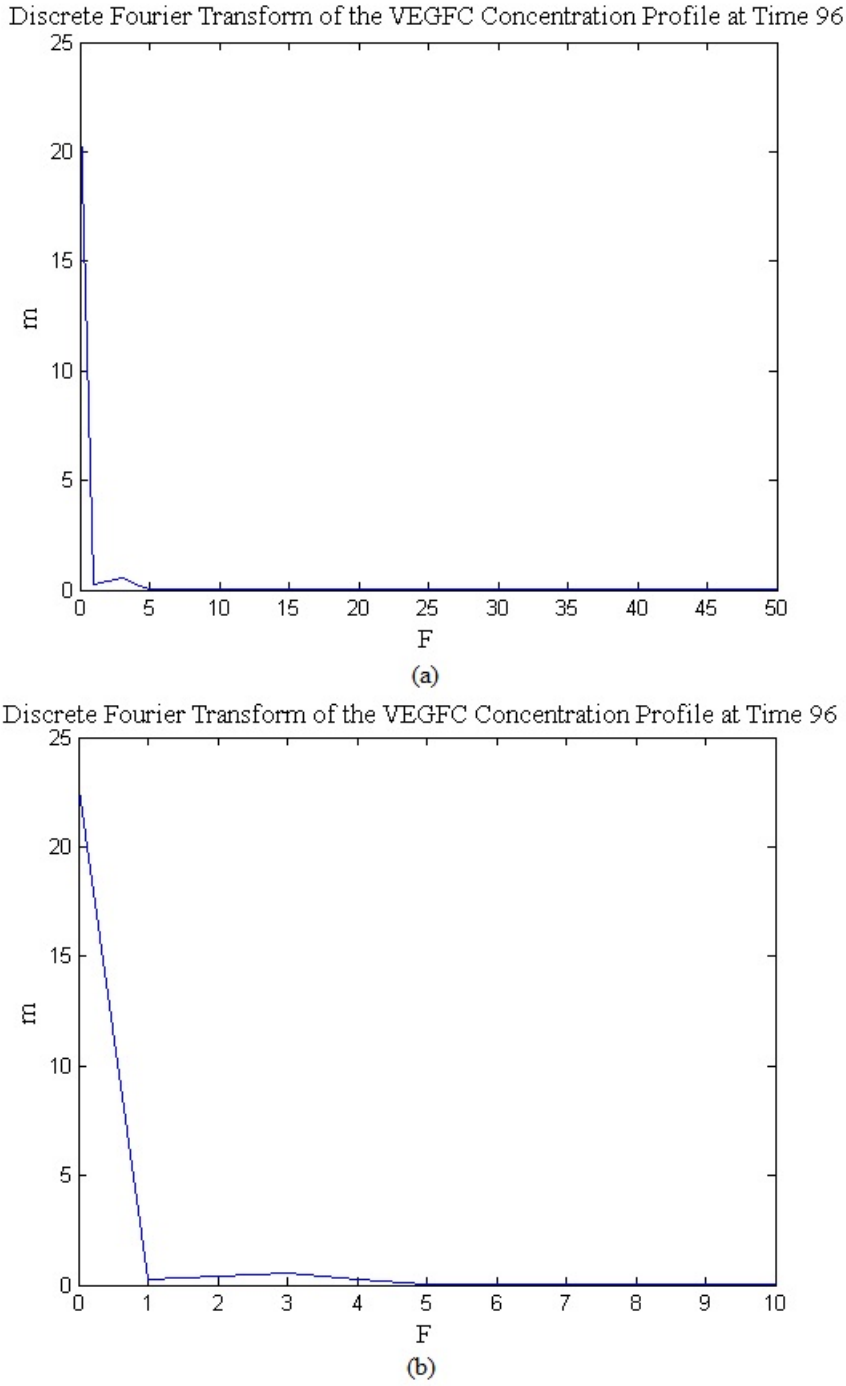

FIGURE 6.10: Discrete Fourier transform of the VEGFC concentration profile in the secondary system, $\tilde{t} = 96$. The system is parametrised at this Turing point: $b_1 = 1.9 \times 10^5$, $b_2 = 1.13$, $b_3 = 22.5$, $b_4 = 356$, $b_5 = 36$, $a_{1,M2} = 4.51$, $a_{1,VC} = 26.6$, $a_{2,M2} = 107$, and $a_{2,VC} = 18.1$. F means frequency in space; m, the magnitude of the transform's output; VEGFC stands for the vascular endothelial growth factor C. (b) is a part of (a).

6.4.3 Two Dimensions

Clearly, the zebrafish is not a line. In chapter 3, we idealised its geometry and defined it as a rectangle with an aspect ratio near 10. In this subsection, we will use a rectangle with an aspect ratio of 10 as our model geometry.

To extend the mathematical model of the secondary system to two dimensions, we need to replace each spatial derivative with respect to $\tilde{x}$ with the gradient operator (∇). The simulation in the two-dimensional secondary system is illustrated by figure 6.11. When $\tilde{t} = 0$, VEGFC is homogeneously distributed, bar noises. As time passes, the concentration range widens. Consistent with our prediction and for the same reasons stated in subsection 6.4.2, three VEGFC-rich regions emerge and vanish in an oscillatory manner.

Finally, we will experiment with the boundary conditions. Because the outer boundaries of the trunk are physical barriers, no-flux boundary conditions apply to VEGFC and MMP2 in the secondary system. If we use periodic boundary conditions instead, the model represents a portion of the trunk; it is far from and not influenced by the boundaries. The two-dimensional secondary system has two pairs of opposing boundaries. We will make each pair periodic by imposing the following. First, the concentrations of all four species on a boundary mirror their counterparts on the opposite boundary. Second, an influx of VEGFC or MMP2 through a boundary is balanced by an outflux through the opposite boundary. The results presented in section 6.3 are still valid despite the new boundary conditions. The four heterogeneous perturbations are now proportional to $\sum_{n=0}^{\infty} e^{\sigma\tilde{t}}\Big[cos(k\tilde{x}) + sin(k\tilde{x})\Big]$, but the dispersion relation for each parametric combination remains the same. The spatiotemporal dynamics of VEGFC in this modified secondary system are illustrated by figure 6.12. The comments on the other two simulations in this chapter apply to this one too. However, as expected, the VEGFC pattern is more regular.

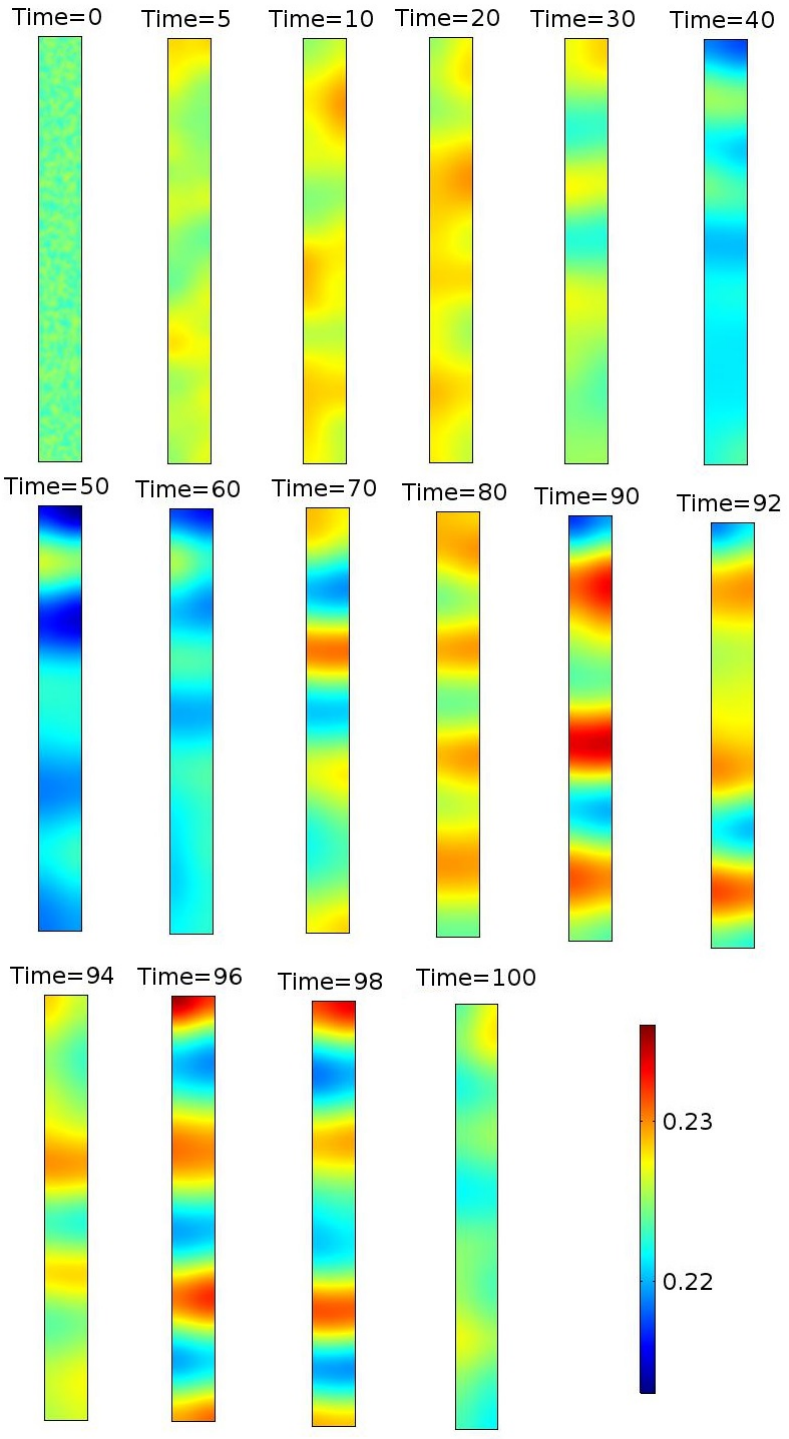

FIGURE 6.11: Spatiotemporal dynamics of VEGFC in the two-dimensional secondary system (no-flux boundary conditions). In this simulation, $b_1 = 1.9 \times 10^5$, $b_2 = 1.13$, $b_3 = 22.5$, $b_4 = 356$, $b_5 = 36$, $a_{1,M2} = 4.51$, $a_{1,VC} = 26.6$, $a_{2,M2} = 107$, and $a_{2,VC} = 18.1$. Vertically, the spatial coordinate $\tilde{y}$ goes from 0 to 1; horizontally, the spatial coordinate $\tilde{x}$ goes from 0 to 0.1. VEGFC stands for the vascular endothelial growth factor C.

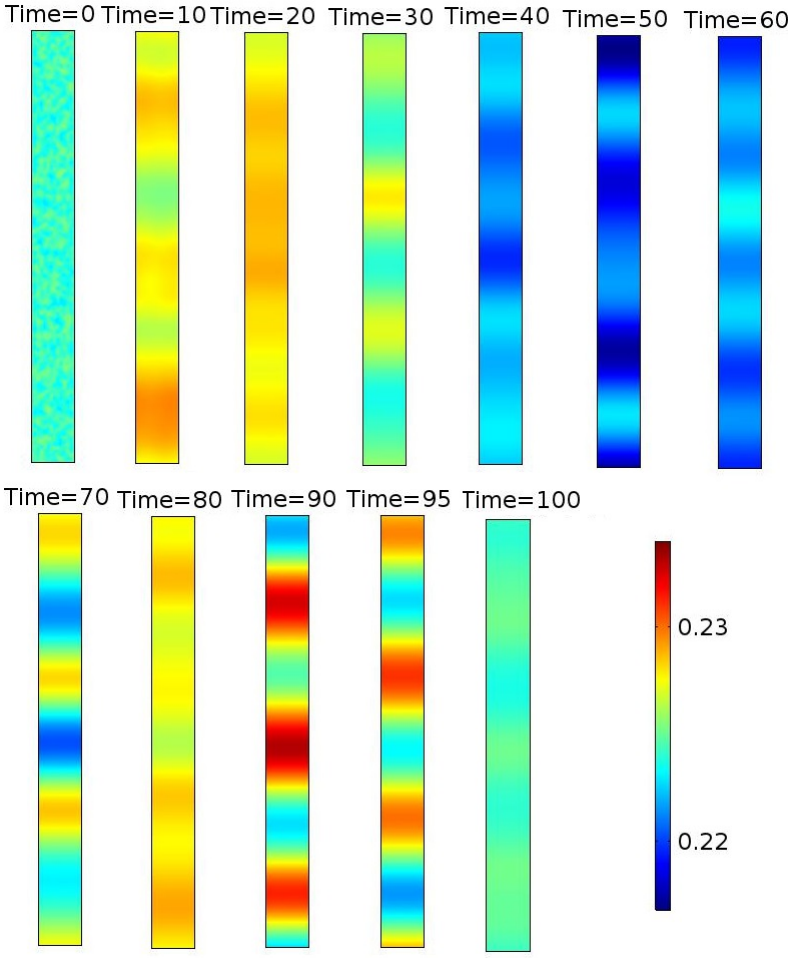

FIGURE 6.12: Spatiotemporal dynamics of VEGFC in the two-dimensional secondary system (periodic boundary conditions). In this simulation, $b_1 = 1.9 \times 10^5$, $b_2 = 1.13$, $b_3 = 22.5$, $b_4 = 356$, $b_5 = 36$, $a_{1,M2} = 4.51$, $a_{1,VC} = 26.6$, $a_{2,M2} = 107$, and $a_{2,VC} = 18.1$. Vertically, the spatial coordinate $\tilde{y}$ goes from 0 to 1; horizontally, the spatial coordinate $\tilde{x}$ goes from 0 to 0.1. VEGFC stands for the vascular endothelial growth factor C.

6.5 Discussion

In this section, we will discuss the results in this chapter in relation to lymphangiogenesis.

6.5.1 Context

Before this chapter, we were interested in the period from 36 to 48 HPF. In this window, as reviewed in chapter 2, LEC progenitors exit the PCV and migrate to the horizontal myoseptum of the zebrafish, differentiating *en route*. Once the LEC progenitors are in the horizontal myoseptum, they are known as the parachordal lymphangioblasts. From 60 HPF onwards, they migrate both ventrally and dorsally along the aISVs, forming the TD and DLLV by 120 HPF. After that, various minor lymphatic structures form throughout the zebrafish trunk, for example, the parachordal lymphatic vessel along the horizontal myoseptum. A schematic of the zebrafish trunk at this stage is given in figure 6.13. At this stage, the constituent cells should simply be called LECs.

The secondary system represents the stage shown in figure 6.13. At this point in time, the LECs are scattered around the zebrafish trunk and they constitute various lymphatic structures. Since they are where they should be and do not move around anymore, collagen I is probably at a higher level than before. This agrees with the production of collagen I and the absence of an interstitial flow in the secondary system. The even distribution of cells also agrees with the production of VEGFC and MMP2 throughout the secondary system. The homogeneous steady state of the secondary system reflects the biochemical profile at this developmental stage. We asked whether random noises can break the symmetry of this profile by Turing's mechanism. We learnt that they can, but parametric fine-tuning is necessary.

6.5.2 Turing's Mechanism

The secondary system is unlike the typical instance of Turing's mechanism (Gierer and Meinhardt, 1972). First, VEGFC and MMP2 do not form a self-activator-self-inhibitor pair. Second, VEGFC binds to the immobile collagen I reversibly. Third, the concentration of collagen I controls the diffusion rates of VEGFC and MMP2. Nonetheless, we demonstrated that the symmetry of the homogeneous steady state can be broken by Turing's mechanism. We sampled 1953125 points in the vicinity of a literature-based reference point in the secondary system's parametric space, including the reference point itself. Turing's mechanism works at 94 of them. We considered why it works at these points using three strategies.

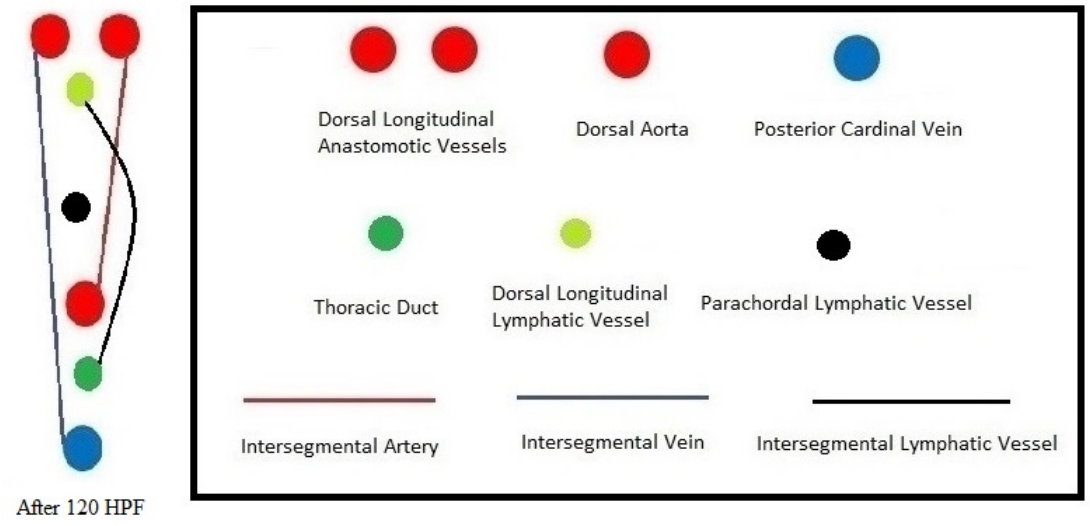

FIGURE 6.13: Schematic of the zebrafish trunk at some point after 120 hours post-fertilisation (HPF).

Our first approach was to study the distribution of each kinetic parameter among the 94 Turing points. The following comments are relative to the reference point. First, a small VEGFC-collagen I binding rate constant is more frequent, while the unbinding rate constant at the reference point is prevalent. The implication is that a smaller degree of VEGFC-collagen I binding favours Turing's mechanism. Second and by the same statistical argument, a higher production rate of collagen I favours Turing's mechanism. Third, a high MMP2 production rate and a high collagen I degradation rate constant are both common; these statistics suggest that collagen I degradation favours Turing's mechanism. Fourth, the statistics about VEGFC production rate suggest that it does not affect Turing's mechanism.

Next, we picked out the ten Turing points closest to the reference point. At these points, the diffusion rate of VEGFC is always higher than that of MMP2. When the kinetic parameters are fixed, an increase in the diffusion rates due to a decrease in viscosity results in fewer unstable noise components with longer wavelengths. Therefore, a low viscosity favours Turing's mechanism by making the resulting pattern more regular.

Finally, we focused on one particular Turing point. Among the ten selected Turing points, it has the most robust dispersion relation in the sense that its most unstable noise component is well-defined. We perturbed the production rates of MMP2 and VEGFC. The results agree with and extend those of our first approach. First, collagen I degradation favours Turing's mechanism. More specifically, it seems to stabilise the secondary system with respect to homogeneous perturbations and create more regular patterns with longer wavelengths. Second, changes in the production rate of VEGFC do not have any significant effects on Turing's mechanism. However, when less VEGFC

is produced, there are slightly fewer noise components with marginally longer wavelengths, thus making the resulting pattern more regular.

6.5.3 VEGFC

As reviewed in chapter 2, in the mouse embryo, the primitive lymphatic plexus matures into different lymphatic ducts after its formation. Due to evolutionary conservation, it is not unthinkable that the lymphatic structures in the zebrafish embryo undergo maturation beyond 120 HPF. We are back to the old question: what is VEGFC's role in this process?

Using our simulation results, we have shown that VEGFC can form Turing patterns in the zebrafish embryo. The simulated patterns have the predicted wavelength too. However, it is difficult to explain lymphangiogenesis in terms of this patterning mechanism. First, the peaks in a pattern of VEGFC must coincide with the TD, PCV, and DLLV. Second, the oscillatory behaviour of VEGFC in the simulations makes it an inconsistent signal; a stationary pattern is necessary. Third, the concentration range of the pattern must be wide enough, threefold according to a rule of thumb (Gurdon and Bourillot, 2001); our simulation results are inconsistent with this requirement. Fourth, the simulations have a nondimensionalised time range from 0 to 100, an interval of almost 12 days. Considering the zebrafish reaches sexual maturity at roughly 3 months post-fertilisation (Nasiadka and Clark, 2012), the simulated dynamics may be too slow.

Taken together, the proposed patterning mechanism is only a part of a larger theory. We need more information before we can use it to explain the lymphatic vessels' maturation after 120 HPF.

6.5.4 Generalisations

Although Turing's mechanism was first proposed decades ago, the secondary system differs from the typical instance of Turing's mechanism (Gierer and Meinhardt, 1972). First, VEGFC and MMP2 do not form a self-activator-self-inhibitor pair. Second, VEGFC binds to the immobile collagen I reversibly. Third, the concentration of collagen I controls the diffusion rates of VEGFC and MMP2. To the best of our knowledge, no one has performed a Turing pattern analysis on this type of biochemical system yet. Therefore, we have proposed a new patterning mechanism.

VEGFC is of course only a candidate morphogen for the maturing lymphatic vessels. Our new mechanism is generic, so it can pattern other candidate morphogens too.

Furthermore, the combination of a patterning species (VEGFC), a matrix protein (collagen I), and a remodelling species (MMP2) is common in biology. We have shown

that the mechanism works for periodic boundary conditions in addition to no-flux boundary conditions. Therefore, it is versatile and can be applied to a wide range of natural and synthetic biological systems, including tissues and organs far from any physical boundaries.

6.5.5 Future Work

Based on our discussion so far, we propose several improvements for this study.

Fundamentally, Turing's mechanism requires a homogeneous steady state. Our assumption of its existence is not based on biochemical data. To adduce evidence for it, we must track the biochemical profile in the zebrafish embryo over time.

In a biochemical system, the production rates' relations to the concentrations are essential to Turing's mechanism. In order to address the uncertainties about our MMP2 and VEGFC production terms, we need to perform experimental studies too.

To find a link between our proposed mechanism and lymphangiogenesis, we must explore the parametric space more selectively. In a dispersion relation, the eigenvalues' real parts determine how fast the Fourier modes grow, and the eigenvalues of oscillatory Fourier modes have imaginary parts. We can limit our Turing points to those whose dominant Fourier modes have real and sufficiently large eigenvalues; these extra constraints ensure stationary VEGFC patterns that reach a sufficient size within a reasonable time frame.

We need two extra mechanisms to link the simulated VEGFC patterns to lymphangiogenesis. First, what makes the vessels lie at the peaks of a VEGFC pattern? Potentially, the constituent cells of the vessels are drawn there by chemotaxis. Although we argued against this scenario in chapter 5, we were considering an earlier stage of lymphangiogenesis. Also, we simply argued on the basis of VEGFC's distribution in the embryo; we did not argue against VEGFC being able to chemoattract the cells. Second, we only found 94 Turing points out of 1953125 candidates, so how does the embryo find the 'right' parameters? To find this link, we must explore the parametric space more extensively and intelligently. For example, an adaptive Monte Carlo algorithm can mimic how the embryo may find the right parameters by trial and error. Then, using a larger sample of Turing points, we can look for correlations among the parameters in order to infer a mechanism.

Finally, even before we find the two missing mechanisms, the proposed mechanism can be generalised. It can pattern other candidate morphogens for this stage of lymphangiogenesis (beyond 120 HPF). We can also use the proposed mechanism to study other natural biochemical systems and design synthetic ones.

6.6 Chapter Summary

We started this chapter with a review of pattern formation in biology. Then, we demonstrated that VEGFC patterns can emerge in the zebrafish trunk by Turing's mechanism.

First, we simplified the primary system (thirteen equations in two spatial domains) to give the secondary system (four equations in one spatial domain). Then, we studied the linear stability of its homogeneous steady state, considering 1953125 points in the parametric space. We identified 94 points where Turing's mechanism works and obtained the dispersion relations there. These points are called Turing points and they reside in the Turing space. From the statistics of the Turing points and the dispersion relations at these points, we gained insights into the Turing space's structure. At one Turing point, we simulated the emergence of VEGFC patterns in different geometries. After 120 HPF, the lymphatic vessels are in place and probably maturing. It is possible that our proposed mechanism patterns VEGFC to regulate their maturation. However, further studies are required to buttress this proposal.

Despite the incomplete nature of this theory about lymphangiogenesis, our results can already be generalised. To the best of our knowledge, this study is the first Turing pattern analysis on VEGFC, MMP2, and collagen I as a unit. It differs from the typical instance of Turing's mechanism (Gierer and Meinhardt, 1972), so we have proposed a new patterning mechanism. It works for both periodic and no-flux boundary conditions, so it is physically versatile. For example, it can pattern tissues and organs unbounded by any physical barriers too. The proposed mechanism can be used to study other candidate morphogens for lymphangiogenesis, other natural biochemical systems, and engineer synthetic ones. The mathematical model of the secondary system is a tool for such studies.

Chapter 7

Thesis Summary

In this final chapter, we will summarise what we have done in this thesis. The aim is to crystallise the main points of our narrative.

7.1 Motivations

We learnt that lymphangiogenesis is an important topic.

The lymphatic system of a vertebrate maintains its homeostasis and mediates its immune responses to pathogens. Therefore, in order to regenerate a tissue or an organ, it is necessary to build a lymphatic network therein.

Lymphangiogenesis, the formation of new lymphatic vessels from existing vessels, is a major means of cancer metastasis. An understanding of lymphangiogenesis will lead to new therapeutic and diagnostic strategies.

7.2 Questions

We asked three important questions about two separate time windows of lymphangiogenesis in the zebrafish embryo.

First, from 36 to 48 HPF, lymphatic progenitors exit the PCV and migrate dorsally until they reach the horizontal myoseptum. Based on what is known about the mouse embryo, the progenitor cells are likely to differentiate during their migration. VEGFC induces their exit, while Cxcl12a guides them into the horizontal myoseptum. We asked what guides their migration and what induces their differentiation *en route*.

Second, at some point after 120 HPF, the lymphatic vessels are in place. Based on what is known about the mouse embryo, they are probably still developing at this stage. We asked what regulates this maturation.

7.3 Answers

Based on our results, VEGFC is likely to be a morphogen for the migrating lymphatic progenitors and potentially for the maturing lymphatic vessels, but it is unlikely to be a chemotactic factor for the former. The dynamics of VEGFC are regulated by ECM remodelling.

7.3.1 Between 36 and 48 HPF: VEGFC

We identified three scenarios where VEGFC is positioned to be a morphogen in the period from 36 to 48 HPF. In scenario 1, diffusion dominates convection and the ECM (collagen I) sequesters VEGFC, thus creating a gradient between the PCV and DA. In scenario 2, convection dominates diffusion, but the ECM protects VEGFC from the interstitial flow, so the morphogen gradient in scenario 1 exists here too. In scenario 3, convection dominates diffusion and the ECM does not bind to VEGFC strongly enough, so a suitable pressure field can create an embryo-spanning morphogen gradient. The gradient in each scenario can induce the lymphatic progenitors' differentiation. Since there are so many scenarios where VEGFC is placed to be their morphogen, chances are it actually is one for them.

On the other hand, it is hard for VEGFC to be a chemotactic factor for them. First, convection must be dominant. Second, the ECM must not shield VEGFC from the interstitial flow's effects. Third, the pressure field driving the flow must be asymmetric and decrease from the PCV to the horizontal myoseptum. These stringent conditions make it difficult for VEGFC to guide the progenitors' migration by chemotaxis.

In general, the pressure field is not a robust regulator or patterning mechanism for lymphangiogenesis. It is because the pressure field in the zebrafish embryo probably changes drastically over time. It is hard for it to be tweaked to suit the embryo's needs and maintained for the whole time window. It is more useful in bioengineering applications such as bioreactors for tissue engineering.

7.3.2 Between 36 and 48 HPF: MMP2 and Collagen I

By remodelling its ECM, the zebrafish embryo can access and get the most out of the scenarios described in the last subsection.

First, in scenario 1, MMP2 has a uniform distribution and degrades collagen I uniformly until convection takes over, leading to scenario 2 or scenario 3. Second, in scenario 3, an asymmetric interstitial flow and MMP2 can combine in a positive feedback mechanism; it can steepen and enhance the asymmetry of the VEGFC concentration gradient in the embryo; it can also create channels of abundant VEGFC and scarce collagen I to guide the migrating lymphatic progenitors. Third, in scenario 2 or scenario 3, the embryo can lower MMP2 production and increase collagen I production to bring back scenario 1.

The above ECM remodelling events occur on the tissue level, so the action of MMP2 is global; it makes the embryo more conducive to cell migration by changing the distributions of VEGFC and collagen I. However, the migrating lymphatic progenitors also need to remove collagen I locally during their move. They rely on MT1-MMP (cell-bound) for this local action.

MMP2 is produced by lymphatic progenitors in general. The production rate depends on the relative concentrations of MT1-MMP, TIMP2, and proMMP2 in the producing cells. On the tissue level, TIMP2 can also bind to MMP2 to change the baseline of the latter's concentration.

The mechanical properties of the ECM depend on many factors, such as the size distribution and spatial arrangement of collagen I fibrils therein, as well as the fibrils' inner structures. Our model only considers the abundance of collagen I, not these molecular details.

7.3.3 After 120 HPF: VEGFC

In the window after 120 HPF, the biochemical profile in the embryo is likely to be homogeneous. The embryo's lymphatic vessels are also in place. However, the dynamics between VEGFC, MMP2, and collagen I can break the profile's symmetry by Turing's mechanism, leading to spatial patterns of VEGFC. This mechanism can potentially create a suitable VEGFC pattern to regulate the lymphatic vessels' maturation. However, we cannot draw a conclusion based on the available evidence.

We need three missing pieces of puzzles. First, the peaks in a VEGFC pattern generated by this mechanism must coincide with the lymphatic vessels. Second, they must be stationary, have sufficiently large amplitudes, and form in a reasonable amount of time. Third, we must explain how the embryo finds the 'right' parameters because the mechanism works in a small region of the parametric space only. Until we have more information about these gaps in our theory, we cannot conclude that VEGFC is positioned to be a morphogen at this developmental stage too.

7.4 Implications

Although this thesis is concerned with lymphangiogenesis in the zebrafish embryo and the role of VEGFC in the process, our results can be generalised. First, VEGFC is only a candidate regulator of lymphangiogenesis. We can use the demonstrated patterning mechanisms to study other candidates. Second and even more generally, we can use them to study other developmental events in other vertebrates, as well as other natural and synthetic biological systems.

7.4.1 Primary System

Using the primary system, we demonstrated a few patterning mechanisms which involve two diffusible species and one immobile species; the diffusible species are a patterning species and an ECM-degrading species; the immobile species is an ECM component. However, species other than VEGFC, MMP2, and collagen I can form this combination, so the mechanisms are generic.

Other candidate morphogens and chemoattractants may behave like VEGFC does in the simulated scenarios. The proposed mechanisms can pattern them too, so they can support alternative hypotheses about lymphangiogenesis. For example, Cxcl12a is expressed in the horizontal myoseptum between 36 and 48 HPF. If it behaves like VEGFC does in scenario 1, it can form a gradient rising towards the horizontal myoseptum. In this gradient, Cxcl12a is well-placed to chemoattract the PCV-derived LECs to the horizontal myoseptum.

More generally, the demonstrated mechanisms can be used to understand other natural biological systems and engineer synthetic ones. For example, they can sculpt other tissues or organs than the lymphatic system. By controlling the production rates of an ECM component and its degrading species, an embryo can distribute a patterning species in many ways to suit different developmental stages. By moving to scenario 1 or scenario 2, it can create short-range and symmetric concentration gradients. By moving to scenario 3, it can create long-range and asymmetric concentration gradients. Staying in scenario 3, the positive feedback mechanism can steepen the gradients and create channels to guide cell migration.

7.4.2 Secondary System

Using the secondary system, we demonstrated that a homogeneous distribution of a patterning species, an ECM-degrading species, and an ECM component may give way to a heterogeneous pattern of the patterning species in the presence of noises. Just like the mechanisms demonstrated with the primary system, this mechanism can pattern

molecules other than VEGFC during lymphangiogenesis. It can be applied to other natural and synthetic biological systems too. It is particularly useful when the cells that produce the three species are uniformly distributed in the tissue or organ they constitute. We also showed that the mechanism can generate more regular patterns when periodic boundary conditions apply, making it physically versatile.

7.5 Extensions

As this thesis draws to a close, we consider the way forward.

7.5.1 VEGFC

Our predictions that VEGFC is a morphogen and not a chemotactic factor are based on simulated scenarios; they require experimental validation. It can easily be done by placing lymphatic progenitors in a VEGFC gradient in a collagen I gel and observing how the cells respond. If VEGFC is a morphogen, they will express different genes in a position-dependent manner; if it is a chemotactic factor, they will migrate up or down the gradient.

7.5.2 Primary System

To the best of our knowledge, the mathematical model of the primary system is the first to consider an interstitial flow, a remodelling ECM, and the sequestration of a mobile species by the ECM holistically.

It can be improved upon by using a more realistic geometry of a larger domain in three dimensions. In three dimensions, we can model the transport of fluid and molecular species along the anterior-posterior axis, such as their excretion through the embryo's anus. More accurate parameters will also help, in particular the binding and unbinding rate constants of VEGFC and collagen I. Finally, we can model more ECM components and ECM-remodelling species because the ECM has such a big impact on VEGFC dynamics.

This model allows further studies. One can change the geometry to study lymphangiogenesis in another organism. One can also change the biochemical reaction network and model parameters to study another candidate regulator of lymphangiogenesis or a completely different event in the zebrafish. For a start, it will be interesting to consider the dynamics of Cxcl12a during lymphangiogenesis in the zebrafish embryo.

7.5.3 Secondary System

The secondary system generates Turing patterns in an atypical manner. This type of system is very common in biology, but to the best of our knowledge, its ability to generate Turing patterns has not been studied by anyone else.

There are two experimental details which will improve our model a lot. First, we need evidence that a homogeneous distribution of VEGFC, MMP2, and collagen I exists at a developmental stage of the zebrafish. Second, the concentration dependence of the production terms is important.

We must address three problems before we can use the secondary system and the mechanism demonstrated with it to explain lymphangiogenesis. First, we should sample the parametric space more selectively. We must choose the Turing points whose dominant Fourier modes have real and sufficiently large eigenvalues only. Second, we must explain how the peaks of a VEGFC Turing pattern 'find' the lymphatic vessels. A promising idea is that VEGFC chemoattracts the constituent cells to where they should be, and subsequently induces their maturation. Third, based on our results, the secondary system's Turing space is a small part of its parametric space. We must explain how the embryo finds the 'right' parameters. To address the third point, we should sample the parametric space more extensively and look for any correlations among the parameters in the resulting sample of Turing points.

7.5.4 Tertiary System

The two mathematical models do not describe cell migration. In the primary system, there is one single lymphatic progenitor (simply called LEC in most of the thesis); it is stationary, does not respond to any biochemical stimuli, and simply serves as a source of MMP2 and TIMP2. The secondary system does not include any cells. We can build a more elaborate model by coupling the spatiotemporal dynamics of LEC density to the concentration dynamics of VEGFC.

This coupling has been modelled in the context of wound healing (Bianchi et al., 2016, 2015). In that context, macrophages, a type of immune cell, are involved in the process. Furthermore, the initial state is a damaged lymphatic network. In our problem, macrophages are not involved and the lymphatic progenitors all originate from the PCV, so this coupling is actually easier to model in our case.

7.6 Chapter Summary

We have reached the end of the thesis. The research reported began in February 2014 and ended in December 2016.

Some of the results were presented at the British Applied Mathematics Colloquium (March 2015 in Cambridge, the United Kingdom) and the European Conference on Mathematical and Theoretical Biology (July 2016 in Nottingham, the United Kingdom). The former was given under the title 'Lymphatic System Development in Zebrafish: A Reaction-Diffusion-Convection Model'; the latter, 'Mathematical Modelling of Lymphatic System Development'.

In May 2016, a manuscript titled 'A Mathematical Model of Lymphangiogenesis in a Zebrafish Embryo' was submitted to the *Bulletin of Mathematical Biology*. Feedback was provided in July 2016 and the corrected manuscript was resubmitted in August 2016. The manuscript is about chapters 1 to 5.

Following the submission of this thesis in December 2016, another manuscript about chapter 6 will be written and submitted to the *Bulletin of Mathematical Biology* in 2017.

Appendix A

Morphogens

A morphogen gradient provides 'positional information' to the cells in an embryo, leading to differential gene expression based on their locations in the gradient; the local morphogen concentration a cell senses determines the set of genes it expresses (Wolpert, 1996). In this appendix, we will learn more about the properties of morphogens, morphogen gradient formation, and morphogen gradient interpretation.

In their review paper, Gurdon and Bourillot (2001) list the criteria that define a morphogen. First, it is released from a localised source to form a concentration gradient in the right place and at the right time. Second, the sensitive cells show at least two qualitatively different responses in a concentration-dependent manner. Third, the morphogen influences the cells directly. Known morphogens are effective at low concentrations ranging from 1×10^{-9} to 1×10^{-11} M; their gradients are active over 50 to 300 µm (Gurdon and Bourillot, 2001). Generalising from the responses of cells to Dpp and activin, a threefold change in a morphogen's concentration over 30 µm is sufficient to induce a response (Gurdon and Bourillot, 2001). However, antagonistic factors can steepen the effective concentration gradient perceived by the morphogen's target cells. In another review, Ashe and Briscoe (2006) agree that a two- to threefold concentration change is sufficient. They add that morphogen gradients can usually achieve between three and seven distinct cellular responses.

The decisive factors in the formation of a morphogen gradient in an embryo are the morphogen's release rate, spread rate, and stability (Gurdon and Bourillot, 2001). The three prevailing ideas about morphogen transmission are diffusion in the interstitial space, cell-to-cell relay by sequential internalisation and re-emission, and cell-cell cytoplasmic transmission (Gurdon and Bourillot, 2001). Gurdon and Bourillot (2001) comment that morphogen gradients form rapidly, usually within a couple of hours. However, the morphogens can be activated before, during, and after gradient formation, while their antagonistic factors can sequester them from their binding receptors.

Gurdon and Bourillot (2001) review morphogen perception by answering three questions. The first is concerned with how sophisticated a cell can respond to its morphogens. In the simple case, it can either respond or not respond; within a population of cells, each cell has its own response threshold. However, there are examples where three or more response thresholds exist for each cell. The second question is concerned with cooperativity: do cells need their neighbours to determine their positions in a morphogen gradient? To this, the experimental evidence reviewed suggests a negative answer. Nonetheless, morphogen transmission and the target cells' exposure to the morphogen are both affected by their neighbours through competition for the morphogen. Third, how do cells distinguish between a high morphogen concentration and a low one? Either there are receptors with different binding characteristics or there is just one type of receptor which signals differently at different morphogen concentrations. The experimental results reviewed indicate that the latter strategy is adopted. Furthermore, the absolute number of occupied receptors is what matters for a cell, not the ratio of occupied to unoccupied receptors. Ashe and Briscoe (2006) agree with this conclusion.

In the pathways from a morphogen receptor to the genes it controls, quantitative differences in the former's occupancy must be translated to qualitative choices about gene expression. Gurdon and Bourillot (2001) argue from experimental examples that the translations do not occur in the signal transduction pathways; they do not amplify a morphogen signal. They may happen at the transcriptional level, however. Ashe and Briscoe (2006) expand this idea: each pathway culminates in the post-translational regulation of a single transcription factor or a family of functionally related transcription factors. This means a two- to threefold change in a morphogen's extracellular concentration translates to an equivalent change in the relevant transcription factor's intracellular concentration; the target genes of the morphogen must be sensitive to this intracellular change.

Ashe and Briscoe (2006) explain how transcription factors regulate gene expression. In one mechanism, they bind to the DNA sequences of different genes with different affinities. In another mechanism, positive and negative transcriptional inputs affect transcription factors by binding to their target gene promoters. Third, following directly from the second point about combinatorial inputs, multiple transcription factors can form complex regulatory networks, such as feedforward and feedback loops. Ashe and Briscoe (2006) argue that different combinations of these mechanisms are needed to interpret different morphogen gradients. They allow cells to exhibit sophisticated responses to morphogens, such as temporal integration of morphogen signals, persistence of cellular responses following transient signals, and robustness despite intrinsic and environmental noises.

Gurdon and Bourillot (2001) end by proposing a theory based on experimental observations. In this theory, the supply of a morphogen limits the cellular responses to

it; the target cells respond to the absolute number of occupied receptors on each cell, at an instant rather than over a time period; and the cells respond faster to a rise in the morphogen's concentration than a fall. This theory disagrees with Ashe and Briscoe (2006) mainly on the second point because it rules out time integration.

Appendix B

Extracellular Matrix Components

In their review, Goody et al. (2015) mention that there are twenty-eight types of collagens in vertebrates and over forty different collagen-encoding genes in the human. They have different structures and undergo many post-translational modifications. In another review, Wiig et al. (2010) explain that LEC survival is promoted by collagen type I. They add that collagen type I also increases the ability of LECs to form tubes without exogenously added growth factors; it induces lymphatic regeneration after skin wounding by promoting cell migration and proliferation. On the other hand, collagen type XVIII and its proteolytic cleavage products, neostatin-7 and endostatin, are anti-lymphangiogenic (Lutter and Makinen, 2014). In another review, Ji (2006) provides further information on endostatin: it works by binding to endothelial cell surface integrins αVβ3 and α5β1, or blocking the activation of endothelial MMPs or their collagenolytic effects.

According to Goody et al. (2015), glycosaminoglycan chains can covalently or non-covalently associate with core proteins to form proteoglycans. Proteoglycans are heavily glycosylated ECM proteins which absorb water to generate hydrous gel; their ability to absorb water comes from the glycosaminoglycan chains. An example of glycosaminoglycan is hyaluronan. As reviewed by Ji (2006), hyaluronan chains are high-molecular-weight and cell-surface glycosaminoglycan chains which are wrapped around collagen fibrils and perhaps attached to them. Again reviewed by Ji (2006), they metabolise rapidly in lymph nodes: they have a half-life of 24 hours. The remnants exit the lymphatic system and undergo terminal hydrolysis within the liver. Functionally, according to Wiig et al. (2010), hyaluronan chains bind to their receptors like LYVE1 to provide pro-lymphangiogenic signals for LECs.

Wiig et al. (2010) inform us that fibronectin is a cell adhesion protein expressed by both LECs and blood endothelial cells (BECs). It mediates cell adhesion and anchorage through integrins. LECs adhere to and proliferate better on fibronectin-coated plates because fibronectin enhances the proliferation of endothelial

cells through VEGFC-VEGFR3 signalling. Integrin α5β1 is an important receptor of fibronectin; their binding may activate both VEGFR3 and its downstream phosphoinositide 3 kinase (PI3K)/AKT signalling pathway to promote LEC survival and proliferation. Ji (2006) adds that fibronectin can transactivate VEGFR3 and compared to vitronectin, fibronectin significantly enhances the phosphorylation of VEGFR3. Wiig et al. (2010) also review another fibronectin receptor, integrin α9β1, which facilitates LEC tube formation and lymph valve development.

Recent studies about the roles of ECM proteins in cell polarity, migration, tissue mechanics, organ laterality, muscle contraction, and regeneration in the zebrafish have been reviewed by Jessen (2014). Although the paper is not specific to lymphatic development, it gives us an idea about the eclectic collection of ECM proteins in the zebrafish.

Appendix C

Activation of VEGFC by Proteolytic Processing

Joukov et al. (1997) have shown that, as proVEGFC is progressively cleaved, its VEGFR3-activating properties increase and eventually, it acquires VEGFR2-activating properties too. The cleavage steps are as follows.

First, proVEGFC (a preproprotein) dimerises intracellularly by disulphide bonds and non-covalent bonds; each half of a dimer has a molecular mass of 58 kDa (Joukov et al., 1997). Second and intracellularly again, the dimer is cleaved to give a tetramer of two N-terminal halves and two C-terminal halves; each N-terminal half has a molecular weight of 31 kDa (Joukov et al., 1997); each C-terminal half, 29 kDa (Joukov et al., 1997); the tetramer has a molecular weight of 120 kDa (Joukov et al., 1997). Intracellular cleavage is unnecessary for the secretion of VEGFC (Siegfried et al., 2003). Third and extracellularly, the N-terminal propeptides are removed to generate two 21-kDa VEGF homology domains bound by non-covalent interactions: a mature copy of VEGFC (Joukov et al., 1997). Figure C.1 summarises these steps.

CCBE1 is pivotal in the third and extracellular step. In a paper authored by Hogan et al. (2009), CCBE1 is described as a secreted protein; each copy contains a signal peptide, a collagen domain, and a calcium-binding-epidermal-growth-factor domain. In the same paper, Hogan et al. (2009) conclude that CCBE1 is expressed by non-endothelial cells. In the zebrafish embryo, its dynamic expression pattern follows the migrating LEC progenitors from the PCV to the horizontal myoseptum. Jeltsch et al. (2014) have proposed a mechanism; it is shown in figure C.2. After secretion from its synthesising cells, VEGFC binds to VEGFR3 on LECs. However, VEGFC cannot stimulate phosphorylation to a meaningful extent without CCBE1; CCBE1 assists in the binding of VEGFC to VEGFR3; after that, CCBE1 enhances the cleavage of VEGFC by ADAMTS3 to remove the N-terminal propeptides of VEGFC *in situ*. Once mature, VEGFC initiates downstream signalling. ADAMTS3 is released

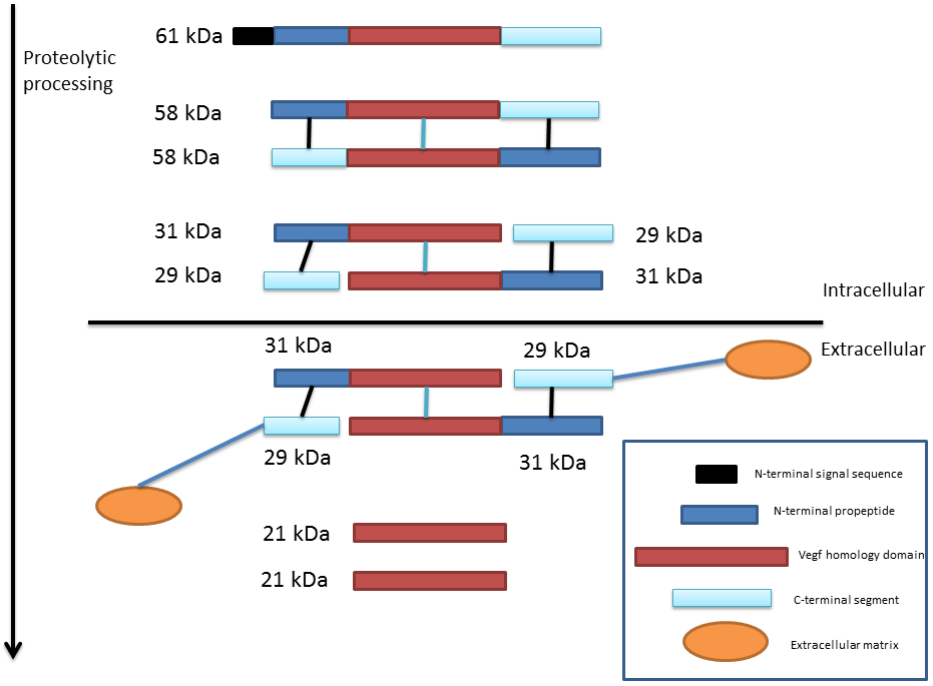

FIGURE C.1: Schematic representation of the proteolytic steps that turn newly synthesised proVEGFC into mature VEGFC. The molecular weight of a fragment is indicated next to the fragment. Disulfide bonds are represented by black lines. Non-covalent bonds are represented by green lines. This schematic is based on a study (Joukov et al., 1997). VEGF stands for vascular endothelial growth factor; VEGFC, vascular endothelial growth factor C; proVEGFC, the preproprotein of VEGFC.

by endothelial cells, but the thrombospondin motif of ADAMTS3 allows it to remain cell-surface-associated.

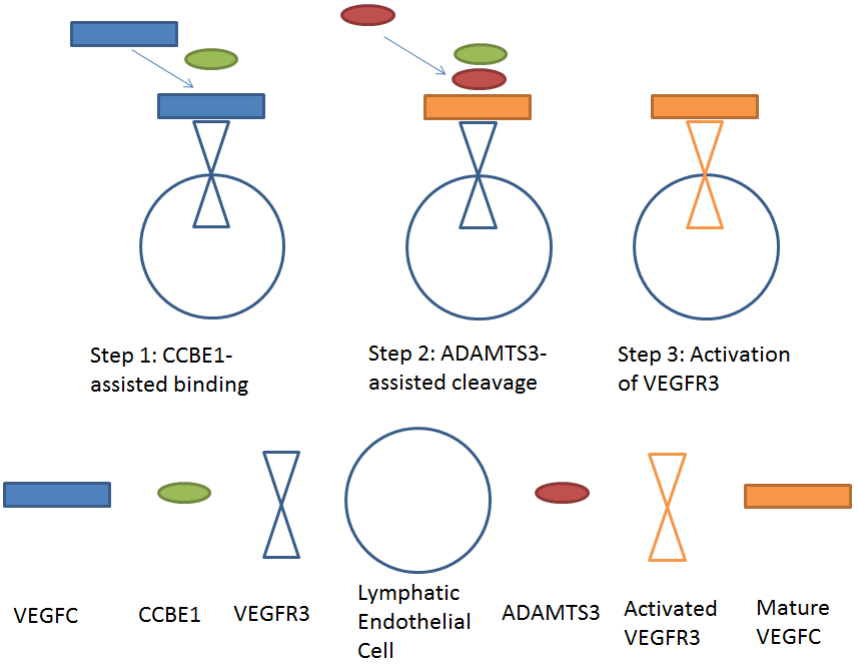

FIGURE C.2: Schematic of the molecular mechanisms that process VEGFC extracellularly. VEGFC binds to VEGFR3 with the aid of CCBE1. Then, CCBE1 assists a cell-surface-associated species called ADAMTS3 in the cleavage and activation of VEGFC. Finally mature, VEGFC activates VEGFR3. This schematic is based on a study (Jeltsch et al., 2014). VEGFC stands for vascular endothelial growth factor C; VEGFR3, vascular endothelial growth factor receptor 3; ADAMTS3, a disintegrin and metalloprotease with thrombospondin motifs-3; CCBE1, collagen-and-calcium-binding-epidermal-growth-factor-domain-containing protein 1.

Appendix D

Primary System

In this appendix, we will summarise the mathematical model representing the primary system. Its derivation is presented in chapters 3 and 4. The simulations described and discussed in chapter 5 are concerned with the primary system or its modified versions.

D.1 Model Equations in the Interstitial Space Domain

First, we will write down the interstitial flow equations,

$$\tilde{\boldsymbol{\nabla}}\tilde{P}^s = -\frac{\tilde{\boldsymbol{u}}\tilde{C}_{C1}^{-\alpha}}{\eta_3} + \tilde{\boldsymbol{\nabla}}^2\tilde{\boldsymbol{u}} \text{ and} \tag{D.1}$$

$$\tilde{\boldsymbol{\nabla}} \cdot \tilde{\boldsymbol{u}} = 0. \tag{D.2}$$

Then, we will write down the reaction-diffusion-convection equations,

$$\frac{\partial \tilde{C}_{M2P}}{\partial \tilde{t}} = \tilde{\boldsymbol{\nabla}} \cdot [\tilde{D}_{M2P}^{eff}\tilde{\boldsymbol{\nabla}}(\frac{\tilde{C}_{M2P}}{\omega}) - \lambda_7\tilde{\boldsymbol{u}}\tilde{C}_{M2P}] - \lambda_{11}\tilde{C}_{M2P}, \tag{D.3}$$

$$\frac{\partial \tilde{C}_{M2}}{\partial \tilde{t}} = \tilde{\boldsymbol{\nabla}} \cdot [\tilde{D}_{M2}^{eff}\tilde{\boldsymbol{\nabla}}(\frac{\tilde{C}_{M2}}{\omega}) - \lambda_7\tilde{\boldsymbol{u}}\tilde{C}_{M2}] - \lambda_{13}\tilde{C}_{M2}\tilde{C}_{T2} + \lambda_{14}\tilde{C}_{M2\cdot T2} - \lambda_{15}\tilde{C}_{M2}, \tag{D.4}$$

$$\frac{\partial \tilde{C}_{T2}}{\partial \tilde{t}} = \tilde{\boldsymbol{\nabla}} \cdot [\tilde{D}_{T2}^{eff}\tilde{\boldsymbol{\nabla}}(\frac{\tilde{C}_{T2}}{\omega}) - \lambda_7\tilde{\boldsymbol{u}}\tilde{C}_{T2}] - \lambda_{19}\tilde{C}_{M2}\tilde{C}_{T2} + \lambda_{20}\tilde{C}_{M2\cdot T2} - \lambda_{21}\tilde{C}_{T2}, \tag{D.5}$$

$$\frac{\partial \tilde{C}_{M2\cdot T2}}{\partial \tilde{t}} = \tilde{\boldsymbol{\nabla}} \cdot [\tilde{D}^{eff}_{M2\cdot T2} \tilde{\boldsymbol{\nabla}} (\frac{\tilde{C}_{M2\cdot T2}}{\omega}) - \lambda_7 \tilde{\boldsymbol{u}} \tilde{C}_{M2\cdot T2}] + \tilde{C}_{M2}\tilde{C}_{T2} - \lambda_{23}\tilde{C}_{M2\cdot T2} - \lambda_{24}\tilde{C}_{M2\cdot T2}, \text{ and} \quad \text{(D.6)}$$

$$\frac{\partial \tilde{C}_{VC}}{\partial \tilde{t}} = \tilde{\boldsymbol{\nabla}} \cdot [\tilde{D}^{eff}_{VC} \tilde{\boldsymbol{\nabla}} (\frac{\tilde{C}_{VC}}{\omega}) - \lambda_7 \tilde{\boldsymbol{u}} \tilde{C}_{VC}] - \lambda_{25}\tilde{C}_{VC}\tilde{C}_{C1} + \lambda_{26}\tilde{C}_{VC\cdot C1} - \lambda_{27}\tilde{C}_{VC}, \quad \text{(D.7)}$$

where

$$\frac{1}{\omega} = 1 + \lambda_5 \tilde{C}_{C1} \text{ and} \quad \text{(D.8)}$$

$$\tilde{D}^{eff}_i = \lambda_{1,i}(1 - \lambda_{2,i}\sqrt{\lambda_3 \tilde{C}_{C1}}). \quad \text{(D.9)}$$

Finally, there are two ODEs,

$$\frac{\partial \tilde{C}_{C1}}{\partial \tilde{t}} = \frac{-\lambda_{28}\tilde{C}_{M2}\tilde{C}_{C1}}{K_M^{M2,C1} + C_{C1,s}\tilde{C}_{C1}} - \lambda_{29}\tilde{C}_{VC}\tilde{C}_{C1} + \lambda_{30}\tilde{C}_{VC\cdot C1} \text{ and} \quad \text{(D.10)}$$

$$\frac{\partial \tilde{C}_{VC\cdot C1}}{\partial \tilde{t}} = \tilde{C}_{VC}\tilde{C}_{C1} - \lambda_{32}\tilde{C}_{VC\cdot C1}. \quad \text{(D.11)}$$

D.2 Model Equations in the LEC Domain

First, there are three PDEs,

$$\frac{\partial \tilde{C}_{M2P}}{\partial \tilde{t}} = \lambda_{1,M2P}\tilde{\boldsymbol{\nabla}}^2\tilde{C}_{M2P} + 1 - \lambda_9\tilde{C}_{MT1\cdot T2}\tilde{C}_{M2P} + \lambda_{10}\tilde{C}_{MT1\cdot T2\cdot M2P}, \quad \text{(D.12)}$$

$$\frac{\partial \tilde{C}_{M2}}{\partial \tilde{t}} = \lambda_{1,M2}\tilde{\boldsymbol{\nabla}}^2\tilde{C}_{M2} + \tilde{C}_{MT1\cdot T2\cdot M2P}\tilde{C}_{MT1}, \text{ and} \quad \text{(D.13)}$$

$$\frac{\partial \tilde{C}_{T2}}{\partial \tilde{t}} = \lambda_{1,T2}\tilde{\boldsymbol{\nabla}}^2\tilde{C}_{T2} + 1 - \lambda_{17}\tilde{C}_{MT1}\tilde{C}_{T2} + \lambda_{18}\tilde{C}_{MT1\cdot T2}. \quad \text{(D.14)}$$

Then, there are three ODEs,

$$\frac{\partial \tilde{C}_{MT1}}{\partial \tilde{t}} = -\lambda_{33}\tilde{C}_{MT1}\tilde{C}_{T2} + \lambda_{34}\tilde{C}_{MT1\cdot T2}, \tag{D.15}$$

$$\frac{\partial \tilde{C}_{MT1\cdot T2}}{\partial \tilde{t}} = \lambda_{35}\tilde{C}_{MT1}\tilde{C}_{T2} - \lambda_{36}\tilde{C}_{MT1\cdot T2} - \lambda_{37}\tilde{C}_{MT1\cdot T2}\tilde{C}_{M2P} + \lambda_{38}\tilde{C}_{MT1\cdot T2\cdot M2P} + \lambda_{39}\tilde{C}_{MT1\cdot T2\cdot M2P}\tilde{C}_{MT1}, \text{ and} \tag{D.16}$$

$$\frac{\partial \tilde{C}_{MT1\cdot T2\cdot M2P}}{\partial \tilde{t}} = \lambda_{40}\tilde{C}_{MT1\cdot T2}\tilde{C}_{M2P} - \lambda_{41}\tilde{C}_{MT1\cdot T2\cdot M2P} - \lambda_{42}\tilde{C}_{MT1\cdot T2\cdot M2P}\tilde{C}_{MT1}. \tag{D.17}$$

D.3 Boundary Conditions

First, we will summarise the boundary conditions for the interstitial flow equations. They are given by the equations,

$$\tilde{P^s} = \frac{1}{\eta_3} \qquad \tilde{\boldsymbol{x}} \in \partial\Omega_{DA}, \tag{D.18}$$

$$\tilde{P^s} = 0 \qquad \tilde{\boldsymbol{x}} \in \partial\Omega_{PCV}, \tag{D.19}$$

$$\tilde{P^s} = 0 \qquad \tilde{\boldsymbol{x}} \in \partial\Omega_{DLAV}, \text{ and} \tag{D.20}$$

$$\tilde{\boldsymbol{u}} = 0 \qquad \tilde{\boldsymbol{x}} \in \partial\Omega_{x,y} \text{ and } \partial\Omega_{LEC/IS+}. \tag{D.21}$$

Next, we will present the boundary conditions for the partial differential equations governing the concentrations of the mobile species.

On the outer boundary surfaces, as well as the PCV and DLAV surfaces, the mobile species obey no-flux boundary conditions; they are represented by the equations,

$$\boldsymbol{n} \cdot [\tilde{D}_i^{eff}\tilde{\boldsymbol{\nabla}}(\frac{\tilde{C}_i}{\omega}) - \lambda_7\tilde{\boldsymbol{u}}\tilde{C}_i] = 0 \qquad \tilde{\boldsymbol{x}} \in \partial\Omega_{x,y}, \tag{D.22}$$

$$\boldsymbol{n} \cdot [\tilde{D}_i^{eff} \tilde{\boldsymbol{\nabla}} (\frac{\tilde{C}_i}{\omega}) - \lambda_7 \tilde{\boldsymbol{u}} \tilde{C}_i] = 0 \qquad \tilde{\boldsymbol{x}} \in \partial\Omega_{PCV}, \text{ and} \tag{D.23}$$

$$\boldsymbol{n} \cdot [\tilde{D}_i^{eff} \tilde{\boldsymbol{\nabla}} (\frac{\tilde{C}_i}{\omega}) - \lambda_7 \tilde{\boldsymbol{u}} \tilde{C}_i] = 0 \qquad \tilde{\boldsymbol{x}} \in \partial\Omega_{DLAV}. \tag{D.24}$$

On the DA surface, proMMP2, MMP2, TIMP2, and MMP2·TIMP2 obey no-flux boundary conditions; they have the form

$$\boldsymbol{n} \cdot [\tilde{D}_i^{eff} \tilde{\boldsymbol{\nabla}} (\frac{\tilde{C}_i}{\omega}) - \lambda_7 \tilde{\boldsymbol{u}} \tilde{C}_i] = 0 \qquad \tilde{\boldsymbol{x}} \in \partial\Omega_{DA}. \tag{D.25}$$

There is a constant flux of VEGFC from the DA surface into the interstitial space domain. This boundary condition is represented by the equation

$$-\boldsymbol{n} \cdot [-\tilde{D}_{VC}^{eff} \tilde{\boldsymbol{\nabla}} (\frac{\tilde{C}_{VC}}{\omega}) + \lambda_7 \tilde{\boldsymbol{u}} \tilde{C}_{VC}] = \lambda_{VC}^{DA} \qquad \tilde{\boldsymbol{x}} \in \partial\Omega_{DA}. \tag{D.26}$$

On the interface between the LEC and interstitial space domains, proMMP2, MMP2, and TIMP2 obey continuity conditions, which are modelled by the equations,

$$\boldsymbol{n} \cdot [\tilde{D}_i^{eff} \tilde{\boldsymbol{\nabla}} (\frac{\tilde{C}_i}{\omega}) - \lambda_7 \tilde{\boldsymbol{u}} \tilde{C}_i]|_{\partial\Omega_{LEC/IS+}} = -\boldsymbol{n} \cdot (\lambda_{1,i} \tilde{\boldsymbol{\nabla}} \tilde{C}_i)|_{\partial\Omega_{LEC/IS-}} \text{ and} \tag{D.27}$$

$$\tilde{C}_i|_{\partial\Omega_{LEC/IS+}} = \tilde{C}_i|_{\partial\Omega_{LEC/IS-}}. \tag{D.28}$$

On the same interface, MMP2·TIMP2 and VEGFC obey no-flux conditions of the form

$$\boldsymbol{n} \cdot [\tilde{D}_i^{eff} \tilde{\boldsymbol{\nabla}} (\frac{\tilde{C}_i}{\omega}) - \lambda_7 \tilde{\boldsymbol{u}} \tilde{C}_i] = 0 \qquad \tilde{\boldsymbol{x}} \in \partial\Omega_{LEC/IS+}. \tag{D.29}$$

D.4 Initial Conditions

At $\tilde{t} = 0$, $\tilde{C}_{C1} = 1$ in the interstitial space domain while the other concentrations are zero; in the LEC domain, $\tilde{C}_{MT1} = 1$ and the other concentrations are zero. The interstitial flow component is a stationary model, so $\tilde{P}$ and $\tilde{\boldsymbol{u}}$ do not require any initial conditions.

TABLE D.1: Characteristic scales of the primary system. M2P abbreviates proMMP2; M2, MMP2; T2, TIMP2; VC, VEGFC; C1, collagen I; MT1, MT1-MMP.

Scale	Description	Value
$C_{C1,s}$	Concentration scale for C1	3.50×10^{-1} mol m^{-3}
$C_{VC,s}$	Concentration scale for VC	1.64×10^{-7} mol m^{-3}
$C_{VC\cdot C1,s}$	Concentration scale for VC·C1	8.93×10^{-2} mol m^{-3}
$C_{M2,s}$	Concentration scale for M2	3.94×10^{-2} mol m^{-3}
$C_{M2P,s}$	Concentration scale for M2P	1.14 mol m^{-3}
$C_{M2\cdot T2,s}$	Concentration scale for M2·T2	6.68×10^{4} mol m^{-3}
$C_{MT1,s}$	Concentration scale for MT1	5.71×10^{-4} mol m^{-3}
$C_{MT1\cdot T2,s}$	Concentration scale for MT1·T2	5.71×10^{-4} mol m^{-3}
$C_{MT1\cdot T2\cdot M2P,s}$	Concentration scale for MT1·T2·M2P	5.71×10^{-4} mol m^{-3}
$C_{T2,s}$	Concentration scale for T2	6.65×10^{-3} mol m^{-3}
L	Length scale	4.34×10^{-4} m
P^{DA}	Pressure scale and DA pressure	24.585 kg m^{-1} s^{-2}
τ	Time scale	43200 s
U	Velocity scale	1.371×10^{-10} m s^{-1}

D.5 Scales and Parameters

To simulate the primary system using the above mathematical model, we need the model parameters. They are tabulated in tables D.1, D.2, and D.3.

TABLE D.2: Dimensionless parameters in the nondimensionalised interstitial flow and reaction-diffusion-convection equations. DA abbreviates dorsal aorta; PCV, posterior cardinal vein; DLAV, dorsal longitudinal anastomotic vessel; M2P, proMMP2; M2, MMP2; T2, TIMP2; VC, VEGFC; C1, collagen I.

Parameter	Form	Value
α	Constant	-2.70
η_1	$\frac{\mu U L}{P^{DA}\beta(M_{C1}C_{C1,s})^{\alpha}}$	1
η_2	$\frac{C_{VC\cdot C1,s}}{C_{C1,s}}$	0.255
η_3	$\frac{\mu U}{L P^{DA}}$	1.542×10^{-11}
η_{DA}	$\frac{L_{DA}P^{DA}}{U}$	1.317×10^{14}
η_{PCV}	$\frac{L_{PCV}P^{DA}}{U}$	1.317×10^{14}
η_{DLAV}	$\frac{2L_{DLAV}P^{DA}}{U}$	2.634×10^{14}
$\lambda_{1,VC}$	$\frac{D^{\infty}_{VC}\tau}{L^2}$	1.15×10^{1}
$\lambda_{1,M2}$	$\frac{D^{\infty}_{M2}\tau}{L^2}$	1.95×10^{1}
$\lambda_{1,M2P}$	$\frac{D^{\infty}_{M2P}\tau}{L^2}$	1.83×10^{1}
$\lambda_{1,M2\cdot T2}$	$\frac{D^{\infty}_{M2\cdot T2}\tau}{L^2}$	1.72×10^{1}
$\lambda_{1,T2}$	$\frac{D^{\infty}_{T2}\tau}{L^2}$	2.52×10^{1}
$\lambda_{2,VC}$	$\frac{k_B T}{6\pi\mu D^{\infty}_{VC} r_f}$	1.81
$\lambda_{2,M2}$	$\frac{k_B T}{6\pi\mu D^{\infty}_{M2} r_f}$	1.07
$\lambda_{2,M2P}$	$\frac{k_B T}{6\pi\mu D^{\infty}_{M2P} r_f}$	1.14
$\lambda_{2,M2\cdot T2}$	$\frac{k_B T}{6\pi\mu D^{\infty}_{M2\cdot T2} r_f}$	1.21
$\lambda_{2,T2}$	$\frac{k_B T}{6\pi\mu D^{\infty}_{T2} r_f}$	8.26×10^{-1}
λ_3	$v_{C1}M_{C1}C_{C1,s}$	7.88×10^{-2}
λ_4	$v_{C1}M_{C1}C_{VC\cdot C1,s}$	2.01×10^{-2}
λ_5	$v_{C1h}M_{C1}C_{C1,s}$	1.98×10^{-1}
λ_6	$v_{C1h}M_{C1}C_{VC\cdot C1,s}$	5.06×10^{-2}
λ_7	$\frac{U\tau}{L}$	1.36×10^{-2}

TABLE D.3: Dimensionless parameters in the nondimensionalised reaction terms. λ_{28} is not really dimensionless and is in mol m^{-3}, but the term $\frac{\lambda_{28}\tilde{C}_{M2}\tilde{C}_{C1}}{K_M^{M2,C1}+C_{C1,s}\tilde{C}_{C1}}$ is dimensionless because the denominator is also in mol m^{-3}. M2P abbreviates proMMP2; M2, MMP2; T2, TIMP2; VC, VEGFC; C1, collagen I; MT1, MT1-MMP; DA, dorsal aorta.

Parameter	Form	Value
λ_8	$\frac{P_{M2P}\tau}{C_{M2P,s}}$	1
λ_9	$k^{on}_{MT1\cdot T2,M2P}\tau C_{MT1\cdot T2,s}$	3.45×10^{3}
λ_{10}	$\frac{k^{off}_{MT1\cdot T2,M2P}\tau C_{MT1\cdot T2\cdot M2P,s}}{C_{M2P,s}}$	1.02×10^{-1}
λ_{11}	$k^{deg}_{M2P}\tau$	4.32
λ_{12}	$\frac{k^{eff}_{act}\tau C_{MT1\cdot T2\cdot M2P,s}C_{MT1,s}}{C_{M2,s}}$	1
λ_{13}	$k^{on}_{M2,T2}\tau C_{T2,s}$	1.69×10^{6}
λ_{14}	$\frac{k^{off}_{M2,T2}\tau C_{M2\cdot T2,s}}{C_{M2,s}}$	4.61×10^{11}
λ_{15}	$k^{deg}_{M2}\tau$	4.32
λ_{16}	$\frac{P_{T2}\tau}{C_{T2,s}}$	1
λ_{17}	$k^{on}_{MT1,T2}\tau C_{MT1,s}$	8.73×10^{4}
λ_{18}	$\frac{k^{off}_{MT1,T2}\tau C_{MT1\cdot T2,s}}{C_{T2,s}}$	7.42×10^{-1}
λ_{19}	$k^{on}_{M2,T2}\tau C_{M2,s}$	1×10^{7}
λ_{20}	$\frac{k^{off}_{M2,T2}\tau C_{M2\cdot T2,s}}{C_{T2,s}}$	2.73×10^{12}
λ_{21}	$k^{deg}_{T2}\tau$	4.32
λ_{22}	$\frac{k^{on}_{M2,T2}\tau C_{M2,s}C_{T2,s}}{C_{M2\cdot T2,s}}$	1
λ_{23}	$k^{off}_{M2,T2}\tau$	2.72×10^{5}
λ_{24}	$k^{deg}_{M2\cdot T2}\tau$	4.32
λ_{25}	$k^{on}_{VC,C1}\tau C_{C1,s}$	5.44×10^{5}
λ_{26}	$\frac{k^{off}_{VC,C1}\tau C_{VC\cdot C1,s}}{C_{VC,s}}$	8.47×10^{7}
λ_{27}	$k^{deg}_{VC}\tau$	4.32
λ^{DA}_{VC}	$\frac{R^{DA}_{VC}\tau}{C_{VC,s}L}$	1
λ_{28}	$k^{cat}_{M2,C1}\tau C_{M2,s}$	7.66×10^{-3}
λ_{29}	$k^{on}_{VC,C1}\tau C_{VC,s}$	2.55×10^{-1}
λ_{30}	$\frac{k^{off}_{VC,C1}\tau C_{VC\cdot C1,s}}{C_{C1,s}}$	3.97×10^{1}
λ_{31}	$\frac{k^{on}_{VC,C1}\tau C_{VC,s}C_{C1,s}}{C_{VC\cdot C1,s}}$	1
λ_{32}	$k^{off}_{VC,C1}\tau$	1.56×10^{2}
λ_{33}	$k^{on}_{MT1,T2}\tau C_{T2,s}$	1.02×10^{6}
λ_{34}	$\frac{k^{off}_{MT1,T2}\tau C_{MT1\cdot T2,s}}{C_{MT1,s}}$	8.64
λ_{35}	$\frac{k^{on}_{MT1,T2}\tau C_{MT1,s}C_{T2,s}}{C_{MT1\cdot T2,s}}$	1.02×10^{6}
λ_{36}	$k^{off}_{MT1,T2}\tau$	8.64
λ_{37}	$k^{on}_{MT1\cdot T2,M2P}\tau C_{M2P,s}$	6.89×10^{6}
λ_{38}	$\frac{k^{off}_{MT1\cdot T2,M2P}\tau C_{MT1\cdot T2\cdot M2P,s}}{C_{MT1\cdot T2,s}}$	2.03×10^{2}
λ_{39}	$\frac{k^{eff}_{act}\tau C_{MT1\cdot T2\cdot M2P,s}C_{MT1,s}}{C_{MT1\cdot T2,s}}$	6.91×10^{1}
λ_{40}	$\frac{k^{on}_{MT1\cdot T2,M2P}\tau C_{MT1\cdot T2,s}C_{M2P,s}}{C_{MT1\cdot T2\cdot M2P,s}}$	6.89×10^{6}
λ_{41}	$k^{off}_{MT1\cdot T2,M2P}\tau$	2.03×10^{2}
λ_{42}	$k^{eff}_{act}\tau C_{MT1,s}$	6.91×10^{1}

Appendix E

Numerical Solution of Partial Differential Equations

In the engineering and natural sciences, the mathematical models are mostly based on PDEs. Generally, these models cannot be solved analytically. In order to make predictions using the models, one must resort to numerical methods. The primary system's mathematical model, summarised in appendix D, is a set of coupled ODEs and PDEs. The numerical solutions of it and its modified forms, presented in chapter 5, were obtained in COMSOL Multiphysics. COMSOL Multiphysics is a software package that uses the finite element method (FEM) to find approximate solutions to PDEs. In this appendix, we will learn about the FEM and other related numerical methods. Our major source is Fletcher (1991) although we will also consult Morton and Mayers (1994) and DuChateau and Zachmann (2011).

These numerical methods have two general stages. First, discretisation turns a system of continuous PDEs into a system of discrete algebraic equations. Second, the algebraic equations are solved. In the first stage, the derivatives in the PDEs are discretised; this step involves truncation errors. The second stage involves round-off errors associated with the mathematical operations carried out by computers. The most common discretisation methods are the finite difference method (FDM), FEM, finite volume method (FVM), and spectral method. Time derivatives are almost always discretised by the FDM; spatial derivatives can be discretised by any of the four.

In the following sections, we will review these discretisation methods one by one before reviewing the criteria used to assess the performance of a numerical method: convergence, stability, and consistency.

E.1 Finite Difference Method

In the FDM, we use finite difference representations to approximate differential operators. This turns a PDE into an algebraic equation. As an example, we will consider the equation

$$\frac{\partial \bar{T}}{\partial t} = H \frac{\partial^2 \bar{T}}{\partial x^2}, \tag{E.1}$$

where $\bar{T}$ is the dependent variable, t is time, x is a spatial coordinate, and H is just a constant. The boundary and initial conditions of equation (E.1) are given by the equations,

$$\bar{T}(0,t) = b, \tag{E.2}$$

$$\bar{T}(1,t) = d, \text{ and} \tag{E.3}$$

$$\bar{T}(x,0) = \bar{T}_0(x) \qquad 0 \leq x \leq 1. \tag{E.4}$$

In order to use this method, we will create a grid in the xt-plane. The grid is a set of points defined by the equation $(x_j, t_n) = (jh, nk)$, where j and n are integers, h and k are the grid sizes for space and time respectively. The space and time derivatives of $\bar{T}$ at the node (x_j, t_n) can be related to the values of $\bar{T}$ at its neighbouring nodes, leading to the equations,

$$\bar{T}^n_{j+1} = \sum_{m=0}^{\infty} \frac{h^m}{m!} \left[\frac{\partial^m \bar{T}}{\partial x^m}\right]^n_j \text{ and} \tag{E.5}$$

$$\bar{T}^{n+1}_j = \sum_{m=0}^{\infty} \frac{k^m}{m!} \left[\frac{\partial^m \bar{T}}{\partial t^m}\right]^n_j. \tag{E.6}$$

Truncating the two series after their second terms, we will obtain the approximations,

$$\left[\frac{\partial \bar{T}}{\partial x}\right]^n_j \approx \frac{\bar{T}^n_{j+1} - \bar{T}^n_j}{h} \text{ and} \tag{E.7}$$

$$\left[\frac{\partial \bar{T}}{\partial t}\right]^n_j \approx \frac{\bar{T}^{n+1}_j - \bar{T}^n_j}{k}, \tag{E.8}$$

which are accurate to $O(h)$ and $O(k)$ respectively. These are the forward difference approximations of the derivatives. If we expand $\bar{T}^n_{j-1}$ and $\bar{T}^{n-1}_j$ at the node (x_j, t_n), we will obtain the backward difference approximations. Averaging the forward and backward approximations will give us the centred difference approximations, which are accurate to $O(h^2)$ and $O(k^2)$. More generally, by expanding $\bar{T}$ at more nodes, including more terms in the resulting Taylor series, and combining the truncated series, we can obtain higher-order approximations of the derivatives. In each case, using smaller h and k reduces the truncation errors due to discretisation. We can also approximate higher-order derivatives in this way.

Using the first-order forward difference approximation for the time derivative and the second-order centred difference approximation for the space derivative, we will turn equation (E.1), a differential equation, into the algebraic equation

$$\frac{T^{n+1}_j - T^n_j}{k} = \frac{H(T^n_{j-1} - 2T^n_j + T^n_{j+1})}{h^2}, \tag{E.9}$$

which can be rearranged to give the equation

$$T^{n+1}_j = T^n_j + \frac{Hk}{h^2}(T^n_{j-1} - 2T^n_j + T^n_{j+1}). \tag{E.10}$$

Equation (E.10) must be applied to each spatial node. We use T^n_j to denote the approximate solution to $\bar{T}^n_j$ in equations (E.9) and (E.10).

Intuitively, we expect the use of higher-order approximations on a finer grid to improve the accuracy of our method. However, it also requires more mathematical operations at more nodes to evaluate higher-order approximations, driving up the computational cost. Furthermore, higher-order approximations tend to produce unstable numerical schemes. Finally, this approach cannot improve the accuracy significantly if the exact solution is discontinuous or has severe gradients, and the grid is too coarse.

E.2 Finite Element Method

The FEM is a kind of weighted residual method. A weighted residual method assumes that the solution to a system of PDEs can be represented analytically. For example, again working with equation (E.1), we will approximate $\bar{T}$ as the series

$$T = T_0(x,t) + \sum_{j=1}^{J} a_j(t)\phi_j(x), \tag{E.11}$$

where the first term satisfies the boundary and initial conditions, $a_j(t)$'s are unknown coefficients, and $\phi_j(x)$'s are known trial functions, making T the trial solution. In our example with just one spatial dimension, the trial functions may be polynomials or trigonometric functions. If we increase the number of trial functions, we will improve the accuracy of the trial solution.

Rewriting equation (E.1), we will get the equation

$$L(\bar{T}) = \frac{\partial \bar{T}}{\partial t} - H\frac{\partial^2 \bar{T}}{\partial x^2} = 0, \tag{E.12}$$

where L is a differential operator. Its operation on equation (E.11) will not result in zero because equation (E.11) is only an approximation of $\bar{T}$. The result is instead an equation residual defined by the equation

$$L(T) = R(x,t). \tag{E.13}$$

We will determine the unknown coefficients by equating the integral of the weighted R over the problem's computational domain to zero. After this step,

$$\int W_m(x)R(x,t)dx = 0. \tag{E.14}$$

If we set up different weight functions where $m = 1, 2, 3, \ldots M$, we will obtain a system of equations; solving it will give the unknown coefficients. In our time-dependent problem, it will be a system of ODEs in time. For stationary problems, a system of algebraic equations is the norm for weighted residual methods. The choice of weight functions determines the specific weighted residual method employed. Examples are the subdomain method, collocation method, least-squares method, and Galerkin method. The weight functions and trial functions used in the Galerkin method belong to one family. Therefore, if the trial functions form a complete set, the residual must be orthogonal to every member of a complete set. When there are an infinite number of weight functions, T converges to $\bar{T}$.

We will subdivide the spatial domain into N subintervals; they are separated by nodes denoted by x_j $(j = 0, 1, 2, \ldots N)$. The coefficients in equation (E.11) are therefore the nodal unknowns T_j's, making T is an interpolation of the local nodal points. This interpolation has the general form

$$T = \sum_{j=0}^{J} T_j \phi_j(x). \tag{E.15}$$

The trial functions are low-order piecewise polynomials and they are restricted to contiguous elements. This choice will lead to relatively few non-zero terms after discretisation and they will be located close to the main diagonal of the coefficient matrix, a feature that will make the subsequent solution step more economical.

Considering linear interpolation first, the trial functions are defined by the equations,

$$\phi_j = 0 \qquad x < x_{j-1} \text{ and } x > x_{j+1}, \tag{E.16}$$

$$\phi_j = \frac{x - x_{j-1}}{x_j - x_{j-1}} \qquad x_{j-1} \le x \le x_j, \tag{E.17}$$

$$\phi_j = 1 \qquad x = x_j, \text{ and} \tag{E.18}$$

$$\phi_j = \frac{x_{j+1} - x}{x_{j+1} - x_j} \qquad x_j \le x \le x_{j+1}. \tag{E.19}$$

We notice their local nature; each trial function is non-zero in two neighbouring elements only and the approximation in each element consists of two trial functions only. In the element between x_{j-1} and x_j, we have the approximating equation

$$T = T_{j-1}\phi_{j-1} + T_j\phi_j. \tag{E.20}$$

Clearly, decreasing the grid spacing and introducing more trial functions will reduce our interpolation error. Apart from that, for the same grid spacing, we can reduce the error by using quadratic interpolation. We will consider quadratic interpolation next; each element consists of three nodes; in each element, the shape function at the midpoint is defined differently from those at the endpoints. For example, in the two elements spanning the five nodes from x_{j-2} to x_{j+2}, x_j is the boundary between the two elements. The shape function there is defined by the equations,

$$\phi_j = 0 \qquad x < x_{j-2} \text{ and } x > x_{j+2}, \tag{E.21}$$

$$\phi_j = \left(\frac{x - x_{j-2}}{x_j - x_{j-2}}\right)\left(\frac{x - x_{j-1}}{x_j - x_{j-1}}\right) \qquad x_{j-2} \le x \le x_j, \text{ and} \tag{E.22}$$

$$\phi_j = \left(\frac{x - x_{j+1}}{x_j - x_{j+1}}\right)\left(\frac{x - x_{j+2}}{x_j - x_{j+2}}\right) \qquad x_j \le x \le x_{j+2}. \tag{E.23}$$

The shape function at the midpoint x_{j-1} is defined by these equations,

$$\phi_{j-1} = 0 \qquad x < x_{j-2} \text{ and } x > x_j \text{ and} \tag{E.24}$$

$$\phi_{j-1} = \Big(\frac{x - x_{j-2}}{x_{j-1} - x_{j-2}}\Big)\Big(\frac{x - x_j}{x_{j-1} - x_j}\Big) \qquad x_{j-2} \leq x \leq x_j. \tag{E.25}$$

The approximation in each element consists of three non-zero shape functions. For example, between x_{j-2} and x_j,

$$T = T_{j-2}\phi_{j-2} + T_{j-1}\phi_{j-1} + T_j\phi_j \approx \bar{T}. \tag{E.26}$$

In general, quadratic interpolation allows a faster increase in accuracy with grid refinement. A natural extension is to increase the order of interpolation further, but the downside is the existence of more non-zero terms after discretisation, driving up the computational cost associated with the solution step. In practice, it is unusual to interpolate at an order higher than two.

This piecewise interpolation over the finite elements connects the local solution in each element to its nodal values. To complete our discretisation, we will generate a set of equations connecting the nodal values (weighted residual construction). To do so, we need to evaluate integrals, so the accuracy of this step depends on the grid size too.

Generally, the solution error of a FEM scheme is larger than its interpolation error because its nodal point solution does not coincide with its exact solution. On the other hand, the two errors decrease at the same rate with grid refinement. Intuitively, the solution error should increase with the interpolation order of the scheme. A higher-order interpolation means there are more terms in the local approximation of each element; there are more mathematical operations and therefore larger round-off errors.

The FEM offers an advantage over the FDM because it can deal with irregular computational domains like curved boundaries, but it is only distinctly superior for problems with two or more dimensions. In two dimensions (2D), bilinear interpolation requires four nodes to define an element, and four trial solutions and therefore four terms to approximate the local solution in the element. Again in 2D, biquadratic interpolation uses nine nodes to define an element, where the approximation is constructed from nine trial functions and therefore nine terms.

E.3 Finite Volume Method

Like the FEM, the finite volume method is suitable for irregular computational domains. It has an additional advantage in that it discretises the conservation form of a mathematical model. As a result, the conservation laws apply even after discretisation. The FEM and FVM are both weighted residual methods. The FVM works like the subdomain method by splitting a computational domain into a finite number of subdomains which may overlap. For each subdomain, there is a weight function which equals unity inside it and zero outside it.

The equation of motion has the generalised form

$$\frac{\partial \bar{q}}{\partial t} + \frac{\partial \bar{F}}{\partial x} + \frac{\partial \bar{G}}{\partial y} = 0. \tag{E.27}$$

Integrating this equation with a general weight function over a computational domain will give the equation

$$\int W_m \left(\frac{\partial \bar{q}}{\partial t} + \frac{\partial \bar{F}}{\partial x} + \frac{\partial \bar{G}}{\partial y}\right) dxdy = 0. \tag{E.28}$$

When the weight function is unity in the finite volume $ABCD$ and zero outside it,

$$\int_{ABCD} \frac{\partial \bar{q}}{\partial t} + \frac{\partial \bar{F}}{\partial x} + \frac{\partial \bar{G}}{\partial y} dxdy = 0. \tag{E.29}$$

Applying Green's theorem and simplifying, we can turn equation (E.29) into a statement of conservation in the form of another integral. By approximating the integral discretely, we can turn it into an ODE in time. Finally, applying the FDM to discretise the time derivative, we can convert the ODE into an algebraic equation.

Applying the above procedures to the entire computational domain, we will acquire a set of discrete algebraic equations, one for each finite volume of the domain.

While the FEM discretises a mathematical model in its differential form, the FVM discretises its integral form. Compared to the FEM, the FVM has good conservation properties and it discretises complicated domains easily. Therefore, the FVM is an excellent choice for computational fluid dynamics problems.

E.4 Spectral Method

The FDM, FEM, and FVM are all local methods because they approximate a problem in terms of functions that are not non-zero throughout the problem's computational

domain. The spectral method is a global method which uses trial and weight functions that are non-zero throughout. In this method, in contrast to the FEM, the unknown coefficients $a_j(t)$'s in equation (E.11) do not equate to the nodal unknowns. Also, the approximating and weight functions are orthogonal. Two functions, $\phi_j(x,y,z)$ and $\phi_m(x,y,z)$, are orthogonal if the following two conditions are true:

$$\iiint \phi_j(x,y,z)\phi_m(x,y,z)dxdydz \neq 0 \qquad m = j \text{ and} \tag{E.30}$$

$$\iiint \phi_j(x,y,z)\phi_m(x,y,z)dxdydz = 0 \qquad m \neq j. \tag{E.31}$$

As an example, we will apply the spectral method to the diffusion equation, equation (E.1). The boundary and initial conditions are given by the equations,

$$\bar{T}(0,t) = 0, \tag{E.32}$$

$$\bar{T}(1,t) = 1, \text{ and} \tag{E.33}$$

$$\bar{T}(x,0) = 5x - 4x^2 \qquad 0 \leq x \leq 1. \tag{E.34}$$

In the spectral method, one suitable approximate solution is the series

$$T = 5x - 4x^2 + \sum_{j=1}^{J} a_j(t) sin(j\pi x), \tag{E.35}$$

where $a_j(t)$'s are unknown coefficients. Plugging the approximate solution into the diffusion equation, we will obtain the residual

$$R = \sum_{j=1}^{J} [\frac{da_j}{dt} + a_j(j\pi)^2 H] sin(j\pi x) + 8H. \tag{E.36}$$

Next, we will evaluate the weighted integral of the residual and equate it to zero. This is represented by the integral equation

$$\sum_{j=1}^{J} [\frac{da_j}{dt} + a_j(j\pi)^2 H] \int_0^1 sin(m\pi x) sin(j\pi x) dx + 8H \int_0^1 sin(m\pi x) dx = 0. \tag{E.37}$$

The first term is only non-zero when $j = m$, so

$$\frac{da_m}{dt} + a_m(m\pi)^2 H + 8H \int_0^1 sin(m\pi x)dx = 0. \tag{E.38}$$

In equation (E.38), m goes from 1 to J. When $m = 1, 3, 5, \ldots,$
$8H \int_0^1 sin(m\pi x)dx = \frac{16H}{m\pi}$; when $m = 2, 4, 6, \ldots, 8H \int_0^1 sin(m\pi x)dx = 0$.

This is a set of ODEs in time. If we discretise the time derivatives by the FDM, we will obtain a set of algebraic equations. Solution of the algebraic equations will give us the unknown coefficients and therefore the approximate solution. As J increases, this method becomes more accurate. However, its error has two components, one associated with the spectral method and one with the time differencing. Considering the error inherent in the spectral method only, a relatively few number of terms can give a high accuracy, making the method computationally efficient.

E.5 Consistency, Convergence, Stability

A good numerical method must satisfy three conditions.

Consistency. A discretisation must be consistent with the ODE or PDE it approximates. This is true if the resulting system of algebraic equations is equivalent to the ODE or PDE at each grid point in the limit that the grid spacing tends to zero.

Convergence. The solution of the algebraic equations must be convergent. This is true if the solution approaches the exact solution of the ODE or PDE for each value of its independent variable or variables as the grid spacing tends to zero.

Stability. The numerical solution must be stable. Because computers carry out every calculation to a finite number of significant figures, round-off errors accumulate as an algorithm runs. One concern is that these errors can grow to such an extent that they drown out the numerical solution. This is generally not a problem when a stable numerical method is used. For an ODE or PDE with a bounded solution, a numerical method is said to be stable if any perturbations from the initial condition stay bounded at all iteration steps over a finite interval.

These three concepts are related in many ways and in different contexts. For example, the Lax equivalence theorem states that given a well-posed linear initial value problem and a finite difference approximation consistent with it, stability is both necessary and sufficient for convergence.

Appendix F

Secondary System

In this appendix, we will summarise the mathematical model representing the secondary system. Its derivation is presented in chapter 6. The Turing pattern analysis presented in chapter 6 is about this model.

F.1 Model Equations

The secondary system has one spatial domain only. In the interstitial space,

$$\frac{\partial \tilde{C}_{M2}}{\partial \tilde{t}} = \frac{\partial}{\partial \tilde{x}}\Big[a_{1,M2} exp\Big(-a_{2,M2}\sqrt{a_3\tilde{C}_{C1} + \frac{a_3 b_4}{b_5}\tilde{C}_{VC\cdot C1}}\Big)\frac{\partial}{\partial \tilde{x}}\Big(\frac{\tilde{C}_{M2}}{1 - a_4\tilde{C}_{C1} - \frac{a_4 b_4}{b_5}\tilde{C}_{VC\cdot C1}}\Big)\Big] + \tilde{C}_{VC}\tilde{C}_{C1} - \tilde{C}_{M2}, \quad \text{(F.1)}$$

$$\frac{\partial \tilde{C}_{VC}}{\partial \tilde{t}} = \frac{\partial}{\partial \tilde{x}}\Big[a_{1,VC} exp\Big(-a_{2,VC}\sqrt{a_3\tilde{C}_{C1} + \frac{a_3 b_4}{b_5}\tilde{C}_{VC\cdot C1}}\Big)\frac{\partial}{\partial \tilde{x}}\Big(\frac{\tilde{C}_{VC}}{1 - a_4\tilde{C}_{C1} - \frac{a_4 b_4}{b_5}\tilde{C}_{VC\cdot C1}}\Big)\Big] + \tilde{C}_{C1} - \tilde{C}_{VC} - b_1(\tilde{C}_{VC}\tilde{C}_{C1} - \tilde{C}_{VC\cdot C1}), \quad \text{(F.2)}$$

$$\frac{\partial \tilde{C}_{C1}}{\partial \tilde{t}} = b_2 - b_3\tilde{C}_{M2} - b_4(\tilde{C}_{VC}\tilde{C}_{C1} - \tilde{C}_{VC\cdot C1}), \text{ and} \quad \text{(F.3)}$$

$$\frac{\partial \tilde{C}_{VC\cdot C1}}{\partial \tilde{t}} = b_5(\tilde{C}_{VC}\tilde{C}_{C1} - \tilde{C}_{VC\cdot C1}). \quad \text{(F.4)}$$

F.2 Boundary Conditions

The secondary system has one dimension only. The boundary conditions where $\tilde{x} = 0$ and $\tilde{x} = 1$ are given by the equations,

$$\frac{\partial}{\partial \tilde{x}} \Big(\frac{\tilde{C}_{M2}}{1 - a_4 \tilde{C}_{C1} - \frac{a_4 b_4}{b_5} \tilde{C}_{VC \cdot C1}} \Big) = 0 \text{ and} \tag{F.5}$$

$$\frac{\partial}{\partial \tilde{x}} \Big(\frac{\tilde{C}_{VC}}{1 - a_4 \tilde{C}_{C1} - \frac{a_4 b_4}{b_5} \tilde{C}_{VC \cdot C1}} \Big) = 0. \tag{F.6}$$

F.3 Initial Conditions

As far as the secondary system is concerned, we are interested in the behaviour of its homogeneous steady state, not its transient dynamics. The initial conditions are the homogeneous steady state concentrations plus noises. At the homogeneous steady state,

$$\tilde{C}_{M2,ss} = \frac{b_2}{b_3}, \tag{F.7}$$

$$\tilde{C}_{VC,ss} = \sqrt{\frac{b_2}{b_3}}, \tag{F.8}$$

$$\tilde{C}_{C1,ss} = \sqrt{\frac{b_2}{b_3}}, \text{ and} \tag{F.9}$$

$$\tilde{C}_{VC \cdot C1,ss} = \frac{b_2}{b_3} = 0. \tag{F.10}$$

TABLE F.1: Characteristic scales of the secondary system. M2 abbreviates MMP2; VC, VEGFC; C1, collagen I.

Scale	Description	Value
$C_{C1,s}$	Concentration scale for C1	5.29×10^{-1} mol m^{-3}
$C_{M2,s}$	Concentration scale for M2	2.64×10^{-1} mol m^{-3}
$C_{VC,s}$	Concentration scale for VC	9.90×10^{-6} mol m^{-3}
$C_{VC\cdot C1,s}$	Concentration scale for VC·C1	5.24×10^{-2} mol m^{-3}
L	Length scale	4.34×10^{-4} m
τ	Time scale	10000 s

TABLE F.2: Dimensionless parameters in the nondimensionalised model of the secondary system. M2 abbreviates MMP2; VC, VEGFC; C1, collagen I.

Parameter	Form	Value
b_1	$k^{on}_{VC,C1}\tau C_{C1,s}$	1.90×10^{5}
b_2	$\frac{P_{C1}\tau}{C_{C1,s}}$	1.13×10^{1}
b_3	$\frac{k^{cat}_{M2,C1}\tau P_{M2}}{k^{deg}_{M2} C_{C1,s}}$	2.25×10^{1}
b_4	$\frac{k^{on}_{VC,C1}\tau P_{VC}}{k^{deg}_{VC}}$	3.56
b_5	$k^{off}_{VC,C1}\tau$	3.60×10^{1}
$a_{1,M2}$	$\frac{D^{\infty}_{M2}\tau}{L^2}$	4.51
$a_{1,VC}$	$\frac{D^{\infty}_{VC}\tau}{L^2}$	2.66
$a_{2,M2}$	$\frac{k_B T}{6\pi\mu D^{\infty}_{M2} r_f}$	1.07
$a_{2,VC}$	$\frac{k_B T}{6\pi\mu D^{\infty}_{VC} r_f}$	1.81
a_3	$v_{C1} M_{C1} C_{C1,s}$	1.19×10^{-1}
a_4	$v_{C1h} M_{C1} C_{C1,s}$	3.00×10^{-1}

F.4 Scales and Parameters

The scales and dimensionless parameters of the model are listed in tables F.1 and F.2.

Appendix G

Python Programs

In this appendix, we will present and comment on the Python programs mentioned in chapter 6. These programs use several Python modules. Therefore, before using them, we must import the modules by the following commands.

```
import string
import numpy as numpy
import heapq as heapq
from matplotlib import *
from sympy import *
from scipy import *
```

G.1 Turing Space Identification

This program identifies the Turing space of the secondary system. It does so by testing each Turing point candidate against the six criteria stated in subsection 6.3.5.

```
#First of all, we need to define two functions used to test a Turing point
    candidate.#

def turing_cand(b1,b2,b3,b4,b5):

#This function checks if the kinetic parameters of a Turing point candidate
    satisfy the first three constraints.#

    score=0

#Constraint two.#

    if b2<b3:
        score=score+1
        print 'Good. Properly scaled.'
    else:
        print 'Bad. Beyond the concentration scales.'

#Use the kinetic parameters to calculate the concentrations at the homogeneous
    steady state.#
```

```
    vc_ss=sqrt(b2/b3)
    c1_ss=sqrt(b2/b3)
    m2_ss=b2/b3
    vcc1_ss=b2/b3

#Constraint one.#

    if c1_ss*5.29e-4>1e-4:
        score=score+1
        print 'Good. There is enough collagen I.'
    else:
        print 'Bad. There is too little collagen I.'

#Find out the eigenvalues of the matrix named A.#

    homo=numpy.array([[-1,c1_ss,vc_ss,0],[0,-1-b1*c1_ss,1-b1*vc_ss,b1],[-b3,-b4*
    c1_ss,-b4*vc_ss,b4],[0,b5*c1_ss,b5*vc_ss,-b5]])
    homo_eig,homo_eigv=numpy.linalg.eig(homo)

#Constraint three.#

    if max(homo_eig.real)<0:
        score=score+1
        print 'Good. The steady state is stable with respect to homogeneous
    perturbations.'
    else:
        print 'Bad. The steady state is unstable with respect to homogeneous
    perturbations.'

#Return the number of constraints out of constraints one, two, and three that are
     satisfied.#

    return score

def turing_in(b1,b2,b3,b4,b5,a1m2,a1vc,a2m2,a2vc,a3,a4,k2):

#This function calculates the real part of the maximum eigenvalue of a Turing
    point candidate at a wavenumber.#
#Use the kinetic parameters to calculate the concentrations at the homogeneous
    steady state.#

    vc_ss=sqrt(b2/b3)
    c1_ss=sqrt(b2/b3)
    m2_ss=b2/b3
    vcc1_ss=b2/b3

#Find out the eigenvalues of the matrix named B.#

    d1m2=a1m2*exp(-a2m2*sqrt(a3*c1_ss+a3*b4*vcc1_ss/b5))/(1-a4*c1_ss-a4*b4*
    vcc1_ss/b5)
    d2m2=a1m2*exp(-a2m2*sqrt(a3*c1_ss+a3*b4*vcc1_ss/b5))*a4*m2_ss/(1-a4*c1_ss-a4*
    b4*vcc1_ss/b5)**2
    d3m2=a1m2*exp(-a2m2*sqrt(a3*c1_ss+a3*b4*vcc1_ss/b5))*a4*b4*m2_ss/(b5*(1-a4*
    c1_ss-a4*b4*vcc1_ss/b5)**2)
    d1vc=a1vc*exp(-a2vc*sqrt(a3*c1_ss+a3*b4*vcc1_ss/b5))/(1-a4*c1_ss-a4*b4*
    vcc1_ss/b5)
    d2vc=a1vc*exp(-a2vc*sqrt(a3*c1_ss+a3*b4*vcc1_ss/b5))*a4*vc_ss/(1-a4*c1_ss-a4*
    b4*vcc1_ss/b5)**2
```

```
    d3vc=a1vc*exp(-a2vc*sqrt(a3*c1_ss+a3*b4*vcc1_ss/b5))*a4*b4*vc_ss/(b5*(1-a4*
    c1_ss-a4*b4*vcc1_ss/b5)**2)

    hete=numpy.array([[-1-k2*d1m2,c1_ss,vc_ss-k2*d2m2,-k2*d3m2],[0,-1-b1*c1_ss-k2
    *d1vc,1-b1*vc_ss-k2*d2vc,b1-k2*d3vc],[-b3,-b4*c1_ss,-b4*vc_ss,b4],[0,b5*c1_ss
    ,b5*vc_ss,-b5]])
    hete_eig,hete_eigv=numpy.linalg.eig(hete)

#Return the real part of the maximum eigenvalue of B.#

    return max(hete_eig.real)

#Having defined the functions, we will now use them to study our 1953125 Turing
    point candidates. They have 3125 combinations of kinetic parameters. Our
    first step is to shortlist these combinations using the first three
    constraints.#

#We will create a list to contain the shortlisted combinations of kinetic
    parameters.#

candidate=[]

#Vary each kinetic parameter by two orders of magnitude in each direction. Test
    if each resulting combination of kinetic parameters satisfies the first three
     constraints.#

for i in [1,0.1,0.01,10,100]:
    for j in [1,0.1,0.01,10,100]:
        for k in [1,0.1,0.01,10,100]:
            for l in [1,0.1,0.01,10,100]:
                for m in [1,0.1,0.01,10,100]:
                    b1=1.9e5*i
                    b2=1.13e1*j
                    b3=2.25e1*k
                    b4=3.56*l
                    b5=3.6e1*m

                    if turing_cand(b1,b2,b3,b4,b5)==3:
                        candidate.append([b1,b2,b3,b4,b5])

#There are 537 combinations of kinetic parameters in the shortlist. It means
    67125 Turing point candidates satisfy the first three constraints. We will
    test if they satisfy the final three constraints and obtain their dispersion
    relations.#

#The shortlisted candidates are either stable or unstable with respect to
    heterogeneous perturbations. Create two lists to contain the two groups of
    candidates.#

unstable=[]
stable=[]
count=0

#Vary each diffusion coefficient and viscosity by two orders of magnitude in each
     direction. Obtain the dispersion relation of each resulting Turing point
    candidate. Check if it satisfies constraint four.#

for i in [1,0.1,0.01,10,100]:
    for j in [1,0.1,0.01,10,100]:
```

```
        for k in [1,0.1,0.01,10,100]:
            for l in candidate:
                a1m2=4.51*i
                a1vc=2.66*j
                a2m2=1.07/i/k
                a2vc=1.81/j/k
                a3=1.19e-1
                a4=3e-1
                b1=l[0]
                b2=l[1]
                b3=l[2]
                b4=l[3]
                b5=l[4]

#For each relevant wavenumber (n from 0 to 87, inclusive), find out the
    eigenvalue of B with the maximum real part. The collection of these
    eigenvalues is the dispersion relation of the Turing point candidate under
    consideration.#

                dispersion=[]
                for k2 in [(n*pi)**2 for n in range (0,88)]:
                    dummy=turing_in(b1,b2,b3,b4,b5,a1m2,a1vc,a2m2,a2vc,a3,a4,k2)
                    dispersion.append(dummy)

#Constraint four. If the Turing point candidate satisfies constraint four, it is
    unstable with respect to heterogeneous perturbations.#

                if max(dispersion)>0:
                    count=count+1
                    print 'New unstable candidate:', count
                    unstable.append([b1,b2,b3,b4,b5,a1m2,a1vc,a2m2,a2vc,a3,a4,
    dispersion])
                else:
                    stable.append([b1,b2,b3,b4,b5,a1m2,a1vc,a2m2,a2vc,a3,a4,
    dispersion])

#Next, we will test if the Turing point candidates that are unstable with respect
     to heterogeneous perturbations satisfy constraints five and six. If a
    candidate satisfies both constraints, it qualifies as a Turing point. If a
    candidate satisfies constraint five only, its dispersion relation has a
    maximum in the relevant range of wavenumbers (2<n<87), but it does not have a
     bounded positive region in the assessed range (n from 0 to 87, inclusive).#
#Create two lists to contain these two classes of Turing point candidates.#

band=[]
maximum=[]
count1=0
count2=0

#Test all the Turing point candidates that are unstable with respect to
    heterogeneous perturbations.#

for i in unstable:

#Pick out the dispersion relation of the candidate being tested.#

    dispersion=i[11]

#Find out its maximum and the corresponding wavenumber or value of n.#
```

```
    max_value=max(dispersion)
    max_index=dispersion.index(max(dispersion))

#Constraint five. If the maximum does not lie where n is 0, 1, 2, or 87, the
    candidate satisfies constraint five.#

    if max_index != 0 and max_index !=1 and max_index !=2 and max_index !=87:
        dispersion_short=dispersion[max_index:]

#Constraint six.#

        if max(dispersion_short)*min(dispersion_short)<0:
            band.append(i)
            count1=count1+1
            print 'New Turing point:', count1
        else:
            maximum.append(i)
            count2=count2+1
            print 'New maximum:', count2

#Finally, we will export our results.#

#This file contains the shortlisted combinations of kinetic parameters. There are
     537 of them, corresponding to 67125 Turing point candidates.#

dataFile = open('shortlist.txt', 'w')
for eachitem in candidate:
    dataFile.write(str(eachitem)+'\n')
dataFile.close()

#This file contains the shortlisted Turing point candidates that are stable with
    respect to heterogeneous perturbations. There are 14951 of them.#

dataFile = open('stable.txt', 'w')
for eachitem in stable:
    dataFile.write(str(eachitem)+'\n')
dataFile.close()

#This file contains the shortlisted Turing point candidates that are unstable
    with respect to heterogeneous perturbations. There are 52174 of them.#

dataFile = open('unstable.txt', 'w')
for eachitem in unstable:
    dataFile.write(str(eachitem)+'\n')
dataFile.close()

#This file contains the Turing points. There are 94 of them.#

dataFile = open('turing1_band.txt', 'w')
for eachitem in band:
    dataFile.write(str(eachitem)+'\n')
dataFile.close()

#This file contains the Turing point candidates that do not satisfy constraint
    six only. There are 32 of them.#

dataFile = open('turing2_maximum.txt', 'w')
for eachitem in maximum:
```

```
    dataFile.write(str(eachitem)+'\n')
dataFile.close()
```

G.2 Ranking Algorithm

For each Turing point, this program calculates its distance from the reference point in the parametric space. Then, it selects the ten points closest to the reference point.

```
#First, we load the file containing the Turing points and their dispersion
    relations. We will put them in a list; each element contains the parameters
    of a Turing point and its dispersion relation.#

file=open('turing1_band.txt','r')
band_temp=file.read().splitlines()
file.close()

band=[]
for i in band_temp:
    band.append(eval(i))

#Define the reference point in the parametric space.#

parameters=[1.9e5, 1.13e1, 2.25e1, 3.56, 3.6e1, 4.51, 2.66, 1.07, 1.81]

#Calculate the distance between each Turing point and the reference point.#

band_distance=[]
for i in band:
    summation=0
    for j in range(9):
        summation=summation+((parameters[j]-i[j])/parameters[j])**2
    band_distance.append(sqrt(summation))

#Pick out the ten Turing points closest to the reference point. This algorithm
    does not distinguish among Turing points that lie at the same distance from
    the reference point. For example, if we input twelve Turing points with the
    same distance from the reference point, the algorithm will return all of them
    .#

band10_distance=heapq.nsmallest(10, band_distance)

band10_distance_set=[]
for i in set(band10_distance):
    band10_distance_set.append(i)
band10_distance_set.sort()

band10_index=[]
for i in band10_distance_set:
    for j, x in enumerate(band_distance):
        if x==i:
            band10_index.append(j)

band10=[]
for i in band10_index:
    band10.append(band[i])
```

```
#Finally, we will export our results.#

dataFile = open('band10.txt', 'w')
for eachitem in band10:
    dataFile.write(str(eachitem)+'\n')
dataFile.close()
```

G.3 Bifurcation

The following two programs calculate the dispersion relations at different values of b_3 and b_4. b_3 is controlled by P_{M2}; b_4 is controlled by P_{VC}. When b_3 or b_4 is varied by the appropriate program, the other parameters of the model are fixed. Each program plots the dispersion relations it generates together for comparison.

G.3.1 MMP2 Production Rate

```
#First, define a function that calculates the real part of the maximum eigenvalue
     of a Turing point candidate at a wavenumber.#

def turing_senb3(b3,k2):

#This function takes two arguments, the b3 value and wavenumber under
    consideration.#
#The other parameters are held constant as follows.#

    b1=1.9e3
    b2=113.0
    b4=3.56
    b5=36.0
    a1m2=0.451
    a1vc=2.66
    a2m2=107.0
    a2vc=18.1
    a3=1.19e-1
    a4=3e-1

#Calculate the homogeneous steady state for the b3 value under consideration.#

    vc_ss=sqrt(b2/b3)
    c1_ss=sqrt(b2/b3)
    m2_ss=b2/b3
    vcc1_ss=b2/b3

#Find out the eigenvalues of the matrix named B.#

    d1m2=a1m2*exp(-a2m2*sqrt(a3*c1_ss+a3*b4*vcc1_ss/b5))/(1-a4*c1_ss-a4*b4*
    vcc1_ss/b5)
    d2m2=a1m2*exp(-a2m2*sqrt(a3*c1_ss+a3*b4*vcc1_ss/b5))*a4*m2_ss/(1-a4*c1_ss-a4*
    b4*vcc1_ss/b5)**2
    d3m2=a1m2*exp(-a2m2*sqrt(a3*c1_ss+a3*b4*vcc1_ss/b5))*a4*b4*m2_ss/(b5*(1-a4*
    c1_ss-a4*b4*vcc1_ss/b5)**2)
```

```
    d1vc=a1vc*exp(-a2vc*sqrt(a3*c1_ss+a3*b4*vcc1_ss/b5))/(1-a4*c1_ss-a4*b4*
    vcc1_ss/b5)
    d2vc=a1vc*exp(-a2vc*sqrt(a3*c1_ss+a3*b4*vcc1_ss/b5))*a4*vc_ss/(1-a4*c1_ss-a4*
    b4*vcc1_ss/b5)**2
    d3vc=a1vc*exp(-a2vc*sqrt(a3*c1_ss+a3*b4*vcc1_ss/b5))*a4*b4*vc_ss/(b5*(1-a4*
    c1_ss-a4*b4*vcc1_ss/b5)**2)

    hete=numpy.array([[-1-k2*d1m2,c1_ss,vc_ss-k2*d2m2,-k2*d3m2],[0,-1-b1*c1_ss-k2
    *d1vc,1-b1*vc_ss-k2*d2vc,b1-k2*d3vc],[-b3,-b4*c1_ss,-b4*vc_ss,b4],[0,b5*c1_ss
    ,b5*vc_ss,-b5]])
    hete_eig,hete_eigv=numpy.linalg.eig(hete)

#Return the real part of the maximum eigenvalue of B.#

    return max(hete_eig.real)

#Create a list of the b3 values of interest. This is a wide range.#

testb3_wide=[2.25e-1,2.25e0,2.25e1,2.25e2,2.25e3]

#Create a list to hold the dispersion relations for the b3 values of interest.#

b3dispersion_wide=[]

#Consider the b3 values one by one.#

for i in testb3_wide:

#Check that the b3 value under consideration gives properly scaled concentrations
     at the homogeneous steady state.#

    if 113.0<i:
        print 'Good. Properly scaled.'
    else:
        print 'Bad. Beyond the concentration scales. b3',i,'is the problem.'

#Check that the b3 value gives a high enough collagen I concentration at the
    homogeneous steady state.#

    if sqrt(113.0/i)*5.29e-4>1e-4:
        print 'Good. There is enough collagen I.'
    else:
        print 'Bad. There is too little collagen I. b3',i,'is the problem.'

#Create a list to hold the real part of the maximum eigenvalue of B at each
    wavenumber.#

    dispersion=[]

#Use the function defined earlier to compute the real part of the maximum
    eigenvalue of B at each wavenumber.#

    for k2 in [(n*pi)**2 for n in range (0,88)]:
        dummy=turing_senb3(i,k2)
        dispersion.append(dummy)

#Place the complete dispersion relation for the b3 value into the list of
    dispersion relations.#
```

```
    b3dispersion_wide.append(dispersion)

#Do the same for a narrower range of b3 values.#

testb3_narrow=[250.0,750.0,1250.0,1750.0,2250.0]

b3dispersion_narrow=[]

for i in testb3_narrow:

    if 113.0<i:
        print 'Good. Properly scaled.'
    else:
        print 'Bad. Beyond the concentration scales. b3',i,'is the problem.'

    if sqrt(113.0/i)*5.29e-4>1e-4:
        print 'Good. There is enough collagen I.'
    else:
        print 'Bad. There is too little collagen I. b3',i,'is the problem.'

    dispersion=[]

    for k2 in [(n*pi)**2 for n in range (0,88)]:
        dummy=turing_senb3(i,k2)
        dispersion.append(dummy)

    b3dispersion_narrow.append(dispersion)

#There are two groups of b3 values, wide and narrow. We will create one big
    figure with two subplots, one for each group.#
#For each subplot, the x-axis represents n which goes from 0 to 87.#

n=range(0,88)

#Create and title one big figure that contains both subplots.#

big=pyplot.figure()
pyplot.suptitle('Bifurcation Analysis of the following Turing Point with Respect
    to b3: \n b1=1900, b2=113, b3=2250, b4=3.56, b5=36, a1m2=0.451, a1vc=2.66,
    a2m2=107, a2vc=18.1')

#Create the first subplot: the wide range of b3 values.#

big.add_subplot(211)
pyplot.plot(n,b3dispersion_wide[0],marker='.',linestyle='None',color='blue',label
    ='b3=0.225')
pyplot.plot(n,b3dispersion_wide[1],marker='*',linestyle='None',color='red',label
    ='b3=2.25')
pyplot.plot(n,b3dispersion_wide[2],marker='o',linestyle='None',color='green',
    label='b3=22.5')
pyplot.plot(n,b3dispersion_wide[3],marker='x',linestyle='None',color='magenta',
    label='b3=225')
pyplot.plot(n,b3dispersion_wide[4],marker='s',linestyle='None',color='yellow',
    label='b3=2250')
pyplot.legend(loc=9)
pyplot.xlabel('n')
pyplot.ylabel('Maximum Eigenvalue (Real Part)')

#Create the second subplot: the narrow range of b3 values.#
```

```
big.add_subplot(212)
pyplot.plot(n,b3dispersion_narrow[0],marker='.',linestyle='None',color='blue',
    label='b3=250')
pyplot.plot(n,b3dispersion_narrow[1],marker='*',linestyle='None',color='red',
    label='b3=750')
pyplot.plot(n,b3dispersion_narrow[2],marker='o',linestyle='None',color='green',
    label='b3=1250')
pyplot.plot(n,b3dispersion_narrow[3],marker='x',linestyle='None',color='magenta',
    label='b3=1750')
pyplot.plot(n,b3dispersion_narrow[4],marker='s',linestyle='None',color='yellow',
    label='b3=2250')
pyplot.legend()
pyplot.xlabel('n')
pyplot.ylabel('Maximum Eigenvalue (Real Part)')
```

G.3.2 VEGFC Production Rate

```
#First, define a function that calculates the real part of the maximum eigenvalue
     of a Turing point candidate at a wavenumber.#

def turing_senb4(b4,k2):

#This function takes two arguments, the b4 value and wavenumber under
    consideration.#
#The other parameters are held constant as follows.#

    b1=1.9e3
    b2=113.0
    b3=2250.0
    b5=36.0
    a1m2=0.451
    a1vc=2.66
    a2m2=107.0
    a2vc=18.1
    a3=1.19e-1
    a4=3e-1

#Calculate the homogeneous steady state for the b4 value under consideration.#

    vc_ss=sqrt(b2/b3)
    c1_ss=sqrt(b2/b3)
    m2_ss=b2/b3
    vcc1_ss=b2/b3

#Find out the eigenvalues of the matrix named B.#

    d1m2=a1m2*exp(-a2m2*sqrt(a3*c1_ss+a3*b4*vcc1_ss/b5))/(1-a4*c1_ss-a4*b4*
    vcc1_ss/b5)
    d2m2=a1m2*exp(-a2m2*sqrt(a3*c1_ss+a3*b4*vcc1_ss/b5))*a4*m2_ss/(1-a4*c1_ss-a4*
    b4*vcc1_ss/b5)**2
    d3m2=a1m2*exp(-a2m2*sqrt(a3*c1_ss+a3*b4*vcc1_ss/b5))*a4*b4*m2_ss/(b5*(1-a4*
    c1_ss-a4*b4*vcc1_ss/b5)**2)
    d1vc=a1vc*exp(-a2vc*sqrt(a3*c1_ss+a3*b4*vcc1_ss/b5))/(1-a4*c1_ss-a4*b4*
    vcc1_ss/b5)
    d2vc=a1vc*exp(-a2vc*sqrt(a3*c1_ss+a3*b4*vcc1_ss/b5))*a4*vc_ss/(1-a4*c1_ss-a4*
    b4*vcc1_ss/b5)**2
```

```
    d3vc=a1vc*exp(-a2vc*sqrt(a3*c1_ss+a3*b4*vcc1_ss/b5))*a4*b4*vc_ss/(b5*(1-a4*
    c1_ss-a4*b4*vcc1_ss/b5)**2)

    hete=numpy.array([[-1-k2*d1m2,c1_ss,vc_ss-k2*d2m2,-k2*d3m2],[0,-1-b1*c1_ss-k2
    *d1vc,1-b1*vc_ss-k2*d2vc,b1-k2*d3vc],[-b3,-b4*c1_ss,-b4*vc_ss,b4],[0,b5*c1_ss
    ,b5*vc_ss,-b5]])
    hete_eig,hete_eigv=numpy.linalg.eig(hete)

#Return the real part of the maximum eigenvalue of B.#

    return max(hete_eig.real)

#Create a list of the b4 values of interest. This is a wide range.#

testb4_wide=[0.0356,0.356,3.56,35.6,356.0]

#Create a list to hold the dispersion relations for the b4 values of interest.#

b4dispersion_wide=[]

#Consider the b4 values one by one.#

for i in testb4_wide:

#Create a list to hold the real part of the maximum eigenvalue of B at each
    wavenumber.#

    dispersion=[]

#Use the function defined earlier to compute the real part of the maximum
    eigenvalue of B at each wavenumber.#

    for k2 in [(n*pi)**2 for n in range (0,88)]:
        dummy=turing_senb4(i,k2)
        dispersion.append(dummy)

#Place the complete dispersion relation for the b4 value under consideration into
     the list of dispersion relations.#

    b4dispersion_wide.append(dispersion)

#Do the same for a narrower range of b4 values.#

testb4_narrow=[3.56/10,3.56/5,3.56,3.56*5,3.56*10]
b4dispersion_narrow=[]

for i in testb4_narrow:
    dispersion=[]

    for k2 in [(n*pi)**2 for n in range (0,88)]:
        dummy=turing_senb4(i,k2)
        dispersion.append(dummy)

    b4dispersion_narrow.append(dispersion)

#There are two groups of b4 values, wide and narrow. We will create one big
    figure with two subplots, one for each group.#
#For each subplot, the x-axis represents n which goes from 0 to 87.#
```

```
n=range(0,88)

#Create and title one big figure that contains both subplots.#

big=pyplot.figure()
pyplot.suptitle('Bifurcation Analysis of the following Turing Point with Respect
    to b4: \n b1=1900, b2=113, b3=2250, b4=3.56, b5=36, a1m2=0.451, a1vc=2.66,
    a2m2=107, a2vc=18.1')

#Create the first subplot: the wide range of b4 values.#

big.add_subplot(211)
pyplot.plot(n,b4dispersion_wide[0],marker='.',linestyle='None',color='blue',label
    ='b4=0.0356')
pyplot.plot(n,b4dispersion_wide[1],marker='*',linestyle='None',color='red',label
    ='b4=0.356')
pyplot.plot(n,b4dispersion_wide[2],marker='o',linestyle='None',color='green',
    label='b4=3.56')
pyplot.plot(n,b4dispersion_wide[3],marker='x',linestyle='None',color='magenta',
    label='b4=35.6')
pyplot.plot(n,b4dispersion_wide[4],marker='s',linestyle='None',color='yellow',
    label='b4=356')
pyplot.legend()
pyplot.xlabel('n')
pyplot.ylabel('Maximum Eigenvalue (Real Part)')

#Create the second subplot: the narrow range of b4 values.#

big.add_subplot(212)
pyplot.plot(n,b4dispersion_narrow[0],marker='.',linestyle='None',color='blue',
    label='b4=0.356')
pyplot.plot(n,b4dispersion_narrow[1],marker='*',linestyle='None',color='red',
    label='b4=0.712')
pyplot.plot(n,b4dispersion_narrow[2],marker='o',linestyle='None',color='green',
    label='b4=3.56')
pyplot.plot(n,b4dispersion_narrow[3],marker='x',linestyle='None',color='magenta',
    label='b4=17.8')
pyplot.plot(n,b4dispersion_narrow[4],marker='s',linestyle='None',color='yellow',
    label='b4=35.6')
pyplot.legend()
pyplot.xlabel('n')
pyplot.ylabel('Maximum Eigenvalue (Real Part)')
```

Appendix H

Dispersion Relations

Ten dispersion relations are presented in figures 6.2 and 6.3 in chapter 6. In this appendix, we will provide larger versions of those dispersion relations.

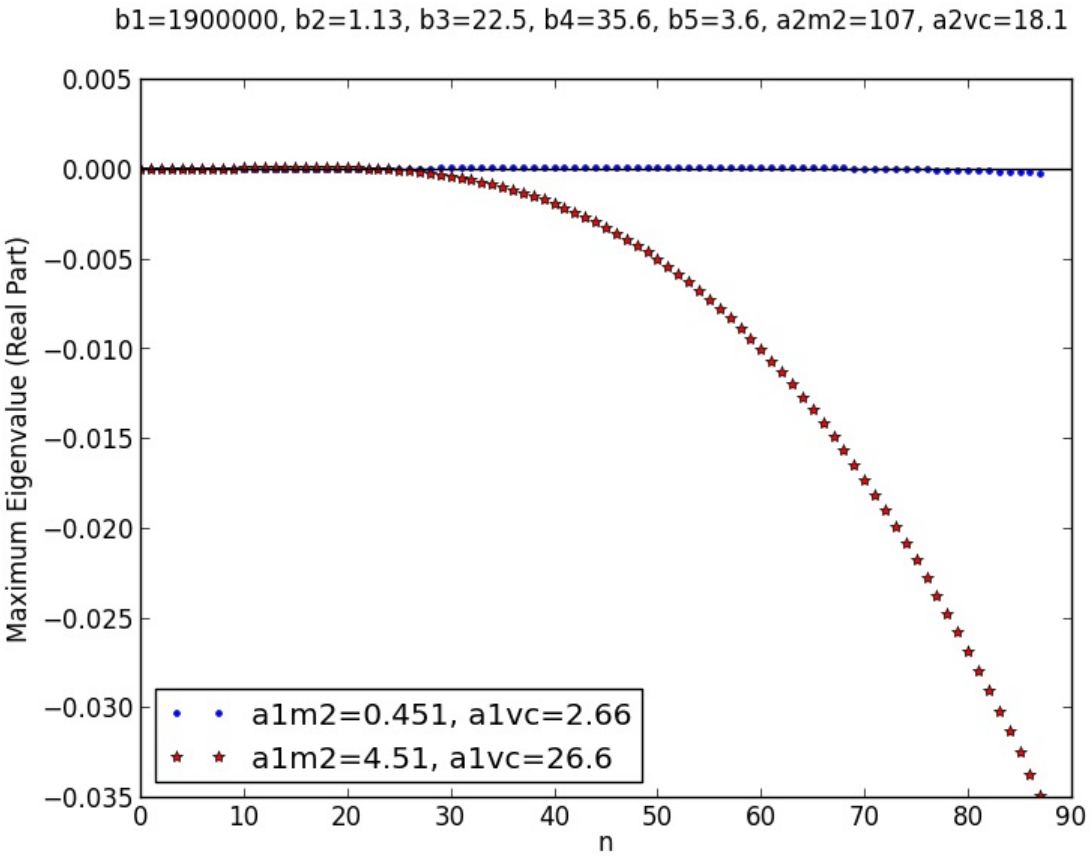

FIGURE H.1: Larger version of figure 6.2(a); comparison plot of two dispersion relations. For both relations, $b_1 = 1.9 \times 10^6$, $b_2 = 1.13$, $b_3 = 22.5$, $b_4 = 35.6$, $b_5 = 3.6$, $a_{2,M2} = 107$, and $a_{2,VC} = 18.1$; for the blue trend, $a_{1,M2} = 0.451$ and $a_{1,VC} = 2.66$; for the red trend, $a_{1,M2} = 4.51$ and $a_{1,VC} = 26.6$. On the x-axis, n is the integer in the wavenumber ($k = n\pi$).

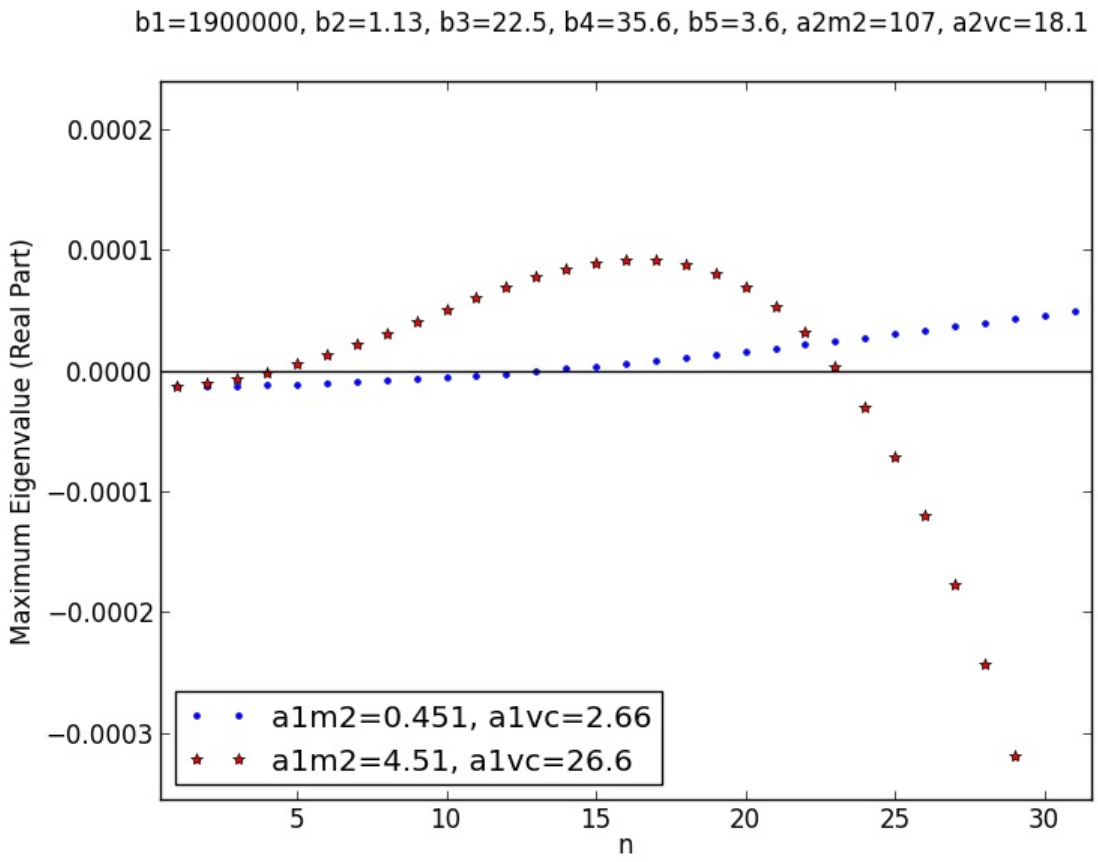

FIGURE H.2: Larger version of figure 6.2(b); comparison plot of two dispersion relations. For both relations, $b_1 = 1.9 \times 10^6$, $b_2 = 1.13$, $b_3 = 22.5$, $b_4 = 35.6$, $b_5 = 3.6$, $a_{2,M2} = 107$, and $a_{2,VC} = 18.1$; for the blue trend, $a_{1,M2} = 0.451$ and $a_{1,VC} = 2.66$; for the red trend, $a_{1,M2} = 4.51$ and $a_{1,VC} = 26.6$. On the x-axis, n is the integer in the wavenumber ($k = n\pi$).

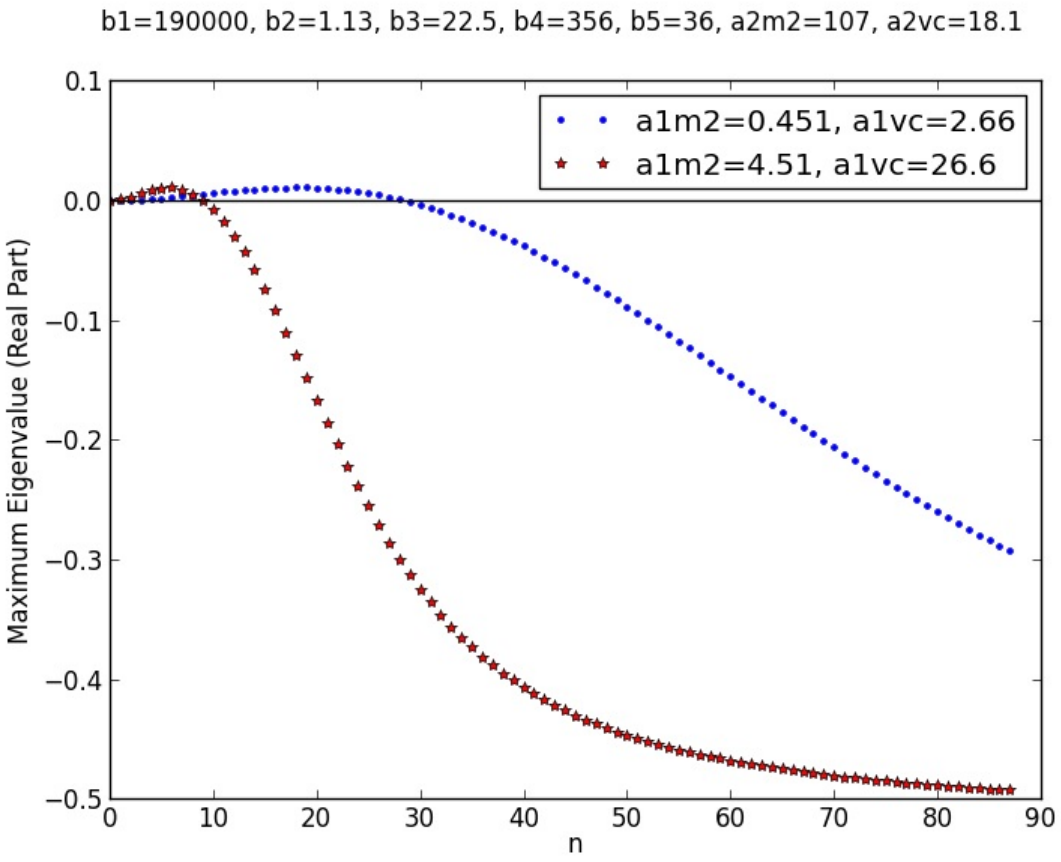

FIGURE H.3: Larger version of figure 6.2(c); comparison plot of two dispersion relations. For both relations, $b_1 = 1.9 \times 10^5$, $b_2 = 1.13$, $b_3 = 22.5$, $b_4 = 356$, $b_5 = 36$, $a_{2,M2} = 107$, and $a_{2,VC} = 18.1$; for the blue trend, $a_{1,M2} = 0.451$ and $a_{1,VC} = 2.66$; for the red trend, $a_{1,M2} = 4.51$ and $a_{1,VC} = 26.6$. On the x-axis, n is the integer in the wavenumber ($k = n\pi$).

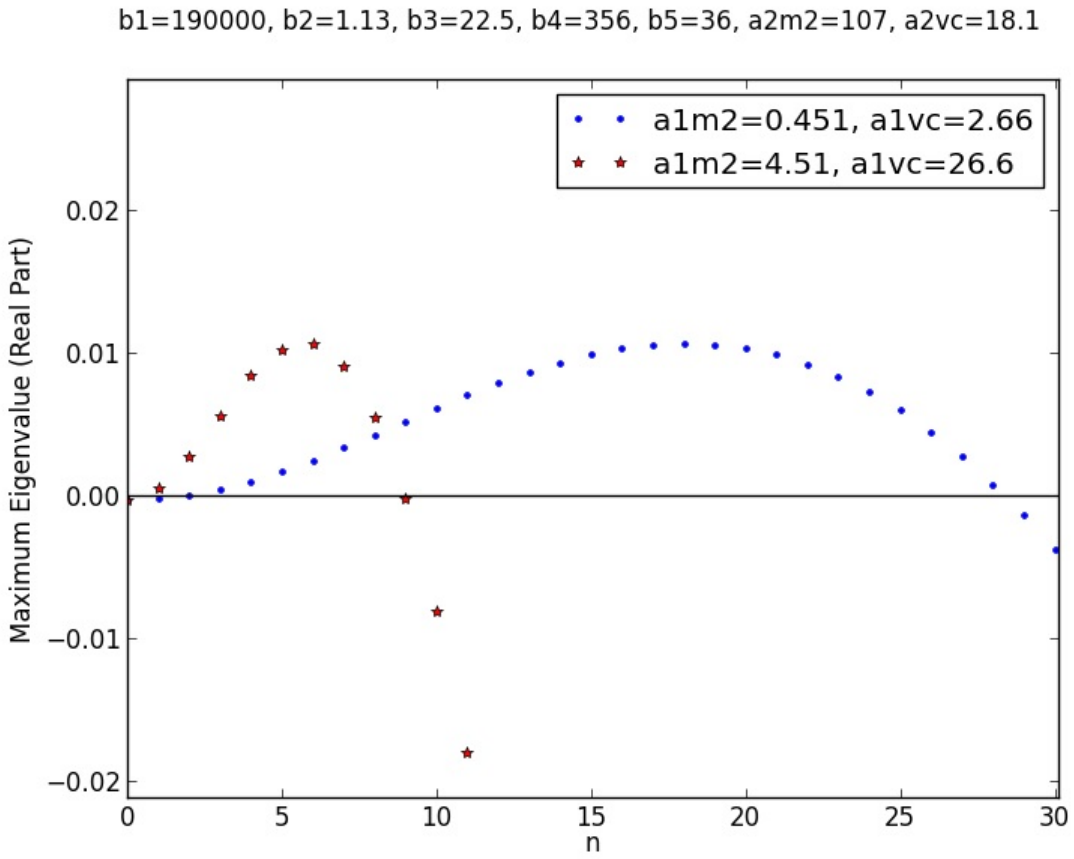

FIGURE H.4: Larger version of figure 6.2(d); comparison plot of two dispersion relations. For both relations, $b_1 = 1.9 \times 10^5$, $b_2 = 1.13$, $b_3 = 22.5$, $b_4 = 356$, $b_5 = 36$, $a_{2,M2} = 107$, and $a_{2,VC} = 18.1$; for the blue trend, $a_{1,M2} = 0.451$ and $a_{1,VC} = 2.66$; for the red trend, $a_{1,M2} = 4.51$ and $a_{1,VC} = 26.6$. On the x-axis, n is the integer in the wavenumber ($k = n\pi$).

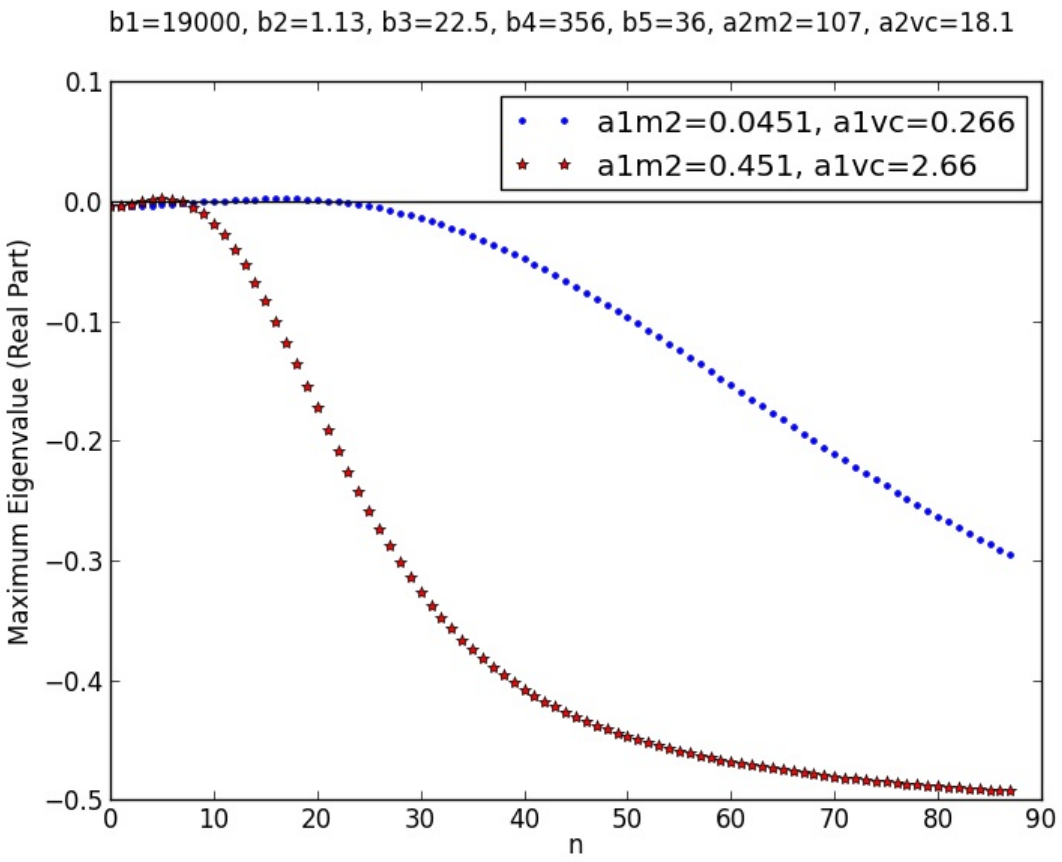

FIGURE H.5: Larger version of figure 6.2(e); comparison plot of two dispersion relations. For both relations, $b_1 = 1.9 \times 10^4$, $b_2 = 1.13$, $b_3 = 22.5$, $b_4 = 356$, $b_5 = 36$, $a_{2,M2} = 107$, and $a_{2,VC} = 18.1$; for the blue trend, $a_{1,M2} = 0.0451$ and $a_{1,VC} = 0.266$; for the red trend, $a_{1,M2} = 0.451$ and $a_{1,VC} = 2.66$. On the x-axis, n is the integer in the wavenumber ($k = n\pi$).

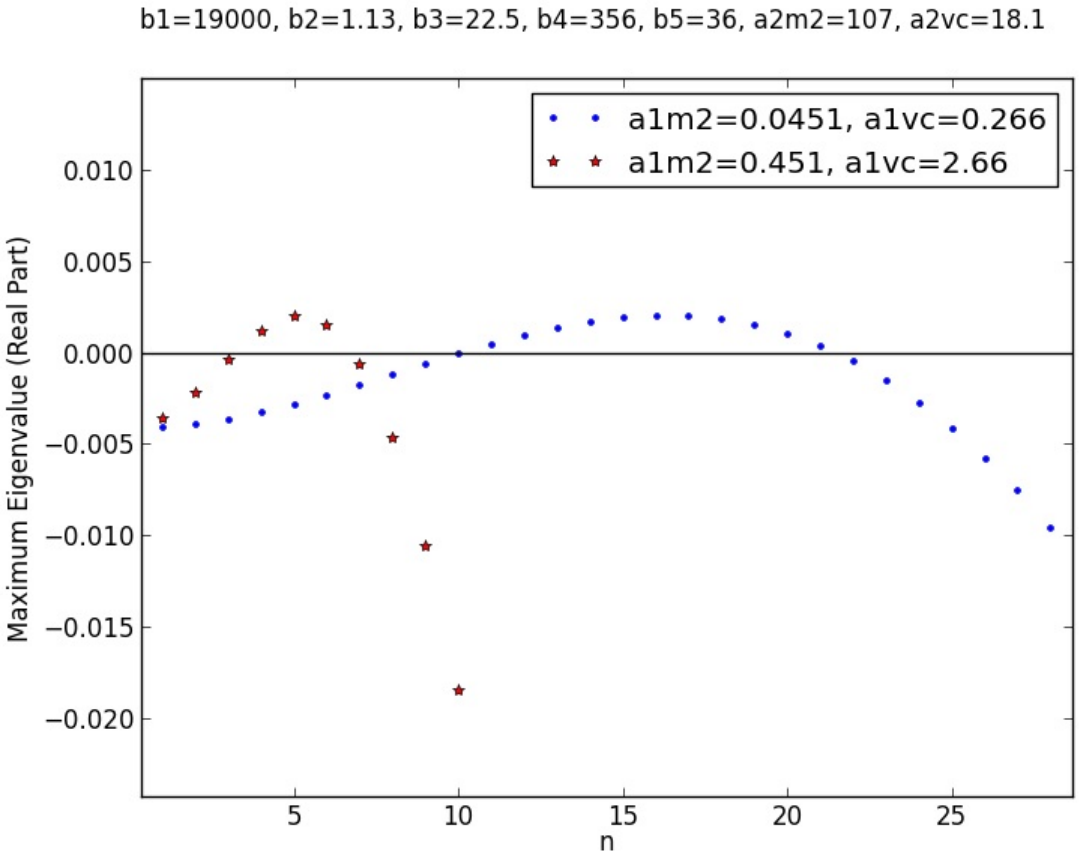

FIGURE H.6: Larger version of figure 6.2(f); comparison plot of two dispersion relations. For both relations, $b_1 = 1.9 \times 10^4$, $b_2 = 1.13$, $b_3 = 22.5$, $b_4 = 356$, $b_5 = 36$, $a_{2,M2} = 107$, and $a_{2,VC} = 18.1$; for the blue trend, $a_{1,M2} = 0.0451$ and $a_{1,VC} = 0.266$; for the red trend, $a_{1,M2} = 0.451$ and $a_{1,VC} = 2.66$. On the x-axis, n is the integer in the wavenumber ($k = n\pi$).

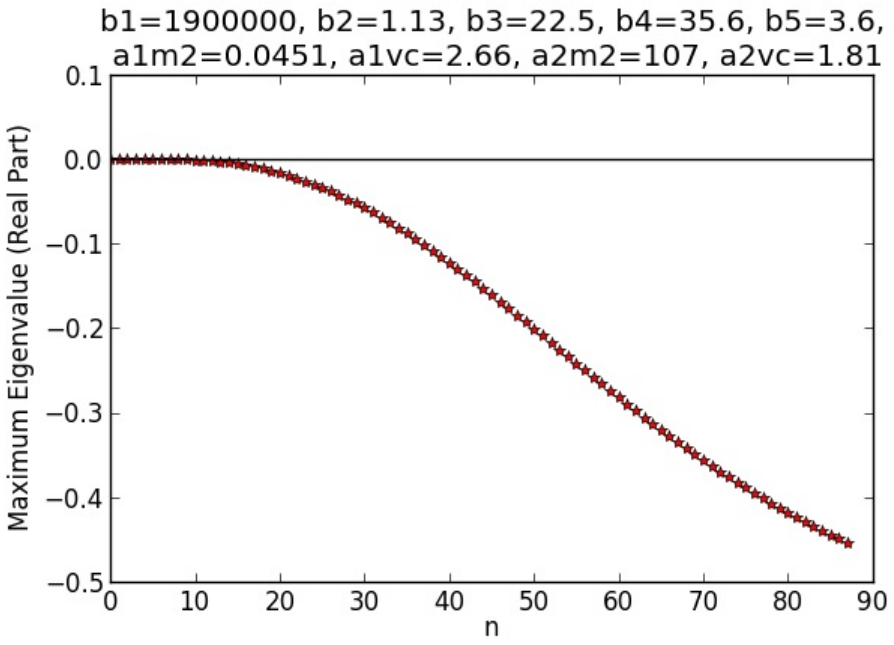

FIGURE H.7: Larger version of figure 6.3(a); a dispersion relation. In this plot, $b_1 = 1.9 \times 10^6$, $b_2 = 1.13$, $b_3 = 22.5$, $b_4 = 35.6$, $b_5 = 3.6$, $a_{1,M2} = 0.0451$, $a_{1,VC} = 2.66$, $a_{2,M2} = 107$, and $a_{2,VC} = 1.81$. On the x-axis, n is the integer in the wavenumber ($k = n\pi$).

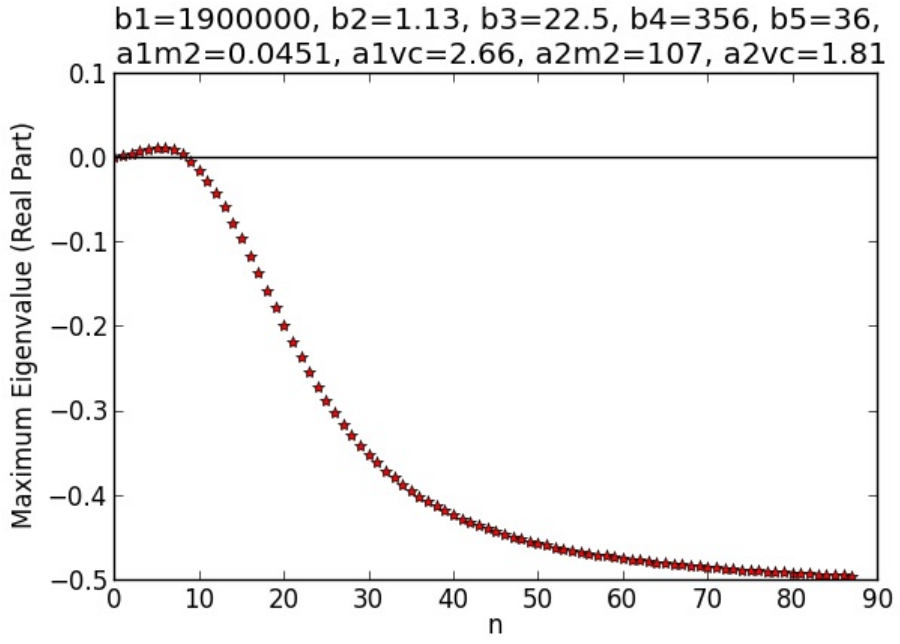

FIGURE H.8: Larger version of figure 6.3(b); a dispersion relation. In this plot, $b_1 = 1.9 \times 10^6$, $b_2 = 1.13$, $b_3 = 22.5$, $b_4 = 356$, $b_5 = 36$, $a_{1,M2} = 0.0451$, $a_{1,VC} = 2.66$, $a_{2,M2} = 107$, and $a_{2,VC} = 1.81$. On the x-axis, n is the integer in the wavenumber ($k = n\pi$).

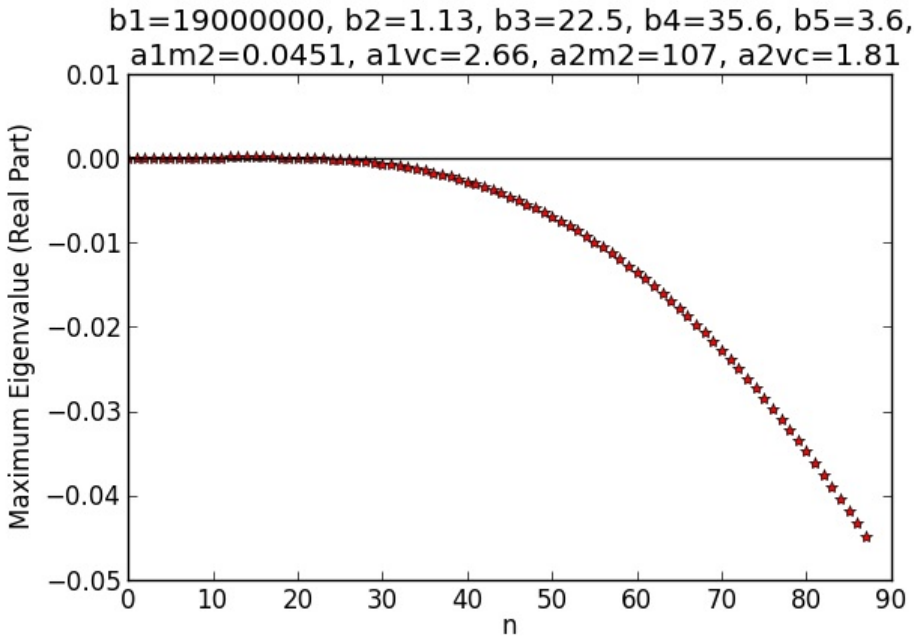

FIGURE H.9: Larger version of figure 6.3(c); a dispersion relation. In this plot, $b_1 = 1.9 \times 10^7$, $b_2 = 1.13$, $b_3 = 22.5$, $b_4 = 35.6$, $b_5 = 3.6$, $a_{1,M2} = 0.0451$, $a_{1,VC} = 2.66$, $a_{2,M2} = 107$, and $a_{2,VC} = 1.81$. On the x-axis, n is the integer in the wavenumber ($k = n\pi$).

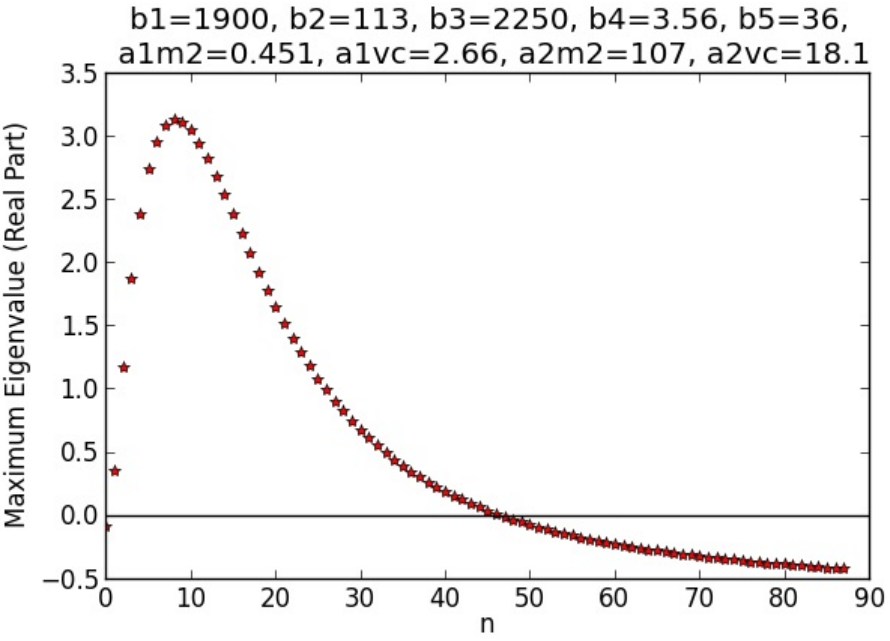

FIGURE H.10: Larger version of figure 6.3(d); a dispersion relation. In this plot, $b_1 = 1.9 \times 10^3$, $b_2 = 113$, $b_3 = 2250$, $b_4 = 3.56$, $b_5 = 36$, $a_{1,M2} = 0.451$, $a_{1,VC} = 2.66$, $a_{2,M2} = 107$, and $a_{2,VC} = 18.1$. On the x-axis, n is the integer in the wavenumber ($k = n\pi$).

Bibliography

Milton Abramowitz and Irene A. Stegun. *Handbook of Mathematical Functions with Formulas, Graphs, and Mathematical Tables*. Dover, New York, ninth dover printing, tenth gpo printing edition, 1964.

Michael Akam. Drosophila development: making stripes inelegantly. *Nature*, 341 (6240):282, 1989a.

Michael Akam. Hox and hom: homologous gene clusters in insects and vertebrates. *Cell*, 57(3):347–349, 1989b.

Hilary L Ashe and James Briscoe. The interpretation of morphogen gradients. *Development*, 133(3):385–394, 2006.

Stephen M Bauer, Richard J Bauer, Zhao-Jun Liu, Haiying Chen, Lee Goldstein, and Omaida C Velazquez. Vascular endothelial growth factor-c promotes vasculogenesis, angiogenesis, and collagen constriction in three-dimensional collagen gels. *Journal of vascular surgery*, 41(4):699–707, 2005.

Eleni Bazigou, John T Wilson, and James E Moore. Primary and secondary lymphatic valve development: Molecular, functional and mechanical insights. *Microvascular research*, 96:38–45, 2014.

DA Berk, F Yuan, M Leunig, and RK Jain. Fluorescence photobleaching with spatial fourier analysis: measurement of diffusion in light-scattering media. *Biophysical journal*, 65(6):2428–2436, 1993.

Arianna Bianchi, Kevin J Painter, and Jonathan A Sherratt. A mathematical model for lymphangiogenesis in normal and diabetic wounds. *Journal of Theoretical Biology*, 383:61–86, 2015.

Arianna Bianchi, Kevin J Painter, and Jonathan A Sherratt. Spatio-temporal models of lymphangiogenesis in wound healing. *arXiv preprint arXiv:1604.04654*, 2016.

Kendrick C Boardman and Melody A Swartz. Interstitial flow as a guide for lymphangiogenesis. *Circulation research*, 92(7):801–808, 2003.

Frank L Bos, Maresa Caunt, Josi Peterson-Maduro, Lara Planas-Paz, Joe Kowalski, Terhi Karpanen, Andreas van Impel, Raymond Tong, James A Ernst, Jeroen Korving, et al. Ccbe1 is essential for mammalian lymphatic vascular development and enhances the lymphangiogenic effect of vascular endothelial growth factor-c in vivo. *Circulation research*, 109(5):486–491, 2011.

Jerome W Breslin. Mechanical forces and lymphatic transport. *Microvascular research*, 96:46–54, 2014.

Françoise Bruyère, Laurence Melen-Lamalle, Silvia Blacher, Guy Roland, Marc Thiry, Lieve Moons, Francis Frankenne, Peter Carmeliet, Kari Alitalo, Claude Libert, et al. Modeling lymphangiogenesis in a three-dimensional culture system. *Nature methods*, 5(5):431–437, 2008.

Jeroen Bussmann, Frank L Bos, Akihiro Urasaki, Koichi Kawakami, Henricus J Duckers, and Stefan Schulte-Merker. Arteries provide essential guidance cues for lymphatic endothelial cells in the zebrafish trunk. *Development*, 137(16):2653–2657, 2010.

Vincent Castets, Etiennette Dulos, Jacques Boissonade, and Patrick De Kepper. Experimental evidence of a sustained standing turing-type nonequilibrium chemical pattern. *Physical Review Letters*, 64(24):2953, 1990.

Young Ryun Cha, Misato Fujita, Matthew Butler, Sumio Isogai, Eva Kochhan, Arndt F Siekmann, and Brant M Weinstein. Chemokine signaling directs trunk lymphatic network formation along the preexisting blood vasculature. *Developmental cell*, 22(4):824–836, 2012.

Hong Chen, Courtney Griffin, Lijun Xia, and R Sathish Srinivasan. Molecular and cellular mechanisms of lymphatic vascular maturation. *Microvascular research*, 96: 16–22, 2014.

M Coffindaffer-Wilson, MP Criag, and JR Hove. Determination of lymphatic vascular identity and developmental timecourse in zebrafish (danio rerio). *Lymphology*, 44(1): 1–12, 2011a.

Mikah Coffindaffer-Wilson, Michael P Craig, and Jay R Hove. Normal interstitial flow is critical for developmental lymphangiogenesis in the zebrafish. *Lymphatic research and biology*, 9(3):151–158, 2011b.

Yong Deng, Deepak Atri, Anne Eichmann, and Michael Simons. Endothelial erk signaling controls lymphatic fate specification. *The Journal of clinical investigation*, 123(3):1202, 2013.

Benoit Detry, Charlotte Erpicum, Jenny Paupert, Silvia Blacher, Catherine Maillard, Françoise Bruyère, Hélène Pendeville, Thibault Remacle, Vincent Lambert, Cédric

Balsat, et al. Matrix metalloproteinase-2 governs lymphatic vessel formation as an interstitial collagenase. *Blood*, 119(21):5048–5056, 2012.

Danielle L Drayton, Shan Liao, Rawad H Mounzer, and Nancy H Ruddle. Lymphoid organ development: from ontogeny to neogenesis. *Nature immunology*, 7(4):344–353, 2006.

P. DuChateau and D. Zachmann. *Schaum's Outline of Partial Differential Equations*. Schaum's Outline Series. McGraw-Hill Education, 2011. ISBN 9780071756181.

Andrew D Economou, Atsushi Ohazama, Thantrira Porntaveetus, Paul T Sharpe, Shigeru Kondo, M Albert Basson, Amel Gritli-Linde, Martyn T Cobourne, and Jeremy BA Green. Periodic stripe formation by a turing mechanism operating at growth zones in the mammalian palate. *Nature genetics*, 44(3):348–351, 2012.

Mac V Edds Jr. Development of collagen in the frog embryo. *Proceedings of the National Academy of Sciences of the United States of America*, 44(4):296, 1958.

Albert Einstein. Über die von der molekularkinetischen theorie der wärme geforderte bewegung von in ruhenden flüssigkeiten suspendierten teilchen. *Annalen der physik*, 322(8):549–560, 1905.

Joakim Eriksson and Jan Löfberg. Development of the hypochord and dorsal aorta in the zebrafish embryo (danio rerio). *Journal of morphology*, 244(3):167–176, 2000.

C.A.J. Fletcher. *Computational techniques for fluid dynamics; Vol 1 (2nd ed)*. Springer, Springer, NY (United States), Dec 1991.

Mark E Fleury, Kendrick C Boardman, and Melody A Swartz. Autologous morphogen gradients by subtle interstitial flow and matrix interactions. *Biophysical journal*, 91 (1):113–121, 2006.

Robert A Frcitas. Exploratory design in medical nanotechnology: a mechanical artificial red cell. *Artificial Cells, Blood Substitutes and Biotechnology*, 26(4): 411–430, 1998.

Alfred Gierer and Hans Meinhardt. A theory of biological pattern formation. *Kybernetik*, 12(1):30–39, 1972.

Michelle F Goody, Roger B Sher, and Clarissa A Henry. Hanging on for the ride: Sadhesion to the extracellular matrix mediates cellular responses in skeletal muscle morphogenesis and disease. *Developmental biology*, 2015.

Aniket V Gore, Kathryn Monzo, Young R Cha, Weijun Pan, and Brant M Weinstein. Vascular development in the zebrafish. *Cold Spring Harbor perspectives in medicine*, 2(5):a006684, 2012.

Jeremy BA Green and James Sharpe. Positional information and reaction-diffusion: two big ideas in developmental biology combine. *Development*, 142(7):1203–1211, 2015.

JB Gurdon and P-Y Bourillot. Morphogen gradient interpretation. *Nature*, 413(6858): 797–803, 2001.

H Gutfreund. *Proteins: structures and molecular properties*. Wiley Online Library, 1993.

Yasmin L Hashambhoy, John C Chappell, Shayn M Peirce, Victoria L Bautch, and Feilim Mac Gabhann. Computational modeling of interacting vegf and soluble vegf receptor concentration gradients. *Frontiers in physiology*, 2, 2011.

Cara-Lynn E Helm, Mark E Fleury, Andreas H Zisch, Federica Boschetti, and Melody A Swartz. Synergy between interstitial flow and vegf directs capillary morphogenesis in vitro through a gradient amplification mechanism. *Proceedings of the National Academy of Sciences of the United States of America*, 102(44): 15779–15784, 2005.

Cara-Lynn E Helm, Andreas Zisch, and Melody A Swartz. Engineered blood and lymphatic capillaries in 3-d vegf-fibrin-collagen matrices with interstitial flow. *Biotechnology and bioengineering*, 96(1):167–176, 2007.

Charles Heppell, Tiina Roose, and Giles Richardson. A model for interstitial drainage through a sliding lymphatic valve. *Bulletin of mathematical biology*, 77(6): 1101–1131, 2015.

Karlien Hermans, Filip Claes, Wouter Vandevelde, Wei Zheng, Ilse Geudens, Fabrizio Orsenigo, Frederik De Smet, Evisa Gjini, Kristof Anthonis, Bin Ren, et al. Role of synectin in lymphatic development in zebrafish and frogs. *Blood*, 116(17):3356–3366, 2010.

Benjamin M Hogan, Frank L Bos, Jeroen Bussmann, Merlijn Witte, Neil C Chi, Henricus J Duckers, and Stefan Schulte-Merker. Ccbe1 is required for embryonic lymphangiogenesis and venous sprouting. *Nature genetics*, 41(4):396–398, 2009.

Norman Hu, David Sedmera, H Joseph Yost, and Edward B Clark. Structure and function of the developing zebrafish heart. *The Anatomical Record*, 260(2):148–157, 2000.

Ke-Jin Huang and Li-Hua Sui. The relevance and role of vascular endothelial growth factor c, matrix metalloproteinase-2 and e-cadherin in epithelial ovarian cancer. *Medical Oncology*, 29(1):318–323, 2012.

George S Huntington and Charles FW McClure. The anatomy and development of the jugular lymph sacs in the domestic cat (felis domestica). *American Journal of Anatomy*, 10(1):177–312, 1910.

Atsuo Iida, Kazuya Sakaguchi, Kiyoaki Sato, Hidetoshi Sakurai, Daigo Nishimura, Aya Iwaki, Miki Takeuchi, Makoto Kobayashi, Kazuyo Misaki, Shigenobu Yonemura, et al. Metalloprotease-dependent onset of blood circulation in zebrafish. *Current Biology*, 20(12):1110–1116, 2010.

Sumio Isogai, Masaharu Horiguchi, and Brant M Weinstein. The vascular anatomy of the developing zebrafish: an atlas of embryonic and early larval development. *Developmental biology*, 230(2):278–301, 2001.

Sumio Isogai, Nathan D Lawson, Saioa Torrealday, Masaharu Horiguchi, and Brant M Weinstein. Angiogenic network formation in the developing vertebrate trunk. *Development*, 130(21):5281–5290, 2003.

Rakesh K Jain. Transport of molecules across tumor vasculature. *Cancer and Metastasis Reviews*, 6(4):559–593, 1987.

Michael Jeltsch, Sawan Kumar Jha, Denis Tvorogov, Andrey Anisimov, Veli-Matti Leppänen, Tanja Holopainen, Riikka Kivelä, Sagrario Ortega, Terhi Kärpanen, and Kari Alitalo. Ccbe1 enhances lymphangiogenesis via a disintegrin and metalloprotease with thrombospondin motifs-3–mediated vascular endothelial growth factor-c activation. *Circulation*, 129(19):1962–1971, 2014.

Jason R Jessen. Recent advances in the study of zebrafish extracellular matrix proteins. *Developmental biology*, 2014.

Rui-Cheng Ji. Lymphatic endothelial cells, lymphangiogenesis, and extracellular matrix. *Lymphatic research and biology*, 4(2):83–100, 2006.

Vladimir Joukov, Katri Pajusola, Arja Kaipainen, Dmitri Chilov, Isto Lahtinen, Eola Kukk, Olli Saksela, Nisse Kalkkinen, and Kari Alitalo. A novel vascular endothelial growth factor, vegf-c, is a ligand for the flt4 (vegfr-3) and kdr (vegfr-2) receptor tyrosine kinases. *The EMBO journal*, 15(2):290, 1996.

Vladimir Joukov, Tarja Sorsa, Vijay Kumar, Michael Jeltsch, Lena Claesson-Welsh, Yihai Cao, Olli Saksela, Nisse Kalkkinen, and Kari Alitalo. Proteolytic processing regulates receptor specificity and activity of vegf-c. *The EMBO journal*, 16(13): 3898–3911, 1997.

Emmanouil D Karagiannis and Aleksander S Popel. A theoretical model of type i collagen proteolysis by matrix metalloproteinase (mmp) 2 and membrane type 1 mmp in the presence of tissue inhibitor of metalloproteinase 2. *Journal of Biological Chemistry*, 279(37):39105–39114, 2004.

Emmanouil D Karagiannis and Aleksander S Popel. Distinct modes of collagen type i proteolysis by matrix metalloproteinase (mmp) 2 and membrane type i mmp during the migration of a tip endothelial cell: insights from a computational model. *Journal of theoretical biology*, 238(1):124–145, 2006.

Linda Klotz, Sophie Norman, Joaquim Miguel Vieira, Megan Masters, Mala Rohling, Karina N Dubé, Sveva Bollini, Fumio Matsuzaki, Carolyn A Carr, and Paul R Riley. Cardiac lymphatics are heterogeneous in origin and respond to injury. *Nature*, 2015.

A Köhn-Luque, W de Back, Y Yamaguchi, K Yoshimura, MA Herrero, and T Miura. Dynamics of vegf matrix-retention in vascular network patterning. *Physical biology*, 10(6):066007, 2013.

Katarzyna Koltowska, Kelly L Betterman, Natasha L Harvey, and Benjamin M Hogan. Getting out and about: the emergence and morphogenesis of the vertebrate lymphatic vasculature. *Development*, 140(9):1857–1870, 2013.

Magda Kucia, Kacper Jankowski, Ryan Reca, Marcin Wysoczynski, Laura Bandura, Daniel J Allendorf, Jin Zhang, Janina Ratajczak, and Mariusz Z Ratajczak. Cxcr4–sdf-1 signalling, locomotion, chemotaxis and adhesion. *Journal of molecular histology*, 35(3):233–245, 2004.

Christian Kunert, James W Baish, Shan Liao, Timothy P Padera, and Lance L Munn. Mechanobiological oscillators control lymph flow. *Proceedings of the National Academy of Sciences*, 112(35):10938–10943, 2015.

JR Levick. Flow through interstitium and other fibrous matrices. *Experimental Physiology*, 72(4):409–437, 1987.

Antoine Louveau, Igor Smirnov, Timothy J Keyes, Jacob D Eccles, Sherin J Rouhani, J David Peske, Noel C Derecki, David Castle, James W Mandell, Kevin S Lee, et al. Structural and functional features of central nervous system lymphatic vessels. *Nature*, 2015.

Sophie Lutter and Taija Makinen. Regulation of lymphatic vasculature by extracellular matrix. In *Developmental Aspects of the Lymphatic Vascular System*, pages 55–65. Springer, 2014.

Hélène Maby-El Hajjami and Tatiana V Petrova. Developmental and pathological lymphangiogenesis: from models to human disease. *Histochemistry and cell biology*, 130(6):1063–1078, 2008.

Taija Mäkinen, Tanja Veikkola, Satu Mustjoki, Terhi Karpanen, Bruno Catimel, Edouard C Nice, Lyn Wise, Andrew Mercer, Heinrich Kowalski, Dontscho Kerjaschki, et al. Isolated lymphatic endothelial cells transduce growth, survival and migratory signals via the vegf-c/d receptor vegfr-3. *The EMBO journal*, 20(17): 4762–4773, 2001.

Erik Maquoi, Francis Frankenne, Agnès Noël, Hans-Willi Krell, Frank Grams, and Jean-Michel Foidart. Type iv collagen induces matrix metalloproteinase 2 activation in ht1080 fibrosarcoma cells. *Experimental cell research*, 261(2):348–359, 2000.

Anna Marciniak-Czochra. *Reaction-Diffusion-ODE Models of Pattern Formation*, pages 387–438. Springer International Publishing, Cham, 2015. ISBN 978-3-319-11322-7.

KN Margaris and Richard Anthony Black. Modelling the lymphatic system: challenges and opportunities. *Journal of The Royal Society Interface*, 9(69):601–612, 2012.

Sean P McGee, Ellen M Cooper, Heather M Stapleton, and David C Volz. Early zebrafish embryogenesis is susceptible to developmental tdcpp exposure. *Environmental health perspectives*, 120(11):1585, 2012.

K.W. Morton and D.F. Mayers. *Numerical Solution of Partial Differential Equations*. Numerical Solution of Partial Differential Equations: An Introduction. Cambridge University Press, 1994. ISBN 9780521418553.

Patrick Müller, Katherine W Rogers, Ben M Jordan, Joon S Lee, Drew Robson, Sharad Ramanathan, and Alexander F Schier. Differential diffusivity of nodal and lefty underlies a reaction-diffusion patterning system. *Science*, 336(6082):721–724, 2012.

Timothy S Mulligan and Brant M Weinstein. Emerging from the pac: Studying zebrafish lymphatic development. *Microvascular research*, 96:23–30, 2014.

James Murray. *Mathematical Biology*. Springer-Verlag, 2 edition, 1993.

Andrzej Nasiadka and Matthew D Clark. Zebrafish breeding in the laboratory environment. *ILAR Journal*, 53(2):161–168, 2012.

Chee Ping Ng, Cara-Lynn E Helm, and Melody A Swartz. Interstitial flow differentially stimulates blood and lymphatic endothelial cell morphogenesis in vitro. *Microvascular research*, 68(3):258–264, 2004.

J Nicenboim, G Malkinson, T Lupo, L Asaf, Y Sela, O Mayseless, L Gibbs-Bar, N Senderovich, T Hashimshony, M Shin, et al. Lymphatic vessels arise from specialized angioblasts within a venous niche. *Nature*, 2015.

Agnès Noel and Nor Eddine Sounni. Mmp-mediated collagen remodeling and vessel functions. In *Proteases: Structure and Function*, pages 471–489. Springer, 2013.

AG Ogston, BN Preston, and JD Wells. On the transport of compact particles through solutions of chain-polymers. *Proceedings of the Royal Society of London. A. Mathematical and Physical Sciences*, 333(1594):297–316, 1973.

Kazuhide S Okuda, Jonathan W Astin, June P Misa, Maria V Flores, Kathryn E Crosier, and Philip S Crosier. lyve1 expression reveals novel lymphatic vessels and new mechanisms for lymphatic vessel development in zebrafish. *Development*, 139 (13):2381–2391, 2012.

Guillermo Oliver. Lymphatic vasculature development. *Nature Reviews Immunology*, 4 (1):35–45, 2004.

V Ottani, M Raspanti, and A Ruggeri. Collagen structure and functional implications. *Micron*, 32(3):251–260, 2001.

David Henry Pashley, FR Tay, C Yiu, M Hashimoto, L Breschi, RM Carvalho, and S Ito. Collagen degradation by host-derived enzymes during aging. *Journal of Dental Research*, 83(3):216–221, 2004.

Jenny Paupert, Nor Eddine Sounni, and Agnès Noël. Lymphangiogenesis in post-natal tissue remodeling: lymphatic endothelial cell connection with its environment. *Molecular aspects of medicine*, 32(2):146–158, 2011.

Cathy Pichol-Thievend, Benjamin M Hogan, and Mathias Francois. Lymphatic vascular specification and its modulation during embryonic development. *Microvascular research*, 96:3–9, 2014.

Darwin J Prockop and Kari I Kivirikko. Collagens: molecular biology, diseases, and potentials for therapy. *Annual review of biochemistry*, 64(1):403–434, 1995.

Jelena Raspopovic, Luciano Marcon, Laura Russo, and James Sharpe. Digit patterning is controlled by a bmp-sox9-wnt turing network modulated by morphogen gradients. *Science*, 345(6196):566–570, 2014.

Joseph M Rutkowski and Melody A Swartz. A driving force for change: interstitial flow as a morphoregulator. *Trends in cell biology*, 17(1):44–50, 2007.

Florence R Sabin. On the origin of the lymphatic system from the veins and the development of the lymph hearts and thoracic duct in the pig. *American Journal of Anatomy*, 1(3):367–389, 1902.

JW Saunders and MT Gasseling. Ectodermal-mesenchymal interactions in the origin of limb symmetry. *Epithelial-mesenchymal interactions*, pages 78–97, 1968.

Alexander F Schier. Nodal morphogens. *Cold Spring Harbor perspectives in biology*, 1 (5):a003459, 2009.

Stefan Schulte-Merker, Amélie Sabine, and Tatiana V Petrova. Lymphatic vascular morphogenesis in development, physiology, and disease. *The Journal of cell biology*, 193(4):607–618, 2011.

Zhong-Dong Shi and John M Tarbell. Fluid flow mechanotransduction in vascular smooth muscle cells and fibroblasts. *Annals of biomedical engineering*, 39(6): 1608–1619, 2011.

Hidetaka Shiratori and Hiroshi Hamada. The left-right axis in the mouse: from origin to morphology. *Development*, 133(11):2095–2104, 2006.

Geraldine Siegfried, Ajoy Basak, James A Cromlish, Suzanne Benjannet, Jadwiga Marcinkiewicz, Michel Chrétien, Nabil G Seidah, Abdel-Majid Khatib, et al. The secretory proprotein convertases furin, pc5, and pc7 activate vegf-c to induce tumorigenesis. *The Journal of clinical investigation*, 111(11):1723–1732, 2003.

Jonathan W Song and Lance L Munn. Fluid forces control endothelial sprouting. *Proceedings of the National Academy of Sciences*, 108(37):15342–15347, 2011.

Steven A Stacker, Steven P Williams, Tara Karnezis, Ramin Shayan, Stephen B Fox, and Marc G Achen. Lymphangiogenesis and lymphatic vessel remodelling in cancer. *Nature Reviews Cancer*, 14(3):159–172, 2014.

Mark D Sternlicht and Zena Werb. How matrix metalloproteinases regulate cell behavior. *Annual review of cell and developmental biology*, 17:463, 2001.

Melody A Swartz and Mark E Fleury. Interstitial flow and its effects in soft tissues. *Annu. Rev. Biomed. Eng.*, 9:229–256, 2007.

Marta Toth, Sonia Hernandez-Barrantes, Pamela Osenkowski, M Margarida Bernardo, David C Gervasi, Yoichiro Shimura, Oussama Meroueh, Lakshmi P Kotra, Beatriz G Gálvez, Alicia G Arroyo, et al. Complex pattern of membrane type 1 matrix metalloproteinase shedding regulation by autocatalytic cell surface inactivation of active enzyme. *Journal of Biological Chemistry*, 277(29):26340–26350, 2002.

Alan Mathison Turing. The chemical basis of morphogenesis. *Philosophical Transactions of the Royal Society of London. Series B, Biological Sciences*, 237(641): 37–72, 1952.

Andreas van Impel and Stefan Schulte-Merker. A fisheye view on lymphangiogenesis. In *Developmental Aspects of the Lymphatic Vascular System*, pages 153–165. Springer, 2014.

Prakash Vempati, Feilim Mac Gabhann, and Aleksander S Popel. Quantifying the proteolytic release of extracellular matrix-sequestered vegf with a computational model. *PloS one*, 5(7):e11860, 2010.

Daniel Vittet. Lymphatic collecting vessel maturation and valve morphogenesis. *Microvascular research*, 96:31–37, 2014.

Helge Wiig, Doruk Keskin, and Raghu Kalluri. Interaction between the extracellular matrix and lymphatics: consequences for lymphangiogenesis and lymphatic function. *Matrix Biology*, 29(8):645–656, 2010.

Lewis Wolpert. Positional information and the spatial pattern of cellular differentiation. *Journal of theoretical biology*, 25(1):1–47, 1969.

Lewis Wolpert. One hundred years of positional information. *Trends in Genetics*, 12 (9):359–364, 1996.

Ying Yang and Guillermo Oliver. Development of the mammalian lymphatic vasculature. *J Clin Invest*, 124(3):888–897, 2014a.

Ying Yang and Guillermo Oliver. Transcriptional control of lymphatic endothelial cell type specification. In *Developmental Aspects of the Lymphatic Vascular System*, pages 5–22. Springer, 2014b.

Karina Yaniv, Sumio Isogai, Daniel Castranova, Louis Dye, Jiro Hitomi, and Brant M Weinstein. Live imaging of lymphatic development in the zebrafish. *Nature medicine*, 12(6):711–716, 2006.

Pengchun Yu, Joe K Tung, and Michael Simons. Lymphatic fate specification: An erk-controlled transcriptional program. *Microvascular research*, 96:10–15, 2014.